



# VYSOKÉ UČENÍ TECHNICKÉ V BRNĚ

BRNO UNIVERSITY OF TECHNOLOGY

## FAKULTA ELEKTROTECHNIKY A KOMUNIKAČNÍCH TECHNOLOGIÍ

FACULTY OF ELECTRICAL ENGINEERING AND COMMUNICATION

### ÚSTAV MIKROELEKTRONIKY

DEPARTMENT OF MICROELECTRONICS

## UHLÍKOVÉ MATERIÁLY V MIKROELEKTRONICE A SENZORICE

CARBON MATERIALS USED IN MICROELECTRONICS AND SENSORS

### HABILITAČNÍ PRÁCE

HABILITATION THESIS

### AUTOR PRÁCE

AUTHOR

Ing. Jan Pekárek, Ph.D.

BRNO 2019

## **Abstrakt**

Práce pojednává o vědeckých výsledcích z vybraných experimentálních a literárních studií autora v oblasti uhlíkových materiálů v mikroelektronice a senzorce. Tyto výsledky byly publikovány v osmi článcích v impaktovaných časopisech během působení autora na Ústavu mikroelektroniky, FEKT VUT, v letech 2015–2019. V práci jsou popsány a diskutovány dva typy studovaných uhlíkových materiálů, a to nanotrubic a grafenu. Uhlíkové nanotrubic jsou zde využívány pro infračervené snímání a tlakový senzor na bázi emise elektrickým polem. Výzkum věnovaný grafenu se zabývá novou metodou modulování fyzikálních vlastností a charakterizace konkrétně monovrstvy grafenu.

## **Abstract**

The thesis summarizes the research results from author selected experimental and literature studies in the field of carbon materials used in microelectronics and for sensing purposes. These research surveys were published in eight papers in impacted journals from 2015 till 2019. The thesis is divided into two main chapters according to the studied carbon material, namely nanotubes for bolometer application and field emission pressure sensor. The chapter related to graphene is focused on research of a new method for modulation of graphene physical properties due to controlled induced mechanical strain.

## **Klíčová slova**

Uhlíkové materiály, nanotrubic, grafen, emise elektrickým polem, infračervené snímání, bolometr, mechanická deformace.

## **Keywords**

Carbon materials, nanotubes, graphene, field emission, infrared radiation sensing, bolometer, mechanical deformation.

# Obsah

Abstrakt .....	2
Abstract.....	2
Klíčová slova .....	2
Keywords.....	2
Obsah.....	3
Úvod .....	4
1 Uhlíkové nanotrubicce .....	6
1.1 Studie emisního senzoru pro měření tlaku s uhlíkovými nanotubicemi .....	7
1.1.1 Návrh a princip emisního senzoru tlaku .....	8
1.1.2 Charakterizace emisního senzoru tlaku .....	8
1.2 Uhlíkové nanotrubicce pro infračervené snímání .....	11
1.2.1 Depozice uhlíkových nanotubic na membrány bolometrů .....	12
1.2.2 Integrovaný vyhodnocovací obvod.....	15
1.2.3 Testování bolometru s integrovaným obvodem.....	16
1.2.4 Řádkový systém bolometrů.....	19
2 Grafen .....	22
2.1 Modulace fyzikálních vlastností grafenu pomocí mechanické deformace .....	23
Závěr.....	27
Reference.....	28
Seznam použitých zkratk .....	33
Vybrané publikace autora k tématu habilitační práce jako přílohy .....	34
Příloha 1.....	35
Příloha 2.....	42
Příloha 3.....	61
Příloha 4.....	69
Příloha 5.....	78
Příloha 6.....	86
Příloha 7.....	92
Příloha 8.....	100

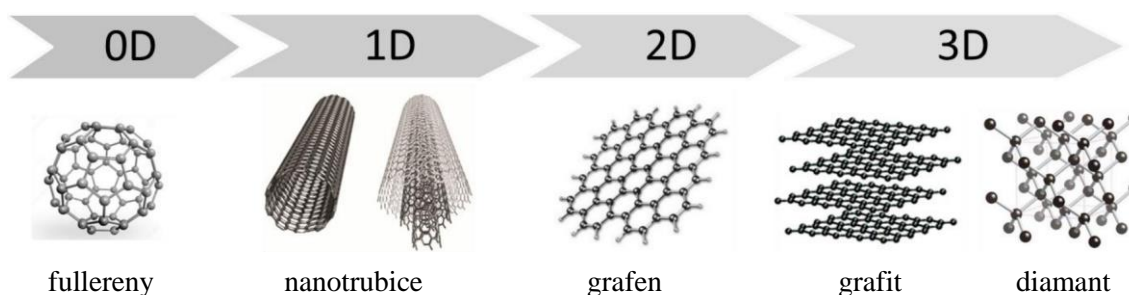
## Úvod

Uhlík je chemický prvek ze IV.A skupiny periodické tabulky. Uhlík tvoří základní stavební kámen všech organických sloučenin, a tím vlastně poskytuje základ života na Zemi. Jeho využití je v mnoha důležitých technologických oblastech od léčiv až po syntetické materiály, a to díky schopnosti uhlíku vázat se na sebe a také na téměř všechny další prvky. Výsledná strukturní rozmanitost organických sloučenin a molekul je doprovázena širokým spektrem chemických a fyzikálních vlastností [1]. Nástroje moderní chemické syntézy umožňují přizpůsobení těchto vlastností řízenou kombinací stavebních a funkčních stavebních bloků v nových cílových systémech.

Elementární uhlík existuje ve dvou přírodních strukturních formách (alotropích) – diamantu a grafitu [2]. Obě formy vykazují jedinečné fyzikální vlastnosti, jako je tvrdost u diamantu, tepelná a elektrická vodivost nebo lubrikační vlastnosti u grafitu. Další uhlíkové alotropie je možné získat změnou vazebného páru v sítích skládajících se z atomů uhlíku [1,3-5].

Podle rozměrů v prostoru (obr. 1), lze uhlíkové nanomateriály rozdělit do čtyř skupin [6]:

- i) nulová dimenze (0D), jako jsou kvantové tečky na bázi uhlíku a fullereny,
- ii) jednorozměrné (1D), jako jsou uhlíkové nanotrubičky (CNTs),
- iii) dvourozměrné (2D), jako jsou grafeny a jejich deriváty,
- iv) třírozměrné (3D), jako jsou grafit a diamant.



Obr. 1: Alotropie uhlíku v mnoha dimenzích. Převzato a upraveno z [7].

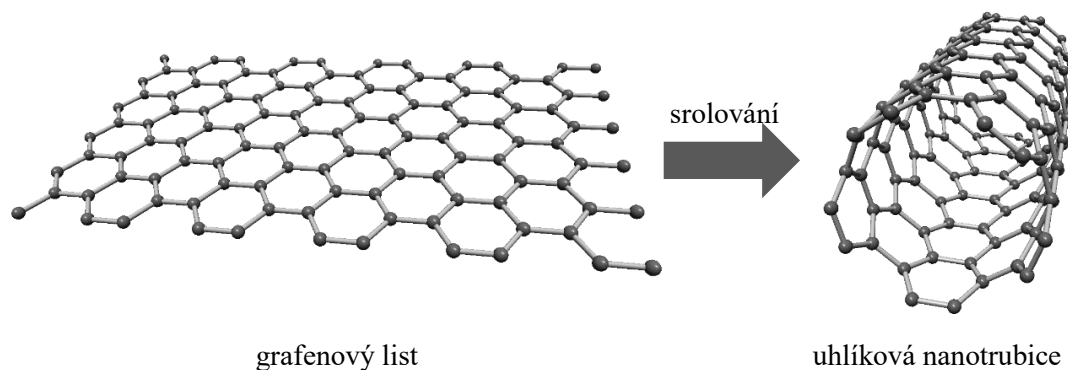
Diamant spolu s grafitem představoval po dlouhou dobu jediné známé alotropy uhlíku. Tato situace se změnila v roce 1985 [8] s příchodem fullerenů, které byly poprvé syntetizovány skupinou vědců z Rice univerzity v Houstonu. Tento objev znamenal začátek éry alotropů syntetického uhlíku a není divu, že za objev fullerenů dostali později Robert F. Curl, Harold Kroto a Richard E. Smalley Nobelovu cenu v oboru chemie. Další velký rozvoj nastal v roce 1991 [9], kdy japonský profesor Iijima zpopularizoval uhlíkové nanotrubičky, a poté v roce 2004 [10], kdy nynější nositelé Nobelovy ceny, nizozemský fyzik ruského původu Geim a jeho britskoruský kolega Novoselov, znovuobjevili grafen. Vzhledem k nespočetně možným orbitálním hybridizacím uhlíku, a tudíž velké rozmanitosti krystalických i neuspořádaných struktur, lze očekávat další objevy uhlíkových forem s různými vlastnostmi [11-14].

Autora této habilitační práce uhlíkové materiály zaujaly již v dobách magisterského studia, kdy se zabýval jejich výrobou především pomocí plasmou posílené chemické depozice z plynné fáze (CVD). Na postgraduálním studiu se již zabýval výzkumem a vývojem moderních emisních senzorů. Kromě jiných perspektivních materiálů se zabýval studiem emisních vlastností právě i uhlíkových nanotrubic. Během postgraduálního studia se také autor zapojil do několika projektů, ve kterých zúročil své znalosti, ve kterých kromě studia základních vlastností nanotrubic byly zjišťovány možnosti využití uhlíkových nanotrubic pro infračervené (IR) snímání. Po úspěšném obhájení disertační práce se zapojil do dvou aplikovaných projektů, které řeší možnost využití CNTs v termokamerách pro oblast THz pásma pro bezpečnostní složky (MVČR) a pro biomedicínské aplikace (H2020). V roce 2018 získal dále juniorský projekt GAČR, kde studuje změnu fyzikálních vlastností grafenu v důsledku mechanické deformace. Rozpočet tohoto projektu je 6,78 milionů Kč na 3 roky.

V následujících kapitolách je shrnutí výše zmíněných oblastí řešení, včetně krátkého shrnutí výsledků disertační práce v oblasti emise elektrickým polem z uhlíkových nanotrubic, které je však doplněno o poznatky, které byly vyzkoumány až po obhájení práce.

# 1 Uhlíkové nanotrubic

V roce 1991 publikoval japonský profesor Iijima ze společnosti NEC článek popisující jeho objev dutých trubiček složených pouze z grafitového uhlíku [9] (obr. 2). Tento článek vyvolal ohromné vzrušení a díky němu se inspirovalo mnoho vědců, kteří nyní studují vlastnosti a možné aplikace uhlíkových nanotrubic. Přestože Iijima získal hodně ocenění za objevení uhlíkových nanotrubic, ukazuje se, že uhlíkové nanotrubic byly objeveny již mnohem dříve.



Obr. 2: Srolování grafitového listu do uhlíkové nanotrubiice, vytvořeno pomocí programu Nanotube Modeler.

Již v roce 1952 L. V. Radushkevič a V. M. Lukyanovič publikovali v sovětském žurnálu fyzikální chemie (*Zhurnal Fizicheskoi Khimii*) jasné snímky uhlíkových vláken o průměru 50 nm, které vznikly tepelným rozkladem CO na železné vrstvě [15]. Tento objev byl prakticky bez odezvy, protože se jednalo o publikaci psanou v ruštině a přístup ostatních vědců k této publikaci především ze západu byl díky studené válce prakticky nemožný. Dalším publikacím o uhlíkových vláknech či trubicích z let 1976 až 1987 je věnované zajímavé review [16].

Iijimův objev uhlíkových nanotrubic byl však převratný ve způsobu přípravy. Jeho metoda úzce souvisí s postupem, který použil profesor W. Krätschmer pro výrobu fullerenu („předchůdci nanotrubic v kulovém tvaru“) v makroskopickém množství v roce 1990 [17]. Metoda je založena na obloukovém výboji mezi dvěma uhlíkovými elektrodami v inertní atmosféře za sníženého tlaku. Právě díky své publikaci v nejprestižnějším časopise *Nature* Iijima představil CNTs vědecké komunitě a jeho publikace tak právem patří k nejvíce citovaným publikacím (v roce 2018 překročila hranici 30 tisíc citací).

CNTs mají vynikající mechanické vlastnosti [18,19], jmenovitě velký Youngův modul pružnosti, velkou pevnost v tahu, velký poměr stran a malou hustotu. Tyto vlastnosti dělají CNTs ideálním materiálem pro výrobu kompozitů [20]. Vzhledem k velmi malým rozměrům je obtížné měřit mechanické vlastnosti přímými metodami [21], a proto byly použity k popisu mechanických vlastností různé experimentální techniky jako skenovací elektronová mikroskopie (SEM), transmisní elektronové mikroskopie (TEM), mikroskopie atomárních sil (AFM), Ramanova spektroskopie, nanoindentace apod. [20,22,23]. Lourie a Wanger [24] zjistili Youngův modul jednostěnných a mnohostěnných CNTs v rozsahu 2,8–3,6 TPa a 1,7–2,4 TPa pomocí mikro-Ramanovy spektroskopie. Yu [22] se svým kolektivem měřil pevnost v tahu jednotlivých mnohostěnných CNTs v rozmezí 11–63 GPa pomocí SEM. Ukázalo se, že

pouze vnější vrstva je schopna odolat vyššímu zatížení, zatímco přenos zátěže mezi jednotlivými vrstvami je velmi slabý. Kromě mechanických vlastností byly studovány také elektrické vlastnosti. Na základě teoretických studií bylo zjištěno, že v závislosti na průměru a asymetrii prostorového rozložení (chiralitě) nanotrubic, může být CNT buď vodivá nebo polovodičová [25,26]. Bylo zjištěno, že asi dvě třetiny nanotrubic jsou polovodičové a jedna třetina nanotrubic je vodivá [27]. Ebbesen [28] a kolektiv měřili elektrickou vodivost jednotlivých mnohostěnných CNTs v rozmezí  $10^7$ – $10^8$  S·m<sup>-1</sup> čtyřbodovým měřením. Elektrický odpor vodivé CNT [29] byl naměřen přibližně  $10^{-8}$  až  $10^{-7}$  Ω·m. Možné strukturální vady v nanotrubicích a jejich vliv na odpor byly také zkoumány a bylo zjištěno, že vady CNTs podstatně zvyšují odpor [30]. CNTs mají také velkou tepelnou vodivost. Berber [31] a kolektiv změřili vysokou hodnotu tepelné vodivosti izolovaných nanotrubic, tj. 6000 W·mK<sup>-1</sup>. Tato hodnota je srovnatelná s monovrstvou grafenu a diamanty. Hone [32] a jeho kolegové měřili tepelnou vodivost jedностěnné CNT v rozsahu teplot 8–350 K a tepelná vodivost byla teplotně závislá a dosahovala hodnot v rozmezí 1750–5800 W·mK<sup>-1</sup>.

## 1.1 Studie emisního senzoru pro měření tlaku s uhlíkovými nanotrubicemi

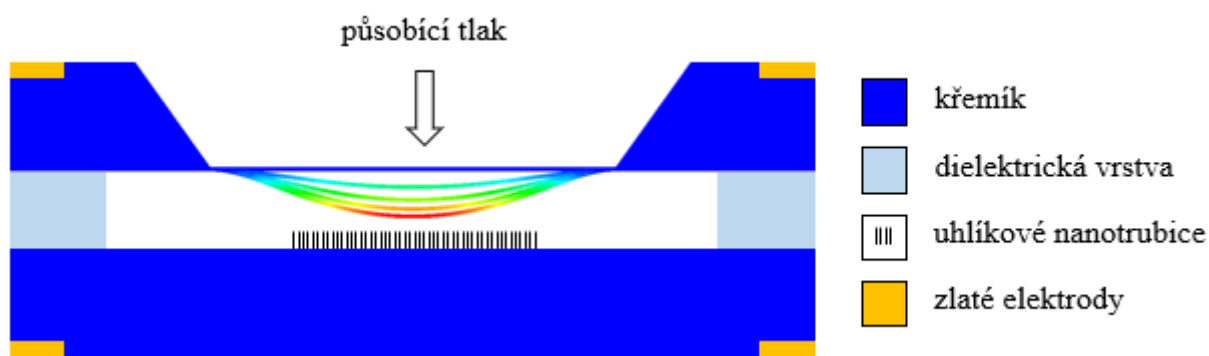
Tlak spolu s teplotou je jednou z nejdůležitějších fyzikálních veličin, které je třeba měřit v různých aplikacích. Nejvyspělejší aplikace snímačů tlaku je možné nalézt např. v automobilovém průmyslu jako snímače tlaku v pneumatikách [33,34] nebo např. v různých jednorázových zdravotnických zařízeních. Tlakový senzor může měřit krevní tlak, nitroděložní tlak během narození nebo vitální znaky pacienta [35]. Navíc jsou senzory tlaku používány v chirurgických zařízeních, nemocničních lůžkách a mnoha dalších zdravotnických zařízeních [36]. V tlakových snímačích mikro-elektro-mechanických systémů (MEMS) jsou změny tlaku transformovány na mechanickou deformaci a/nebo napětí, které se měří změnami kapacity, indukčnosti nebo odporu snímače [37,38]. Další princip snímače tlaku je založen na změnách emisního proudu na senzorových elektrodách [39].

Uhlíkové materiály různých forem přitahují velký zájem v oblasti elektronové emise, protože mohou emitovat elektrony při relativně malých hodnotách elektrické intenzity. Emitory by měly mít co největší poměr délky a průměr a také nízkou výstupní práci na svém povrchu. Přestože jsou mikrohroty ideální pro zvětšení emisní plochy, jsou také nejtěžší a nejnákladnější struktury pro výrobu. Aby se snížily výrobní náklady, pokračuje úsilí o vyvíjení plošných emitorů ze studené katody, zejména na bázi diamantových tenkých vrstev [40–42] a uhlíkových nanostrukturních materiálů s vysokým poměrem stran [43]. První rozsáhlá studie o emisích elektrickým polem z CNTs byla publikována Bonarem a jeho kolektivem v roce 1998 [44]. Později byly CNTs využívány jako emitory v displejích [45] nebo elektronových zdrojích v elektronové mikroskopii [46].

### 1.1.1 Návrh a princip emisního senzoru tlaku

Snímač tlaku MEMS na principu elektrické emise [47] byl navržen jako struktura diody (obr. 3). Skládá se ze dvou silně dopovaných křemíkových elektrod, z nichž anoda je anizotropně leptaná do tenké, ohybné membrány. Emisní materiál, v tomto případě vertikálně orientované CNTs, je umístěn na katodě. Obě elektrody jsou odděleny dielektrickou vrstvou s integrovanou vakuovou komorou. Dielektrická vrstva může být vyrobena z pyrexového skla s využitím technologie anodické vazby nebo ze skleněných frit.

Napětí mezi katodou a anodou tvoří extrakční pole. Vzdálenost mezi elektrodami musí být odpovídajícím způsobem upravena. Emisní proud lze regulovat buď regulací napětí nebo změnou vzdálenosti katody od anody. Regulace napětí ovlivňuje energii elektronů na anodě a vyžaduje komplexní napájecí zdroje. Změna vzdálenosti katody od anody vyžaduje mechanické ovládání. Anoda je tvořena tenkou membránou, která se ohýbá působením vnějšího tlaku. Pokud je přiložené napětí mezi elektrodami fixní, změní se intenzita elektrického pole, stejně jako emisní proud pole. Princip je podobný snímačům tlaku pracujících na kapacitním principu, ve kterých je měřenou veličinou kapacita.

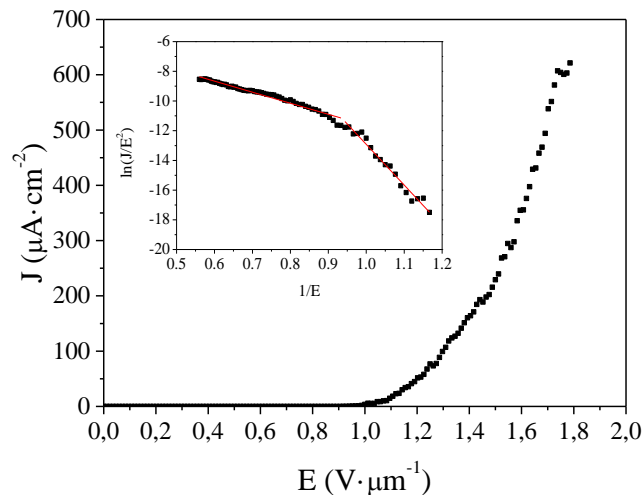


Obr. 3: Schematický pohled na senzor tlaku MEMS s emitory z uhlíkových nanotrubic.

### 1.1.2 Charakterizace emisního senzoru tlaku

Všechna měření probíhala ve vakuové komoře při tlaku nižším než  $10^{-4}$  Pa. Na elektrodě byly deponované nanotrubičky pomocí plasmou posílené CVD metody na ploše  $16 \text{ mm}^2$ . Vzdálenost mezi emitory z CNTs a anodou byla nastavena na  $120 \text{ }\mu\text{m}$  za použití tuhé dielektrické fólie. Napětí bylo automaticky nastaveno pomocí programového vybavení komunikujícího se zdroji napětí přes rozhraní GPIB od 0 do 150 V. Hustota elektrického proudu v závislosti na intenzitě elektrického pole (obr. 4) byla vypočtena z naměřených výsledků.

Stejná měření byla provedena pro deset vzdáleností mezi emitory a anodou v rozmezí od  $84 \text{ }\mu\text{m}$  do  $120 \text{ }\mu\text{m}$ . Pro těchto deset vzdáleností byly stejné výsledky získány opakovaně a všechny odpovídaly přepočítaným výsledkům na proudovou hustotu v závislosti na intenzitě elektrického pole na obr. 4.



Obr. 4: Závislost proudové hustoty na intenzitě elektrického pole z uhlíkových nanotrubic sloužících jako emitory. Ve výřezu je vynesena odpovídající F–N závislost.

Výřez v obr. 4 zobrazuje odpovídající závislost podle Fowler–Nordheimovy (F–N) teorie [48]. Přímký ve F–N závislosti označují kvantové mechanické tunelování charakteristické pro emisi elektrickým polem. Příмка ve F–N závislosti je odvozena za použití F–N rovnice:

$$I = (A\alpha\beta^2 V^2 / d^2 \phi) \exp[-B\phi^{3/2} d / (\beta V)], \quad (1)$$

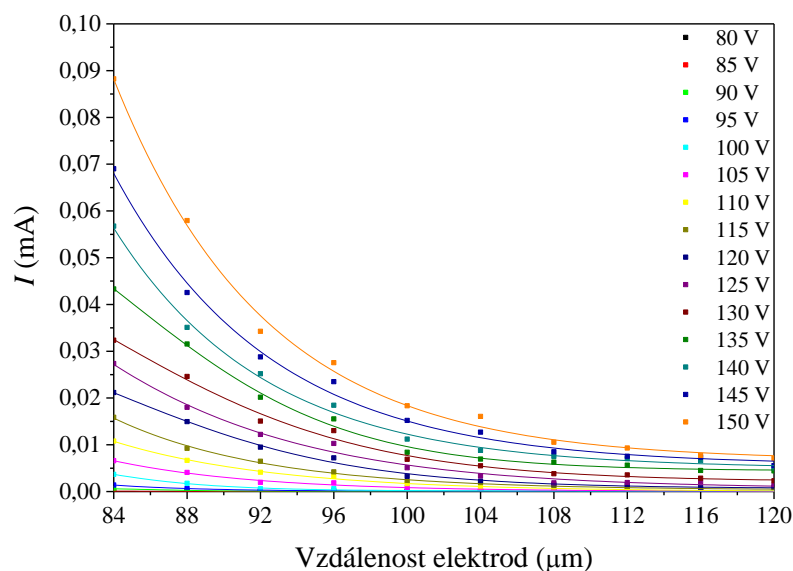
kde  $I$  je emisní proud,  $A=1,56 \cdot 10^{-6} \text{ A} \cdot \text{V}^{-2} \cdot \text{eV}$  a  $B=6,83 \cdot 10^9 \text{ eV}^{-3/2} \cdot \text{V} \cdot \text{m}^{-1}$  jsou F–N konstanty,  $\alpha$  je emisní plocha,  $\beta$  je koeficient zvětšení elektrického pole,  $\phi$  je výstupní práce,  $d$  je vzdálenost mezi anodou a emitory a  $V$  je přiložené elektrické napětí. Aby bylo možné emitovat hodně elektronů při nízkém napětí, je zapotřebí nízká výstupní práce ( $\phi$ ) a vysoký koeficient zvětšení elektrického pole ( $\beta$ ). Tento koeficient je možné zjistit jednoduše ze směrnice přímk za použití F–N závislosti ( $\ln(J/E^2)$  vs.  $1/E$ ). F–N závislost pro vzorky s uhlíkovými nanotrubicemi může být rozdělena na dvě části, a to menší a větší než  $0,9 \mu\text{m} \cdot \text{V}^{-1}$ , se dvěma různými koeficienty zvětšení elektrického pole.

Takové chování F–N závislosti není neobvyklé a může být způsobeno různými vlivy, jako je elektrický odpor uhlíkových nanotrubic [49,50], prostorový náboj [51], absorpce plynů na povrchu [52], změna struktury emitore [53,54], nerovnost emitore [55,56], lokalizované stavy [57], non-Schottky-Nordheimova bariéra [58,59] nebo vzájemná interakce mezi emitory [60].

Za předpokladu, že  $\phi_{\text{CNT}} = 5 \text{ eV}$  [61], je vypočítaná směrnice F–N závislosti  $-7,4 \pm 0,2$  pro  $1/E < 0,9 \mu\text{m} \cdot \text{V}^{-1}$ , tj. oblast vysoké intenzity elektrického pole a  $-27,4 \pm 1,1$  pro  $1/E > 0,9 \mu\text{m} \cdot \text{V}^{-1}$ , tj. oblast nízké intenzity elektrického pole. Z vypočítaných hodnot vyplývá, že nárůst proudu je rychlejší pro oblast nízkých intenzit elektrického pole, a proto je teoreticky výhodnější používat snímač v této oblasti. Vzhledem k velmi malým hodnotám emisního proudu je však nutné používat snímač v silném elektrickém poli.

Obecně platí, že se u aplikací s emisí elektrickým polem stanovuje tzv. otevírací intenzita elektrického pole, kdy hustota emisního proudu dosáhne hodnoty  $10 \mu\text{A}\cdot\text{cm}^{-2}$ . U vzorků s CNTs byla dosažena nejnižší otevírací intenzita elektrického pole menší než  $1 \text{ V}\cdot\mu\text{m}^{-1}$  a nejvyšší proudová hustota byla dosažena již při intenzitě elektrického pole  $1.8 \text{ V}\cdot\mu\text{m}^{-1}$ .

Naměřené výsledky se podle očekávání řídí Fowler–Nordheimovým zákonem. Křivky na obr. 5 ukazují, že naměřený emisní proud závisí na vzdálenosti elektrod a zároveň roste s klesající vzdáleností elektrod, tj. zvyšující se intenzitou elektrického pole. Stejně tak pro konstantní vzdálenost elektrod a zvyšující se napětí, roste i emisní proud. Toto potvrzuje očekávané chování emisního senzoru pro měření tlaku s uhlíkovými nanotrubicemi. Z naměřených charakteristik lze také konstatovat, že je výhodné pracovat s vyšším elektrickým polem a nižšími vzdálenostmi elektrod. Při těchto podmínkách vede malá deformace membrány vlivem působícího tlaku k velké změně emisního proudu, tzn. je dosaženo vyšší citlivosti senzoru, tj. vyššího poměru  $\Delta I/\Delta p$  při stejné změně vzdálenosti  $\Delta d$ . Tento stav může být ještě vylepšen výběrem vhodného rozměru a tloušťky membrány [47].



Obr. 5: Závislost emisního proudu na vzdálenosti anody od emitorů z CNTs, kde je elektrické napětí jako parametr. Body – naměřené hodnoty, čáry – proložení F–N modelem.

Jak bylo uvedeno výše, emisní proud je silně ovlivněn parametry tlakového senzoru (velikost a tloušťka membrány) a intenzitou elektrického pole (použité napětí a vzdálenost anody a emitorů z CNTs). Vzhledem k tomu, že průhyb membrány odpovídá změně vzdálenosti anody od emitorů z CNTs, může být použita závislost na obr. 5 jako ukázka očekávané hodnoty emisního proudu pro daný tlak. V tomto případě je vzdálenost anody od CNTs nahrazena tlakem a může být přímo odvozena očekávaná hodnota emisního proudu pro zvolené parametry systému (počáteční intenzita elektrického pole, tj. použité elektrické napětí a vzdálenost anody od CNTs, velikost a tloušťka membrány).

Jednoduchou matematickou úvahou a porovnáním naměřených a simulovaných výsledků průhybu membrány [47] lze vyvodit, že pokud bude použito pole CNTs o ploše  $1 \text{ cm}^2$ , počáteční vzdálenost anody od emitorů bude  $10 \text{ }\mu\text{m}$ , napájecí napětí bude  $12 \text{ V}$  a membrána bude mít velikost  $10\,000 \text{ }\mu\text{m} \times 10\,000 \text{ }\mu\text{m} \times 100 \text{ }\mu\text{m}$ , bude emisní proud z pole CNTs  $50 \text{ }\mu\text{A}$ . Při působení tlaku na membránu o velikosti  $1 \text{ kPa}$  a zanedbání poloměru průhybu membrány, bude průhyb membrány zhruba  $0,75 \text{ }\mu\text{m}$ , a tím pádem bude emisní proud z pole CNTs přibližně  $90 \text{ }\mu\text{A}$ . Citlivost lze tedy stanovit na rozsahu  $0$  až  $1 \text{ kPa}$  na  $40 \text{ }\mu\text{A} \cdot \text{kPa}^{-1}$ . Při vyšších tlacích, resp. intenzitách elektrického pole, lze očekávat vyšší citlivost. Se ztenčující se membránou se zvýší citlivost senzoru, ale sníží se maximální měřitelný tlak. To stejné platí i pro zvětšující se membránu.

## 1.2 Uhlíkové nanotrubičky pro infračervené snímání

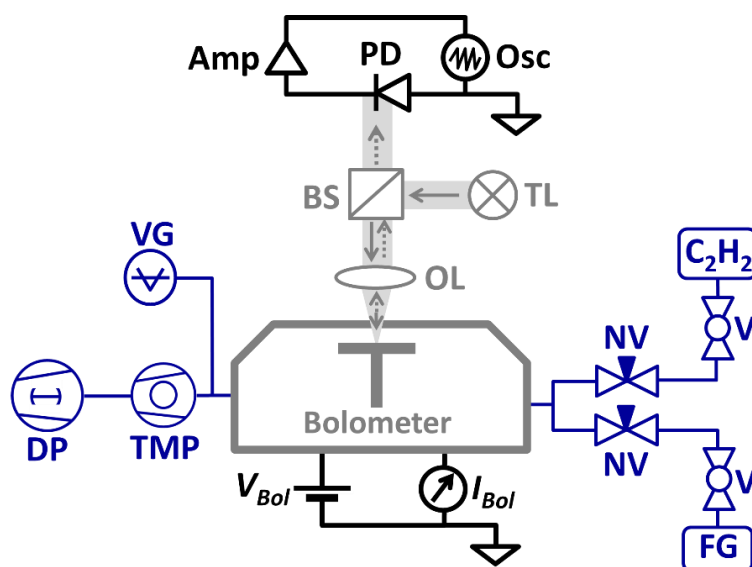
Bolometr byl vynalezen americkým astronautem S. P. Langleyem v roce 1880 [62] a je určený pro měření energie dopadajícího IR záření prostřednictvím ohřevu materiálu s teplotně závislým odporem. Bolometr velice často obsahuje absorpční vrstvu, která je jedním z klíčových parametrů, protože zvyšuje účinnost na dopadající záření celého detekčního systému. Mezi nejvíce používané absorpční materiály patří oxidy vanadu ( $\text{VO}_x$ ), amorfni křemík ( $\alpha\text{-Si}$ ) nebo křemíkové diody [63-65]. Výzkumný tým na ústavu mikroelektroniky se zaměřil na bolometrických aplikace, kde slouží CNTs jako absorpční vrstva. Díky tomu je teoreticky možné zvýšit rozsah detekovatelných vlnových délek a také zvýšit citlivost bolometru na dopadající IR záření.

Uhlíkové nanotrubičky je možné připravit mnoha způsoby, a to od přípravy pomocí obloukového výboje mezi uhlíkovými elektrodami přes laserovou ablací uhlíkového terče až po CVD. Nejrozšířenější technikou přípravy je právě zmíněná chemická depozice z plynné fáze, která je založená na dekompozici uhlovodíku v přítomnosti katalytického materiálu, jako je např. železo, nikl nebo kobalt. Podmínky růstu jsou ovlivněny depoziční teplotou, typem použitého uhlovodíku a volbou katalytického materiálu. V nepoužívanějších CVD procesech se využívá teploty vyšší než  $700 \text{ }^\circ\text{C}$ . Teplota při růstu může být dále snížena pod  $500 \text{ }^\circ\text{C}$  díky využití plasmou posílené CVD [19] metody.

Integrace vrstvy absorbující IR záření na vyhodnocovací integrované obvody (ROIC) vyrobené pomocí techniky doplňkového kov-oxid-polovodiče (CMOS) představuje několik technologických výzev. Ačkoliv je plocha růstu uhlíkových nanotrubic jednoduše definována pomocí katalytické vrstvy, růst CNTs vyžaduje zvýšenou teplotu substrátu nad běžně přípustnou mez, a to právě představuje největší problém při integraci. Využití plasmou posílených CVD metod je také problematické, protože teplo z plazmového výboje způsobuje poškození tepelně izolovaných membrán. Plazmové procesy dále indukují náboj v tenkých vrstvách  $\text{SiO}_2$ , což způsobuje změny v prahových napětích tranzistorů CMOS. Přebytkový náboj může být odstraněn následným žíháním, avšak tento proces je nekompatibilní s ROIC. Konvenční CVD procesy vyžadují teploty hodně nad limitem, které poškodí CMOS ROIC zařízení. Nejvyšší teplota, které CMOS zařízení nepoškodí, je obvykle nižší než  $475 \text{ }^\circ\text{C}$ .

### 1.2.1 Depozice uhlíkových nanotrubic na membrány bolometru

Pro depozici uhlíkových nanotrubic na povrch membrány bolometru byl proto vynalezen unikátní způsob, pomocí kterého je možné deponovat nanostruktury jen na membráně bolometru a zároveň teplota na zbytku substrátu zůstává při pokojové teplotě. Vyrobený a podleptaný čip bolometru byl proto umístěn do bezvývodového keramického pouzdra typu LCC68 a byl s ním propojen pomocí bondovacích drátků. Toto pouzdro bylo poté umístěno do vakuové komory, která byla vybavena skleněným průzorem, dvěma trubičkami pro přívod a čerpání plynů a také elektrickými průchodkami (obr. 6). Komora má objem  $\approx 100 \text{ cm}^3$ . Komora s čipem bolometru byla poté umístěna pod optický mikroskop s objektivem se zvětšením  $50\times$ , pracovní vzdáleností 9 mm a numerickou aperturou (NA) 0,55. Přibližně 7 mm vzdálenost mezi membránou bolometru a skleněným oknem umožňuje pozorování bolometry s vysokým rozlišením a zároveň sledovat růst CNTs během procesu v reálném čase pomocí CMOS kamery [66].

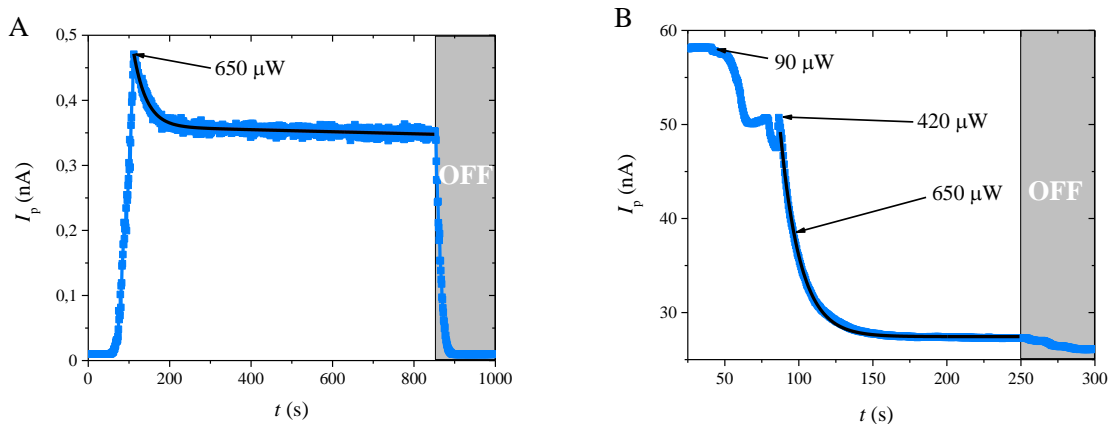


Obr. 6: Schematický náčrt komory pro depozici uhlíkových nanotrubic. Bolometr byl umístěn do vakuové komory se vstupem pro přívod plynů a čerpacím otvorem. Průtok plynů byl řízen jehlovými ventily (NV). Čerpání komory bylo prováděno pomocí turbomolekulární vývěvy (TMP) s předčerpáním pomocí suché vakuové vývěvy (DP). Díky optickému mikroskopu s objektivem se zvětšením  $50\times$  (OL) bylo možné monitorování procesu růstu CNTs v reálném čase. Měření odrazu během růstu CNTs bylo provedeno pomocí wolframové lampy (TL) ve spojení s děličem světla (BS) pro osvětlení membrány bolometru. Emise a odraz při růstu CNTs byly měřeny použitím křemíkové fotodiody (PD). Fotoproud  $I_p$  byl převeden na napětí pomocí proudového předzesilovače (Amp), který byl následně sledován pomocí osciloskopu (Osc). Rozptýlený výkon v membráně bolometru  $P$  byl nastaven pomocí systému zpětné vazby regulováním amplitudy  $V_{BOL}$  při měření  $I_{BOL}$  a udržování  $P$  při konstantní hodnotě.

Před samotnou depozicí nanostruktur na povrch membrány bolometru byla membrána elektricky zahřívána pomocí rozptýleného Joulova tepla o výkonu  $P \approx 200 \mu\text{W}$  při proudění formovacího plynu po dobu přibližně 15 minut, aby došlo ke stabilizaci teplotních podmínek a vyžhání katalytické vrstvy. Během celého procesu byl udržován konstantní výkon  $P$  pomocí řízení napětí  $V$  přiloženého na membránu bolometru a současného měření proudu  $I$  tekoucího odporem titanové vrstvy membrány bolometru. Součin  $V \cdot I$  byl udržován konstantní díky použití systému s uzavřenou zpětnovazební smyčkou. Poté byly stabilizovány podmínky růstu, a to

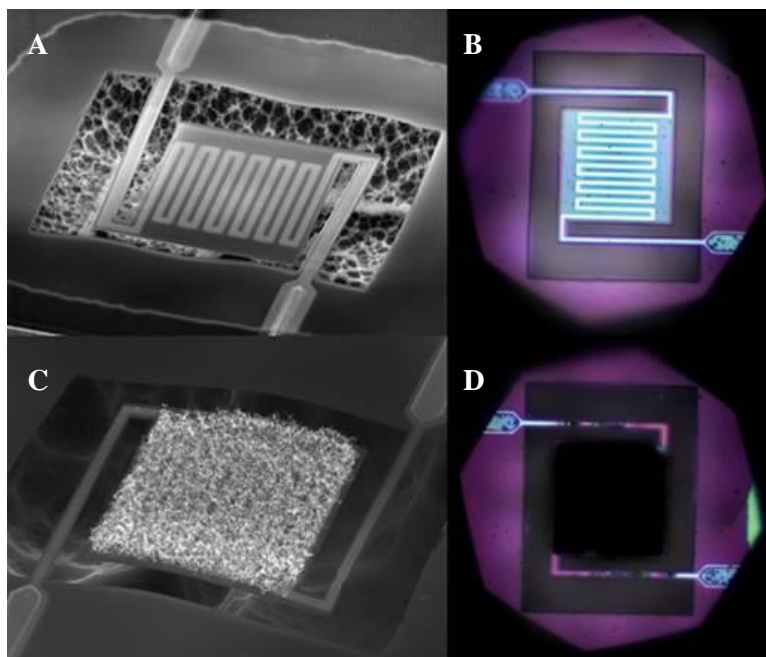
především tlak uvnitř komory  $\approx 5$  Pa, úprava průtoku acetyleny na  $500 \text{ cm}^3 \cdot \text{min}^{-1}$  a formovacího plynu na  $200 \text{ cm}^3 \cdot \text{min}^{-1}$ . Během experimentu byl následně výkon zahřívající membránu bolometru zvyšován, dokud nebyl emitovaný proud  $I_P$  z membrány zachycen na fotodiodě uchycené k optickému mikroskopu. Tento fotoproud byl zobrazován na osciloskopu poté, co byl převeden na napětí pomocí proudového předzesilovače s aktivním filtrem typu dolní propust a nastaveném útlumem 20 dB na dekádu, mezním kmitočtem 20 Hz a zesílením  $10 \text{ pA} \cdot \text{V}^{-1}$ . Toto nastavení umožnilo sledovat chování bolometru během růstu CNTs. Dále byl zvyšován výkon rozptýlený v membráně bolometru s krokem  $8 \text{ } \mu\text{W} \cdot \text{s}^{-1}$  začínajícím v čase 56 s, dokud nebylo dosaženo rozptýleného výkonu v membráně bolometru  $650 \text{ } \mu\text{W}$  (dosaženo v čase 112 s) a poté byl udržován konstantní výkon po dobu 700 s (obr. 7A). Fotoproud  $I_P$  jako funkce času  $t$  může být proložen exponenciální křivkou prvního řádu. Z aproximace byla poté určena časová konstanta emise  $\tau_1$ , jejíž hodnota je  $\approx 35$  s.

S využitím podobného sestavení byl sledován odraz od membrány bolometru jako funkce růstu CNTs při řízení amplitudy výkonu  $P$ . V experimentu byla membrána bolometru osvětlena halogenovou žárovkou o výkonu 100 W. Rychlost odezvy na odraz je v porovnání s měřením emisivity rychlejší (obr. 7B). Jakmile začal růst uhlíkových nanotrubic při výkonu  $420 \text{ } \mu\text{W}$ , klesla amplituda odraženého záření z membrány bolometru s exponenciální závislostí prvního řádu s časovou konstantou  $\tau_2 \approx 13$  s. Menší časová konstanta  $\tau_2$  ve srovnání s  $\tau_1$ , ukazuje, že se absorpce elektromagnetického záření ve viditelném spektru třikrát zrychluje než záření emitované při růstu uhlíkových nanotrubic.



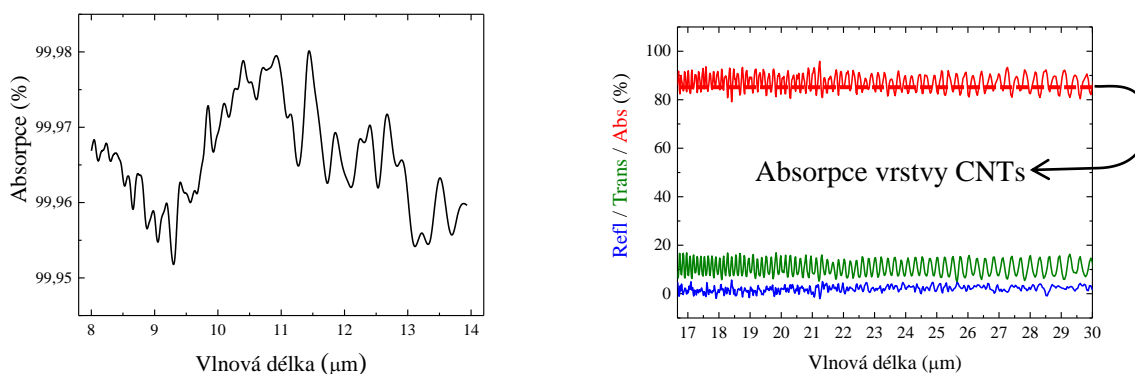
Obr. 7: A) Typická optická emise z membrány bolometru v závislosti na čase během depozice CNTs. Byl měřen fotoproud excitovaný v křemíkové fotodiodě umístěné na optickém mikroskopu. Rozptýlené Joulovo teplo se postupně zvyšovalo a v čase 56 s membrána bolometru začala emitovat světlo na detekovatelné úrovni. V čase 112 s při nastaveném výkonu  $650 \text{ } \mu\text{W}$  dosáhla emise z membrány bolometru svého maxima. V tomto čase začaly růst na povrchu membrány bolometru uhlíkové nanotrubice, došlo ke zvýšení emisivity z povrchu membrány a díky tomu se snížila teplota membrány bolometru. V čase 850 s byl vypnut ohřev bolometru, CNTs přestaly růst, a proto světelná emise rychle klesla na nulovou hodnotu. B) Experiment byl proveden při stejných podmínkách s výjimkou času měření optického odrazu od povrchu membrány bolometru. V čase 40 s byl výkon zvyšován z ustáleného stavu  $90 \text{ } \mu\text{W}$  a odrazivost od membrány bolometru začala klesat. Uhlíkové nanotrubice začaly růst v čase 86,5 s s rozptýleným výkonem  $420 \text{ } \mu\text{W}$ . Nově rostoucí vrstva uhlíkových nanotrubic dále snižovala odrazivost od membrány bolometru s časovou konstantou  $\approx 13$  s. Maximální výkon Joulova tepla  $650 \text{ } \mu\text{W}$  byl dosažen v čase 96 s. V čase 250 s byl ohřev bolometru vypnut, ale amplituda odrazu se změnila jen nepatrně.

Na obr. 8 je zobrazena analýza membrány bolometru před a po depozici uhlíkových nanotrubic pomocí elektronové a optické mikroskopie.



Obr. 8: Analýza pomocí skenovacího elektronového (A, C) a optického (B, D) mikroskopu membrány mikrobolometru s lokálně deponovanými uhlíkovými nanotrubicemi před (A, B) a po (C, D) depozici.

Použitelnost uhlíkových nanotrubic jako citlivé vrstvy pro IR záření byla hodnocena prostřednictvím řady zkoušek a také měření za využití infračervené spektroskopie s Fourierovou transformací (FTIR). Výsledky vyhodnocující absorpci uhlíkových nanotrubic pro různé vlnové délky jsou zobrazeny na obr. 9.



Obr. 9: IR absorpce ve vrstvě uhlíkových nanotrubic měřena pomocí FTIR ukazující, že vrstva je vynikající IR absorbér i v THz oblastech.

Z naměřených výsledků vyplývá, že uhlíkové nanotrubice mohou sloužit jako vynikající černé těleso s absorpcí mezi 90 % a 99,9 % v širokém rozsahu spektra pokrývající viditelnou oblast až po oblast THz. Navíc je jejich depozice díky CVD metodě plně kompatibilní s výrobou MEMS a jejich růst probíhá pouze na lokálně zahřátých membránách bolometru a teplota zbytku čipu zůstává při pokojové teplotě. Toto umožňuje kombinovat využití vrstvy uhlíkových nanotrubic spolu s bolometry založených na maticovém uspořádání včetně možnosti integrace

vyhodnocovacích obvodů CMOS. Aplikace vyžaduje velmi dobrou kontrolu růstu absorpční vrstvy, což vyvinutá metoda umožňuje, pro získání dobrého souběhu všech parametrů bolometrů.

## 1.2.2 Integrovaný vyhodnocovací obvod

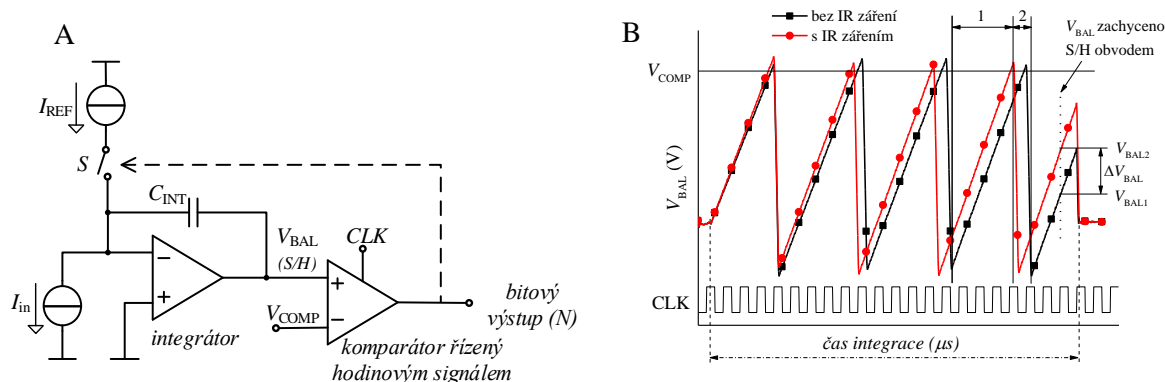
Signály z bolometrů jsou dále zpracovávány pomocí ROIC, aby nakonec mohl být vytvořen obraz IR záření. Díky integraci výstupního signálu bolometru dochází ke zlepšení klíčového parametru - poměr odstupů signálu k šumu (SNR). Základní problém u měření bolometrů je právě malá změna odporu způsobená dopadajícím IR zářením, která je o několik řádů nižší než jmenovitá hodnota odporu  $R$ . Navíc hodnota odporu  $R$  kolísá z důvodu nejistoty v procesu výroby bolometrů.

ROIC založený na nesaturujícím integrátoru  $\Delta\Sigma$  prvního řádu [67] se skládá z proudového integrátoru, po kterém následuje komparátor řízený hodinovým signálem. Zdroj proudu  $I_{REF}$  se aktivuje na základě stavu komparátoru, aby udržel integrátor mimo oblast saturace (obr. 10A).

Výstupní napětí integrátoru  $V_{BAL}$  v čase  $t$  může být popsáno rovnicí:

$$V_{BAL} = \frac{1}{C_{INT}} \left( \int_0^t I_{in} dt - I_{REF} \cdot T \cdot N - \int_{t_0}^{t_1} I_{REF} dt \right), \quad (2)$$

kde  $C_{INT}$  je hodnota kapacity integračního kapacitoru,  $I_{in}$  je vstupní proud integrátoru,  $T$  je perioda hodinového signálu,  $N$  je počet (kladné celé číslo) period hodinového signálu, kdy byl  $I_{REF}$  deaktivován a  $t_1$  je čas, kdy začala poslední perioda a spínač pro  $I_{REF}$  byl aktivní. Pokud nebyl aktivní, poslední integrál v rovnici (2) má hodnotu 0 V.



Obr. 10: A) Princip nesaturujícího integrátoru založeném na  $\Delta\Sigma$  modulátoru prvního řádu. Když napěťová úroveň výstupního napětí z integrátoru  $V_{BAL}$  dosáhne úrovně nastavené  $V_{COMP}$ , komparátor řízený hodinovým signálem aktivuje  $I_{REF}$  a tento přídatný elektrický proud v opačném směru sníží amplitudu  $V_{BAL}$  a zároveň udrží integrátor mimo režim saturace. B) (černá) Signál  $V_{BAL}$  bez IR záření. (červená) Odpor bolometru vzroste díky zahřátí membrány bolometru IR zářením, vzroste  $\Delta I$  vstupního proudu  $I_{in}$ , což způsobuje zvýšení  $V_{BAL}$ .

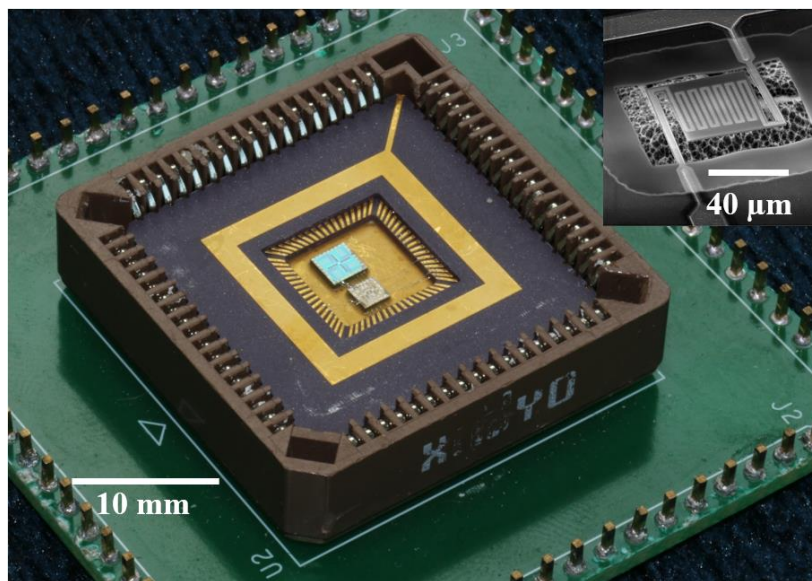
Tento systém vytváří vzorek dvou logických úrovní na výstupu komparátoru řízeným hodinovým signálem, zbytkovou hodnotu  $V_{BAL}$  a výstup integrátoru na konci převodu. Velikost neznámého proudu  $I_{in}$  pak může být vypočítána z hodnoty  $N$  a  $I_{REF}$ . Jedná se o typický příklad využití převodníku AD založeném na modulátoru  $\Delta\Sigma$ , zatímco zbytková hodnota  $V_{BAL}$  na konci převodu je zanedbávaná.

Bylo navrženo využití tohoto systému pro extrakci hodnoty IR záření z buňky bolometru. Absolutní hodnota  $N$  představuje jmenovitý odpor bolometru a jeho změnu, často nazývanou tzv. vzor šum (FPN – fixed pattern noise). Výkon IR záření zvýší hodnotu amplitudy signálu  $V_{BAL}$ .

Systém nejprve skenuje celou matici bolometrů s uzavřenou clonou a uloží všechny hodnoty výstupů hodnot  $V_{BAL1}$  a  $N$  z celé matice bolometrů do vnitřní nebo vnější paměti. Dále se matice bolometrů znovu naskenuje při otevřené cloně a zaznamenávají se nové výstupy  $V_{BAL2}$ . Obraz IR záření se pak vytvoří odečtením  $\Delta V_{BAL} = V_{BAL2} - V_{BAL1}$  (obr. 10B) z každého pixelu matice bolometrů a zároveň se porovnají hodnoty  $N$  s a bez IR záření. V ideální situaci jsou hodnoty  $N$  z rovnice (2) pro oba signály  $V_{BAL}$  s IR zářením a bez IR záření totožné (oblast 1 na obr. 10B). Existují však případy s různými hodnotami  $N$  (oblast 2 na obr. 10B) s a bez IR záření, tj. v době, kdy je  $V_{BAL1}$  bez aktivovaného spínače  $S$  a  $V_{BAL2}$  s aktivovaným přepínačem  $S$  a naopak. V těchto případech musí být vypočítána ekvivalentní hodnota  $\Delta V_{BAL}$  pomocí dalšího zpracování digitálního signálu (DSP). Tento DSP modul pro konstrukci obrazu může také např. provádět úlohu kalibrace čipu a výpočet výstupu integrátoru jako funkce času.

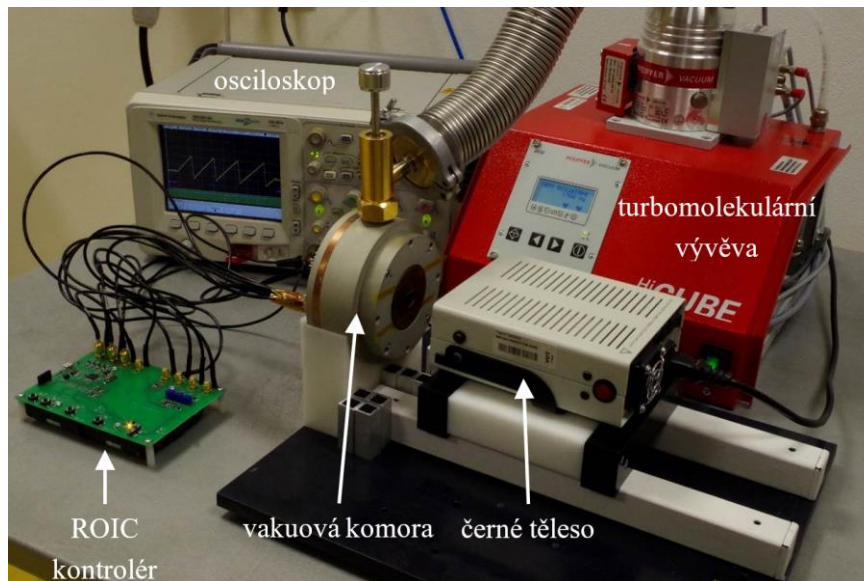
### 1.2.3 Testování bolometru s integrovaným obvodem

Pro testování bolometru spolu s integrovaným obvodem byl čip senzoru bolometru umístěn spolu s ROIC do bezvývodového keramického pouzdra typu LCC68 a byl s ním propojen pomocí bondovacích drátků (obr. 11).



Obr. 11: Fotografie ROIC čipu a čipu bolometru umístěném v pouzdře LCC68, které je zasazeno v testovací patici. Ve výřezu obrázku je SEM analýza vyrobeného bolometru.

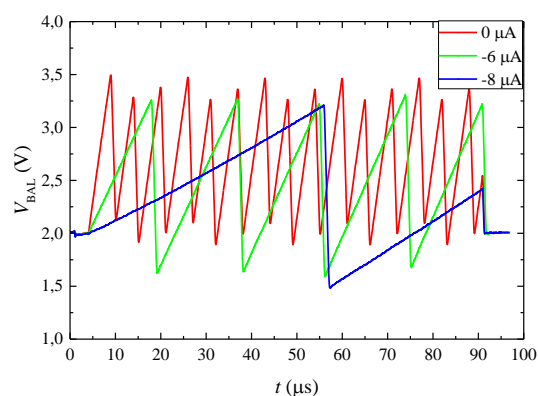
Pouzdro LCC68 s osazeným ROIC a snímacím čipem bolometru je pak umístěno do vakuové komory, která je vybavena germaniovým průzorem. Germaniový průzor byl zvolen s ohledem na transparentnost pro IR záření. Vakuová komora je poté čerpána pomocí turbomolekulární vývěvy na tlak menší než  $4 \cdot 10^{-4}$  Pa (obr. 12).



Obr. 12: Fotografie testovací sestavy pro měření bolometru s vyhodnocovacím čipem. Skládá se z černého tělesa a vakuové komory čerpané pomocí turbomolekulární vývěvy. Dále pak z kontroléru nastavujícího signály pro ROIC a osciloskopu.

Patice pro testování byla poté propojena pomocí vakuových průchodek s měřicí elektronikou, která byla umístěna mimo vakuovou komoru. Čip snímacího bolometru byl poté vystaven působení IR záření o různých výkonech emitovaných z kalibrovaného černého tělesa. Změna výkonu IR záření byla definována pomocí rozdílné vzdálenosti mezi čipem bolometru a kalibrovaným černým tělesem.

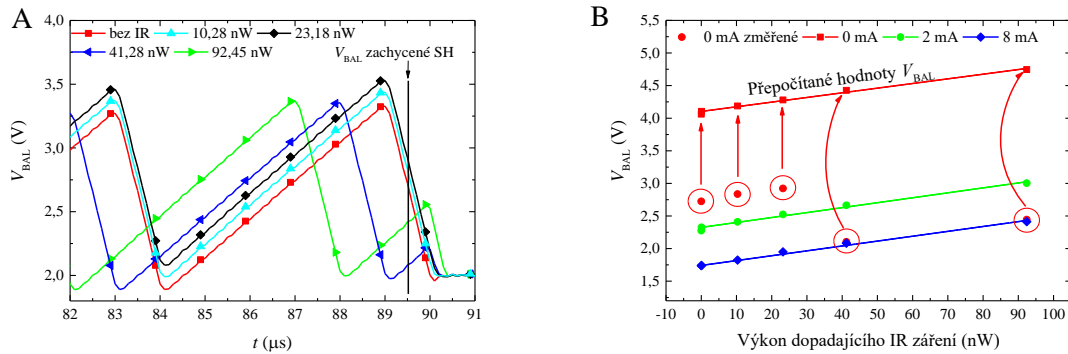
Výstupní signál z bolometru byl poté měřen pomocí ROIC. Během měření bylo sledováno zejména napětí  $V_{BAL}$  v závislosti na čase pro různé kompenzační proudy  $I_{COMP}$ , které ukazují použitelnost nesaturujícího integrátoru v nekonvenční aplikaci (obr. 13). Pomocí různě nastaveného kompenzačního proudu  $I_{COMP}$  bylo možné napodobit variaci jmenovitého odporu bolometru (FPN). Spínaný komparátor neumožňuje integrátoru přetečení bez ohledu na rychlost nabíjení  $C_{INT}$ . Pokud vstup komparátoru překročí rozhodovací úroveň, kompenzace  $I_{in}$  je aktivována a kondenzátor  $C_{INT}$  je vybit.



Obr. 13: Časová závislost výstupního napětí pro různé hodnoty kompenzačního proudu  $I_{COMP}$ , které napodobují rozdíly v jmenovitých odporech snímacího a referenčního bolometru.

Následně byla nastavována různá vzdálenost mezi černým tělesem a čipem bolometru pomocí kovových kostek stejných rozměrů (12 mm). Vyzařovací deska černého tělesa měla průměr 28,6 mm a emisivitu 0,95 a byla nastavena na teplotu 400 °C. Pro šest různých vzdáleností mezi černým tělesem a bolometru to odpovídá výkonu dopadajícího záření na membránu bolometru 0, 7,54, 10,28, 14,80, 23,18, 41,28 a 92,45 nW (obr. 14A). Na obr. 14B je poté zobrazena závislost  $V_{BAL}$  zaznamenaná v čase integrace 89,5  $\mu$ s jako funkce dopadajícího výkonu IR záření s kompenzačním proudem  $I_{COMP}$  jako parametr.

Výsledky citlivosti ROIC pro  $I_{COMP}$  jako parameter jsou uvedeny v tabulce 1. Průměrná citlivost systému byla stanovena  $(7,43 \pm 0,20)$  mV $\cdot$ nW $^{-1}$  (střední hodnota  $\pm$  směrodatná odchylka) nezávislá na amplitudě  $I_{COMP}$ , což ukazuje na vynikající metodu potlačení FPN. Hodnoty s nastaveným kompenzačním proudem o hodnotě 4  $\mu$ A nebyly pro výpočet průměrné hodnoty citlivosti použity, neboť zde byla pravděpodobně chyba měření.



Obr. 14: A) Časová závislost napětí  $V_{BAL}$  pro různé hodnoty výkonu IR záření blízko konce integrační periody (od 82  $\mu$ s do 91  $\mu$ s). Funkce kompenzace byla vypnuta pomocí externího signálu. B)  $V_{BAL}$  zaznamenané v čase integrace 89,5  $\mu$ s jako funkce dopadajícího výkonu IR záření s kompenzačním proudem  $I_{COMP}$  jako parametr. Hodnoty označené šipkami byly přepočítány podle rovnice (2).

Tab. 1 Citlivost ROIC s  $I_{COMP}$  jako parametr

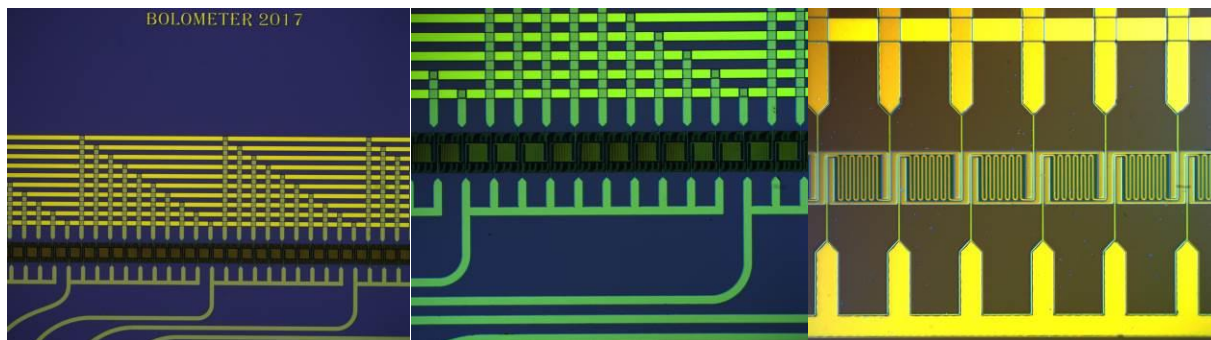
$I_{COMP}$ ( $\mu$ A)	Citlivost ROIC (střední hodnota $\pm$ směrodatná odchylka) (mV $\cdot$ nW $^{-1}$ )
0	$7,14 \pm 0,32$
2	$7,58 \pm 0,39$
4	$6,00 \pm 0,45$
6	$7,54 \pm 0,51$
8	$7,47 \pm 0,39$
Průměrná citlivost	$7,43 \pm 0,20$

Z tabulky 1 je zřejmé, že nesaturující integrátor zlepšuje citlivost vyčítání výstupního signálu z původní odezvy  $\mathcal{R}_R$  ( $7,08 \pm 0,24$ ) kV $\cdot$ W $^{-1}$  až na citlivost snímání s ROIC ( $7,43 \pm 0,20$ ) mV $\cdot$ nW $^{-1}$ , obě hodnoty udávány ve tvaru (střední hodnota  $\pm$  směrodatná odchylka), což je zlepšení  $\approx 1000\times$  v amplitudě výstupního signálu z bolometru díky integrování signálu, a při tom nezáleží na amplitudě kompenzačního proudu  $I_{COMP}$ . Kompenzační proud  $I_{COMP}$  byl použit k emulaci odchylky jmenovité hodnoty odporu bolometru, známé jako FPN.

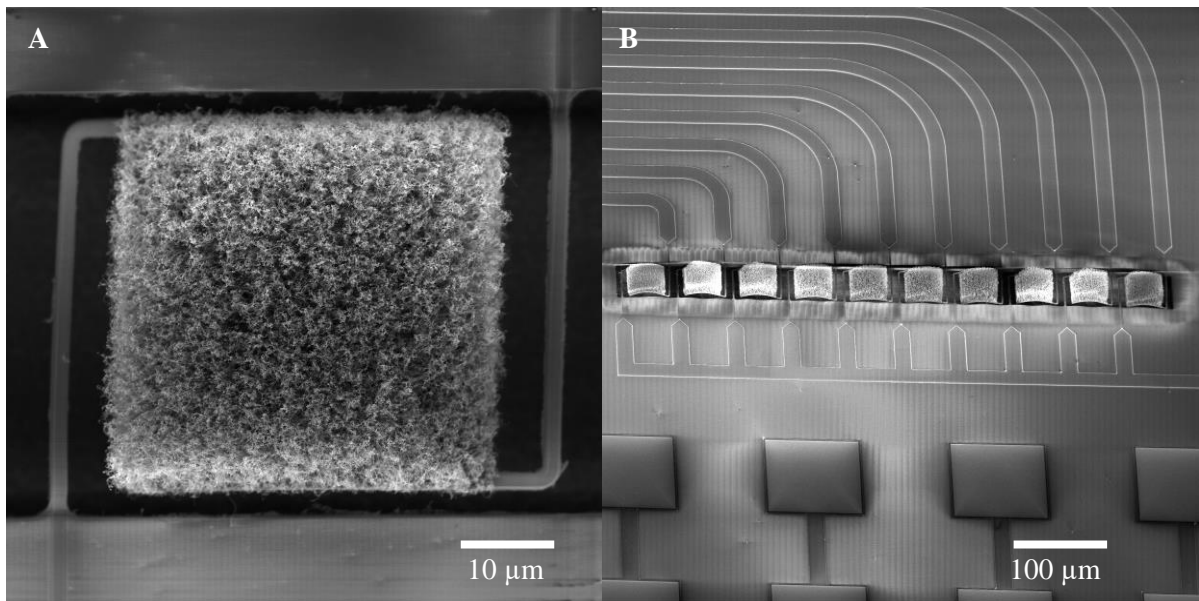
Ze směrodatné odchylky lze dále odvodit limit citlivosti systému  $V_{BAL}$  na  $200\mu V$ . Toto odpovídá výkonu IR záření  $200\text{ pW}$ . Citlivost systému může být dále zlepšena použitím bolometru s vrstvou Ti s hodnotou teplotního součinitele elektrického odporu (TCR) bližší jeho objemovým vlastnostem, tj.  $0,38 \cdot 10^{-3}\text{ K}^{-1}$ . Ti vrstva u testované generace bolometru měla změřenou hodnotu TCR pouze  $0,05 \cdot 10^{-3}\text{ K}^{-1}$ , což je přibližně  $7\times$  méně než jeho objemová hodnota. Vyšší napětí na bolometrech může také zvýšit citlivost systému, i když výstupní signál je lineárně úměrný napětí na bolometrech a vlastní ohřev struktury je dokonce úměrné třetí mocnině napětí na bolometrech. S použitím vyhodnocovacího obvodu s nesaturačním integrátorem  $\Sigma\Delta$  je vlastní ohřev struktury potlačen a vůbec tak neovlivňuje signál  $V_{BAL}$ .

#### 1.2.4 Řádkový systém bolometrů

Na základě předchozích výsledků je nyní konstruován řádkový systém bolometrů. Bylo vytvořeno 100 měřicích membrán bolometrů (pixelů) a pouze 10 referenčních používaných při kompenzaci až 10 měřicích bolometrů pomocí přepínačů. Koncepce tak využívá serio-paralelní způsob měření, který potřebuje pouze 10 měřicích obvodů (ROIC). Detektor je postaven s využitím dvou čipů (MEMS a ROIC) vzájemně propojených bondovacími drátky. Čip MEMS obsahuje membrány bolometru (jednotlivé pixely), které slouží pro detekci IR záření a jsou vyrobeny na křemíkovém substrátu pomocí CMOS kompatibilních procesů. Nejdůležitější snímací část je tvořena z membrány ( $\text{SiO}_2$ ), uvnitř které je integrován odporový meandr (Ti). Při dopadu IR záření na snímací element dojde k jeho ohřátí, a to vyvolá změnu odporu. Tepelné ztráty do substrátu jsou minimalizovány díky tenkým závěsům, na kterých je membrána zavěšena (viz snímky z optického mikroskopu na obr. 15 a elektronového mikroskopu na obr. 16).

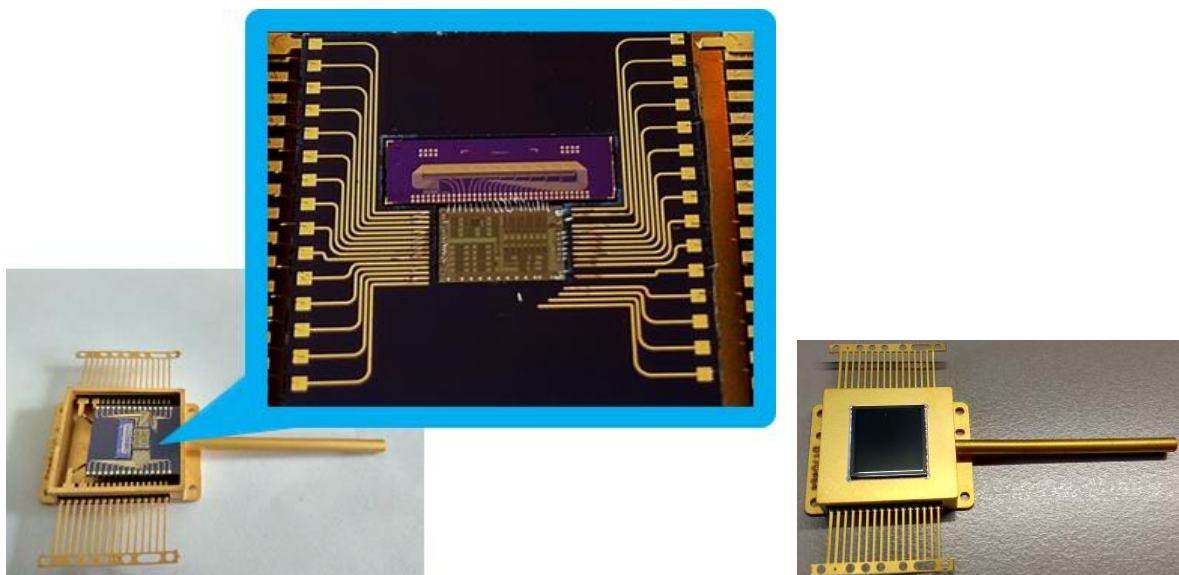


Obr. 15: Snímky vyrobeného jednořádkového MEMS z optického mikroskopu při různém zvětšení. Membrána bolometru má velikost  $40\text{ }\mu\text{m} \times 40\text{ }\mu\text{m}$ .



Obr. 16: Analýza SEM membrán bolometru s uhlíkovými nanotrubicemi: A) Detail jedné membrány bolometru. B) Detail na 10 referenčních membrán bolometru s uhlíkovými nanotrubicemi.

ROIC řádkového bolometru se 110 bolometry (100 měřících + 10 referenčních) byl navržen kolegy ze skupiny návrhu integrovaných obvodů a poté v rámci projektu EURORACTICE byl i tento integrovaný obvod vyroben v technologii AMIS I2T100 s napájecím napětím 5 V, pracovním kmitočtem modulátoru 1 MHz s předpokládaným rozsahem měřené změny teploty bolometru 1–256 mK. Velikost čipu byla 15,13 mm<sup>2</sup>. ROIC byl integrován spolu se 100 pixelovým MEMS bolometrem do jednoho pouzdra, které bylo poté vyčerpáno do vakua o tlaku menším než  $4 \cdot 10^{-2}$  Pa. Dále byl navržen a vyroben rozšiřující čip, pomocí kterého bylo možné propojit oba čipy s ploškami uvnitř jednoho vakuového pouzdra (obr. 17).



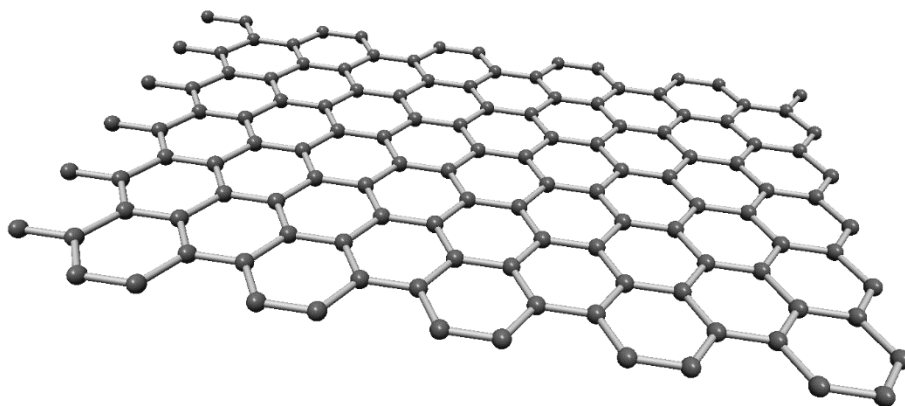
Obr. 17: Detail ROIC řádkového bolometru (uprostřed) a 100 pixelového MEMS bolometru (fialová barva) vložené do otvoru v rozšiřujícím čipu a vzájemně propojené mezi sebou, rozšiřujícím čipem a ploškami pouzdra pomocí bondovacích drátů.

Vakuové pouzdro má připájené germaniové víčko, které podle jeho parametrů umožňuje detekci ve vlnových délkách až téměř 20  $\mu\text{m}$ . V současné době probíhají jednání se společností TYDEX o nahrazení germaniového okna pomocí destičky ze syntetického diamantu, který má lepší propustnost v THz pásmu vlnových délek. Byla připravena pouzdra, která budou podle pokynů upravena pomocí číslicově řízené frézy a pak k nim bude připájena diamantová destička. Celá sestava poté bude připájena nebo přivařena na pouzdro s čipem bolometru s ROIC.

Prostředí okolo čipu je vyčerpáno pomocí trubičky, která je součástí vakuového pouzdra. Tato trubička je zmáčknuta speciálním krimpovacím nástrojem, který byl vyroben na zakázku. Konec trubičky je ještě pro jistotu uzavřen vakuovým epoxidem.

## 2 Grafen

Monovrstva vázaných atomů uhlíku složených do pravidelné šestiúhelníkové struktury podobné včelím plástvím (obr. 18) nazývaná grafen byla poprvé predikována v roce 1946 Wallecem [68] a poprvé připravena v roce 2004 Novoselovem a Geimem na Univerzitě v Manchesteru. Od té doby vznikly stovky publikací [69-71] věnujících se unikátním elektronickým vlastnostem a možným aplikacím [72]. 2D materiál má dále výjimečné tepelné [73], mechanické [74] a optické vlastnosti. Jako jednoatomární vrstva má také neobvyklou mechanickou pružnost a ambipolární přenos elektrických nábojů [71].



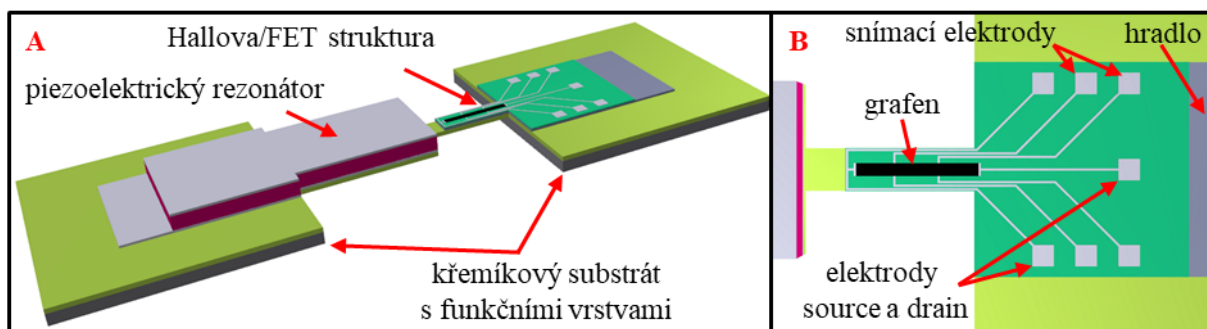
Obr. 18: Monovrstva grafenu tvořená jednoatomární vrstvou atomů uhlíku s šestiúhelníkovou strukturou, vytvořeno pomocí programu Nanotube Modeler.

Grafen se jako jedinečný materiál používá ke snímání fyzikálních a chemických vlastností materiálů. Různé typy nanosenzorů, které používají jednu vrstvu nebo vícevrstvý grafen, byly publikovány pro měření plynů a chemických par. Nejběžnějšími konfiguracemi jsou odporové snímače [75], struktury s tranzistory řízenými elektrickým polem (FET) [76], snímače povrchových akustických vln (SAW) [77], křemenné krystalové mikrováhy (QCM) [78], gravimetrické snímače s MEMS nebo nano-elektro-mechanickými systémy (NEMS) [79] a hybridní senzory oxidu kovu [80].

Nanosenzory založené na grafenu jsou schopny detekovat jednotlivé molekuly, které se přitahují (adsorbují) nebo odpuzují (desorbují) od povrchu. Mimořádnou citlivost grafenu komentoval Andre Geim: "Grafen má maximální citlivost, protože v zásadě nemůže být poražen, nemůžete být citlivější než na jednu molekulu." [81] Protože každý atom grafenové vrstvy je povrchovým atomem, existuje možnost interakce pouze s jednou molekulou detekované látky [75]. Adsorpce a desorpce molekul mění koncentraci volných elektronů. Toto zvýšení nebo snížení koncentrace volných elektronů závisí na detekované molekule, která se chová jako donor nebo akceptor, což vede ke změně elektrické vodivosti nanosenzoru založeného na grafenu. Detekce koncentrace adsorbovaných molekul je možná díky této změně vodivosti.

## 2.1 Modulace fyzikálních vlastností grafenu pomocí mechanické deformace

Cílem projektu poskytnutého Grantovou agenturou České republiky, jehož je autor této práce řešitelem, je výzkum nové metody pro modulování fyzikálních vlastností a charakterizaci monovrstvy grafenu. Vlastnosti mohou být nezávisle řízeny mechanickou deformací piezoelektrického rezonátoru a elektrickým polem struktury FET. Projekt je tedy zaměřen na výzkum nové metody modulace a charakterizace fyzikálních vlastností grafenu při přesně definovaných podmínkách tak, že se spojí grafenová struktura FET s piezoelektrickým rezonátorem. Vlastnosti grafenu na této struktuře jsou modulovány amplitudou a kmitočtem rezonátoru. Tato metoda je založena na možnosti samostatného a přesného řízení elektrického pole, indukovaného pnutí, kmitočtu vibrací a výchylky rezonátoru, které ovlivňují monovrstvu grafenu (obr. 19).



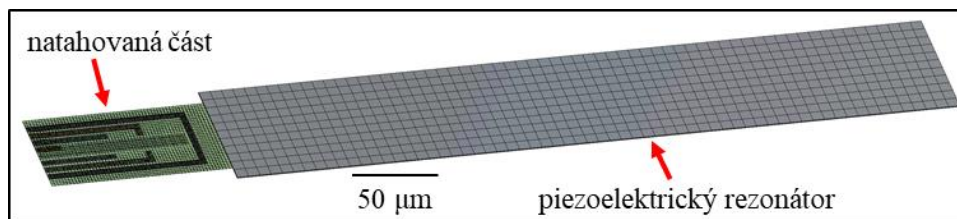
Obr. 19: Koncept a princip navržené struktury pro modulování fyzikálních vlastností a charakterizaci monovrstvy grafenu: A) piezoelektrický rezonátor mechanicky spojený s Hallovou/FET strukturou; B) Detail natahované části s Hallovou/FET strukturou s monovrstvou grafenu pro elektrická měření vlastností grafenu.

Toto řešení dává možnost charakterizovat elektrické vlastnosti grafenu na základě přesně kontrolovatelného mechanického pnutí ve statickém i dynamickém režimu. Tento přístup má velký aplikační potenciál pro měření a sledování buněk, enzymů, aminokyselin, deoxyribonukleových kyselin (DNA) a ribonukleových kyselin (RNA) při pokojové teplotě a dále měření toxických, výbušných, skleníkových plynů nebo chemických zplodin.

K výrobě navrhovaného řešení jsou používány křemíkové substráty pokryté nízkostresovou vrstvou  $\text{SiO}_2$ . Piezoelektrický rezonátor je vyroben z piezoelektrické vrstvy  $\text{AlN}$ , která je mezi dvěma elektrodami. S piezoelektrickými vrstvami z tohoto materiálu jsou dobré zkušenosti a jeho mikrobrábění je kompatibilní s navrhovanou technologií. Jako izolační vrstva slouží  $\text{SiO}_2$ ,  $\text{HfO}_2$  nebo  $\text{Si}_3\text{N}_4$ . Na povrchu izolační vrstvy jsou potom vytvářeny elektrody Hallova typu či struktury FET. V předposledním kroku při výrobě struktury je přenesena a vytvářována monovrstva grafenu na Hallovu či FET strukturu. Nakonec se odstraní křemíkový substrát pod strukturou pomocí suchého leptání a tím se uvolní rezonátor. V projektu jsou také zkoumány polymerní materiály s vysokou elasticitou jako konstrukční a izolační vrstvy pro část obsahující strukturu FET. Tyto polymery dosahují vyšší hodnoty deformace.

Díky navrhovanému řešení je možné řídit vlastnosti monovrstvy grafenu jako je vodivost, pohyblivost a hustota nosičů náboje a také poloha Diracova bodu (kužele). Tyto parametry ovlivňují citlivost, selektivitu a dobu odezvy a regenerace pro snímání plynů, par a biomolekul.

U navrhovaného řešení, respektive struktury byla nejdříve provedena strukturální simulace pomocí metody konečných prvků (FEM) v simulačním programu ANSYS. Simulace byla provedena pro jednostranně vetknutý piezoelektrický rezonátor, který je mechanicky spojený s opět jednostranně vetknutým nosníkem, který reprezentuje namáhanou část struktury s grafenem na povrchu (obr. 20). Příslušné materiálové vlastnosti byly nastaveny pro každou část modelu. Pro numerickou diskretizaci byl použit prvek SOLID226 (20 uzlová cihla) podporující piezoelektrickou analýzu.

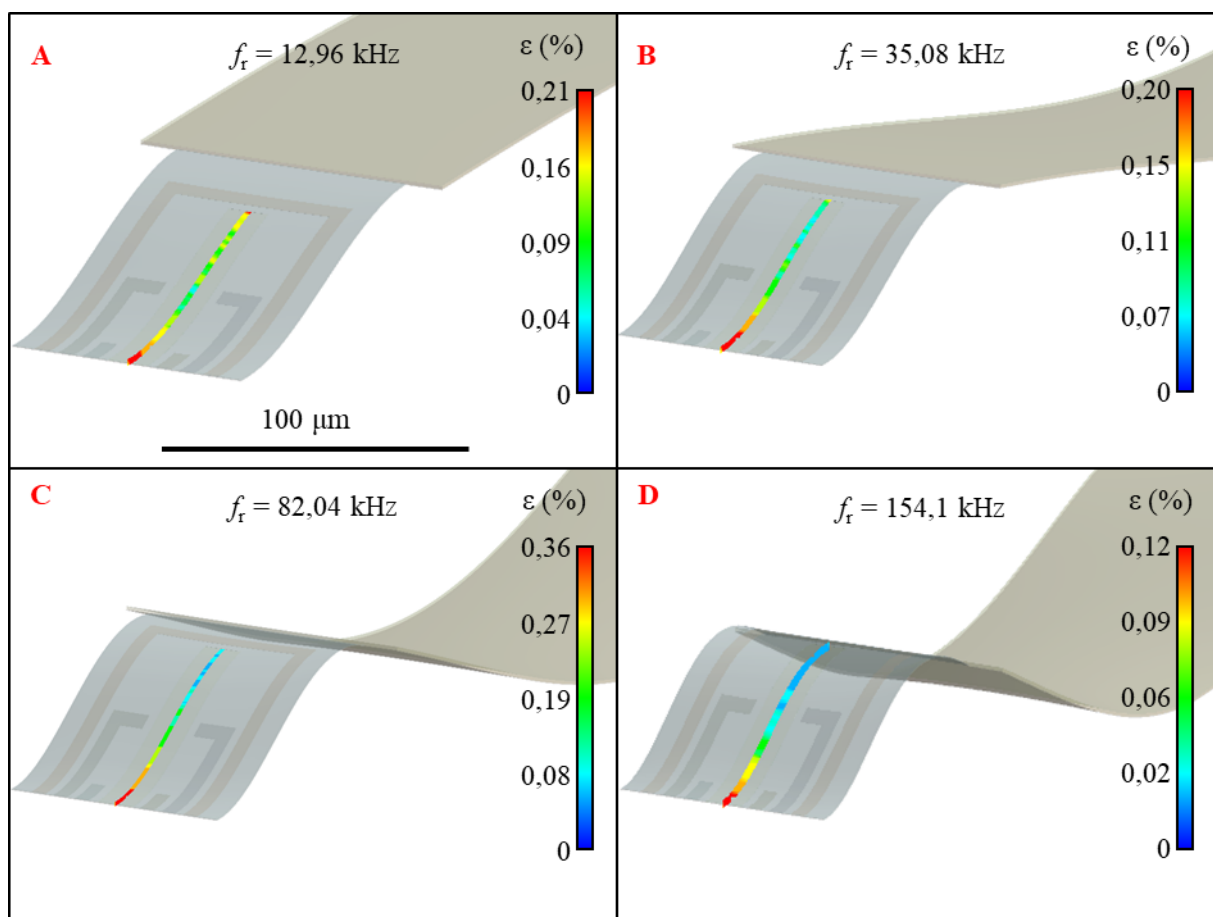


Obr. 20: Zesíťovaný model jednostranně vetknutého piezoelektrického rezonátoru mechanicky připojeného k natahované části reprezentující grafenovou strukturu s Hallovou/FET strukturou.

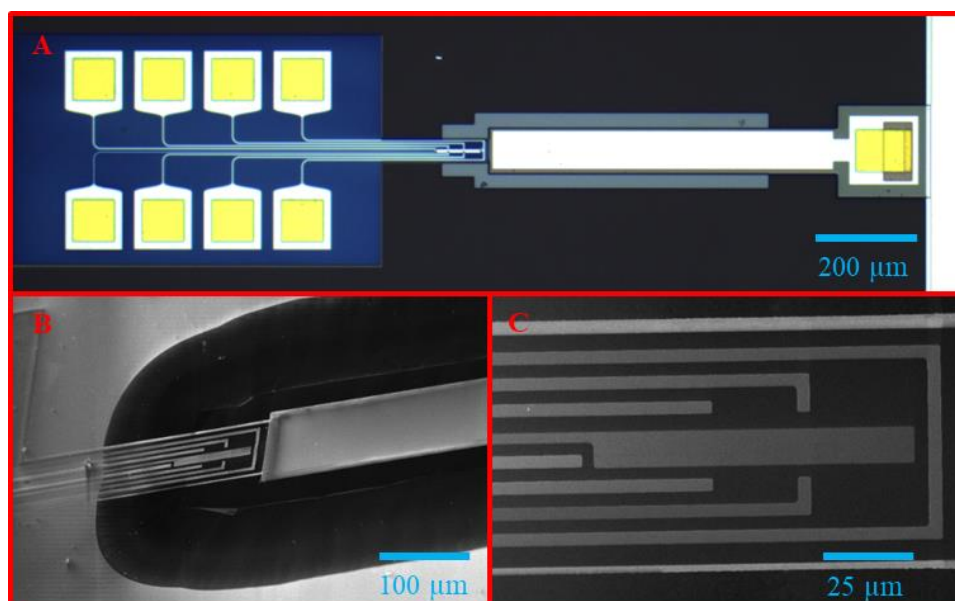
K určení přirozených kmitočtů a tvarů struktury byla použita modální analýza. Přirozené kmitočty a tvarové změny v jednotlivých módech jsou důležitými parametry při návrhu rozměru a složení struktury při dynamickém zatížení. Pro dosažení dobré konvergence simulačního programu byl nastaven faktor tlumení s hodnotou 0,005 [82].

Strukturální analýza FEM (obr. 21) ukázala vliv ohýbání rezonátoru na indukovaný stres ( $\epsilon$ ) do natahované části, která je mechanicky spojena s rezonátorovou částí. Velikost rezonátorové části byla  $600 \mu\text{m} \times 100 \mu\text{m}$  a velikost natahované části byla  $100 \mu\text{m} \times 75 \mu\text{m}$ . Harmonická analýza byla provedena v rozsahu od 0 do 200 kHz a byly zjištěny čtyři rezonance (obr. 21). Třetí a šestý rezonanční kmitočet se v modální analýze neprojevil, protože při něm docházelo k odlišnému směru ohýbání (torzní).

Dále bylo simulováno rozložení pnutí jako funkce přiloženého střídavého napětí na elektrody piezoelektrického rezonátoru až do hodnoty 20 V. Maximální zjištěné indukované pnutí bylo  $\approx 0,36 \%$  v dynamickém režimu v místě umístění grafenu (obr. 21C). Indukované pnutí je nižší, než kterého dosáhly jiné výzkumné skupiny [83,84]. Na druhou stranu může být indukované pnutí jednoduše měněno laděním kmitočtu rezonátoru.



Obr. 21: Rozložení pnutí uvnitř grafenu umístěném na natahované části. Natahovaná část je mechanicky spojena s jednostranně vetknutým piezoelektrickým rezonátorem: A) 1. rezonanční kmitočet při 12,96 kHz; B) 2. rezonanční kmitočet při 35,08 kHz; C) 4. rezonanční kmitočet při 82,04 kHz; D) 5. rezonanční kmitočet při 154,1 kHz. Černé měřítko je stejné pro všechny části obrázku.



Obr. 22: Vyrobená struktura pro charakterizace grafenu: A) snímek z optického mikroskopu celé struktury; B) analýza SEM uvolněné (podleptané) části; C) detail natahované části s elektrodami (Hallova/FET struktura)

Hodnota deformace může být dále jednoduše zvýšena změnou rozměrů a tvarů rezonátoru. Dlouhá a užší část rezonátoru spolu s kratší natahovanou částí rapidně zvyšuje maximální indukované pnutí v grafenu. Simulované struktury byly již vyrobeny (obr. 22) a nyní probíhá jejich testování s monovrstvou grafenu.

Výsledky z projektu GAČR s grafenem byly již publikovány na prestižní konferenci *Euroensors 2018* [85] (nová metoda pro studium 2D materiálů pomocí řízeného mechanického pnutí) a v časopise *Thin Solid Films* [86] (příprava bezstresových vrstev AlN).

## Závěr

Práce shrnuje teoretické a experimentální výsledky výzkumu autora zaměřené na uhlíkové materiály, které jsou využívány v mikroelektronice a senzorce na Ústavu mikroelektroniky Fakulty elektrotechniky a komunikačních technologií, VUT v Brně.

Uhlíkové nanotrubic jsou využívány jako zdroje elektronů v emisním senzoru tlaku, kde jejich unikátnost spočívá především ve výrazném zvýšení hodnoty měřeného emisního proudu v porovnání s emisními senzory založených na mikrorohotech. V bolometrických aplikacích pak nanotrubic výrazně zvětšují absorpci nejen v IR pásmu. Způsob jejich depozice na membránách bolometru je také unikátní díky pokojové teplotě substrátu a tím pádem možné implementaci a kompatibilitě s technikou výroby integrovaných obvodů CMOS.

Výzkum grafenu se týká nové metody pro modulování fyzikálních vlastností a charakterizaci monovrstvy grafenu. Toto řešení umožňuje charakterizovat elektrické vlastnosti grafenu na základě přesně řízeného mechanického pnutí ve statickém i dynamickém režimu. Tento přístup má velký aplikační potenciál pro měření a sledování buněk, enzymů, aminokyselin, DNA a RNA při pokojové teplotě a dále měření toxických, výbušných, skleníkových plynů nebo chemických zplodin.

Práce je dále doplněna publikacemi, které vznikly k řešeným tématům. Jedná se o studium vlastností CNTs deponovaných v plasmovém výboji pro senzorické aplikace v časopise *Sensors* [19] (IF<sub>2017</sub> = 2,475), měření mechanických, elektrických a povrchových vlastností uhlíkových nanotubic pomocí AFM v časopise *Sensors and Actuators A-Physical* [18] (IF<sub>2017</sub> = 2,311) a studii emise elektrickým polem z uhlíkových nanotubic v časopise *IEEE Sensors Journal* [47] (IF<sub>2017</sub> = 2,617).

Z oblasti využití CNTs pro snímání IR záření vznikly 3 publikace, a to *in situ* pozorování unikátního způsobu růstu uhlíkových nanotubic na bolometrech se substrátem při pokojové teplotě v časopise *Journal of Applied Physics* [66] (IF<sub>2017</sub> = 2,176), přesné stanovení teplotních parametrů mikrobolometrů v časopise *Infrared Physics & Technology* [87] (IF<sub>2017</sub> = 1,851) a samokompensující metoda pro odečítání signálů z mikrobolometrů v časopise *Sensors and Actuators A-Physical* [67] (IF<sub>2017</sub> = 2,311).

Ze studia grafenu vznikla publikace věnující se stresu a přenosu náboje v uniaxiálně napnutém grafenu v časopise *Physica Status Solidi B-Basic Solid State Physics* [88] (IF<sub>2017</sub> = 1,729) a rešerše ohledně dalších potenciálních monoelementárních 2D materiálů založených na FET strukturách pro snímání nejen fyzikálních veličin v časopise *TRAC-Trends in Analytical Chemistry* [89] (IF<sub>2017</sub> = 7,030).

Výzkum autora v oblasti využití uhlíkových materiálů v mikroelektronice a senzorce pokračuje a chtěl by se dále věnovat studiu i dalších, především nových 2D materiálů, které mají velký aplikační potenciál a kde je možné očekávat publikace ve vysoce hodnocených a citovaných časopisech.

## Reference

- [1] HIRSCH, A. The era of carbon allotropes. *Nature Materials*, 2010, vol. 9, no. 11, pp. 868-871. ISSN 1476-1122.
- [2] KARFUNKEL, H. R. a DRESSLER, T. New hypothetical carbon allotropes of remarkable stability estimated by modified neglect of diatomic overlap solid-state self-consistent field computations. *Journal of the American Chemical Society*, 1992, vol. 114, no. 7, pp. 2285-2288. ISSN 0002-7863.
- [3] CATALDO, F. Polyynes: a new class of carbon allotropes. About the formation of dicyanopolyynes from an electric arc between graphite electrodes in liquid nitrogen. *Polyhedron*, 2004, vol. 23, no. 11, pp. 1889-1896. ISSN 0277-5387.
- [4] BURCHFIELD, L. A. et al. Novamene: a new class of carbon allotropes. *Heliyon*, 2017, vol. 3, no. 2. ISSN 2405-8440.
- [5] VILLARREAL, C. C. et al. Carbon allotropes as sensors for environmental monitoring. *Current Opinion in Electrochemistry*, 2017, vol. 3, no. 1, pp. 106-113. ISSN 2451-9103.
- [6] TIWARI, S. K. et al. Magical allotropes of carbon: prospects and applications. *Critical Reviews in Solid State and Materials Sciences*, 2016, vol. 41, no. 4, pp. 257-317. ISSN 1040-8436.
- [7] KANOUN, O. et al. Potential of flexible carbon nanotube films for high performance strain and pressure sensors. In ALIOFKHAZRAEI, M. *Nanotechnology for optics and sensors*. Iran: One Central Press, 2015, pp. 148-183. ISBN 978-1-910-08609-4.
- [8] KROTO, H. W. et al. C-60 - Buckminsterfullerene. *Nature*, 1985, vol. 318, no. 6042, pp. 162-163. ISSN 0028-0836.
- [9] IJIMA, S. Helical microtubules of graphitic carbon. *Nature*, 1991, vol. 354, no. 6348, pp. 56-58. ISSN 0028-0836.
- [10] NOVOSELOV, K. S. et al. Electric field effect in atomically thin carbon films. *Science*, 2004, vol. 306, no. 5696, pp. 666-669. ISSN 1095-9203.
- [11] GEORGAKILAS, V. et al. Broad family of carbon nanoallotropes: classification, chemistry, and applications of fullerenes, carbon dots, nanotubes, graphene, nanodiamonds, and combined superstructures. *Chemical Reviews*, 2015, vol. 115, no. 11, pp. 4744-4822. ISSN 0009-2665.
- [12] RODE, A. V. et al. Structural analysis of a carbon foam formed by high pulse-rate laser ablation. *Applied Physics a-Materials Science & Processing*, 1999, vol. 69, pp. S755-S758. ISSN 0947-8396.
- [13] ZHAO, C.-X. et al. C-57 carbon: a two-dimensional metallic carbon allotrope with pentagonal and heptagonal rings. *Computational Materials Science*, 2019, vol. 160, pp. 115-119. ISSN 0927-0256.
- [14] NULAKANI, N. V. R. a SUBRAMANIAN, V. Superprismane: a porous carbon allotrope. *Chemical Physics Letters*, 2019, vol. 715, pp. 29-33. ISSN 0009-2614.
- [15] RADUSHKEVICH, L. V. a LUKYANOVICH, V. M. O structure ugleroda, obrazuyushchegosya pri termicheskom razlozhenii okisi ugleroda na zheleznom kontakte. *Zhurnal Fizicheskoi Khimii*, 1952, vol. 26, pp. 88-95. ISSN 0044-4537.
- [16] MONTHIOUX, M. a KUZNETSOV, V. L. Who should be given the credit for the discovery of carbon nanotubes? *Carbon*, 2006, vol. 44, no. 9, pp. 1621-1623. ISSN 0008-6223.
- [17] KRÄTSCHMER, W. et al. The infrared and ultraviolet absorption spectra of laboratory-produced carbon dust: evidence for the presence of the C60 molecule. *Chemical Physics Letters*, 1990, vol. 170, no. 2-3, pp. 167-170. ISSN 0009-2614.

- [18] SVATOŠ, V. et al. Single measurement determination of mechanical, electrical, and surface properties of a single carbon nanotube via force microscopy. *Sensors and Actuators, A: Physical*, 2018, vol. 271, pp. 217-222. ISSN 0924-4247.
- [19] MAJZLÍKOVÁ, P. et al. Sensing properties of multiwalled carbon nanotubes grown in MW plasma torch: electronic and electrochemical behavior, gas sensing, field emission, IR absorption. *Sensors (Basel)*, 2015, vol. 15, no. 2, pp. 2644-2661. ISSN 1424-8220.
- [20] TREACY, M. M. J. et al. Exceptionally high Young's modulus observed for individual carbon nanotubes. *Nature*, 1996, vol. 381, no. 6584, pp. 678-680. ISSN 0028-0836.
- [21] THOSTENSON, E. T. et al. Advances in the science and technology of carbon nanotubes and their composites: a review. *Composites Science and Technology*, 2001, vol. 61, no. 13, pp. 1899-1912. ISSN 0266-3538.
- [22] YU, M. F. et al. Tensile loading of ropes of single wall carbon nanotubes and their mechanical properties. *Physical Review Letters*, 2000, vol. 84, no. 24, pp. 5552-5555. ISSN 0031-9007.
- [23] YU, M. F. et al. Strength and breaking mechanism of multiwalled carbon nanotubes under tensile load. *Science*, 2000, vol. 287, no. 5453, pp. 637-640. ISSN 0036-8075.
- [24] LOURIE, O. a WAGNER, H. D. Evaluation of Young's modulus of carbon nanotubes by micro-Raman spectroscopy. *Journal of Materials Research*, 1998, vol. 13, no. 9, pp. 2418-2422. ISSN 0884-2914.
- [25] MINTMIRE, J. W. et al. Are fullerene tubules metallic. *Physical Review Letters*, 1992, vol. 68, no. 5, pp. 631-634. ISSN 0031-9007.
- [26] HAMADA, N. et al. New one-dimensional conductors - graphitic microtubules. *Physical Review Letters*, 1992, vol. 68, no. 10, pp. 1579-1581. ISSN 0031-9007.
- [27] ODOM, T. W. et al. Atomic structure and electronic properties of single-walled carbon nanotubes. *Nature*, 1998, vol. 391, no. 6662, pp. 62-64. ISSN 0028-0836.
- [28] EBBESEN, T. W. et al. Electrical conductivity of individual carbon nanotubes. *Nature*, 1996, vol. 382, no. 6586, pp. 54-56. ISSN 0028-0836.
- [29] CHARLIER, J. C. a ISSI, J. P. Electrical conductivity of novel forms of carbon. *Journal of Physics and Chemistry of Solids*, 1996, vol. 57, no. 6-8, pp. 957-965. ISSN 0022-3697.
- [30] DAI, H. J. et al. Probing electrical transport in nanomaterials: Conductivity of individual carbon nanotubes. *Science*, 1996, vol. 272, no. 5261, pp. 523-526. ISSN 0036-8075.
- [31] BERBER, S. et al. Unusually high thermal conductivity of carbon nanotubes. *Physical Review Letters*, 2000, vol. 84, no. 20, pp. 4613-4616. ISSN 0031-9007.
- [32] HONE, J. et al. Thermal conductivity of single-walled carbon nanotubes. *Physical Review B*, 1999, vol. 59, no. 4, pp. R2514-R2516. ISSN 1098-0121.
- [33] HSU, T.-R. *MEMS & microsystems: design, manufacture, and nanoscale engineering*. John Wiley & Sons, 2008. ISBN 978-0-470-08301-7.
- [34] *MEMS materials and processes handbook*. London: Springer, 2011. 1224 ISBN 978-0-387-47316-1.
- [35] TAN, R. et al. Development of a fully implantable wireless pressure monitoring system. *Biomed Microdevices*, 2009, vol. 11, no. 1, pp. 259-264. ISSN 1572-8781.
- [36] PONMOZHI, J. et al. Smart sensors/actuators for biomedical applications: review. *Measurement*, 2012, vol. 45, no. 7, pp. 1675-1688. ISSN 0263-2241.
- [37] ESASHI, M. Revolution of sensors in micro-electromechanical systems. *Japanese Journal of Applied Physics*, 2012, vol. 51, no. 8. ISSN 0021-4922.
- [38] JENSEN, K. F. Silicon-based microchemical systems: characteristics and applications. *Mrs Bulletin*, 2006, vol. 31, no. 2, pp. 101-107. ISSN 0883-7694.
- [39] *Carbon nanotubes: science and applications*. Boca Raton, Florida: CRC Press LLC, 2005. ISBN 0-8493-2111-5.

- [40] JIANG, X. et al. Ultrahigh boron doping of nanocrystalline diamond films and their electron field emission characteristics. *Journal of Applied Physics*, 2002, vol. 92, no. 5, pp. 2880-2883. ISSN 0021-8979.
- [41] SUBRAMANIAN, K. et al. A review of recent results on diamond vacuum lateral field emission device operation in radiation environments. *Microelectronic Engineering*, 2011, vol. 88, no. 9, pp. 2924-2929. ISSN 0167-9317.
- [42] ZOU, Y. et al. Field emission from diamond-coated multiwalled carbon nanotube "teepee" structures. *Journal of Applied Physics*, 2012, vol. 112, no. 4. ISSN 0021-8979.
- [43] JOAG, D. et al. *Field emission from nanowires*. Rijeka, Croatia: InTech, 2011. ISBN 978-953-307-318-7.
- [44] BONARD, J. M. et al. Field emission properties of multiwalled carbon nanotubes. *Ultramicroscopy*, 1998, vol. 73, no. 1-4, pp. 7-15. ISSN 0304-3991.
- [45] GUO, P. S. et al. Fabrication of field emission display prototype utilizing printed carbon nanotubes/nanofibers emitters. *Solid-State Electronics*, 2008, vol. 52, no. 6, pp. 877-881. ISSN 0038-1101.
- [46] NAKAHARA, H. et al. Evaluations of carbon nanotube field emitters for electron microscopy. *Applied Surface Science*, 2009, vol. 256, no. 4, pp. 1214-1217. ISSN 0169-4332.
- [47] PEKÁREK, J. et al. MEMS carbon nanotubes field emission pressure sensor with simplified design: performance and field emission properties study. *IEEE Sensors Journal*, 2015, vol. 15, no. 3, pp. 1430-1436. ISSN 1530-437x.
- [48] FOWLER, R. H. a NORDHEIM, L. Electron emission in intense electric fields. *Proceedings of the Royal Society A: Mathematical, Physical and Engineering Sciences*, 1928, vol. 119, no. 781, pp. 173-181. ISSN 1364-5021.
- [49] CHENG, C. Y. et al. Low threshold field emission from nanocrystalline diamond/carbon nanowall composite films. *Diamond and Related Materials*, 2012, vol. 27-28, pp. 40-44. ISSN 0925-9635.
- [50] LI, Z. et al. *Field electron emission of nanorods of semiconductors of wide energy band gaps*. Vacuum Nanoelectronics Conference, 2005. IVNC 2005. Technical Digest of the 18th International. 10-14 July 2005. 0-7803-9384-8.
- [51] BARBOUR, J. P. et al. Space-charge effects in field emission. *Physical Review*, 1953, vol. 92, no. 1, pp. 45-51. ISSN 0031-899x.
- [52] DEAN, K. A. a CHALAMALA, B. R. Current saturation mechanisms in carbon nanotube field emitters. *Applied Physics Letters*, 2000, vol. 76, no. 3, pp. 375-377. ISSN 0003-6951.
- [53] BINGQIANG, C. et al. A template-free electrochemical deposition route to ZnO nanoneedle arrays and their optical and field emission properties. *Nanotechnology*, 2005, vol. 16, no. 11, pp. 2567. ISSN 0957-4484.
- [54] MAY, P. W. et al. Field emission conduction mechanisms in chemical vapor deposited diamond and diamondlike carbon films. *Applied Physics Letters*, 1998, vol. 72, no. 17, pp. 2182-2184. ISSN 0003-6951.
- [55] EDA, G. et al. Field emission from graphene based composite thin films. *Applied Physics Letters*, 2008, vol. 93, no. 23, pp. 233502. ISSN 0003-6951.
- [56] OBRAZTSOV, A. N. et al. Non-classical electron field emission from carbon materials. *Diamond and Related Materials*, 2003, vol. 12, no. 3-7, pp. 446-449. ISSN 0925-9635.
- [57] XU, X. a BRANDES, G. R. A method for fabricating large-area, patterned, carbon nanotube field emitters. *Applied Physics Letters*, 1999, vol. 74, no. 17, pp. 2549-2551. ISSN 1077-3118.
- [58] BULDUM, A. a LU, J. P. Electron field emission properties of closed carbon nanotubes. *Physical Review Letters*, 2003, vol. 91, no. 23, pp. 236801. ISSN 1079-7114.

- [59] HAN, S. et al. Dynamical simulation of field emission in nanostructures. *Physical Review B*, 2002, vol. 65, no. 8, pp. 085405. ISSN 2469-9969.
- [60] COLLINS, P. G. a ZETTL, A. Unique characteristics of cold cathode carbon-nanotube-matrix field emitters. *Physical Review B*, 1997, vol. 55, no. 15, pp. 9391-9399. ISSN 2469-9969.
- [61] SHIRAIISHI, M. a ATA, M. Work function of carbon nanotubes. *Carbon*, 2001, vol. 39, no. 12, pp. 1913-1917. ISSN 0008-6223.
- [62] LANGLEY, S. P. The Bolometer. *Nature*, 1881, vol. 25, pp. 14. ISSN 1476-4687.
- [63] LANG, W. et al. Absorbing layers for thermal infrared detectors. *Sensors and Actuators a-Physical*, 1992, vol. 34, no. 3, pp. 243-248. ISSN 0924-4247.
- [64] MORENO, M. et al. *Un-Cooled microbolometers with amorphous germanium-silicon (a-GexSi<sub>y</sub>: H) thermo-sensing films*. InTech, 2012. ISBN 953-510-235-4.
- [65] NIKLAUS, F. et al. MEMS-based uncooled infrared bolometer arrays - a review. *Mems/Moems Technologies and Applications Iii*, 2008, vol. 6836. ISSN 0277-786x.
- [66] SVATOŠ, V. et al. In situ observation of carbon nanotube layer growth on microbolometers with substrates at ambient temperature. *Journal of Applied Physics*, 2018, vol. 123, no. 11. ISSN 1089-7550.
- [67] PEKÁREK, J. et al. Self-compensating method for bolometer-based IR focal plane arrays. *Sensors and Actuators, A: Physical*, 2017, vol. 265, pp. 40-46. ISSN 0924-4247.
- [68] WALLACE, P. R. The band theory of graphite. *Physical Review*, 1947, vol. 71, no. 9, pp. 622-634. ISSN 0031-899x.
- [69] ALLEN, M. J. et al. Honeycomb carbon: a review of graphene. *Chemical Reviews*, 2010, vol. 110, no. 1, pp. 132-145. ISSN 0009-2665.
- [70] FIORI, G. et al. Electronics based on two-dimensional materials. *Nat Nano*, 2014, vol. 9, no. 10, pp. 768-779. ISSN 1748-3387.
- [71] NOVOSELOV, K. S. et al. A roadmap for graphene. *Nature*, 2012, vol. 490, no. 7419, pp. 192-200. ISSN 0028-0836.
- [72] CASTRO NETO, A. H. et al. The electronic properties of graphene. *Reviews of Modern Physics*, 2009, vol. 81, no. 1, pp. 109-162. ISSN 1539-0756.
- [73] CHOI, W. a LEE, J. *Graphene: synthesis and applications*. Taylor & Francis, 2011. ISBN 978-143-986-187-5.
- [74] LEE, C. et al. Measurement of the elastic properties and intrinsic strength of monolayer graphene. *Science*, 2008, vol. 321, no. 5887, pp. 385-388. ISSN 1095-9203.
- [75] SCHEDIN, F. et al. Detection of individual gas molecules adsorbed on graphene. *Nature Materials*, 2007, vol. 6, no. 9, pp. 652-655. ISSN 1476-1122.
- [76] OHNO, Y. et al. Chemical and biological sensing applications based on graphene field-effect transistors. *Biosensors & Bioelectronics*, 2010, vol. 26, no. 4, pp. 1727-1730. ISSN 0956-5663.
- [77] ARASH, B. et al. Detection of gas atoms via vibration of graphenes. *Physics Letters A*, 2011, vol. 375, no. 24, pp. 2411-2415. ISSN 0375-9601.
- [78] YAO, Y. et al. Graphene oxide thin film coated quartz crystal microbalance for humidity detection. *Applied Surface Science*, 2011, vol. 257, no. 17, pp. 7778-7782. ISSN 0169-4332.
- [79] BASU, S. a BHATTACHARYYA, P. Recent developments on graphene and graphene oxide based solid state gas sensors. *Sensors and Actuators B-Chemical*, 2012, vol. 173, pp. 1-21. ISSN 0925-4005.
- [80] YI, J. et al. Vertically aligned ZnO nanorods and graphene hybrid architectures for high-sensitive flexible gas sensors. *Sensors and Actuators B-Chemical*, 2011, vol. 155, no. 1, pp. 264-269. ISSN 0925-4005.

- [81] BOOTH, T. J. et al. Macroscopic graphene membranes and their extraordinary stiffness. *Nano Letters*, 2008, vol. 8, no. 8, pp. 2442-2446. ISSN 1530-6984.
- [82] PUTNIK, M. et al. Simulation and modelling of the drive mode nonlinearity in MEMS-gyroscopes. *Proceedings of the 30th Anniversary Eurosensors Conference - Eurosensors 2016*, 2016, vol. 168, pp. 950-953. ISSN 1877-7058.
- [83] DONG, J. et al. Investigation of strain-induced modulation on electronic properties of graphene field effect transistor. *Physics Letters A*, 2017, vol. 381, no. 4, pp. 292-297. ISSN 0375-9601.
- [84] CHOI, S.-M. et al. Controlling energy gap of bilayer graphene by strain. *Nano Letters*, 2010, vol. 10, no. 9, pp. 3486-3489. ISSN 1530-6984.
- [85] GABLECH, I. et al. A new method for 2D materials properties modulation by controlled induced mechanical strain. *Proceedings*, 2018, vol. 2, no. 13, pp. 1513. ISSN 2504-3900.
- [86] GABLECH, I. et al. Preparation of high-quality stress-free (001) aluminum nitride thin film using a dual Kaufman ion-beam source setup. *Thin Solid Films*, 2019, vol. 670, pp. 105-112. ISSN 0040-6090.
- [87] SVATOŠ, V. et al. Precise determination of thermal parameters of a microbolometer. *Infrared Physics and Technology*, 2018, vol. 93, pp. 286-290. ISSN 1350-4495.
- [88] BOUŠA, M. et al. Stress and charge transfer in uniaxially strained CVD graphene. *Physica Status Solidi B-Basic Solid State Physics*, 2016, vol. 253, no. 12, pp. 2355-2361. ISSN 0370-1972.
- [89] GABLECH, I. et al. Monoelemental 2D materials-based field effect transistors for sensing and biosensing: Phosphorene, antimonene, arsenene, silicene, and germanene go beyond graphene. *Trac-Trends in Analytical Chemistry*, 2018, vol. 105, pp. 251-262. ISSN 0165-9936.

## Seznam použitých zkratk

<b>Zkratka</b>	<b>Význam</b>
AFM	Mikroskop atomárních sil
DSP	Zpracování digitálního signálu
FEM	Metoda konečných prvků
FET	Tranzistory řízené elektrickým polem
FPN	Fixed pattern šum
FTIR	Infračervená spektroskopie s Fourierovou transformací
CMOS	Doplňkový kov-oxid-polovodič
CNTs	Uhlíkové nanotrubic
CVD	Chemická depozice z plynné fáze
DNA	Deoxyribonukleová kyselina
F–N	Fowler–Nordheimova teorie (model, závislost)
GAČR	Grantová agentura České republiky
GPIB	Rozhraní pro měřicí a zkušební přístroje a zařízení
H2020	Rámcový program pro výzkum a inovace EU Horizont 2020
IR	Infračervený
LCC68	Bezvývodové keramické pouzdro
MEMS	Mikro-elektro-mechanické systémy
MVČR	Ministerstvo vnitra České republiky
NA	Numerická apertura
NEMS	Nano-elektro-mechanické systémy
QCM	Křemenné krystalové mikrováhy
RNA	Ribonukleová kyselina
ROIC	Vyhodnocovací integrované obvody (z angl. read-out integrated circuit)
SAW	Povrchové akustické vlny
SEM	Skenovací elektronový mikroskop
SNR	Poměr odstupu signálu k šumu
TCR	Teplotní součinitel elektrického odporu
TEM	Transmisní elektronová mikroskopie
VUT	Vysoké učení technické v Brně

## Vybrané publikace autora k tématu habilitační práce jako přílohy

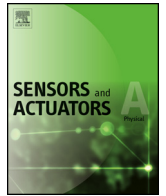
- [18] SVATOŠ, V. et al. Single measurement determination of mechanical, electrical, and surface properties of a single carbon nanotube via force microscopy. *Sensors and Actuators, A: Physical*, 2018, vol. 271, pp. 217-222. ISSN 0924-4247.
- [19] MAJZLÍKOVÁ, P. et al. Sensing properties of multiwalled carbon nanotubes grown in MW plasma torch: electronic and electrochemical behavior, gas sensing, field emission, IR absorption. *Sensors (Basel)*, 2015, vol. 15, no. 2, pp. 2644-2661. ISSN 1424-8220.
- [47] PEKÁREK, J. et al. MEMS carbon nanotubes field emission pressure sensor with simplified design: performance and field emission properties study. *IEEE Sensors Journal*, 2015, vol. 15, no. 3, pp. 1430-1436. ISSN 1530-437x.
- [66] SVATOŠ, V. et al. In situ observation of carbon nanotube layer growth on microbolometers with substrates at ambient temperature. *Journal of Applied Physics*, 2018, vol. 123, no. 11. ISSN 1089-7550.
- [67] PEKÁREK, J. et al. Self-compensating method for bolometer-based IR focal plane arrays. *Sensors and Actuators, A: Physical*, 2017, vol. 265, pp. 40-46. ISSN 0924-4247.
- [87] SVATOŠ, V. et al. Precise determination of thermal parameters of a microbolometer. *Infrared Physics and Technology*, 2018, vol. 93, pp. 286-290. ISSN 1350-4495.
- [88] BOUŠA, M. et al. Stress and charge transfer in uniaxially strained CVD graphene. *Physica Status Solidi B-Basic Solid State Physics*, 2016, vol. 253, no. 12, pp. 2355-2361. ISSN 0370-1972.
- [89] GABLECH, I. et al. Monoelemental 2D materials-based field effect transistors for sensing and biosensing: Phosphorene, antimonene, arsenene, silicene, and germanene go beyond graphene. *Trac-Trends in Analytical Chemistry*, 2018, vol. 105, pp. 251-262. ISSN 0165-9936.

## Příloha 1

SVATOŠ, V. et al. Single measurement determination of mechanical, electrical, and surface properties of a single carbon nanotube via force microscopy. *Sensors and Actuators, A: Physical*, 2018, vol. 271, pp. 217-222. ISSN 0924-4247.

### ABSTRAKT

Uhlíkové nanotrubičky přitahují velkou pozornost kvůli svým pozoruhodným mechanickým a elektrickým vlastnostem. Přestože se předpokládá, že nejdůležitější otázky týkající se CNTs již byly vyřešeny, opak je pravdou. CNTs mají vysokou mechanickou tuhost a elektrickou vodivost a vzhledem k jejich malému průměru a velikosti je měření těchto vlastností na úrovni nanometrů velice náročné. Zde uvádíme jedinečnou metodu pro určení jejich mechanických a elektrických vlastností pomocí interakcí mezi vertikálně orientovanými mnohostěnnými CNTs a pokoveným hrotem AFM. Použili jsme metodu měření síly-vzdálenosti se souběžným sledováním elektrického proudu. Můžeme identifikovat počet CNTs v kontaktu s hrotem, tuhost jednotlivé CNT, adhezní sílu mezi hrotem a jednotlivými CNTs a elektrickou vodivost každé CNTs. Tato metoda je vhodná pro charakterizaci i jiných vertikálně uspořádaných nanostruktur nebo nanočástic. Metoda řeší dlouhotrvající problém určování vlastností nanostrukturálních materiálů a je důležitým doplňkem k metodám charakterizace v oblasti nanotechnologií.



# Single Measurement Determination of Mechanical, Electrical, and Surface Properties of a Single Carbon Nanotube *via* Force Microscopy

Vojtěch Svatoš<sup>a</sup>, Wanxin Sun<sup>b</sup>, Radek Kalousek<sup>a</sup>, Imrich Gablech<sup>a</sup>, Jan Pekárek<sup>a</sup>, Pavel Neužil<sup>a,c,\*</sup>

<sup>a</sup> SIX Center, Brno University of Technology, Technická 3058/10, 616 00 Brno, Czech Republic

<sup>b</sup> Bruker Nano Surface, 11 Biopolis Way #10-10, 138667, Singapore

<sup>c</sup> Northwestern Polytechnical University, 127 West Youyi Road, Xi'an, Shaanxi, PR China

## ARTICLE INFO

### Article history:

Received 24 October 2017

Received in revised form

24 December 2017

Accepted 8 January 2018

Available online 3 February 2018

## ABSTRACT

Carbon nanotubes (CNTs) have attracted significant attention due to their remarkable mechanical and electrical properties. Although it is assumed that the most important questions about CNTs have been addressed, the opposite is true. CNTs have high mechanical stiffness and electrical conductivity and, due to their small diameter and size, the measurement of those properties at nanoscale level is challenging. Here, we present a unique method to determine their mechanical and electrical properties by using interactions between vertically aligned multiwall CNTs and a metal-coated tipless atomic force microscope cantilever. We used a force–distance measurement (FDM) method with concurrent monitoring of electrical current. We could identify the number of CNTs in contact with the cantilever, stiffness of each individual CNT, the adhesion force between the cantilever and individual CNTs, and the electrical conductivity of each CNT. The method is also suitable for characterizing other vertically aligned nanostructured materials, such as nanowires. This method addresses the long-standing problem of property determination of materials such as CNTs and nanowires and is an important addition to the toolbox of nanoscale characterization methods.

© 2018 Elsevier B.V. All rights reserved.

## 1. Introduction

Carbon nanotubes (CNTs) were first reported in 1970 [1] and since then their remarkable properties have been discussed many times [2,3]. The widespread interest in this material was triggered by the publication of preparation methods for multiwall CNTs (MWCNTs) and single-wall CNTs (SWCNTs) in 1991 [4] and 1993 [5], respectively. The CNTs were predicted to be a material with an extremely high Young's modulus ( $E$ ) in the range from hundreds of GPa (MWCNTs) to 3 TPa (SWCNTs) [6]. The experimental verification of CNTs' mechanical properties is challenging due to their diameter in the nanometer range and difficulties in manipulation [7]. The first experimental determination of CNTs'  $E$  was achieved in 1997 by measuring the amplitude of their intrinsic thermal vibration in the transmission electron microscope [8] or vibrations induced by an electrostatic field [9]. Subsequently, researchers tried to bend individual CNTs by using an atomic force

microscope (AFM) tip [10,11] and they derived the nanotube stiffness from the tip–tube interaction force curve [12]. The method was reliable but, unfortunately, it required isolated individual CNT and it is rather difficult to separate CNTs from each other. In 2009, a fluorescence-based technique was used to determine the MWCNT spring constant [13]. The nano-indentation technique was also reported to determine the mechanical properties of CNTs [14,15]. So far, this is the only method that allows the determination of mechanical properties of CNTs without time-consuming sample preparation. However, the drawback was the uncertainty of the tip–CNT contact angle, which induces measurement error [16].

The electrical properties have also been studied by using a four-probe method [17] or AFM-based techniques [18–20]. This again required labor intensive sample preparation as the CNTs were randomly placed on the planar surface structure of the electrode. The contact resistance between an individual nanotube and a deposited metal film was controlled by laser ablation technique to tailor the CNT length [21]. The CNT electrical resistance was also studied as a function of CNT length [22]. All the above-mentioned methods require labor intensive sample preparation such as the careful separation of an individual CNT as well as firmly anchoring it to the substrate.

\* Corresponding author at: Brno University of Technology, Technická3058/10, 616 00 Brno, Czech Republic.

E-mail address: [pavel.neuzil@npwu.edu.cn](mailto:pavel.neuzil@npwu.edu.cn) (P. Neužil).

CNTs are currently produced by several methods [6,23,24], which results in CNTs with different properties and shapes. The chemical vapor deposition (CVD) technique allows producing vertically aligned nanotubes (VACNTs) in the form of a nanometer-sized bamboo-like forest. These VACNTs are closely packed and have almost identical height. An earlier method, called “force–distance measurement” (FDM) [25] was presented to determine the interaction between an individual gecko lizard spatula and the tipless AFM cantilever to investigate the gecko’s adhesion force [26]. The cantilever came into contact with individual spatulas even though they were in close proximity to each other. Here, we present a unique FDM as a method to determine mechanical, electrical, and surface properties of a single CNT from a VACNTs “forest” by analyzing the CNT–cantilever interaction. This method addresses the long-standing problem of property determination of materials such as CNTs and nanowires and is an important addition to the toolbox of nanoscale characterization methods.

## 2. Experimental Details

### 2.1. CNT Growth

The vertically aligned forest of MWCNTs was fabricated using different CVD methods. A thermally grown silicon dioxide layer with thickness of  $\approx 500$  nm on a silicon wafer with [100] crystallographic orientation was used as a starting substrate. Subsequently, a catalytic layer of Co with a thickness of  $\approx 5$  nm was deposited by e-beam evaporation. The thickness was determined by monitoring the change of natural frequency of quartz crystal microbalance. The CNTs growth was conducted by decomposition of ethylene diamine  $C_2H_4(NH_2)_2$  at temperature of  $\approx 900$  °C for  $\approx 600$  s as described elsewhere [27]. The CNTs for electrical properties measurements were prepared by decomposition of  $CH_4$  using the plasma-enhanced chemical deposition technique (PECVD) with Fe as catalyst at pressure of  $\approx 1133$  Pa ( $\approx 8.5$  torr) for  $\approx 120$  s at temperature of  $\approx 800$  °C on an electrically conductive substrate [28].

### 2.2. Measurement of Mechanical Properties

The interaction between two objects, such as the AFM cantilever and the sample, can be monitored by FDM, where the interacting force ( $F$ ) is a function of the cantilever displacement in the Z-direction ( $\Delta Z$ ). The AFM cantilever is brought down (or sam-

ple is raised) until it comes into close proximity with the sample. All surfaces are at ambient environment covered with a layer of water with thickness of a few nanometers [29]. At close proximity between the AFM cantilever and the sample, a spontaneous water condensation occurs, forming a water bridge between them and causing the cantilever to snap to the substrate, which is shown as a little dip on the FDM curve. The dip amplitude depends on the surface properties, relative humidity, and applied electric field, if there is any [30]. With the cantilever further pushed against the sample, the cantilever bends up and the sample deforms with the force exerted by the cantilever. The cantilever–sample interaction provides the sample stiffness as well as the sample surface properties.

A scanning electron microscope image of a typical VACNTs sample is shown in Fig. 1A and an AFM image with a line profile analysis to determine a CNT diameter in Fig. 1B and C. The diameter, length and spring constant will be used to determine the modulus  $E$  of the CNTs.

The Z-direction resolution of the AFM is significantly better than the height difference among adjacent CNTs; thus, we are able to determine the individual events of interaction between CNTs and the cantilever similar to the earlier reported measurement of the gecko lizard adhesion force [26]. We assumed that the interaction between a sample consisting of VACNTs and an AFM tipless cantilever will be similar to the previously measured interaction with gecko feet covered with seta [31]. While the cantilever comes into contact with the CNT at a typical angle of  $\approx 12^\circ$  (Fig. 2A) during FDM, it first snaps and then starts to bend itself as well as the CNT (Fig. 2B). Further pushing cantilever against the VACNT results in the cantilever interaction with more CNTs (Fig. 2C and D). We derived (Supplementary Section 1) the composite spring constant ( $k_T$ ) of both the cantilever and the CNT as:

$$k_T = \frac{k_C k_{CNT} \cos \theta}{k_C \sin^2 \theta + k_{CNT}}, \quad (1)$$

where  $k_C$  and  $k_{CNT}$  are the spring constants of cantilever and CNT, respectively, and  $\theta$  is the angle between the cantilever and horizontal plane.

### 2.3. Measurement of Electrical Properties

We also propose to measure the CNT electrical conductivity from the interaction between a tipless cantilever coated at its bot-

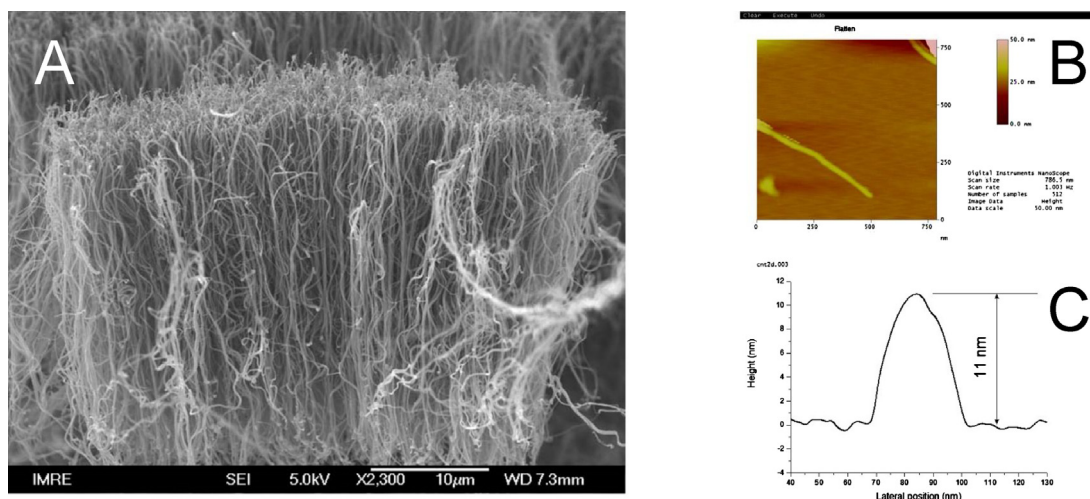


**Fig. 1.** (A) Scanning electron microscope image of a typical sample of VACNTs. The sample with CNTs was scratched with a needle and some CNTs were transferred onto a freshly cleaved mica substrate. (B) Sample topography was determined by an AFM in a tapping mode. (C) CNT diameter was extracted from a single scan across the CNT and found to be  $\approx 11$  nm.

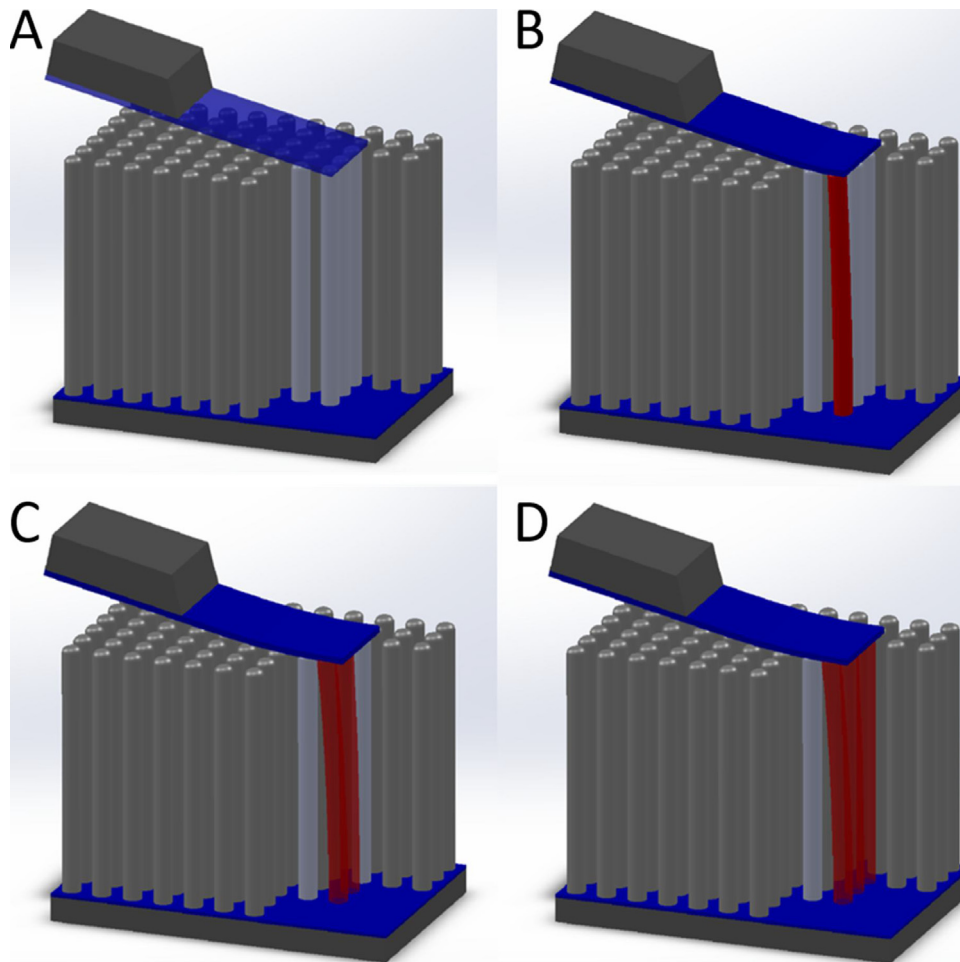


**Fig. 2.** Schematic representation of the interaction between CNTs and the AFM cantilever using computer aided design (A) starting with no contact, (B) contact with a single CNT, (C) two CNTs, and (D) three CNTs. CNTs in contact with the cantilever are labeled with red color. Every new interaction between the cantilever and another CNT will be detectable at the FDM curve.

tom side with an electrically conductive material, such as metal, and the CNTs grown on the electrically conductive substrate. Once the cantilever is biased by a small amplitude of DC voltage  $V_B$  (such as a few V), we can determine the total resistance ( $R_T$ ) consisting of the CNT ( $R_{CNT}$ ), CNT-substrate contact ( $R_S$ ), and the leadout ( $R_L$ ) resistance by measuring the electrical current flowing through the CNT ( $I_R$ ) as  $I_R = V_B/R_T$ . We can then perform the FDM with applied  $V_B$  to obtain the amplitude of  $I_R$  as well as number of CNTs in contact at any point of time.

#### 2.4. Simulation of Force–Distance Measurement

We developed and performed simulations based on numerical solution to the differential equation for the elastic line of a bent rod (Supplementary Section 2). In these simulations, both the cantilever and the CNT were considered as thin elastic rods with one end clamped and the other free. The core of the simulation is to calculate the deformations and forces between the cantilever and the CNT when the cantilever is pushed against the CNT. The movement of contact point between the cantilever and CNT due to the change of their shape under deformation was also taken into account. As the output of the simulation, the calculated force spectrum is represented by the force acting on the cantilever vs. cantilever displacement (Supplementary Section 3). This simulation was controlled by a program with a user-friendly interface (Supplementary Section 4).

We set the  $k_C$  to (0.05, 0.20, and 1.00) N·m<sup>-1</sup> by calculating it from Eq. (S16) in Supplementary Section 2 from setting the Young's modulus of cantilever ( $E_C$ ) and the second area moment of cantilever ( $I_C$ ). We then simulated the FDM for various values of  $k_{CNT}$ , determined again from CNT Young's modulus ( $E_{CNT}$ ) and the second area moment of CNT ( $I_{CNT}$ ) in a range from 1 mN·m<sup>-1</sup> to 50 mN·m<sup>-1</sup> (Fig. 3A) with all parameters listed in Supplementary Section 5. An average slope  $k_T = dF/d\Delta Z$  at the point of contact was extracted from the FDM curves as a linear parameter of curve fitting with a second order polynomial function, setting the intercept to 0 with an adjusted  $R^2$  value of  $(0.99970 \pm 7 \cdot 10^{-5})$  (mean  $\pm$  fitting error). The values of  $k_T$  were then plotted as function of  $k_{CNT}$  (Fig. 3B) and we performed curve fitting using a simplified version of Eq. (1):

$$k_T = \frac{a \cdot k_{CNT}}{b + k_{CNT}}, \quad (2)$$

where

$$a = k_C \cdot \cos\theta \text{ and } b = k_C \cdot \sin^2\theta \quad (3)$$

The fitting resulted in an excellent correlation coefficient of 0.99999. Fitting parameters are shown in Table 1.

We could then solve the set of Eq. (3) to back-calculate  $k_C$  and  $\theta$  (marked with “\*\*”). There are four solutions, but only two are fully rational and only one has both  $k_C$  and  $\theta$  positive as shown in Table 2.

The back-calculated values of  $k_C$  are slightly higher than the set ones while the  $\theta$  values are practically identical as the set ones. The change of  $k_C$  is probably caused by the shifting of the

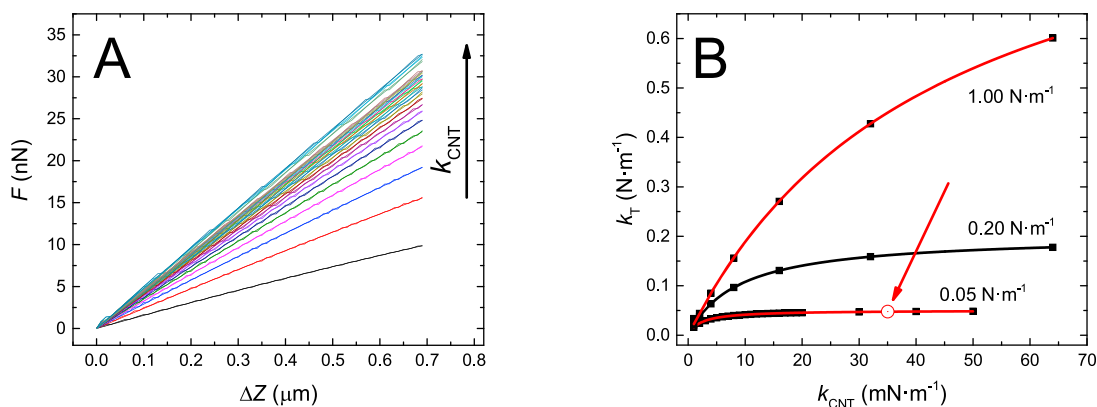


**Fig. 3.** (A) Computer simulation of FDM curve of an AFM cantilever with  $k_C$  set to  $0.05 \text{ N}\cdot\text{m}^{-1}$  and a CNT using the program described in Supplementary Section 3. The graphs for  $k_C$  set to  $0.20 \text{ N}\cdot\text{m}^{-1}$  and  $1.00 \text{ N}\cdot\text{m}^{-1}$  are not shown here. The  $k_{CNT}$  was used as parameter with value set from  $1 \text{ mN}\cdot\text{m}^{-1}$  to  $50 \text{ mN}\cdot\text{m}^{-1}$ . (B) Extracted  $k_T$  values (slope) from (A) plotted as function of parameter of  $k_{CNT}$ . We performed curve fitting using Eq. (2) and obtained an excellent correlation coefficient with value of  $\approx 0.9997$ . The red circle marked with an arrow is the  $k_{CNT}$  value extracted from the measurement.

**Table 1**  
Extracted  $a$  and  $b$  parameters for  $k_C$  of ( $0.05, 0.20$  and  $1.00$ )  $\text{N}\cdot\text{m}^{-1}$ .

$k_C$ ( $\text{N}\cdot\text{m}^{-1}$ )	$a$ ( $\text{N}\cdot\text{m}^{-1}$ )	$b$ ( $\text{N}\cdot\text{m}^{-1}$ )
0.05	$0.05042 \pm 0.00002$	$2.171 \pm 0.005$
0.20	$0.20205 \pm 0.00014$	$8.741 \pm 0.018$
1.00	$1.010 \pm 0.023$	$43.5 \pm 1.9$

**Table 2**  
Back-calculation of  $k_C$  values and cantilever angle  $\theta$ . There are only small discrepancies between set  $k_C$  and back calculated values demonstrating quality of the simulation.

$k_C$ ( $\text{N}\cdot\text{m}^{-1}$ )	$k_C^*$ ( $\text{N}\cdot\text{m}^{-1}$ )	$\theta^*$ (rad)	$\theta^*$ ( $^\circ$ )
0.05	0.05152	0.2067	11.84
0.20	0.20646	0.2072	11.87
1.00	1.03154	0.2069	11.85

CNT–cantilever interaction point due to CNT bending. As this point moves toward the cantilever base, the cantilever effective length becomes shorter, resulting in a higher  $k_C$  and this is presumably the discrepancy between set and back-calculated  $k_C$  values.

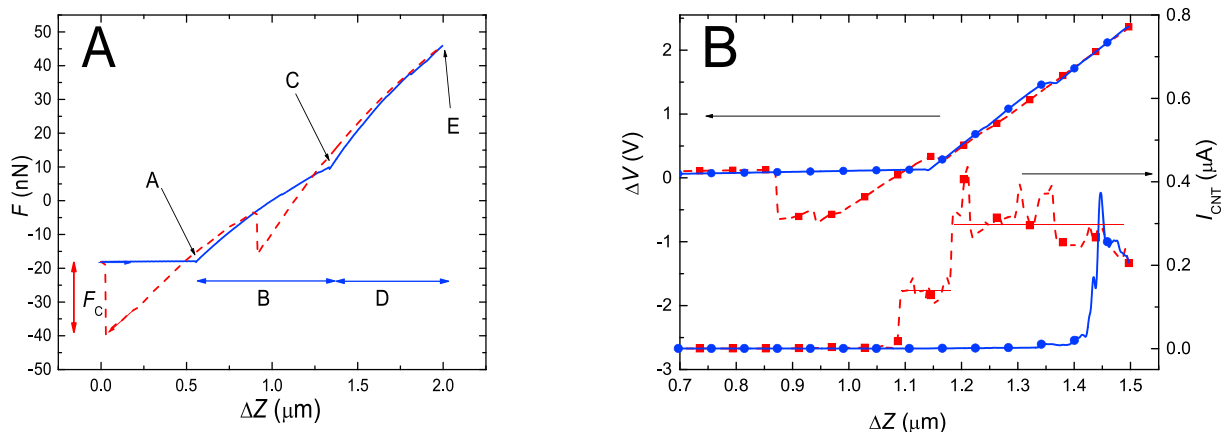


**Fig. 4.** (A) Typical FDM curve between relatively soft CNTs (with respect to the stiffness of the applied AFM cantilever) and the AFM cantilever. Blue and red arrows show the direction of the curve. At point A, the cantilever snapped to a CNT in the closest proximity due to the sudden collapse of the water bridge and was then pushed against the CNT (region B). Another water bridge collapse between the cantilever and the second CNT occurs at point C, and the cantilever was further pushed against two CNTs at a time (region D) until the motion of the cantilever is reversed. Similar behavior of disengaging can be observed with the only difference in jump-off force amplitude ( $F_C$ ). (B) FDM (left axis) and electrical measurement (right axis). The application of  $V_B$  of  $\approx 200 \text{ mV}$  between the cantilever and the substrate affected the force distance measurement. Due to this interaction, the FDM and the current–distance measurement (with  $V_B = 0 \text{ V}$ ) cannot be performed concurrently. One can see that the snap in a location is different for force–distance as well as for the electrical measurement due to the mentioned effect. Nevertheless, in the scanned region from  $\Delta Z \approx 0.70 \mu\text{m}$  to  $\approx 1.55 \mu\text{m}$  there was only interaction between a cantilever and first CNT followed by a second CNT.

As per the hypothesis above, we only need to perform the FDM with an actual CNT. Then, we fit the FDM curve with the second-order polynomial function and from the linear coefficient (equivalent to  $k_T$ ) we can determine the  $k_{CNT}$  value using Eq. (2) as:

$$k_{CNT} = \frac{b \cdot k_T}{a - k_T} \quad (4)$$

### 3. Results and Discussion

We placed the sample with VACNTs on a sample holder of a commercial AFM tool. We mounted a tipless cantilever with  $k_C$  of  $\approx 0.05 \text{ N}\cdot\text{m}^{-1}$  to the cantilever holder. We then used the built-in function “engage” to bring the cantilever into contact with the sample the same way as described before [26]. The typical FDM curve between the CNT sample and the AFM cantilever is shown in Fig. 4A. From the engaging curve, it can be seen that there is an interaction between the cantilever and a single CNT occurred first after the formation of the water bridge [29]. The cantilever was pushed against the CNT, which started to bend until the second CNT came into contact with the cantilever. There is also a tiny dip due to the second water

bridge formation. A similar behavior is observed in reverse order for the disengagement of the cantilever.

We performed curve fitting using the second order polynomial function from the first section of FDM curves where only a single CNT is in a contact with the cantilever. The linear coefficient of the fitting polynomial curve achieved an excellent adjusted  $R^2$  value of  $\approx 0.9998$ . The linear fitting coefficient ( $k_T$ ) had value of  $(47.65 \pm 0.03) \text{ mN}\cdot\text{m}^{-1}$  (mean  $\pm$  fitting error). Using Eq. (3), we can then determine the  $k_{\text{CNT}}$  value as  $(35.02 \pm 0.44) \text{ mN}\cdot\text{m}^{-1}$ , in the range of (1–50)  $\text{mN}\cdot\text{m}^{-1}$ , which was reported earlier for different CNTs by fluorescent method [13].

Besides  $k_{\text{CNT}}$  determination, we can also measure the adhesion force between the cantilever and sample of  $\approx 21.54 \text{ nN}$  (labeled as  $F$  in Fig. 4A) as well as identifying the number of CNTs in contact with the cantilever at any given time.

The measurement of electrical and mechanical parameters had to be done consequently as the applied electrical potential affected water bridge formation and, thus the FDM curve as well [30]. The results of the electrical measurement showed (Fig. 4B) the average values of  $I_R$  through a single CNT and two CNTs were  $\approx 135 \text{ nA}$  and  $\approx 299 \text{ nA}$ , respectively, as marked by the two red lines. That corresponds to an  $R_T$  of  $\approx 1.430 \text{ M}\Omega$  and  $\approx 672 \text{ k}\Omega$  for one CNT and two CNTs in parallel configuration, respectively, showing that two CNTs in parallel have practically half the resistance of a single one, which is expected. The results of the electrical measurement can be improved by using AC methods and implementation of lock-in amplification technique as well as the four-point measurement technique.

#### 4. Conclusion

We demonstrated a simple and effective method to study mechanical and electrical properties of VACNTs using the AFM tool. From only a single measurement, we were able to determine several parameters such as the force  $F_C$  between a single CNT and the cantilever, the value of a spring constant  $k_C$  and a resistance  $R_T$  of a single CNT as well as the number of CNTs in contact with the AFM cantilever at any point of time. This method can be extended to measure parameters of other vertically oriented nanostructures as many electrical and electronic properties can be then extracted from results of current–voltage ( $I$ – $V$ ) and electrical conductivity–voltage ( $dI/dV$ – $V$ ) measurements, while the cantilever is contact with the sample. The obtained experimental data are crucial for understanding and tailoring nanomaterials for targeted applications.

#### 5. Methods

Appendix 1 Derivation of the total spring constant of the system cantilever + CNT

Appendix 2 Theory of elastic bending of thin rods

Appendix 3 Simulations of the deformation of the cantilever being pushed against a CNT

Appendix 4 Graphical user interface of the software

Appendix 5 Setting of simulation parameters

#### Acknowledgement

The authors V. Svatoš, I. Gablech, J. Pekárek, and P. Neuzil would like to acknowledge financial support of MVCR (# VI20152019043) as well as the support of SIX and CEITEC-Nano Research Infrastructure (ID LM2015041, MEYS CR, 2016–2019).

#### References

- [1] K. Tsuno, E. Morinobu, O. Yoshiharu, Carbon Fibers Obtained by Thermal Decomposition of Vaporized Hydrocarbon, *Jpn J Appl Phys* 11 (1972) 445–449.
- [2] H.P. Boehm, The first observation of carbon nanotubes, *Carbon* 35 (1997) 581–584.
- [3] M.S. Dresselhaus, G. Dresselhaus, P. Avouris, Carbon nanotubes: synthesis, structure, properties, and applications, Springer, New York, 2001.
- [4] S. Iijima, Helical Microtubules of Graphitic Carbon, *Nature* 354 (1991) 56–58.
- [5] S. Iijima, T. Ichihashi, Single-Shell Carbon Nanotubes of 1-nm Diameter, *Nature* 363 (1993) 603–605.
- [6] D.H. Robertson, D.W. Brenner, J.W. Mintmire, Energetics of Nanoscale Graphitic Tubules, *Phys Rev B* 45 (1992) 12592–12595.
- [7] R.S. Ruoff, D. Qian, W.K. Liu, Mechanical properties of carbon nanotubes: theoretical predictions and experimental measurements, *Comptes Rendus Physique* 4 (2003) 993–1008.
- [8] M.M.J. Treacy, T.W. Ebbesen, J.M. Gibson, Exceptionally high Young's modulus observed for individual carbon nanotubes, *Nature* 381 (1996) 678–680.
- [9] P. Poncharal, Z.L. Wang, D. Ugarte, W.A. de Heer, Electrostatic deflections and electromechanical resonances of carbon nanotubes, *Science* 283 (1999) 1513–1516.
- [10] J.P. Salvetat, A.J. Kulik, J.M. Bonard, G.A.D. Briggs, T. Stockli, K. Metenier, et al., Elastic modulus of ordered and disordered multiwalled carbon nanotubes, *Adv Mater* 11 (1999) 161–165.
- [11] Y.H. Yang, W.Z. Li, Radial elasticity of single-walled carbon nanotube measured by atomic force microscopy, *Appl Phys Lett* 98 (2011), 041901 (3pp).
- [12] F.A. Ghavanini, H. Jackman, P. Lundgren, K. Svensson, P. Enoksson, Direct measurement of bending stiffness and estimation of Young's modulus of vertically aligned carbon nanofibers, *J Appl Phys* 113 (2013), 194308 (5pp).
- [13] S. Kwon, H. Park, H.C. Shim, H.W. Lee, Y.K. Kwak, S. Kim, Experimental determination of the spring constant of an individual multiwalled carbon nanotube cantilever using fluorescence measurement, *Appl Phys Lett* 95 (2009), 013110 (3pp).
- [14] H.J. Qi, K.B.K. Teo, K.K.S. Lau, M.C. Boyce, W.I. Milne, J. Robertson, et al., Determination of mechanical properties of carbon nanotubes and vertically aligned carbon nanotube forests using nanoindentation, *J Mech Phys Solids* 51 (2003) 2213–2237.
- [15] M. Minary-Jolandan, M.F. Yu, Reversible radial deformation up to the complete flattening of carbon nanotubes in nanoindentation, *J Appl Phys* 103 (2008), 073516 (5pp).
- [16] J.F. Waters, L. Riestler, M. Jouzi, P.R. Guduru, J.M. Xu, Buckling instabilities in multiwalled carbon nanotubes under uniaxial compression, *Appl Phys Lett* 85 (2004) 1787–1789.
- [17] T.W. Ebbesen, H.J. Lezec, H. Hiura, J.W. Bennett, H.F. Ghaemi, T. Thio, Electrical conductivity of individual carbon nanotubes, *Nature* 382 (1996) 54–56.
- [18] S. Frank, P. Poncharal, Z.L. Wang, W.A. de Heer, Carbon nanotube quantum resistors, *Science* 280 (1998) 1744–1746.
- [19] P.R. Bandaru, Electrical properties and applications of carbon nanotube structures, *J Nanosci Nanotechnol* 7 (2007) 1239–1267.
- [20] B. Zhao, H. Qi, D. Xu, Resistance measurement of isolated single-walled carbon nanotubes, *Measurement* 45 (2012) 1297–1300.
- [21] L. Chun, S. Pornsak, B.A. Placidus, S.F. Timothy, X. Xianfan, G.R. Ronald, Measurement of metal/carbon nanotube contact resistance by adjusting contact length using laser ablation, *Nanotechnology* 19 (2008), 125703 (7pp).
- [22] N. Chiodarelli, S. Masahito, Y. Kashiwagi, Y.L. Li, K. Arstila, O. Richard, et al., Measuring the electrical resistivity and contact resistance of vertical carbon nanotube bundles for application as interconnects, *Nanotechnology* 22 (2011), 085302 (7pp).
- [23] P. Calvert, Materials Science - Strength in Disunity, *Nature* 357 (1992) 365–366.
- [24] G. Overney, W. Zhong, D. Tomanek, Structural Rigidity and Low-Frequency Vibrational-Modes of Long Carbon Tubules, *Z Phys D Atom Mol Cl* 27 (1993) 93–96.
- [25] B. Cappella, G. Dietler, Force-distance curves by atomic force microscopy, *Surf Sci Rep* 34 (1999) 1–104.
- [26] W.X. Sun, P. Neuzil, T.S. Kustandi, S. Oh, V.D. Samper, The nature of the gecko lizard adhesive force, *Biophys J* 89 (2005) L14–L17.
- [27] W.D. Zhang, Y. Wen, J. Li, G.Q. Xu, L.M. Gan, Synthesis of vertically aligned carbon nanotubes films on silicon wafers by pyrolysis of ethylenediamine, *Thin Solid Films* 422 (2002) 120–125.
- [28] Y. Chai, Z.Y. Xiao, P.C.H. Chan, Low-Resistance Carbon Nanotube Contact Plug to Silicon, *IEEE Electr Device L* 30 (2009) 811–813.
- [29] T. Thundat, X.Y. Zheng, G.Y. Chen, S.L. Sharp, R.J. Warmack, L.J. Schowalter, Characterization of Atomic-Force Microscope Tips by Adhesion Force Measurements, *Appl Phys Lett* 63 (1993) 2150–2152.
- [30] G.M. Sacha, A. Verdager, M. Salmeron, Induced water condensation and bridge formation by electric fields in atomic force microscopy, *J Phys Chem B* 110 (2006) 14870–14873.
- [31] T.S. Kustandi, V.D. Samper, D.K. Yi, W.S. Ng, P. Neuzil, W. Sun, Self-assembled nanoparticles based fabrication of gecko foot-hair-inspired polymer nanofibers, *Adv Funct Mater* 17 (2007) 2211–2218.

## Biographies



**Vojtěch Svatoš** is a PhD student at Central European Institute of Technology (CEITEC) in Brno, Czech Republic. He entered the PhD program of Advanced Materials and Nanosciences in 2014. His current research interests are microelectromechanical systems and nanotechnology for thermal imaging and calorimetric measurement.



**Imrich Gablech** is currently a PhD student at Central European Institute of Technology (CEITEC) at Brno University of Technology, Brno, Czech Republic. He entered the PhD program of Advanced Materials and Nanosciences in 2014. His main areas of interest are microelectromechanical systems, piezoelectric materials and properties of thin films.



**Wanxin Sun** received his PhD in Physics in National University of Singapore in 2003 and worked as a research scientist in Institute of Bioengineering and Nanotechnology till 2006. He is now with Bruker Nano Surface working on the developments of surface characterization techniques for quantitative physical property at nanoscale level.



**Jan Pekárek** received the M.S. and Ph.D. degrees in electrical engineering from the Brno University of Technology in 2008 and 2014, respectively. He is currently a Junior researcher at Centre of SIX at Brno University of Technology and at Central European Institute of Technology. His current research interest includes development and fabrication of devices based on micro- or nanostructured surfaces. He is an author and co-author of 32 publications and his h-index is 5.



**Radek Kalousek** received his PhD at the Brno University of Technology. He was focused on theoretical description of processes during measurements with an atomic force microscope. Afterwards, his research continued with an investigation of the diffusion of adatoms on various surfaces (at TU Wien, Austria) and formation of water meniscus between the tip and sample surface during local anodic oxidation. Currently, he is involved in solving theoretical problems concerning the physics at the mezo- and nanoscale, for instance: plasmonics (optical properties of metallic nanostructures, etc.); elastic deformations and mechanical vibrations of AFM cantilevers; mechanical properties of piezoceramics in slip-stick actuators; heat



**Pavel Neužil** obtained his PhD in Electrical Engineering from Czech Technical University, Czech Republic. He worked at University of Illinois, Stanford University (both USA), A\*STAR institutes in Singapore, KIST-Europe, Germany, Brno University of Technology, Czech Republic and Northwestern Polytechnical University, P.R. China. His research interests are advanced MEMS and nanotechnology for applications such as magneto optical recording and thermal imaging as well as medical devices for molecular diagnostics such as portable real-time PCR. He is a co-author of 78 journal publications and a co-inventor of 10 patents.

transfer during sintering of ceramic materials; nanomagnetism (formation and trajectory of magnetic vortices in external magnetic field, etc.); mechanical stress in deformed thin films; and others.

## Příloha 2

MAJZLÍKOVÁ, P. et al. Sensing properties of multiwalled carbon nanotubes grown in MW plasma torch: electronic and electrochemical behavior, gas sensing, field emission, IR absorption. *Sensors (Basel)*, 2015, vol. 15, no. 2, pp. 2644-2661. ISSN 1424-8220.

### ABSTRAKT

Vertikálně uspořádané mnohostěnné uhlíkové nanotrubic s průměrem okolo 80 nm a výšce vrstvy okolo 16  $\mu\text{m}$  byly připraveny v mikrovlnném výboji za atmosférického tlaku. Na vrstvách byly testovány vybrané funkční vlastnosti. Infračervená absorpce důležitá pro konstrukci bolometrů byla studována Fourierovou transformační infračervenou spektroskopií. Základní elektrochemická charakterizace byla provedena cyklickou voltametrií. Porovnáním získaných výsledků se standardními elektrodami a elektrodami modifikovanými uhlíkovými nanotrubicemi bylo zjištěno, že modifikované elektrody mají velký potenciál v elektrochemických senzorech. Odporový senzor plynu s vrstvou uhlíkových nanotrubic ukázal dobrou citlivost vůči čpavku už při pokojové teplotě. Detekovaný emisní proud z pole uhlíkových nanotrubic ukázal také možnost využití uhlíkových nanotrubic pro snímání tlaku v diodovém uspořádání s pružnou membránou. Díky výhodám mikrovlnného plazmového výboje za atmosférického tlaku při růstu uhlíkových nanotrubic, tj. rychlá depozice a univerzálnost procesu, může být tato metoda využita pro integraci uhlíkových nanotrubic na povrch substrátů v různých snímacích aplikacích.

Article

## Sensing Properties of Multiwalled Carbon Nanotubes Grown in MW Plasma Torch: Electronic and Electrochemical Behavior, Gas Sensing, Field Emission, IR Absorption

Petra Majzlíková<sup>1,2</sup>, Jiří Sedláček<sup>1,2</sup>, Jan Prášek<sup>1,2</sup>, Jan Pekárek<sup>1,2</sup>, Vojtěch Svatoš<sup>1</sup>, Alexander G. Bannov<sup>3</sup>, Ondřej Jašek<sup>3,4</sup>, Petr Synek<sup>3</sup>, Marek Eliáš<sup>3,4</sup>, Lenka Zajíčková<sup>3,4</sup> and Jaromír Hubálek<sup>1,2\*</sup>

<sup>1</sup> Central European Institute of Technology, Brno University of Technology, Technická 3058/10, CZ-61600 Brno, Czech Republic; E-Mails: businova@feec.vutbr.cz (P.M.); xsedla44@stud.feec.vutbr.cz (J.S.); prasek@feec.vutbr.cz (J.P.); pekarek@feec.vutbr.cz (J.P.); vojtech.svatos@ceitec.vutbr.cz (V.S.)

<sup>2</sup> Centre of Sensors, Information and Communication Systems, Faculty of Electrical Engineering and Communication, Technická 3058/10, CZ-61600 Brno, Czech Republic

<sup>3</sup> Central European Institute of Technology, Masaryk University, Kamenice 5, CZ-62500 Brno, Czech Republic; E-Mails: 234860@mail.muni.cz (A.G.B.); jasek@physics.muni.cz (O.J.); synek@physics.muni.cz (P.S.); mareke@physics.muni.cz (M.E.); lenkaz@physics.muni.cz (L.Z.)

<sup>4</sup> Department of Physical Electronics, Faculty of Science, Masaryk University, Kotlářská 2, CZ-61137 Brno, Czech Republic

\* Author to whom correspondence should be addressed; E-Mail: hubalek@feec.vutbr.cz; Tel.: +420-541-146-195; Fax: +420-541-146-288.

Academic Editor: Libuše Trnková

Received: 15 November 2014 / Accepted: 16 January 2015 / Published: 26 January 2015

---

**Abstract:** Vertically aligned multi-walled carbon nanotubes (VA-MWCNTs) with an average diameter below 80 nm and a thickness of the uniform VA-MWCNT layer of about 16  $\mu\text{m}$  were grown in microwave plasma torch and tested for selected functional properties. IR absorption important for a construction of bolometers was studied by Fourier transform infrared spectroscopy. Basic electrochemical characterization was performed by cyclic voltammetry. Comparing the obtained results with the standard or MWCNT-modified screen-printed electrodes, the prepared VA-MWCNT electrodes indicated their high potential for the construction of electrochemical sensors. Resistive CNT gas sensor revealed a good sensitivity to ammonia taking into account room temperature operation. Field

emission detected from CNTs was suitable for the pressure sensing application based on the measurement of emission current in the diode structure with bending diaphragm. The advantages of microwave plasma torch growth of CNTs, *i.e.*, fast processing and versatility of the process, can be therefore fully exploited for the integration of surface-bound grown CNTs into various sensing structures.

**Keywords:** carbon nanotubes; microwave torch; plasma enhanced chemical vapor deposition; electronic properties; electrochemical sensor; gas sensor; field emission; IR absorption

---

## 1. Introduction

Carbon nanotubes (CNTs), a synthetic carbon allotrope, are made of  $sp^2$  hybridized carbon atoms. Single-walled CNT (SWCNT) is a graphene sheet rolled-up into a seamless cylinder and multi-walled CNT (MWCNT) is composed of several such cylinders, nested concentrically [1,2]. CNTs are often synthesized by a chemical vapor deposition (CVD) in the presence of a catalyst, nanoparticles of transition metals. In thermal CVD, a carbon-containing gas mixture is heated typically to 550–1100 °C by a conventional heat source. Plasma enhanced CVD (PECVD) activates the gas mixture by ignition of plasma discharge but a separate heating of the substrate might be required too [3]. General arguments for the PECVD include low-temperature, easily achieved vertical alignment and large area processing [4]. The CVD methods are used for a CNT volume-synthesis and a surface-bound growth of vertically aligned and micropatterned CNT arrays [5]. The vertically-aligned CNTs (VA-CNTs) are highly desirable for the integration into functional devices. The aligned growth can produce CNTs free from amorphous carbon with a very narrow range of tube lengths and diameters, which is an additional advantage for many applications [6].

Unique physical and electrical properties of CNTs, *i.e.*, high electrical conductivity, remarkable mechanical strength, and thermal and chemical stability, predestinate them for many nanotechnology-based applications in electronic, optical and biomedical devices, sensors and composites [7,8]. The application potential of CNTs depends on their properties that are given by their structure and the form in which they are applied. Separated MWCNTs exhibited a non-linearity in I-V characteristics that were relatively large in case of the contacts made by underlying gold electrodes but almost diminished if the contacts were placed on the top of partially etched nanotubes [9]. Theoretically predicted impedance of SWCNT bundles at high frequencies is quite complex, employing resistance R, inductance L and capacitance C, and their validation proved to be difficult [10]. The experimentally proposed circuit model of SWCNTs contains a parallel RC element resulting from the contacts in series with R and L representing the SWCNT intrinsic behavior [10,11]. Similarly, an equivalent circuit model consisting of RC networks is constructed to simulate the electrical responses of MWCNT/polymer composites [12,13].

The optical properties of CNTs help to understand their structure [14], evaluate their purity [15] and open new applications for optical sensing [16,17]. MWCNT-based infrared detectors have received much attention due to MWCNT band gap of 0.4–6.0 eV and high absorption efficiency in IR [18]. A bolometer based on CNT/polymer composites was constructed for the detection of infrared radiation

from the range 0.2–20  $\mu\text{m}$  [19] and it was shown that the sensitivity and response time of the CNT-based bolometers can be substantially improved by an appropriate functionalization and selection of organic matrix [19,20].

CNTs exhibit also a great potential for electrochemical sensing due to their unique electrical properties, high surface area, fast heterogeneous electron transfer, and electrochemical stability [21–25]. The CNTs implemented as a VA-CNT film provide other advantages such as a controlled growth in defined areas and an easy modification of their surface demanded for particular sensing or biosensing applications [6]. The as-prepared VA-CNT-based sensors have been successfully applied to detect rutin [26] and salbutamol [27], a prohibited drug in sports. The VA-CNT thin films have also been tested as candidate platforms for DNA immobilization and detection of DNA hybridization [28]. The VA-CNT electrode modified by gold nanoparticles has been used for non-enzymatic detection of uric acid [29] and a platinum nanoparticle-modified VA-CNT electrode for detection of L-cysteine [30].

The CNTs belong to a group of new materials that have been extensively tested for gas sensing during the last 10 years and much effort has been put into the development of gas sensors working at room temperature. In spite of many papers devoted to SWCNT-based gas sensors [31–33], the MWCNTs can be also successfully used [34–36] and are preferable because of their low costs. The construction of room temperature ammonia ( $\text{NH}_3$ ) sensors is an important task because  $\text{NH}_3$  is a dangerous gas having a negative influence on the environment and humans. Cui *et al.* created a sensor with MWCNTs decorated by Ag nanocrystals that exhibited an enhanced response of 9% to 10,000 ppm of  $\text{NH}_3$  as well as fast recovery [37]. A high sensitivity—6.2% to 4000 ppm of  $\text{NH}_3$ —was proven for  $\text{Co}_{1-x}\text{Ni}_x\text{Fe}_2\text{O}_4/\text{MWCNT}$  composites [38]. Varghese *et al.* investigated sensitivity of resistive and capacitive MWCNT sensors for different gases such as water vapors,  $\text{NH}_3$ ,  $\text{CO}_2$  and CO [39].

CNTs have been also considered as promising field emitters due to their low turn-on field, long emitter lifetime and good emission stability [40]. The field-emitter configuration should have the highest aspect ratio and low work function at its surface. The first extensive study of field emission from CNTs has been published by Bonard *et al.* in 1998 [41]. Later on, CNTs were used as field-emitters in flat-panel field-emission displays [42] or electron sources in electron microscopes [43].

In the present work, a promising application potential of VA-MWCNTs grown by PECVD in microwave (MW) plasma torch [44,45] is explored in detail. Previous studies of the CNTs deposited by the MW plasma torch revealed possible improvements of the process [46] and provided a basic structural characterization of the CNTs using scanning and transmission electron microscopies and Raman spectroscopy [47]. The technology based on the MW torch is a high speed process that takes only 60–120 s including catalyst activation (restructuralization of a catalytic thin film into nanoparticles) and does not require any external heating source of the substrate. Besides starting the CNT growth with a thin catalytic film deposited on the substrate in a separate technological step, it offers the possibility to prepare catalytic nanoparticles during the same process, *i.e.*, using the MW plasma torch [48]. Another advantage is a successful preparation of vertically aligned MWCNTs directly on Si without using a barrier  $\text{SiO}_2$  layer [3]. A direct contact between the VA-CNTs and the Si substrate can be very important for some applications and it enables the construction of a field-emission based pressure sensor [49]. Besides the field emission, other functional properties (electrical and electrochemical, gas sensing, IR absorption) of the CNTs from the MW plasma torch are tested. Thus, the present work investigates and summarizes the CNT properties

directly related to particular sensing applications and in some cases (field-emission pressure sensor, electrochemical sensor, gas sensor) describes the sensor structure and its preparation.

## 2. Experimental Section

### 2.1. CNT Deposition and Structural Characterization

The VA-MWCNT layers were deposited from Ar/CH<sub>4</sub>/H<sub>2</sub> mixtures using the atmospheric pressure MW plasma torch operated at the power of 210 W. The flow rates of Ar, CH<sub>4</sub> and H<sub>2</sub> were  $Q_{Ar} = 700$  sccm,  $Q_{CH_4} = 19\text{--}38$  sccm and  $Q_{H_2} = 250$  sccm, respectively. The substrate for the CNT growth was heated by the interaction with plasma, and its temperature (950–1050 K) was regulated by the distance from the plasma torch nozzle. The CNT growth time, that included also the catalyst activation phase, varied from 60 to 120 s.

The aim of the present work was to investigate functional properties of the CNTs deposited by MW torch and, in some cases, integrate them into sensing devices. Most of the measurement structures were based on Si due to its compatibility with microelectronic chips and microelectromechanical systems (MEMS). CNTs were grown either on a polished single crystal silicon (c-Si) substrate, the c-Si coated with an adhesive metallic interlayer or the c-Si coated with in a thermal silicon oxide (SiO<sub>2</sub>) film. The latter is used if the application requires a dielectric or thermal separation of the CNTs. The thickness of SiO<sub>2</sub> film did not play a significant role and was chosen arbitrarily. The substrate details are given in the following sections describing each particular measurement structure.

A vacuum evaporated Fe film, 5 nm in thickness, or Fe nanoparticles (NPs) deposited on the substrate by MW torch from iron pentacarbonyl (Fe(CO)<sub>5</sub>) vapors were used as catalysts. The details of the NPs deposition are described in previous papers [50,51]. The Ar flow through the central torch nozzle and through the blower with liquid Fe(CO)<sub>5</sub> were 700 and 28 sccm, respectively. The Ar flow of 28 sccm through the blower with the liquid corresponds to 0.1 sccm of Fe(CO)<sub>5</sub>. The deposition time was 10 s.

Surfaces and cross sections of the prepared CNT samples were checked by the Tescan MIRA II LMU scanning electron microscope (SEM, TESCAN, Brno, Czech Republic) using 15 kV acceleration voltage.

### 2.2. Characterization of Electrical Behavior of CNTs

The CNTs for electrical characterization, such as I-V characteristics and sheet resistance measurements, were grown in the MW plasma torch on p-type, boron-doped, c-Si substrates (8 mm × 8 mm, thickness 525 μm, resistivity <6 Ω·cm<sup>-1</sup>) coated by the SiO<sub>2</sub> film, 300 nm in thickness, and the top Fe catalytic layer. The square chips fully covered with CNT films were finished by vacuum evaporation of gold pads (0.5 mm × 0.5 mm) in each sample corner.

The chips were investigated at the probe station Cascade M150 connected to the Keithley SCS-4200 semiconductor analyzer (Keithley Instruments, Inc., Cleveland, OH, USA). The I-V characteristics of the films were measured between the opposite corners in the voltage range from -5 V to +5 V. The specific electrical resistance was determined by Van der Pauw measurement which was carried out automatically by the Keithley SCS-4200 analyzer.

For the impedance spectroscopy, the CNTs were grown on a SITAL glass-ceramic substrate (10 mm × 15 mm, thickness 525 μm) using Fe catalytic layer. This substrate was chosen to suppress the

effect of Si substrate properties during the impedance spectroscopy measurement. The VA-MWCNTs were deposited on a central circular area, 6 mm in diameter. Two circular gold contacts of 3 mm in diameter were prepared by vacuum evaporation. The impedance was measured using the Agilent E4980A Precision LCR meter (Agilent Technologies, Santa Clara, CA, USA) and data acquisition by LabView software (National Instruments, Austin, TX, USA). The measurements were performed in the frequency range from 20 Hz to 2 MHz with the voltage level of 0.5 V.

### 2.3. IR Absorption

The FTIR measurement procedure is a simple way to compare samples with or without grown CNTs in order to consider CNTs as possible IR detector. The CNTs for infrared absorption measurements were grown on the same substrates as described in the previous Section 2.2, *i.e.*, c-Si substrate with the SiO<sub>2</sub>/Fe double layer. In the case of the bolometer, thin SiO<sub>2</sub> layer is needed for construction of low thickness MEMS diaphragm to suppress thermal losses to the substrate mass [52].

The IR absorption of VA-CNTs on the Si substrate covered by 300 nm thick SiO<sub>2</sub> film was investigated with the Fourier transform infrared (FTIR) spectrometer Nicolet iS50 in the attenuated total reflection (ATR) mode. The ATR crystal was pressed against the sample and the measurement was performed in the wavelength range 2.5–22.5 μm. The absorbance of the VA-CNT sample was compared to the absorbance of Si substrate covered by 300 nm thick SiO<sub>2</sub> film and 5 nm thick Fe film used as catalyst of the CNT growth.

### 2.4. Electrochemical Characterization

The preparation of samples for the electrochemical measurements started with n-type, highly antimony-doped, c-Si substrates (5 mm × 30 mm, thickness 525 μm, resistivity <0.02 Ω·cm<sup>-1</sup>) coated by the SiO<sub>2</sub> film, 300 nm in thickness. The working electrode had dimensions 4.5 mm × 4.5 mm and consisted of the CNTs deposited in the MW plasma torch (Section 2.1). Before the CNT growth, the SiO<sub>2</sub> insulating film was removed from the working electrode area by a wet chemical etching in buffered HF and the area of the working electrode was covered by magnetron sputtered Ti (10 nm)/Ta (250 nm) double layer and vacuum evaporated top Fe film, the catalyst for the CNT growth. The Ti/Ta coating was necessary to ensure a good adhesion of the CNTs that otherwise peeled off the substrate when immersed in an electrolyte. The highly doped Si substrate was needed for a good electrical connection between the CNT layer and the contact pads which were situated on the opposite end of the substrate with the same dimensions as the electrode.

Electrochemical response of the [Fe(CN)<sub>6</sub>]<sup>4-/3-</sup> redox couple mediated by the CNT electrode was investigated by the cyclic voltammetry (CV) with AUTOLAB PGSTAT 204 potentiostat/galvanostat controlled by Nova 1.10 software (Metrohm Autolab B.V., Utrecht, The Netherlands). A standard three-electrode voltammetric cell employing an Ag/AgCl reference electrode (type 6.0729.100, Metrohm, Herisau, Switzerland) and a platinum auxiliary electrode (type 6.0343.000, Metrohm) was used for all the experiments. The electrolyte was an equimolar solution of 2.5 mM potassium ferrocyanide and potassium ferricyanide ([Fe(CN)<sub>6</sub>]<sup>4-/3-</sup>) in 0.1 M KCl. The cyclic voltammograms were recorded in the potential range from -1 V to +1 V with scan rates (*v*) from 5 to 500 mV·s<sup>-1</sup>.

### 2.5. Gas Sensing Properties

The CNTs for testing the gas sensing properties were prepared on the p-type, boron-doped, c-Si substrates (8 mm × 8 mm, thickness 525 μm, resistivity <math><6 \Omega \cdot \text{cm}^{-1}</math>) coated with the 92 nm thick SiO<sub>2</sub> film. The catalytic Fe nanoparticles were deposited by the MW plasma torch (see Section 2.1) in the central area, 4 mm × 4 mm, of the substrate. This form of the Fe catalyst was chosen for the growth of a less dense CNT mesh because the gas sensing application requires a large surface area and dense CNTs mask each other. The CNTs were grown from Fe NPs in the MW plasma torch (Ar = 700 sccm, H<sub>2</sub> = 250 sccm, CH<sub>4</sub> = 38 sccm, deposition time 60 s, deposition temperature 973 K) as described in Section 2.1. The measurement chip was finished by vacuum evaporated gold contacts (15 nm NiCr adhesion layer with 350 nm Au layer on the top) with a size of 2 mm × 6 mm centered symmetrically to the middle of the sensor.

The gas sensing properties were determined as a change of the sample resistance during its exposure to a gaseous analyte, either ammonia (NH<sub>3</sub>) or isobutane (iC<sub>4</sub>H<sub>10</sub>). The measurements were performed in a custom-built gas station equipped with two gas channels and one chamber for two sensors' characterization at once. One gas channel is used for the synthetic air as a carrier gas. The second gas channel supplies diluted analytes, NH<sub>3</sub> or iC<sub>4</sub>H<sub>10</sub> in nitrogen. The response of the sensors was determined at different analyte concentrations, namely 100 ppm, 250 ppm and 500 ppm. Before each measurement, a sample conditioning was carried out for 30 min at 200 °C in the air flow of 1000 sccm. The sensor response was defined as

$$\Delta R/R_0 = ((R - R_0)/R_0) \times 100\% \quad (1)$$

where R is the resistance of the sensor exposed to the analyte and R<sub>0</sub> is the sensor resistance in pure air. The sensitivity tests were performed at two temperatures, room temperature and 200 °C. The resistance R<sub>0</sub> was determined from 60 min measurement in air flow of 500 sccm. The sensor response to analyte was measured as three 10 min cycles (for 100 ppm, 250 ppm and 500 ppm of analyte) alternated with three 10 min cycles in air flow. The total gas flow rate was kept constant at 500 sccm.

### 2.6. Field Emission Properties for Pressure Sensing

The MEMS field emission pressure sensor was designed as a diode structure (see Figure 1). It consisted of two n-type, highly antimony-doped, c-Si electrodes (10 mm × 15 mm, thickness 525 μm, resistivity <math><0.02 \Omega \cdot \text{cm}^{-1}</math>). One of them was anisotropically etched to a bending diaphragm. The other was coated by an emissive material, the VA-MWCNTs deposited in the MW plasma torch (see Section 2.1). The highly doped Si substrate was needed for a good electrical connection between the CNT layer and the contact pads. The Fe catalytic film, required for the growth of CNTs, was deposited in the center of the substrate on the area of 4 mm × 4 mm. A native oxide film on Si was removed by HF prior to the deposition of the Fe film, thus ensuring the electrical contact between CNTs and Si. The field-emission pressure sensor is proposed to be constructed by the separation of the electrodes with a dielectric layer creating an integrated evacuated volume. The dielectric layer can be made of Pyrex or Simax glass using anodic bonding technology or made of glass frit using a screen printing process.

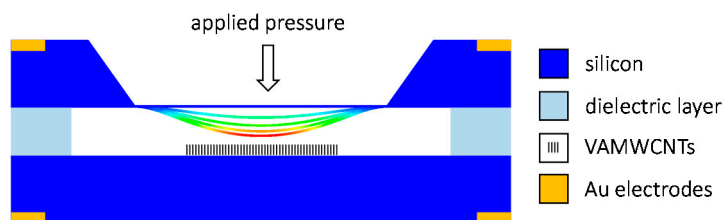


**Figure 1.** Schematic view of the MEMS pressure sensor with carbon nanotubes emitters.

The measurements of the field emission properties were carried out in a vacuum chamber at pressure lower than  $10^{-4}$  Pa. A diaphragm bending was simulated by the linear nano-motion drive SmarAct enabling precise changes of the distance between the two electrodes inside the vacuum chamber with the step from 50 nm to 1000 nm. The initial distance of 120  $\mu\text{m}$  was established using a solid dielectric foil that was then removed and the emitter-to-anode distance was set up with the SmarAct drive from 84  $\mu\text{m}$  to 120  $\mu\text{m}$ . The measurement voltage from 0 to 150 V was automatically applied using software communicating via GPIB with the voltage supply.

### 3. Results and Discussion

#### 3.1. SEM of CNTs

A fast growth of VA-MWCNT films on the c-Si and c-Si/SiO<sub>2</sub> substrates has been achieved in MW plasma torch operated at atmospheric pressure without an external heating source [44,45]. The characterization of the VA-MWCNT films by SEM, transmission electron microscopy (TEM), Raman spectroscopy and the influence of process parameters on the CNT growth were discussed in detail in our previous publications [3,46,47]. Typical SEM images of prepared VA-MWCNT film are shown in Figure 2. Although the cross-sectional view in Figure 2b confirms the vertical alignment of the CNT film, the top view (Figure 2a) reveals that the alignment at the end of nanotubes is not perfect. The CNTs having a high aspect ratio, less than 80 nm in the diameter and a length of about 16  $\mu\text{m}$ , are curled at the top end due to different heights. Therefore, top view micrographs cannot provide sufficient information about the structure of all the CNT film.

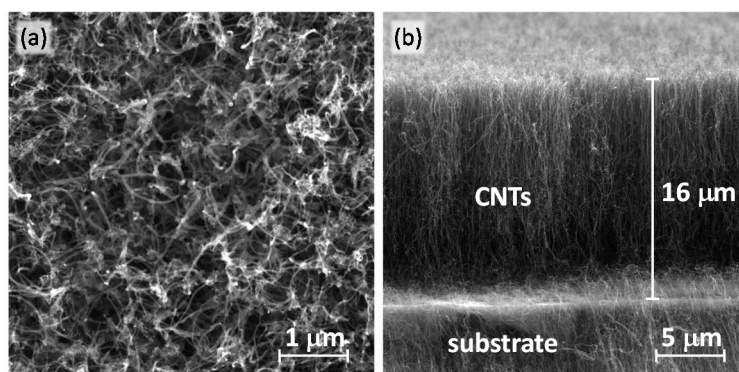


**Figure 2.** Typical SEM micrographs of the silicon substrate covered with VA-MWCNTs prepared in MW plasma torch (Ar = 700 sccm, H<sub>2</sub> = 250 sccm, CH<sub>4</sub> = 25 sccm, deposition time 60 s, deposition temperature 973 K): (a) top view of VA-MWCNTs and (b) cross-sectional view of the VA-MWCNT film.

### 3.2. Electrical Properties of CNTs

The measured I-V characteristics of the VA-MWCNT samples were nearly linear as documented in Figure 3a for the sample shown in Figure 2. The resistance was in the range of 1–1.3 k $\Omega$ . The specific electrical resistance was about 0.5  $\Omega$ -cm as calculated from Van der Pauw measurement and the film thickness of 16  $\mu$ m determined by SEM. A small nonlinearity was revealed when the difference of the sample resistance and its linear approximation was plotted (Figure 3b). The deviation from linear behavior was governed by an exponential growth with a small exponent. The nonlinearity of the CNT resistance did not exceed 6  $\Omega$  which corresponded to 0.5% of the film resistance.

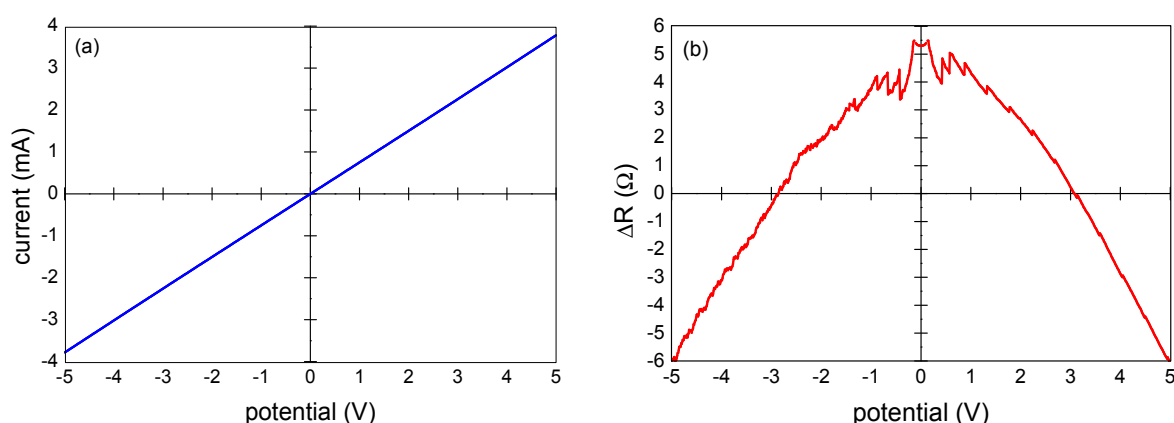


**Figure 3.** (a) I-V characteristic and (b) deviation of measured resistance from linear regression.

Fitting of the impedance measurements confirmed a simple RC model of two resistances and capacitances in parallel (Figure 4). According to Plombon *et al.* [10], the contact pads added a significant part of the RC circuit element. The  $R_c/C_c$  circuit represents the contact impedance, and  $R_{CNT}/C_{CNT}$  stands for the impedance of the vertically aligned CNT film. The resistances of the contact and the CNT films were 500 and 700  $\Omega$ , respectively. The capacitance of the contacts was much higher, about 15 nF, than the capacitance of the CNT film, 3.5 nF. It means that the surface of nanotubes is not pure enough to create a good contact. Adsorbed molecules such as water, CO<sub>2</sub> and O<sub>2</sub> can create a dielectric film that contributes to its high capacitance.

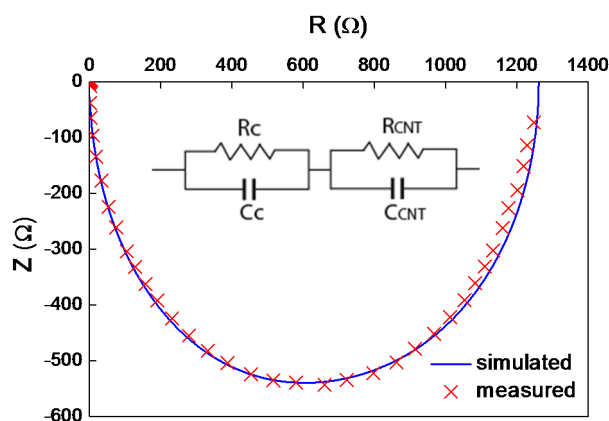


**Figure 4.** Impedance characteristics, crossed markers are measured data, dashed line is simulated according the inset equivalent circuit.

### 3.3. IR Absorption

The results of the ATR-FTIR study are shown in Figure 5. They indicate that the VA-MWCNTs can be affectionately applied as a possible absorption layer for IR detection. The mean absorbance value of nearly 80% was obtained. In Figure 5, the interval from 2.5  $\mu\text{m}$  to 7.5  $\mu\text{m}$  represents the absorbance of substrate. The local low points of the curve at approximately 9.0  $\mu\text{m}$  show the typical progression for the atmospheric humidity. The absorbance of the CNTs is mostly seen in the interval from 8  $\mu\text{m}$  to 22  $\mu\text{m}$  which therefore includes the atmospheric window for IR detection.

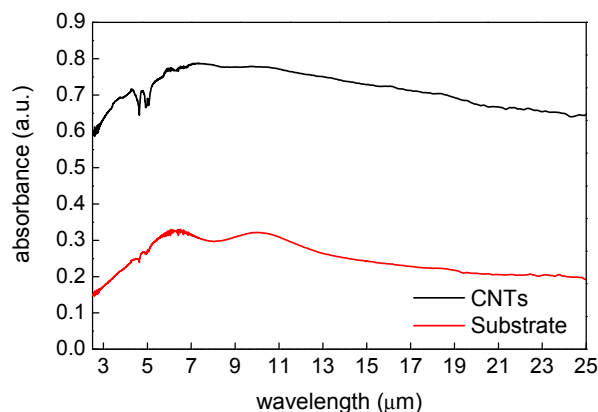


**Figure 5.** ATR-FTIR spectra obtained for the substrate with the catalytic layer (red line), and the CNT structure (black line).

From the physical principle of the material absorption, it has been well known the particle dipole moment is necessary. No modification is required for CNTs to create the dipole moment according to this measurement. The absorption in the IR region causes changes of vibrational and rotational status of the molecules. The absorption intensity depends on the IR photon energy which can be transferred to the molecule and this depends on the change of the dipole moment that occurs as a result of molecular vibration. As a consequence, a particle will absorb the IR light only if the absorption causes a change in the dipole moment. The absorption frequency is dependent on the vibrational frequency of the molecule.

### 3.4. Electrochemical Properties

A representative cyclic voltammogram recorded at  $50 \text{ mV}\cdot\text{s}^{-1}$  with the VA-MWCNT electrode and  $2.5 \text{ mM } [\text{Fe}(\text{CN})_6]^{4-/3-}$  (1:1) solution in  $0.1 \text{ M KCl}$  is shown in Figure 6a. Two well-defined symmetric redox peaks separated by  $\Delta E_p = (E_{pa} - E_{pc}) = 83 \text{ mV}$  were observed. The ratio of the anodic and cathodic peak currents reached unity ( $I_{pa}/I_{pc} = 1.01$ ). The results indicated that the VA-MWCNT electrode promote electron transfer quite well.

The effect of varying scan rates was studied for the scan rate range  $5\text{--}500 \text{ mV}\cdot\text{s}^{-1}$ . The corresponding cyclic voltammograms are given in Figure 6b. The anodic ( $I_{pa}$ ) and cathodic ( $I_{pc}$ ) peak currents varied linearly with the square root of the scan rate ( $v^{1/2}$ ), as shown in Figure 6c. It demonstrates that the electrode process is controlled by a diffusion. The stability of the VA-MWCNT electrode was studied for the  $[\text{Fe}(\text{CN})_6]^{4-/3-}$  in  $0.1 \text{ M KCl}$  at  $50 \text{ mV}\cdot\text{s}^{-1}$  using 10 cycles of CV. The results, depicted in Figure 6d, revealed that both, the oxidative and reductive, peak currents of the studied redox couple remained

practically constant throughout all 10 potential cycles and, therefore, the CNT-based working electrodes with the Ti/Ta adhesive interlayers are suitable for repeated measurements.

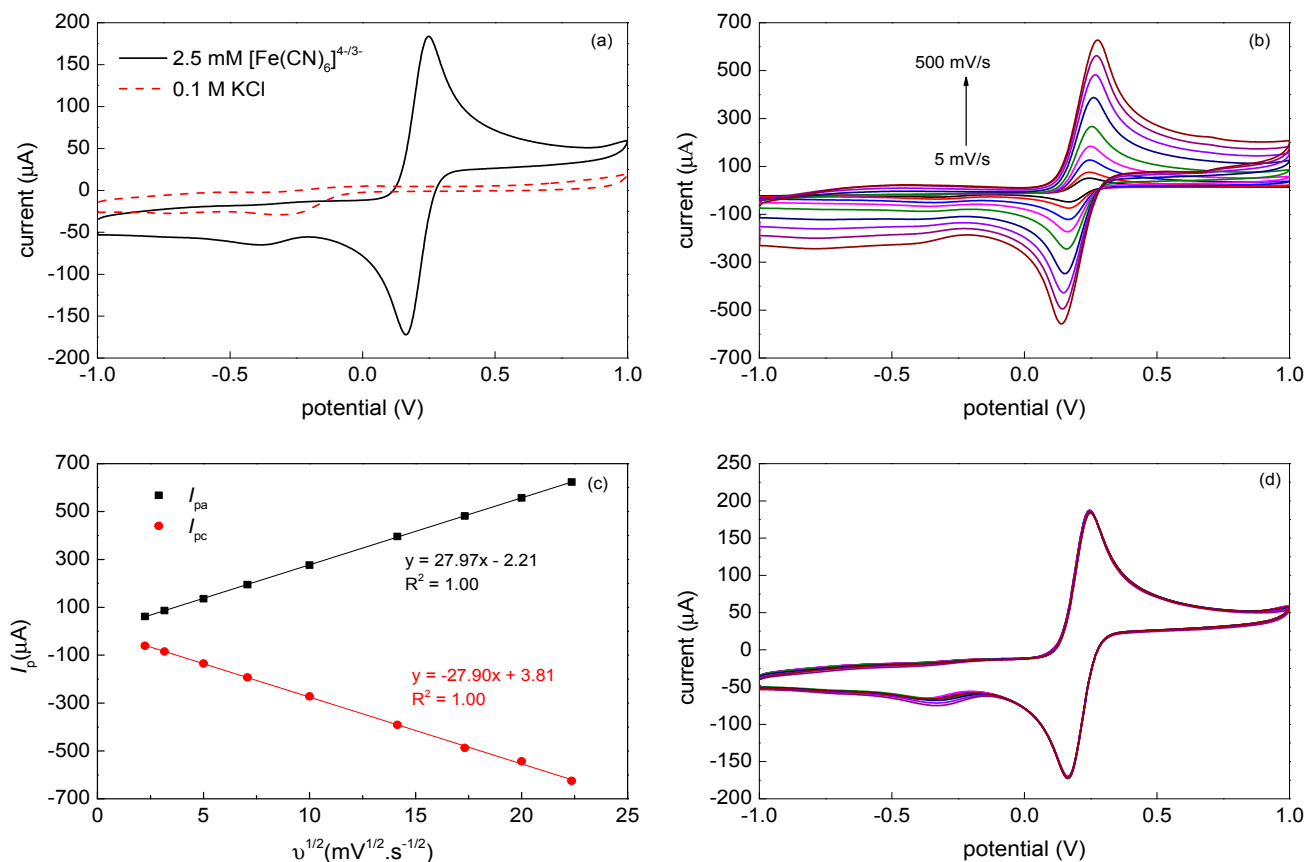


**Figure 6.** (a) Cyclic voltammograms obtained for 0.1 M KCl and 2.5 mM [Fe(CN)<sub>6</sub>]<sup>4-/3-</sup> in 0.1 M KCl at  $v = 50 \text{ mV}\cdot\text{s}^{-1}$  using VAMWCNT-based working electrode; (b) Cyclic voltammograms obtained for 2.5 mM [Fe(CN)<sub>6</sub>]<sup>4-/3-</sup> in 0.1 M KCl at various scan rates ( $v = 5, 10, 25, 50, 100, 200, 300, 400$  and  $500 \text{ mV}\cdot\text{s}^{-1}$ ) using VAMWCNT-based working electrode; (c)  $I_{pa}$  vs.  $v^{1/2}$  and  $I_{pc}$  vs.  $v^{1/2}$  curves; (d) 10 cycles of CV obtained in 2.5 mM [Fe(CN)<sub>6</sub>]<sup>4-/3-</sup> in 0.1 M KCl at  $v = 50 \text{ mV}\cdot\text{s}^{-1}$  using VAMWCNT-based working electrode.

Comparing the obtained results with the standard or MWCNT-modified screen-printed electrodes [53], the prepared VA-MWCNT electrodes indicate their high potential for construction of electrochemical sensors or biosensors detecting substances in aqueous solutions.

### 3.5. Gas Sensing Properties

The results of the CNT sensor response to NH<sub>3</sub> at room temperatures and 200 °C are shown in Figure 7a. Since the sensor resistance increased during ammonia exposure, it is concluded that free carriers—the holes—in MWCNTs were neutralized by electrons coming from adsorbed NH<sub>3</sub> and, therefore, MWCNTs exhibited p-type nature. This phenomenon has been already described in previous studies. Hoa *et al.* supposed that MWCNT is a p-type semiconductor and the adsorption of electron donor compound such as NH<sub>3</sub> decreases the charge carrier concentration, thus inducing an increase of the resistance [54]. The same mechanism of interaction of adsorbed electron-donor compound with

*p*-type CNTs was also described in [34,55–57]. The main interaction mechanism of ammonia with CNTs is a reversible adsorption. Vikramaditya *et al.* assume that  $\text{NH}_3$  is physisorbed on non-doped CNTs [58]. Thus, the sensing mechanism of ammonia with CNTs consists of two main steps, (i) physical adsorption of gas molecules and (ii) a charge transfer between adsorbed molecules and CNTs [59,60]. Testing of the sensor sensitivity to isobutane was carried out at room temperature (Figure 8) and revealed that the sensor is insensitive to a non-polar molecule such as  $\text{iC}_4\text{H}_{10}$ .

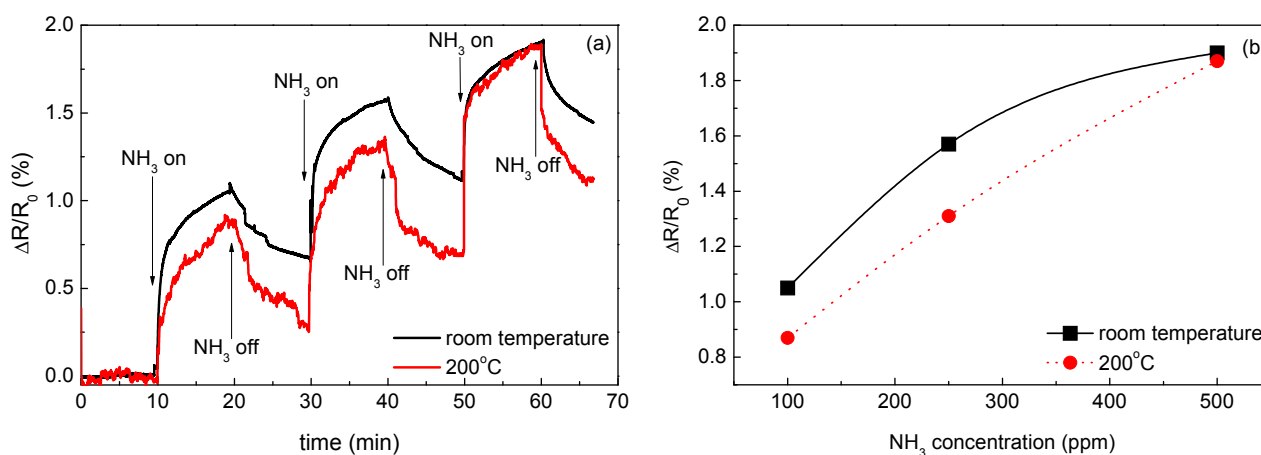


**Figure 7.** (a) Time dependent response of the CNT sensor to  $\text{NH}_3$  at room temperature and at 200 °C and (b) the response of the sensor determined after 10 min of the exposure as a function of  $\text{NH}_3$  concentration.

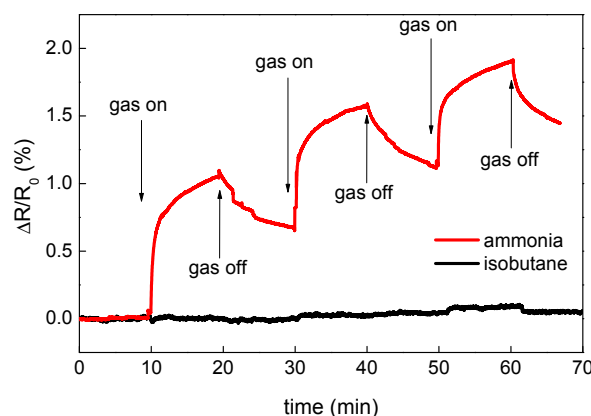


**Figure 8.** Time dependent response of the CNT sensor to  $\text{NH}_3$  and  $\text{iC}_4\text{H}_{10}$  at room temperature.

According to the data presented in Figure 7b, the sensor exhibited higher response to  $\text{NH}_3$  at the room temperature than at 200 °C. Since the adsorption is an exothermal process, it is enhanced with the decreasing temperature. The response  $\Delta R/R_0$  ranged from 0.87% to 1.9%. The dependence of the sensor response  $\Delta R/R_0$  determined after 10 min of the exposure on the concentration of  $\text{NH}_3$  was almost linear at 200 °C whereas the relation became strongly nonlinear at room temperature. It can be linked to an incomplete desorption of  $\text{NH}_3$  at room temperature.

The obtained response of the sensors to  $\text{NH}_3$  was quite high taking into account that MWCNTs were not treated or modified for sensing. The highest response, 1.9%, was achieved at room temperature for 500 ppm of  $\text{NH}_3$ . For comparison, Hoa *et al.* [54] achieved 8% response for 6% of  $\text{NH}_3$  in  $\text{N}_2$ , *i.e.*, for

60,000 ppm. Here, the reported sensor was not tested for such a high concentration of  $\text{NH}_3$  but its response to a  $120\times$  lower concentration was only four times lower. A response of 9%, but to a lower concentration of 1% (10,000 ppm), was reported by Cui *et al.* for Ag-decorated MWCNTs [37].

In conclusion, the described sensor preparation technique is quite simple and allows achieving a sufficiently high response. The direct nanotube growth on the substrate allows managing the response by synthesis conditions that is critical for a scale-up production. The present CNT sensor can be further improved by a suitable functionalization and/or a decoration of the CNTs with metallic nanoparticles using the same set-up or a different procedure.

### 3.6. Field Emission Properties for Pressure Sensing

The measurements of field emission current were carried out multiple times at 10 emitter-to-anode distances from  $84\ \mu\text{m}$  to  $120\ \mu\text{m}$ . The current density in dependence on the electric field intensity calculated from measured results is shown in Figure 9a and the corresponding Fowler-Nordheim (F-N) plot is in Figure 9b. Straight lines in the F-N plot indicates the quantum mechanical tunneling characteristic of the electron field emission and are based on the F-N equation

$$I = (A\alpha\beta^2V^2 / x^2\phi) \exp[-B\phi^{3/2}x / (\beta V)] \quad (2)$$

where  $I$  is the emission current,  $A = 1.56 \times 10^{-6}\ \text{A}\cdot\text{V}^{-2}\cdot\text{eV}$ ,  $B = 6.83 \times 10^9\ \text{eV}^{-3/2}\cdot\text{V}\cdot\text{m}^{-1}$ ,  $\alpha$  is the emission area,  $\beta$  is the field enhancement factor,  $\phi$  is the work function,  $x$  is the distance between the anode and the emitter, and  $V$  is the applied voltage. Emission of many electrons at a low applied voltage requires a low work function ( $\phi$ ) and a high field enhancement factor ( $\beta$ ). Using the F-N plot,  $\ln(J/E^2)$  vs.  $1/E$ , the field enhancement factor can be determined from the slope of the straight line. The measured data can be divided into two sections, below and above  $0.9\ \mu\text{m}\cdot\text{V}^{-1}$ , that have different enhancement factors. Such behavior of the plot is not unusual and can be caused by various reasons, such as resistance, gas absorption, localized states or interaction between emitters [61,62].

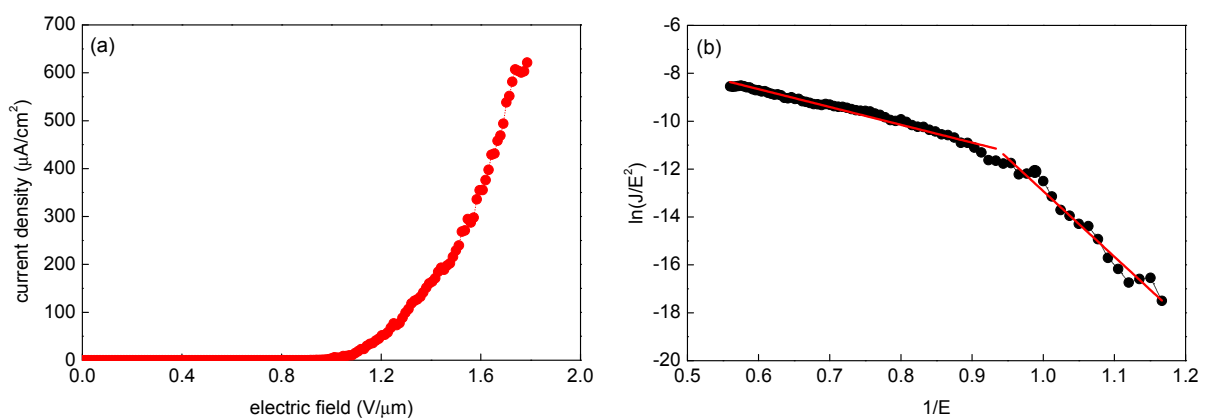


**Figure 9.** (a) Current density in dependence on field intensity for the CNT array field emitters; (b) The relevant Fowler-Nordheim curve.

The turn-on field, defined as the field intensity enabling the emission current density of  $10\ \mu\text{A}\cdot\text{cm}^{-2}$ , was determined to be below  $1\ \text{V}\cdot\mu\text{m}^{-1}$ . The current density of hundreds of  $\mu\text{A}$  was achieved already at  $1.8\ \text{V}\cdot\mu\text{m}^{-1}$ . The measured data follow the Fowler-Nordheim law in Equation (2) concerning the

dependence of the emission current on the electrode distance when the applied voltage is fixed. Similarly, for the fixed distance between the electrodes, the emission current increases with increasing voltage. This confirms the expected behavior of our field emission electrode as proposed in the pressure sensor design. From the measured characteristics, one could also conclude that it is of advantage to operate at a higher electric field and shorter distances. In these conditions, a bigger change of the emission current with changing diaphragm deformation (pressure) leads to the higher sensitivity of the sensor, *i.e.*, higher  $\Delta I/\Delta p$  with the identical  $\Delta d$ . This effect can be strengthened with the proper choice of diaphragm [49].

#### 4. Conclusions

Selected functional properties of VA-MWCNT films were investigated in different types of measurement devices that integrated CNTs prepared in a microwave plasma torch. The average diameter of prepared MWCNTs was lower than 80 nm and the thickness of uniform VA-MWCNT layers was about 16  $\mu\text{m}$ . Electrical measurements of CNTs showed their resistive behavior with a low resistance of 0.5  $\Omega\cdot\text{cm}$ , and non-linearity of about 0.5%. A parallel capacitance proposed in previously published papers was confirmed by dynamic measurements. The FTIR analysis demonstrated a high absorption in the IR range of 8–22  $\mu\text{m}$  allowing VA-MWCNT application in IR thermometers such as bolometers usually used in thermo-vision. Cyclic voltammetry using redox couple of  $[\text{Fe}(\text{CN})_6]^{4-/3-}$  were used to investigate the electrochemical response of the working electrodes coated by plasma grown VA-MWCNTs. The obtained results indicated good electrochemical properties ( $I_{pa}/I_{pc} = 1.01$ ,  $\Delta E_p = 83$  mV) and confirmed that studied VA-MWCNT working electrodes can be successfully used in the construction of electrochemical sensors.

The constructed resistive sensor based on VA-MWCNTs exhibited increasing resistance of the VA-MWCNT layer when exposed to  $\text{NH}_3$  that must be explained by the p-type semiconducting behavior of CNTs when adsorbed ammonia gas molecules donate electrons to CNTs. The field emission properties of the electrode with VA-MWCNTs grown directly on silicon were investigated with the aim to use the electrode in pressure sensing applications. The measured dependencies showed that emission current from the CNTs is stable, and a relatively low noise can be achieved for smaller electrode distances and higher voltage between the electrodes. The characteristics were reversible, with low turn-on field ( $1 \text{ V}\cdot\mu\text{m}^{-1}$ ), and current of hundreds of  $\mu\text{A}$  for the electric field was around  $1.8 \text{ V}\cdot\mu\text{m}^{-1}$ . It indicated that plasma-grown VA-MWCNTs are well suited for pressure sensing.

#### Acknowledgments

This work has been performed in laboratories supported by the operational program Research and Development for Innovation, by the SIX project CZ.1.05/2.1.00/03.0072 and supported by Grant Agency of the Czech Republic under the contracts GACR P205/10/1374 and GA13-19947S. Petr Synek would like to acknowledge the project “Employment of Newly Graduated Doctors of Science for Scientific Excellence” (CZ.1.07/2.3.00/30.0009) co-financed from European Social Fund and the state budget of the Czech Republic.

## Author Contributions

P.M. and J.P. (Jan Prášek) designed, performed, evaluated and wrote the experiments related to the electrochemical and surface characterization and finalized the paper; J.S. designed and performed the experiments related to the standard electrical characterization which was analyzed, evaluated and written by J.H.; J.P. (Jan Pekárek) designed, performed, evaluated and wrote the experiments related to the field emission properties; V.S. designed, performed, evaluated and wrote the experiments related to the optical characterization; A.G.B. designed, performed, evaluated and wrote the experiments related to the gas sensing properties; O.J., P.S. and M.E. fabricated electrodes and described the fabrication process; L.Z. described the fabrication process and made the final proofs.

## Conflicts of Interest

The authors declare no conflict of interest.

## References

1. Meyyappan, M. *Carbon Nanotubes: Science and Applications*, 1st ed.; CRC Press: Boca Raton, FL, USA, 2005; p. 304.
2. Backes, C. *Noncovalent Functionalization of Carbon Nanotubes: Fundamental Aspects of Dispersion and Separation in Water*; Springer: Berlin, Germany, 2012; p. 203.
3. Zajíčková, L.; Jašek, O.; Eliáš, M.; Synek, P.; Lazar, L.; Schneeweiss, O.; Hanzlíková, R. Synthesis of carbon nanotubes by plasma-enhanced chemical vapor deposition in an atmospheric-pressure microwave torch. *Pure Appl. Chem.* **2010**, *82*, 1259–1272.
4. Yen, J.H.; Leu, I.C.; Wu, M.T.; Lin, C.C.; Hon, M.H. Density control for carbon nanotube arrays synthesized by ICP-CVD using AAO/Si as a nanotemplate. *Electrochem. Solid State Lett.* **2004**, *7*, H29–H31.
5. Prášek, J.; Drbohlavová, J.; Chomoucká, J.; Hubálek, J.; Jašek, O.; Adam, V.; Kizek, R. Methods for carbon nanotubes synthesis-review. *J. Mater. Chem.* **2011**, *21*, 15872–15884.
6. Chen, H.; Roy, A.; Baek, J.B.; Zhu, L.; Qu, J.; Dai, L.M. Controlled growth and modification of vertically-aligned carbon nanotubes for multifunctional applications. *Mater. Sci. Eng. R-Rep.* **2010**, *70*, 63–91.
7. Tsierkezos, N.G.; Szroeder, P.; Ritter, U. Multi-walled carbon nanotubes as electrode materials for electrochemical studies of organometallic compounds in organic solvent media. *Monatshefte Chem.-Chem. Mon.* **2011**, *142*, 233–242.
8. Tsierkezos, N.G.; Szroeder, P.; Ritter, U. Application of Films Consisting of Carbon Nanoparticles for Electrochemical Detection of Redox Systems in Organic Solvent Media. *Fuller. Nanotub. Carbon Nanostruct.* **2011**, *19*, 505–516.
9. Ahlskog, M.; Hakonen, P.; Paalanen, M.; Roschier, L.; Tarkiainen, R. Multiwalled carbon nanotubes as building blocks in nanoelectronics. *J. Low Temp. Phys.* **2001**, *124*, 335–352.
10. Plombon, J.J.; O'Brien, K.P.; Gstrein, F.; Dubin, V.M.; Jiao, Y. High-frequency electrical properties of individual and bundled carbon nanotubes. *Appl. Phys. Lett.* **2007**, *90*, doi:10.1063/1.2437724.

11. Ksenevich, V.K.; Gorbachuk, N.I.; Poklonski, N.A.; Samuilov, V.A.; Kozlov, M.E.; Wieck, A.D. Impedance of Single-Walled Carbon Nanotube Fibers. *Fuller. Nanotub. Carbon Nanostruct.* **2012**, *20*, 434–438.
12. Geng, S.N.; Wang, P.; Ding, T.H. Impedance characteristics and electrical modelling of multi-walled carbon nanotube/silicone rubber composites. *Compos. Sci. Technol.* **2011**, *72*, 36–40.
13. Allaoui, A.; Hoa, S.V.; Pugh, M.D. The electronic transport properties and microstructure of carbon nanofiber/epoxy composites. *Compos. Sci. Technol.* **2008**, *68*, 410–416.
14. Popov, V.N. Carbon nanotubes: Properties and application. *Mater. Sci. Eng. R Rep.* **2004**, *43*, 61–102.
15. Goak, J.C.; Lee, H.S.; Han, J.H.; Park, J.-Y.; Seo, Y.; Kim, K.B.; Lee, N. New metric for evaluating the purity of single-walled carbon nanotubes using ultraviolet–visible–near infrared absorption spectroscopy. *Carbon* **2014**, *75*, 68–80.
16. Kruss, S.; Hilmer, A.J.; Zhang, J.; Reuel, N.F.; Mu, B.; Strano, M.S. Carbon nanotubes as optical biomedical sensors. *Adv. Drug Deliv. Rev.* **2013**, *65*, 1933–1950.
17. Huang, H.; Zou, M.; Xu, X.; Liu, F.; Li, N.; Wang, X. Near-infrared fluorescence spectroscopy of single-walled carbon nanotubes and its applications. *TrAC Trends Anal. Chem.* **2011**, *30*, 1109–1119.
18. Gohier, A.; Dhar, A.; Gorintin, L.; Bondavalli, P.; Bonnassieux, Y.; Cojocar, C.S. All-printed infrared sensor based on multiwalled carbon nanotubes. *Appl. Phys. Lett.* **2011**, *98*, doi:10.1063/1.3552686.
19. Aliev, A.E. Bolometric detector on the basis of single-wall carbon nanotube/polymer composite. *Infrared Phys. Technol.* **2008**, *51*, 541–545.
20. Afrin, R.; Shah, N.A.; Abbas, M.; Amin, M.; Bhatti, A.S. Design and analysis of functional multiwalled carbon nanotubes for infrared sensors. *Sens. Actuators A Phys.* **2013**, *203*, 142–148.
21. Gao, C.; Guo, Z.; Liu, J.-H.; Huang, X.-J. The new age of carbon nanotubes: An updated review of functionalized carbon nanotubes in electrochemical sensors. *Nanoscale* **2012**, *4*, 1948–1963.
22. Vashist, S.K.; Zheng, D.; Al-Rubeaan, K.; Luong, J.H.T.; Sheu, F.-S. Advances in carbon nanotube based electrochemical sensors for bioanalytical applications. *Biotechnol. Adv.* **2011**, *29*, 169–188.
23. Jacobs, C.B.; Peairs, M.J.; Venton, B.J. Review: Carbon nanotube based electrochemical sensors for biomolecules. *Anal. Chim. Acta* **2010**, *662*, 105–127.
24. Ahammad, A.J.S.; Lee, J.J.; Rahman, M.A. Electrochemical Sensors Based on Carbon Nanotubes. *Sensors* **2009**, *9*, 2289–2319.
25. Agüí, L.; Yáñez-Sedeño, P.; Pingarrón, J.M. Role of carbon nanotubes in electroanalytical chemistry: A review. *Anal. Chim. Acta* **2008**, *622*, 11–47.
26. Ye, M.L.; Xu, B.; Zhang, W.D. Voltammetric Behavior of Rutin at a Vertically Aligned Multiwalled Carbon Nanotubes Electrode. *Sens. Lett.* **2013**, *11*, 321–327.
27. Karuwan, C.; Wisitsoraat, A.; Sappat, A.; Jaruwongrungrongsee, K.; Patthanasettakul, V.; Tuantranont, A. Vertically Aligned Carbon Nanotube Based Electrochemical Sensor for Salbutamol Detection. *Sens. Lett.* **2010**, *8*, 645–650.
28. Berti, F.; Lozzi, L.; Palchetti, I.; Santucci, S.; Marrazza, G. Aligned carbon nanotube thin films for DNA electrochemical sensing. *Electrochim. Acta* **2009**, *54*, 5035–5041.
29. Wang, J.A.; Zhang, W.D. Sputtering deposition of gold nanoparticles onto vertically aligned carbon nanotubes for electroanalysis of uric acid. *J. Electroanal. Chem.* **2011**, *654*, 79–84.

30. Ye, M.L.; Xu, B.; Zhang, W.D. Sputtering deposition of Pt nanoparticles on vertically aligned multiwalled carbon nanotubes for sensing L-cysteine. *Microchim. Acta* **2011**, *172*, 439–446.
31. Feng, X.; Irle, S.; Witek, H.; Morokuma, K.; Vidic, R.; Borguet, E. Sensitivity of ammonia interaction with single-walled carbon nanotube bundles to the presence of defect sites and functionalities. *J. Am. Chem. Soc.* **2005**, *127*, 10533–10538.
32. Ndiaye, A.; Bonnet, P.; Pauly, A.; Dubois, M.; Brunet, J.; Varenne, C.; Guerin, K.; Lauron, B. Noncovalent Functionalization of Single-Wall Carbon Nanotubes for the Elaboration of Gas Sensor Dedicated to BTX Type Gases: The Case of Toluene. *J. Phys. Chem. C* **2013**, *117*, 20217–20228.
33. Datta, K.; Ghosh, P.; More, M.A.; Shirsat, M.D.; Mulchandani, A. Controlled functionalization of single-walled carbon nanotubes for enhanced ammonia sensing: A comparative study. *J. Phys. D Appl. Phys.* **2012**, *45*, doi:10.1088/0022-3727/45/35/355305.
34. Zhou, Y.; Jiang, Y.D.; Xie, G.Z.; Du, X.S.; Tai, H.L. Gas sensors based on multiple-walled carbon nanotubes-polyethylene oxide films for toluene vapor detection. *Sens. Actuators B: Chem.* **2014**, *191*, 24–30.
35. Cava, C.E.; Salvatierra, R.V.; Alves, D.C.B.; Ferlauto, A.S.; Zarbin, A.J.G.; Roman, L.S. Self-assembled films of multi-wall carbon nanotubes used in gas sensors to increase the sensitivity limit for oxygen detection. *Carbon* **2012**, *50*, 1953–1958.
36. Ahn, K.S.; Kim, J.H.; Lee, K.N.; Kim, C.O.; Hong, J.P. Multi-wall carbon nanotubes as a high-efficiency gas sensor. *J. Korean Phys. Soc.* **2004**, *45*, 158–161.
37. Cui, S.M.; Pu, H.H.; Lu, G.H.; Wen, Z.H.; Mattson, E.C.; Hirschmugl, C.; Gajdardziska-Josifovska, M.; Weinert, M.; Chen, J.H. Fast and Selective Room-Temperature Ammonia Sensors Using Silver Nanocrystal-Functionalized Carbon Nanotubes. *ACS Appl. Mater. Int.* **2012**, *4*, 4898–4904.
38. Tang, Y.; Zhang, Q.H.; Li, Y.G.; Wang, H.Z. Highly selective ammonia sensors based on  $\text{Co}_{1-x}\text{Ni}_x\text{Fe}_2\text{O}_4$ /multi-walled carbon nanotubes nanocomposites. *Sens. Actuators B Chem.* **2012**, *169*, 229–234.
39. Varghese, O.K.; Kichambre, P.D.; Gong, D.; Ong, K.G.; Dickey, E.C.; Grimes, C.A. Gas sensing characteristics of multi-wall carbon nanotubes. *Sens. Actuators B Chem.* **2001**, *81*, 32–41.
40. Wilfert, S.; Edelman, C. Field emitter-based vacuum sensors. *Vacuum* **2012**, *86*, 556–571.
41. Bonard, J.M.; Maier, F.; Stockli, T.; Chatelain, A.; de Heer, W.A.; Salvetat, J.P.; Forro, L. Field emission properties of multiwalled carbon nanotubes. *Ultramicroscopy* **1998**, *73*, 7–15.
42. Guo, P.S.; Chen, T.; Chen, Y.W.; Zhang, Z.J.; Feng, T.; Wang, L.L.; Lin, L.F.; Sun, Z.; Zheng, Z.H. Fabrication of field emission display prototype utilizing printed carbon nanotubes/nanofibers emitters. *Solid State Electron.* **2008**, *52*, 877–881.
43. Nakahara, H.; Kusano, Y.; Kono, T.; Saito, Y. Evaluations of carbon nanotube field emitters for electron microscopy. *Appl. Surf. Sci.* **2009**, *256*, 1214–1217.
44. Zajičková, L.; Eliáš, M.; Jašek, O.; Kudrle, V.; Frgala, Z.; Matějková, J.; Buršík, J.; Kadlečiková, M. Atmospheric pressure microwave torch for synthesis of carbon nanotubes. *Plasma Phys. Control. Fusion* **2005**, *47*, B655–B666.
45. Jašek, O.; Eliáš, M.; Zajičková, L.; Kudrle, V.; Bublan, M.; Matějková, J.; Rek, A.; Buršík, J.; Kadlečiková, M. Carbon nanotubes synthesis in microwave plasma torch at atmospheric pressure. *Mater. Sci. Eng. C* **2006**, *26*, 1189–1193.

46. Jašek, O.; Eliáš, M.; Zajíčková, L.; Kučerová, Z.; Matějková, J.; Rek, A.; Buršík, J. Discussion of important factors in deposition of carbon nanotubes by atmospheric pressure microwave plasma torch. *J. Phys. Chem. Solids* **2007**, *68*, 738–743.
47. Zajíčková, L.; Eliáš, M.; Jašek, O.; Kučerová, Z.; Synek, P.; Matějková, J.; Kadlečková, M.; Klementová, M.; Buršík, J.; Vojáčková, A. Characterization of Carbon Nanotubes Deposited in Microwave Torch at Atmospheric Pressure. *Plasma Process. Polym.* **2007**, *4*, S245–S249.
48. Zajíčková, L.; Synek, P.; Jašek, O.; Eliáš, M.; David, B.; Buršík, J.; Pizurová, N.; Hanzlíková, R.; Lazar, L. Synthesis of carbon nanotubes and iron oxide nanoparticles in MW plasma torch with Fe(CO)<sub>5</sub> in gas feed. *Appl. Surf. Sci.* **2009**, *255*, 5421–5424.
49. Pekárek, J.; Vrba, R.; Prášek, J.; Jašek, O.; Majzlíková, P.; Pekárková, J.; Zajíčková, L. MEMS Carbon Nanotubes Field Emission Pressure Sensor with Simplified Design: Performance and Field Emission Properties Study. *IEEE Sens. J.* **2015**, *15*, 1430–1436.
50. Synek, P.; Jašek, O.; Zajíčková, L.; David, B.; Kudrle, V.; Pizurová, N. Plasmachemical synthesis of maghemite nanoparticles in atmospheric pressure microwave torch. *Mater. Lett.* **2011**, *65*, 982–984.
51. Synek, P.; Jašek, O.; Zajíčková, L. Study of Microwave Torch Plasmachemical Synthesis of Iron Oxide Nanoparticles Focused on the Analysis of Phase Composition. *Plasma Chem. Plasma Process.* **2014**, *34*, 327–341.
52. Bhan, R.K.; Saxena, R.S.; Jalwania, C.R.; Lomash, S.K. Uncooled Infrared Microbolometer Arrays and their Characterisation Techniques. *Def. Sci. J.* **2009**, *59*, 580–589.
53. Majzlíková, P.; Prášek, J.; Eliáš, M.; Jašek, O.; Pekárek, J.; Hubálek, J.; Zajíčková, L. Comparison of different modifications of screen-printed working electrodes of electrochemical sensors using carbon nanotubes and plasma treatment. *Phys. Status Solidi* **2014**, *211*, 2756–2764.
54. Hoa, N.D.; van Quy, N.; Cho, Y.; Kim, D. An ammonia gas sensor based on non-catalytically synthesized carbon nanotubes on an anodic aluminum oxide template. *Sens. Actuators B Chem.* **2007**, *127*, 447–454.
55. Sidek, R.M.; Yusof, F.A.M.; Yasin, F.M.; Wagiran, R.; Ahmadun, F. Electrical response of multi-walled carbon nanotubes to ammonia and carbon dioxide. In Proceedings of the 2010 IEEE International Conference on Semiconductor Electronics (ICSE), Melaka, Malaysia, 28–30 June 2010; pp. 263–266.
56. Firouzi, A.; Sobri, S.; Yasin, F.M.; Ahmadun, F. Synthesis of Carbon Nanotubes by Chemical Vapor Deposition and their Application for CO<sub>2</sub> and CH<sub>4</sub> Detection. In Proceedings of the 2010 International Conference on Nanotechnology and Biosensors, Hong Kong, China, 28–30 December 2011; Volume 2, pp. 169–172.
57. Han, J.W.; Kim, B.; Li, J.; Meyyappan, M. A carbon nanotube based ammonia sensor on cellulose paper. *RSC Adv.* **2014**, *4*, 549–553.
58. Vikramaditya, T.; Sumithra, K. Effect of Substitutionally Boron-Doped Single-Walled Semiconducting Zigzag Carbon Nanotubes on Ammonia Adsorption. *J. Comput. Chem.* **2014**, *35*, 586–594.
59. Teerapanich, P.; Myint, M.T.Z.; Joseph, C.M.; Hornyak, G.L.; Dutta, J. Development and Improvement of Carbon Nanotube-Based Ammonia Gas Sensors Using Ink-Jet Printed Interdigitated Electrodes. *IEEE Trans. Nanotechnol.* **2013**, *12*, 255–262.

60. Van Hieu, N.; Dung, N.Q.; Tam, P.D.; Trung, T.; Chien, N.D. Thin film polypyrrole/SWCNTs nanocomposites-based NH<sub>3</sub> sensor operated at room temperature. *Sens. Actuators B Chem.* **2009**, *140*, 500–507.
61. Cheng, C.Y.; Nakashima, M.; Teii, K. Low threshold field emission from nanocrystalline diamond/carbon nanowall composite films. *Diam. Relat. Mater.* **2012**, *27–28*, 40–44.
62. Obraztsov, A.N.; Zakhidov, A.A.; Volkov, A.P.; Lyashenko, D.A. Non-classical electron field emission from carbon materials. *Diam. Relat. Mater.* **2003**, *12*, 446–449.

© 2015 by the authors; licensee MDPI, Basel, Switzerland. This article is an open access article distributed under the terms and conditions of the Creative Commons Attribution license (<http://creativecommons.org/licenses/by/4.0/>).

## Příloha 3

PEKÁREK, J. et al. MEMS carbon nanotubes field emission pressure sensor with simplified design: performance and field emission properties study. *IEEE Sensors Journal*, 2015, vol. 15, no. 3, pp. 1430-1436. ISSN 1530-437x.

### ABSTRAKT

Tlakové snímače se v posledních letech objevily v mnoha oblastech základního a aplikovaného výzkumu. V tomto článku obsahuje snímač tlaku založený na mikro-elektromechanickém systému (MEMS) nanostrukturní elektrodu sestávající z pole uhlíkových nanotrubic. Tyto nanotrubic jsou přímo rostlé na elektrodě v plazmovém výboji za atmosférického tlaku. Tato metoda růstu nám umožňuje použít jednoduchou strukturu elektrody bez potřeby bariérové vrstvy a časově náročného litografického procesu. Kombinací emise elektrickým polem z pole uhlíkových nanotrubic a vynikajících mechanických vlastností MEMS je umožněno zvýšit citlivost snímače. Emisní vlastnosti uhlíkových nanotrubic jsou měřeny nově vyvinutým systémem umožňujícím přesné měření vlastností, jako je závislost na vzdálenosti membrány (horní elektrody), použitém napětí a určit stabilitu snímače. Naměřené hodnoty jsou porovnány s numerickým modelem membránového systému v softwaru CoventorWare pomocí metody konečných prvků. Je navrženo také zapouzdření snímače pomocí skelných frit, protože tato metoda je vhodná i pro vysoké nároky na vakuum při emisi elektrickým polem.

# MEMS Carbon Nanotubes Field Emission Pressure Sensor With Simplified Design: Performance and Field Emission Properties Study

Jan Pekarek, Radimir Vrba, Jan Prasek, Ondrej Jasek, Petra Majzlikova, Jana Pekarkova, and Lenka Zajickova

**Abstract**—The pressure sensor application gained recently substantial interest in many fields of basic and applied research and applications. In this paper, microelectromechanical system (MEMS)-based pressure sensor contains nanostructured electrode consisting of carbon nanotube (CNT) array. CNTs are directly grown on such electrode by plasma-enhanced chemical vapor deposition method using microwave plasma torch at atmospheric pressure. This growth method enables us to use a simple electrode structure without need of buffer layer and time-consuming lithography process. Combination of CNTs field emission and MEMS membrane mechanical properties make possible to enhance sensitivity of the sensor. Field emission properties of CNTs are measured by newly developed system enabling us precise measurement of expecting properties, such as dependence on diaphragm (upper electrode) distance, applied voltage, and stability of the sensor. Measured values are compared with a numerical modeling of the membrane system in CoventorWare software by finite-element method. We also suggest encapsulating the sensor using glass frit bonding because such method is more suitable for high vacuum requirements of the field emission operation.

**Index Terms**—Carbon nanotubes, field emitter arrays, microelectromechanical systems, microwave torch.

## I. INTRODUCTION

**M**ICROELECTROMECHANICAL SYSTEMS (MEMS) have gained increased interests during the last 10 years because of their distinct advantages such as miniaturized size, light weight, low power consumption, and extremely low cost due to a potential batch fabrication capability. A large field of potential applications of MEMS devices is in the area of sensing. Pressure, together with temperature, is one of the most important physical quantities that has to be measured in various applications.

Manuscript received July 8, 2014; revised September 25, 2014; accepted October 9, 2014. Date of publication October 22, 2014; date of current version December 11, 2014. This work was supported in part by the Grant Agency of the Czech Republic under Project 205/10/1374, and in part by Project “CEITEC” Central European Institute of Technology CZ.1.05/1.1.00/02.0068. The associate editor coordinating the review of this paper and approving it for publication was Prof. Zeynep Celik-Butler.

J. Pekarek, R. Vrba, J. Prasek, P. Majzlikova, and J. Pekarkova are with the Department of Microelectronics, Brno University of Technology, Brno 602 00, Czech Republic (e-mail: pekarek@feec.vutbr.cz; vrbar@feec.vutbr.cz; prasek@feec.vutbr.cz; businova@feec.vutbr.cz; chomoucka@feec.vutbr.cz).

O. Jasek and L. Zajickova are with the Department of Physical Electronics, Masaryk University, Brno 601 77, Czech Republic (e-mail: jasek@physics.muni.cz; lenkaz@physics.muni.cz).

Color versions of one or more of the figures in this paper are available online at <http://ieeexplore.ieee.org>.

Digital Object Identifier 10.1109/JSEN.2014.2363213

The most progressive application of pressure sensor is in car industry as tire pressure sensors with automatic built-in tire pumps [1], [2] or application in a variety of disposable medical devices. The pressure sensor can measure blood pressure, intrauterine pressure during birth and patient’s vital signs [3]. Moreover, pressure sensors are used in surgery devices, hospital beds and many other medical devices [4].

In MEMS pressure sensors the pressure variations are transformed into a mechanical deformation and/or stress that are measured via changes of capacitance, inductance, or resistance of the sensor [5], [6].

Another principle of the pressure sensor is based on the changes of field emission current from on the sensor electrodes [7], [8].

The voltage applied between the cathode and the anode provides the extraction field. The distance between the electrodes has to be adapted accordingly. The emission current can be controlled either by regulating the voltage or by changing the emitter-to-anode distance. The voltage regulation affects the energy of the electrons at the anode and requires complex power supplies. Changing the emitter-to-anode distance requires mechanical controls. The anode is formed by a thin diaphragm that bends due to external pressure. If the applied voltage between electrodes is fixed, then the electrical field intensity is changing as well as the field emission current. The principle is similar to capacitive pressure sensors in which the measured quantity is the capacity.

Carbon materials of various kinds have attracted great interest in the field of electron emission because of their properties to emit electrons at relatively low applied electric fields. The field-emitter configuration should have the highest aspect ratio and low work function at its surface. Even though microtips are ideal for field enhancement, they are also the most difficult and costly structures to manufacture. To reduce manufacturing costs, there is an ongoing effort to develop planar cold-cathode field emitters, particularly based on diamond thin films [9]–[11] and high aspect ratio carbon nanostructured materials [12]. The first extensive study of field emission from CNTs has been published by Bonard et al. in 1998 [13]. Later on, CNTs were used as field-emitters in flat-panel field-emission displays [14] or electron sources in electron microscopy [15].

Taak et al introduced field emission pressure sensor with fully embedded carbon nanotubes [16]. In this study,

anode/cathode spacing was set up to  $1.3 \mu\text{m}$  and 60–100 V was used as operating voltage range.

The most similar approach to our sensor has been described by Qian *et al* [17]–[19]. In his studies, higher distances and higher applied voltages were used. The field emission was then operated in the vacuum cavity with the pressure  $10^{-3}$  Pa. This pressure is surprising, because of the field emission cannot be operated under pressure lower than  $10^{-4}$  Pa [12], [13], [20]. Therefore it's very important to obtain properly encapsulated sensor for its reliable operation. Besides the usual method to insulate upper and lower electrode in the field emission system, dielectric tape, it is also possible to use glass frit bonding. This technology is widely used in industrial microsystems applications where fully processed silicon wafers have to be bonded [21]. This end-of-process-line bonding has to achieve some very specific requirements, such as: process temperature limited to  $450 \text{ }^\circ\text{C}$  to prevent any temperature-related damage to wafers or carbon nanotubes, no aggressive cleaning to avoid metal corrosion, high process yield since wafer processing to this stage is expensive, bonding of wafers with certain surface roughness or even surface steps resulting from metal lines electrically running at the bonding interface to enable electrical connections into the cavity sealed by the bonding, as well as a mechanically strong, hermetically sealed, reliable bond [22], [23]. All of these requirements are fulfilled by the glass frit bonding process, which in addition can be very universally applied since it can be used to bond almost all surfaces common in microelectronics and microsystem technologies. In our previous work we have suggested the pressure sensor based on the measurement of emission current from carbon nanotubes that are grown on the cathode of the sensor using innovative plasma technique, mw plasma torch [24]–[27].

Our sensor was designed to reduce the power, complexity, and cost of the gate drive/modulation circuitry by reducing the emitter-to-anode distance which also allows the reduction of the voltage required for controlling electron emission to few units or tens of volts. In this work, detailed study of the field emission from CNTs grown in mw torch has been performed. In the current set up, the study could be first time performed extensively for different distances between CNTs on cathode and the anode. This study is unique due to usage of linear nano-motion drive in the vacuum chamber that simulated the diaphragm bending. Carbon nanotubes were deposited using innovative plasma technique, mw plasma torch. This method is very fast (tents of seconds) in comparison to standard CVD methods (units of hours). During the CVD growth the interaction with the material under the catalyst is of importance especially in the case of integration on the Si substrates. At temperatures of CNT growth, the metal catalyst can react with the Si substrate and the catalytic particles change from pure metal to metal silicide. It was found that application of a buffer layer between the Si-supporting substrate and metal catalyst significantly improves the catalytic function of the created particles and consequently the CNT growth because the formation of metal silicides is suppressed [28]. The material of the buffer layer varied from the frequently used  $\text{SiO}_2$  [29] to  $\text{TiN}$  [28]. The influence of several different

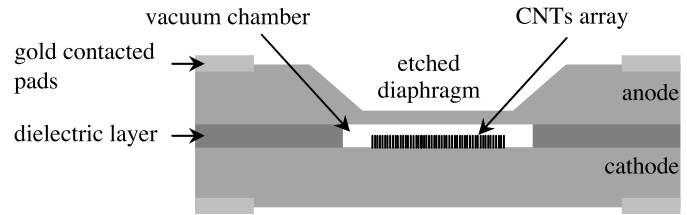


Fig. 1. Schematic view of the MEMS pressure sensor with carbon nanotubes emitters.

buffer layers was compared by Arcos *et al.* [30]. In the microwave (mw) torch deposition, the silicon substrate without the silicon dioxide barrier can be used and carbon nanotubes grow without any problem as described [31].

## II. EXPERIMENTAL

### A. Design and Fabrication of CNTs Based MEMS Field Emission Pressure Sensor

The MEMS field emission pressure sensor was designed as a diode structure (see Fig. 1). It consisted of two highly doped silicon electrodes, one of them anisotropically etched to a bending diaphragm. Emissive material, in our case the vertically aligned CNTs, is deposited on the cathode as described below. Both electrodes are separated by dielectric layer with integrated vacuum chamber. The dielectric layer can be made of pyrex glass using anodic bonding technology or made of glass frit using screen printing process.

The silicon material can be etched using several techniques. Anisotropic wet chemical etching of silicon is frequently used for shaping quite intricate three-dimensional structures. An easy technique is to use KOH-water solution. This solution etches the silicon anisotropically and the angle between the sidewalls and the  $\langle 100 \rangle$  plane is  $54.7$  degrees.

The etching mask for KOH etching was made from patterned  $\text{SiO}_2$  as hardmask using standard lithography technique. Such a mask has a good etch selectivity toward Si and  $\text{SiO}_2$ . The KOH-water solution was prepared by diluting commercially available KOH pellets (p.a. pure, Merck, Czech Republic). All etching experiments were carried out in a closed Teflon container with a constant temperature bath. The external mechanical stirring was used in etch bath of KOH during experiments to obtain the uniform etching. The KOH concentration varied from 20 to 50 wt% and temperature of the etch bath from 50 to  $80 \text{ }^\circ\text{C}$  in steps of  $10 \text{ }^\circ\text{C}$ . The best results were obtained with concentration 30 wt% of KOH-water solution and temperature of the etch bath  $80 \text{ }^\circ\text{C}$ . The etching rate was set to  $1 \mu\text{m}$  per minute. The potassium hydroxide causes that the small crystals are created on the surface. Therefore the substrate was polished in nitrogen acid mixed with Buffer-oxide-etchant to obtain a smooth surface.

### B. Deposition and Analysis of Carbon Nanotubes

For this experiment, multiwalled carbon nanotubes (MWCNTs) were deposited using a mw torch at atmospheric pressure. The typical deposition conditions in torch were: flow rates of argon, methane and hydrogen  $Q_{\text{Ar}} = 700$  sccm,  $Q_{\text{CH}_4} = 40$  sccm and  $Q_{\text{H}_2} = 250$  sccm, respectively,



Fig. 2. Vacuum chamber for I-V characteristics measurement.

mw power of 210 W, substrate temperature 900 to 1100 K, deposition time 90 seconds. The substrates for CNTs growth were 10 mm × 15 mm conductive Si wafers (n-type, antimony, resistivity  $<0.02 \Omega\text{-cm}^{-1}$ , orientation  $\langle 100 \rangle$ ) without barrier layer with 4 mm × 4 mm Fe catalyst layer (5 nm) prepared by vacuum evaporation. A detailed study of the microwave torch for deposition of MWCNTs and their characterization were published in [31] and [32].

Electrode surface was characterized optically using scanning electron microscope (SEM) MIRA II (TESCAN, Czech Republic).

### C. Measurement Method

The measurements were carried out in vacuum chamber (see Fig 2). For the simulation of diaphragm bending, the chamber was equipped with linear nano-motion drive SmarAct that enables precise changes of the distance between two electrodes inside the vacuum chamber with step width from 50 nm to 1000 nm. A special software, enabling to set up the step size, number of the steps and speed of the motion, was developed for its control. Additionally, a measurement control unit and the software were prepared for an automatic electrical measurement.

## III. RESULTS AND DISCUSSION

### A. Simulation of Diaphragm Bending

The performance of the bending diaphragm, that is the part of the sensor anode, was simulated before the sensor fabrication in order to find its structural parameters for the given pressure range. The model assumed a diaphragm with clamped edges and a constant residual stress. The latter assumption is justified by the fact that the material of diaphragm and the anode are the same. The simulations were performed with CoventorWare simulation tool using Finite Elements Analysis (FEA). The goal of the simulations was to find optimum diaphragm area and thickness.

The diaphragm bending was simulated for square and circular diaphragms with the dimensions from 100  $\mu\text{m}$  × 100  $\mu\text{m}$  to 5000  $\mu\text{m}$  × 5000  $\mu\text{m}$  and diameter of

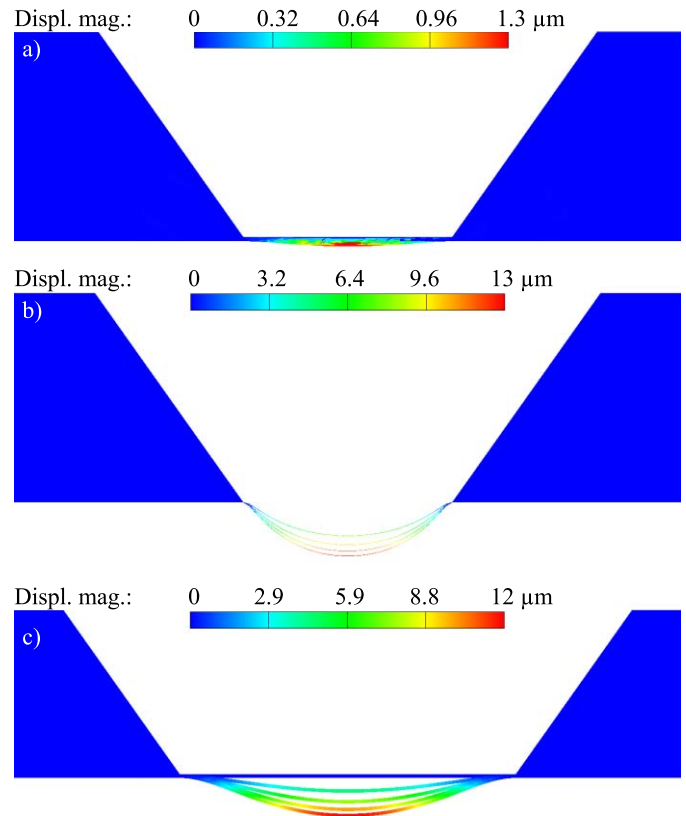


Fig. 3. Simulation of silicon diaphragm deflection for pressures 0, 50, 100, 150 and 200 kPa with exaggeration displacement 10: (a) diaphragm dimension: 500  $\mu\text{m}$  × 500  $\mu\text{m}$  × 10  $\mu\text{m}$ ; (b) diaphragm dimension: 500  $\mu\text{m}$  × 500  $\mu\text{m}$  × 1  $\mu\text{m}$ ; and (c) diaphragm dimension: 1000  $\mu\text{m}$  × 1000  $\mu\text{m}$  × 10  $\mu\text{m}$ .

100–5000  $\mu\text{m}$ , respectively. Its thickness was varied from 100 nm to 100  $\mu\text{m}$ . The examples of the simulations for square shapes and the pressure range 0–200 kPa are shown in Fig. 3. The maximum displacement of the 500  $\mu\text{m}$  × 500  $\mu\text{m}$  × 10  $\mu\text{m}$  membrane was about 1.3  $\mu\text{m}$  for 200 kPa as demonstrated in Fig. 3a. If the diaphragm was thinner, e.g. 1  $\mu\text{m}$ , the maximum displacement increased for the same pressure to 13  $\mu\text{m}$  (see Fig. 3b). An enlargement of the maximum displacement can be achieved also by changing the diaphragm dimensions. The maximum displacement of the 1000  $\mu\text{m}$  × 1000  $\mu\text{m}$  × 10  $\mu\text{m}$  diaphragm was about 12  $\mu\text{m}$  under the pressure of 200 kPa (see Fig. 3c). The summary of maximum deflection results for the 1000  $\mu\text{m}$  × 1000  $\mu\text{m}$  diaphragm with varied thickness and the pressure 0–100 kPa is given in Fig. 4.

As discussed above the sensor sensitivity can be enhanced by a reduction of the diaphragm thickness and enlargement of its area but it is necessary to avoid a diaphragm damage, i.e., to take care of maximum stress induced in the material. Therefore, the maximum inertia load that the device can withstand before it fails by yielding was also studied. The maximum misses stress of 400 MPa that occurred at the edges of the 1000  $\mu\text{m}$  × 1000  $\mu\text{m}$  × 10  $\mu\text{m}$  diaphragm at 200 kPa pressure load (see Fig. 5a), is still acceptable because it is less than the yield strength of the silicon, i.e. 7 GPa [33]. The detail of stress distribution in the diaphragm is shown in the Fig. 5b.

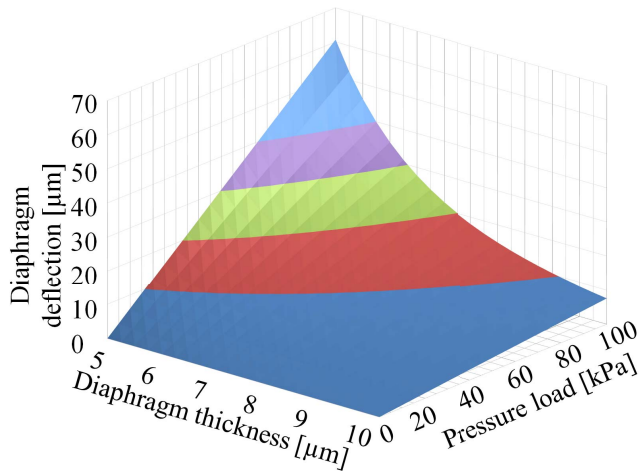


Fig. 4. Simulation of deflection for square shape silicon diaphragm for its thickness from 5 to 10  $\mu\text{m}$  in the pressure range from 0 to 100 kPa. The dimension of diaphragm was 1000  $\mu\text{m} \times 1000 \mu\text{m}$ .

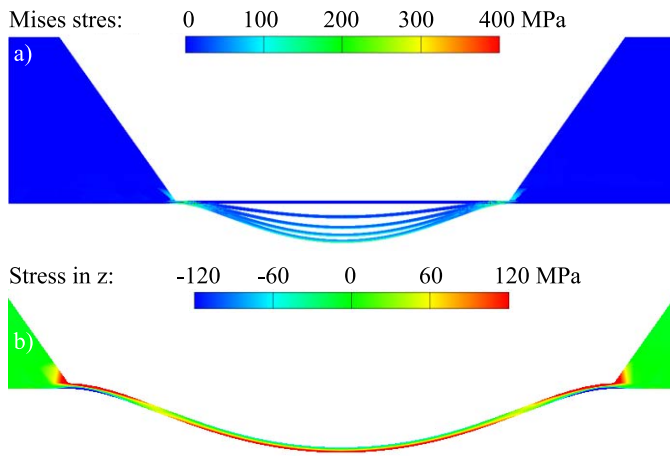


Fig. 5. (a) Von Mises stress distribution for diaphragm dimension: 1000  $\mu\text{m} \times 1000 \mu\text{m} \times 10 \mu\text{m}$  for pressures 0, 50, 100, 150 and 200 kPa with exaggeration displacement 10. (b) Detail of stress distribution for diaphragm dimension: 1000  $\mu\text{m} \times 1000 \mu\text{m} \times 10 \mu\text{m}$  for pressure 200 kPa.

### B. MWCNTs Based Electrode Analysis

Successfully fabricated MWCNTs based electrodes were systematically characterized by scanning electron microscopy. Although the CNTs were vertically aligned on the substrate by the crowding effect, as revealed by any side view into an artificially made scratch of the CNTs forest, a magnified top view showed their mutual interconnection (Fig. 6). The height of the CNTs forest was around 10  $\mu\text{m}$  and nanotubes diameter was around 20 nm. The CNTs forest covered the whole area (4 mm  $\times$  4 mm) with prepared Fe catalyst.

### C. Measurement Results

Measurements were performed in the vacuum chamber at pressure lower than  $10^{-4}$  Pa for the electrode with CNTs array with dimension of 4 mm  $\times$  4 mm. The emitter-to-anode distance was set up for 120  $\mu\text{m}$  using solid dielectric foil. The applied voltage was automatically set up using software communicating with sources via GPIB from 0 to 150 V.

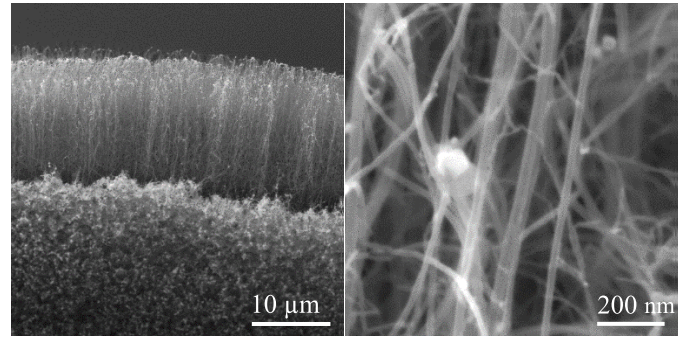


Fig. 6. SEM micrographs of CNTs in the scratch with magnification of 5 kx and the detailed image with magnification of 217 kx.

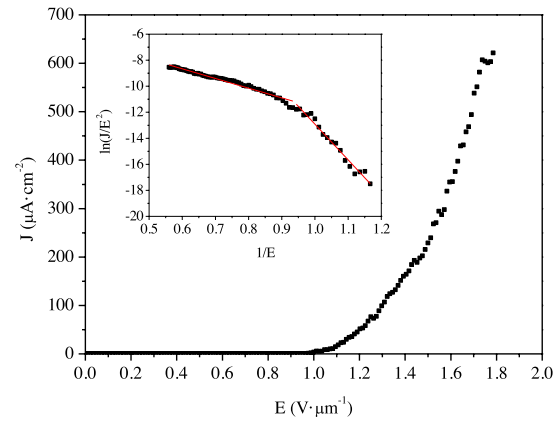


Fig. 7. Current density in dependence on field intensity for the CNT array field-emission. The inset is the relevant F-N curve.

The current density in dependence on field intensity (see Fig. 7) was calculated from measured results. The same measurements were made for ten emitter-to-anode distances—from 84  $\mu\text{m}$  to 120  $\mu\text{m}$ . For these ten distances, the same results were obtained for multiple times and all were corresponding with converted results for current density in dependence on field intensity in Fig. 7.

The inset in Fig. 7 shows the corresponding Fowler–Nordheim (F–N) plot. The straight line(s) in the F–N plot indicates the quantum mechanical tunneling characteristic of the electron field emission. The straight line in F–N plot is derived using the F–N equation:

$$I = (A\alpha\beta^2 V^2/x^2\varphi) \exp[-B\varphi^{3/2}d/(\beta V)], \quad (1)$$

where  $I$  is the emission current,  $A = 1.56 \times 10^{-6} \text{ A}\cdot\text{V}^{-2}\cdot\text{eV}$ ,  $B = 6.83 \times 10^9 \text{ eV}^{-3/2}\cdot\text{V}\cdot\text{m}^{-1}$ ,  $\alpha$  is the emission area,  $\beta$  is the field enhancement factor,  $\varphi$  is the work function,  $x$  is the distance between the anode and the emitter, and  $V$  is the applied voltage. To emit many electrons at a low applied voltage, a low work function ( $\varphi$ ) and a high field enhancement factor ( $\beta$ ) are needed. Using F–N plot ( $\ln(I/V^2)$  vs.  $1/V$ ) the field enhancement factor can be determined from the slope of the straight line. Our sample F–N plot can be divided into the two sections, below and above 0.9  $\mu\text{m}\cdot\text{V}^{-1}$ , with two different enhancement factors. Such behavior of the plot is not unusual and can be caused by various reasons such as resistance [34], [35], space charge

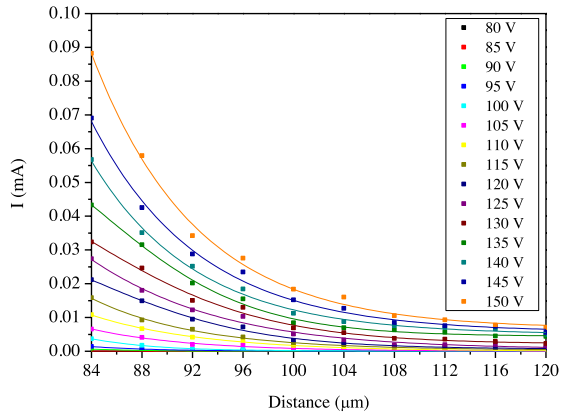


Fig. 8. The current dependence on anode-emitter distance for different applied voltage. Points – measured values, lines - model fit.

effect [36], gas absorption [37], structure change of emission site [38], [39], non-uniformity of emission sites [40], [41], localized states [42], non-Schottky-Nordheim barrier [43], [44] or interaction between emitters [45].

Assuming the work function of the CNTs to be 5.0 eV [46], the F-N plot slope of the array of our carbon nanotubes emitters can be calculated as  $-7.4 \pm 0.2$  for  $I/E$  below  $0.9 \mu\text{m}\cdot\text{V}^{-1}$  (higher electric field) and  $-27.4 \pm 1.1$  (lower electric field) for  $I/E$  above  $0.9 \mu\text{m}\cdot\text{V}^{-1}$ . From these values one could assume that it would be of advantage to operate the sensor in lower electric field regime because of faster current rise. Unfortunately, due to the very low emission current in this region it is not possible and also other parameters of the sensor suggest operation in high electric field is more advantageous.

Generally, in the carbon nanotube field emitter, the turn-on field is referred as the field intensity value when emission current density reaches the value of  $10 \mu\text{A}\cdot\text{cm}^{-2}$ . In our samples the low turn-on field (smaller than  $1 \text{V}\cdot\mu\text{m}^{-1}$ ) and high current density at  $1.8 \text{V}\cdot\mu\text{m}^{-1}$  are achieved.

The measured results follow the Fowler-Nordheim law as expected. The curves in Fig. 8 show that the measured emission current depends on electrode distance when the applied voltage is fixed and grows with decreasing distance, increasing electric field intensity. Similarly, for the fixed distance between the electrodes, the emission current is increasing with increasing voltage. This confirms the expected behavior of our field emission electrode as proposed in the pressure sensor design. From the measured characteristics one could also conclude that it is of advantage to operate at higher electric field and lower distances. At these conditions the bigger change of the emission current with changing membrane deformation (pressure) leads to the higher sensitivity of the sensor, higher  $\Delta I/\Delta p$  with the identical  $\Delta d$ . This effect can be strengthened with the proper choice of the membrane parameters as discussed in section of the diaphragm bending simulation.

As discussed above the emission current is strongly influenced by the pressure sensor parameters (diaphragm size and thickness) and electric field intensity (applied voltage and electrode anode-emitter distance). As the diaphragm deflection corresponds to anode-emitter distance change we can use

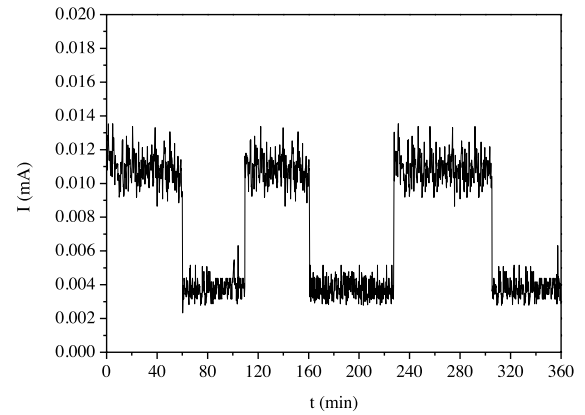


Fig. 9. Field emission stability test for 6 h. The distance between electrodes from  $120 \mu\text{m}$  to  $100 \mu\text{m}$  and back was changed during the test.

dependence in Fig. 8 to show expected emission current value for given pressure. In this case anode-emitter distance is substituted by pressure and we can directly derive expected value of emission current for chosen system parameters (initial field intensity i.e. applied voltage and anode-emitter distance, diaphragm size and thickness).

Field emission stability is one of the most important parameters for the real application of CNT-based field emitters and the pressure sensor itself. In our sample we applied constant voltage to the field emission electrode and kept it for 6 h. We monitored the change of the emission current to investigate the field emission stability (see Fig. 9). During the test, we moved the electrode with the nano-motion drive and changed the distance between electrodes from  $120 \mu\text{m}$  to  $100 \mu\text{m}$  and back.

The electrode exhibited a stable emission current during the stability test. The emission current from the carbon nanotubes electrode gradually decreased from an initial current of about  $12 \mu\text{A}$  to around  $10 \mu\text{A}$  during the 6 hour test. There was no rapid degradation of the emission current from the carbon nanotubes electrode during the stability test. We attribute the good field emission stability of our carbon nanotubes emitters to the good sample morphology and the strong adhesion between CNTs and the silicon substrate. The emission current variability (difference between the average and boundary values of the emission current) was around 20 percent. This values also leads to conclusion that it is of advantage to work in the regime with the higher electric field intensity to credibly distinguish between the various pressure changes.

#### D. Packaging

A method for packaging emission pressure sensor was also tested so the emission could exist outside the laboratory vacuum chamber. The entire sensor could be encapsulated using glass frit bonding. Our first successfully encapsulated wafer is shown in Fig. 10. The cavities in the bond region were created purposely to monitor and evaluate the optimal parameters of the glass frit layer.

For evaluating the bonding strength, the bonded substrates were glued on holders for tensile testing. The measured

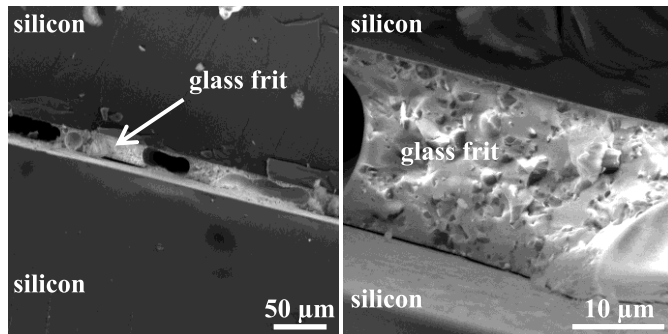


Fig. 10. SEM analysis of the cross section of glass frit bonding.

bonding strength was over 15 MPa and the cracks occur on the glass, i.e. the bonding strength of the bond is over the mechanical strength of the glass. Glass frit bonding is a suitable method for packaging of the emission pressure sensor due to its very good reliability, very low mechanical stress on bonded mechanical components. Glass frit bonding is a very safe and reproducible process.

#### IV. CONCLUSION

We studied operational characteristics of simplified micromechanical pressure sensor based on the field emission of CNTs. We performed detailed simulation study of silicon diaphragm bending to investigate the influence of the pressure difference on mechanical properties of such membrane. We conclude that even very thin membrane below 10  $\mu\text{m}$ , with area of 1000  $\mu\text{m} \times 1000 \mu\text{m}$  is suitable for this type of sensor. Therefore this type of electrode could be used as the anode in our sensor. For the cathode operation we use direct growth of vertically aligned carbon nanotubes on conductive silicon wafer without barrier layer using microwave plasma torch at atmospheric pressure. Such electrode is prepared without any lithography steps and CNTs arrays are deposited on the electrode with good uniformity and in short deposition time. We have in detail investigated field emission properties of such prepared electrode. The measured dependencies show that emission current from the CNTs is stable and of low noise. The characteristics are reversible, with low turn-on field ( $1 \text{ V} \cdot \mu\text{m}^{-1}$ ) and current of hundreds of  $\mu\text{A}$  for fields around  $1.8 \text{ V} \cdot \mu\text{m}^{-1}$ . To suppress the noise influence on the sensor operation we suggest to use operational parameters with lower electrode distances and higher voltage between electrodes. This leads us to the conclusion that our simplified preparation process of cathode electrode can be used for enhanced pressure sensing. We also introduced, glass frit bonding, as suitable method for the packaging of the emission pressure sensor for application outside the laboratory vacuum chamber.

We conclude that the desirable pressure sensor with the broad measurement range and sensitivity can be obtained by changing the thickness of the flexible diaphragm and the distance between the anode and the cathode. The experimental results show that our sensor structure is fully functional and presents a new path in the fabrication of the field emission pressure sensor.

#### REFERENCES

- [1] T.-R. Hsu, *MEMS & Microsystems: Design, Manufacture, and Nanoscale Engineering*. New York, NY, USA: Wiley, 2008.
- [2] R. Ghodssi and P. Lin, *MEMS Materials and Processes Handbook*. London, U.K.: Springer-Verlag, 2011.
- [3] R. Tan *et al.*, "Development of a fully implantable wireless pressure monitoring system," *Biomed. Microdevices*, vol. 11, no. 1, pp. 259–264, Feb. 2009.
- [4] J. Ponomozhi, C. Frias, T. Marques, and O. Frazão, "Smart sensors/actuators for biomedical applications: Review," *Measurement*, vol. 45, no. 7, pp. 1675–1688, 2012.
- [5] M. Esashi, "Revolution of sensors in micro-electromechanical systems," *Jpn. J. Appl. Phys.*, vol. 51, no. 8R, p. 080001, Aug. 2012.
- [6] K. F. Jensen, "Silicon-based microchemical systems: Characteristics and applications," *MRS Bulletin*, vol. 31, no. 2, pp. 101–107, Feb. 2006.
- [7] R. H. Fowler and L. Nordheim, "Electron emission in intense electric fields," *Proc. Roy. Soc. A, Math., Phys. Eng. Sci.*, vol. 119, no. 781, pp. 173–181, 1928.
- [8] M. Meyyappan, Ed., *Carbon Nanotubes: Science and Applications*. Boca Raton, FL, USA: CRC Press, 2005.
- [9] X. Jiang, F. C. K. Au, and S. T. Lee, "Ultrahigh boron doping of nanocrystalline diamond films and their electron field emission characteristics," *J. Appl. Phys.*, vol. 92, no. 5, pp. 2880–2883, Sep. 2002.
- [10] K. Subramanian, W. P. Kang, J. L. Davidson, N. Ghosh, and K. F. Galloway, "A review of recent results on diamond vacuum lateral field emission device operation in radiation environments," *Microelectron. Eng.*, vol. 88, no. 9, pp. 2924–2929, Sep. 2011.
- [11] Y. Zou, P. W. May, S. M. C. Vieira, and N. A. Fox, "Field emission from diamond-coated multiwalled carbon nanotube 'teepee' structures," *J. Appl. Phys.*, vol. 112, no. 4, p. 044903, Aug. 2012.
- [12] D. S. Joag, M. A. More, and F. J. Sheini, "Field emission from nanowires," in *Nanowires—Implementations and Applications*, D. A. Hashim, Ed., 1st ed. Rijeka, Croatia: InTech, 2011.
- [13] J.-M. Bonard *et al.*, "Field emission properties of multiwalled carbon nanotubes," *Ultramicroscopy*, vol. 73, nos. 1–4, pp. 7–15, Jun. 1998.
- [14] P. S. Guo *et al.*, "Fabrication of field emission display prototype utilizing printed carbon nanotubes/nanofibers emitters," *Solid-State Electron.*, vol. 52, no. 6, pp. 877–881, 2008.
- [15] H. Nakahara, Y. Kusano, T. Kono, and Y. Saito, "Evaluations of carbon nanotube field emitters for electron microscopy," *Appl. Surf. Sci.*, vol. 256, no. 4, pp. 1214–1217, 2009.
- [16] S. Taak, S. Rajabali, S. Darbari, and S. Mohajerzadeh, "High sensitive/wide dynamic range, field emission pressure sensor based on fully embedded CNTs," *J. Phys. D, Appl. Phys.*, vol. 47, no. 4, p. 045302, 2014.
- [17] K. Qian *et al.*, "Research on carbon nanotube array field emission pressure sensors," *Electron. Lett.*, vol. 41, no. 14, pp. 824–825, Jul. 2005.
- [18] K. Qian *et al.*, "Studies on vacuum microelectronic pressure sensors based on carbon nanotubes arrays," *Phys. E, Low-Dimensional Syst. Nanostruct.*, vol. 31, no. 1, pp. 1–4, Jan. 2006.
- [19] K. Qian *et al.*, "Simulation and fabrication of carbon nanotubes field emission pressure sensors," *Appl. Surf. Sci.*, vol. 252, no. 12, pp. 4198–4201, Apr. 2006.
- [20] Y. Yang, L. Liu, K. Jiang, and S. Fan, "A vacuum sensor using field emitters made by multiwalled carbon nanotube yarns," *Vacuum*, vol. 86, no. 7, pp. 885–888, 2012.
- [21] R. Knechtel, M. Wiemer, and J. Frömel, "Wafer level encapsulation of microsystems using glass frit bonding," *Microsyst. Technol.*, vol. 12, no. 5, pp. 468–472, 2006.
- [22] C. Jin-Sheng, L. Jing-Yuan, H. Shu-Ching, and L. Yao-Jung, "Wafer level glass frit bonding for MEMS hermetic packaging," in *Proc. 5th Int. Microsyst. Packag. Assembly Circuits Technol. Conf. (IMPACT)*, Oct. 2010, pp. 1–4.
- [23] R. Knechtel, M. Wiemer, and B. Michel, "Special issue on WaferBond'11," *Microsyst. Technol.*, vol. 19, pp. 645–646, May 2013.
- [24] R. Ficek, M. Elias, L. Zajickova, O. Jasek, and R. Vrba, "Gas pressure sensor based on PECVD grown carbon nanotubes," in *Proc. MRS Symp.*, 2007, pp. 169–173.
- [25] R. Ficek, R. Vrba, O. Jasek, M. Elias, L. Zajickova, and H. Hornochova, "Carbon nanostructures in MEMS applications," in *Proc. 3rd Int. Conf. Syst. ICONS*, 2008, pp. 93–96.
- [26] J. Pekárek *et al.*, "Perspective carbon materials as electron emitters," in *Proc. 5th Int. Conf. Nanomater. (NANOCON)*, 2013, pp. 1–5.
- [27] J. Pekárek *et al.*, "Carbon nanotube emitters in sensoric application," in *Proc. 7th Int. Conf. Quantum, Nano Micro Technol. (ICQNM)*, Barcelona, Spain, 2013, pp. 67–70.

- [28] T. de los Arcos *et al.*, "Influence of iron-silicon interaction on the growth of carbon nanotubes produced by chemical vapor deposition," *Appl. Phys. Lett.*, vol. 80, no. 13, pp. 2383-2385, 2002.
- [29] S. Pisana, M. Cantoro, A. Parvez, S. Hofmann, A. C. Ferrari, and J. Robertson, "The role of precursor gases on the surface restructuring of catalyst films during carbon nanotube growth," *Phys. E, Low-Dimensional Syst. Nanostruct.*, vol. 37, nos. 1-2, pp. 1-5, 2007.
- [30] T. de los Arcos *et al.*, "Strong influence of buffer layer type on carbon nanotube characteristics," *Carbon*, vol. 42, no. 1, pp. 187-190, 2004.
- [31] L. Zajickova *et al.*, "Synthesis of carbon nanotubes by plasma-enhanced chemical vapor deposition in an atmospheric-pressure microwave torch," *Pure Appl. Chem.*, vol. 82, no. 6, pp. 1259-1272, Jun. 2010.
- [32] O. Jasek, P. Synek, L. Zajickova, M. Elias, and V. Kudrle, "Synthesis of carbon nanostructures by plasma enhanced chemical vapour deposition at atmospheric pressure," *J. Elect. Eng.*, vol. 61, pp. 311-313, Sep./Oct. 2010.
- [33] K. E. Petersen, "Silicon as a mechanical material," *Proc. IEEE*, vol. 70, no. 5, pp. 420-457, May 1982.
- [34] C. Y. Cheng, M. Nakashima, and K. Teii, "Low threshold field emission from nanocrystalline diamond/carbon nanowall composite films," *Diamond Rel. Mater.*, vols. 27-28, pp. 40-44, Jul./Aug. 2012.
- [35] Z. Li, W. Wang, D. Shaozhi, and X. Ningsheng, "Field electron emission of nanorods of semiconductors of wide energy band gaps," in *18th Int. Vac. Nanoelectron. Conf. Tech. Dig. (IVNC)*, Jul. 2005, pp. 9-10.
- [36] J. P. Barbour, W. W. Dolan, J. K. Trolan, E. E. Martin, and W. P. Dyke, "Space-charge effects in field emission," *Phys. Rev.*, vol. 92, no. 1, pp. 45-51, 1953.
- [37] K. A. Dean and B. R. Chalamala, "Current saturation mechanisms in carbon nanotube field emitters," *Appl. Phys. Lett.*, vol. 76, no. 3, pp. 375-377, 2000.
- [38] C. Bingqiang, C. Weiping, D. Guotao, L. Yue, Z. Qing, and Y. Dapeng, "A template-free electrochemical deposition route to ZnO nanoneedle arrays and their optical and field emission properties," *Nanotechnology*, vol. 16, no. 11, p. 2567, 2005.
- [39] P. W. May, S. Hohn, W. N. Wang, and N. A. Fox, "Field emission conduction mechanisms in chemical vapor deposited diamond and diamondlike carbon films," *Appl. Phys. Lett.*, vol. 72, no. 17, pp. 2182-2184, Apr. 1998.
- [40] G. Eda, H. E. Unalan, N. Rupasinghe, G. A. J. Amaratunga, and M. Chhowalla, "Field emission from graphene based composite thin films," *Appl. Phys. Lett.*, vol. 93, no. 23, p. 233502, 2008.
- [41] A. N. Obratsov, A. A. Zakhidov, A. P. Volkov, and D. A. Lyashenko, "Non-classical electron field emission from carbon materials," *Diamond Rel. Mater.*, vol. 12, nos. 3-7, pp. 446-449, Mar./Jul. 2003.
- [42] X. Xu and G. R. Brandes, "A method for fabricating large-area, patterned, carbon nanotube field emitters," *Appl. Phys. Lett.*, vol. 74, no. 17, pp. 2549-2551, 1999.
- [43] A. Buldum and J. P. Lu, "Electron field emission properties of closed carbon nanotubes," *Phys. Rev. Lett.*, vol. 91, no. 23, p. 236801, 2003.
- [44] S. Han, M. H. Lee, and J. Ihm, "Dynamical simulation of field emission in nanostructures," *Phys. Rev. B*, vol. 65, no. 8, p. 085405, 2002.
- [45] P. G. Collins and A. Zettl, "Unique characteristics of cold cathode carbon-nanotube-matrix field emitters," *Phys. Rev. B*, vol. 55, no. 15, pp. 9391-9399, 1997.
- [46] M. Shiraishi and M. Ata, "Work function of carbon nanotubes," *Carbon*, vol. 39, no. 12, pp. 1913-1917, 2001.



**Jan Pekarek** was born in Ostrava, Czech Republic, in 1984. He received the B.S. and M.S. degrees in electrical engineering from the Brno University of Technology, Brno, Czech Republic, in 2006 and 2008, respectively, where he is currently pursuing the Ph.D. degree in microelectronics and technology. His current research interests include development and fabrication of devices based on micro or nanostructured surfaces.



**Radimir Vrba** was born in Brno, Czech Republic, in 1950. He received the Ph.D. degree in measurement from the Brno University of Technology, Brno, in 1979, where he was the Dean of the Faculty of Electrical Engineering and Communication from 2002 to 2010. Since 2009, he has been the Director of the Central European Institute of Technology, Brno University of Technology. His research and professional activities are concentrated on new circuits for signal processing, development of new applications of electronic and microelectronic circuits, including microsystems and microsensors, smart sensors, and embedded systems.



**Jan Prasek** was born in Blansko, Czech Republic, in 1976. He received the Ph.D. degree in microelectronics from the Brno University of Technology, Brno, Czech Republic, in 2007, where he is currently a Junior Scientist with the Central European Institute of Technology. His research interests include electrochemical sensors and semiconducting metal oxide gas sensors using various nanomaterials for active layers fabrication. He has authored or co-authored 38 ISI-indexed peer-reviewed articles or book chapters.



31 publications with 112 citations, and an H-index of 7.

**Ondrej Jasek** was born in Bruntal, Czech Republic, in 1975. He received the M.S. degree in physics and the Ph.D. degree in plasma physics from Masaryk University, Brno, Czech Republic, in 1998 and 2005, respectively, where he is currently a Junior Scientist with the Central European Institute of Technology and the Faculty of Science. His current research interests include the synthesis, characterization, and applications of carbon nanotubes, grapheme, and various forms of nanocrystalline iron oxides. He has authored or co-authored



**Petra Majzlikova** was born in Moravska Trebova, Czech Republic, in 1981. She received the B.S. and M.S. degrees in physical and applied chemistry from the Brno University of Technology, Brno, Czech Republic, in 2003 and 2005, respectively, where she is currently pursuing the Ph.D. degree in physical chemistry. Her research interests include synthesis and characterization of various nanoparticles for sensing and biosensing applications, electrochemical sensors, and electrochemical analysis.



**Jana Pekarkova** was born in Brno, Czech Republic, in 1981. She received the Ph.D. degree in physical chemistry from the Brno University of Technology, Brno, in 2008, where she is currently a Junior Scientist with the Central European Institute of Technology. Her current research interests include synthesis of various types of nanoparticles, including paramagnetic particles and quantum dots. She has authored or co-authored 25 peer-reviewed articles and four book chapters.



**Lenka Zajickova** was born in Brno, Czech Republic, in 1971. She received the Ph.D. degree in plasma physics from Masaryk University, Brno, in 1999, where she has been an Associate Professor with the Department of Physical Electronics, Faculty of Science since 2009. In 2011, she was appointed as the Leader of the RG Plasma Technologies of Central European Institute of Technology, Masaryk University. Her current research interests include the plasma deposition of thin films-based organosilicons and carbon nanoparticles, plasma modification of surfaces, and diagnostics of plasma. She has authored or co-authored 78 ISI-indexed publications with 657 citations, and an H-index of 15.

## Příloha 4

SVATOŠ, V. et al. In situ observation of carbon nanotube layer growth on microbolometers with substrates at ambient temperature. *Journal of Applied Physics*, 2018, vol. 123, no. 11. ISSN 1089-7550.

### ABSTRAKT

Uhlíkové nanotrubic mají téměř 100% absorpci v infračervené oblasti spektra, což je činí extrémně atraktivní pro infračervené zobrazovací zařízení. Vzhledem k tomu, že růst uhlíkových nanotubic nastává při vysokých teplotách, je jejich integrace s infračervenými zobrazovacími zařízeními náročná a dosud nebyla dosažena. Představujeme metodu implementace uhlíkových nanotubic jako infračerveného absorbéru za použití ohřevu tepelně izolovaných mikrobolometrických membrán v prostředí  $C_2H_2$ . Během procesu byly katalyticky deponovány uhlíkové nanotrubic na povrchu lokálně vyhřívané membrány, zatímco substrát zůstal při pokojové teplotě. Růst uhlíkových nanotubic byl monitorován v reálném čase za použití optické mikroskopie. Během růstu jsme změřili intenzitu emise světla a odraženého světla ze zahřátého mikrobolometru. Naše měření výkonu mikrobolometru ukazuje, že vrstva uhlíkových nanotubic na povrchu membrány mikrobolometru zvyšuje odezvu na infračervené záření zhruba 2,3×. Tato práce otevírá možnosti integrace uhlíkových nanotubic jako vynikajícího absorbéru v infračervené oblasti i v zařízeních, která jsou vyrobená v technologii komplementární kov-oxid-polovodič (CMOS).

# *In situ* observation of carbon nanotube layer growth on microbolometers with substrates at ambient temperature F

Cite as: J. Appl. Phys. **123**, 114503 (2018); <https://doi.org/10.1063/1.5016465>

Submitted: 20 November 2017 . Accepted: 01 March 2018 . Published Online: 20 March 2018

Vojtěch Svatoš, Imrich Gablech, B. Robert Ilic , Jan Pekárek, and Pavel Neuzil

## COLLECTIONS

F This paper was selected as Featured



View Online



Export Citation



CrossMark

## ARTICLES YOU MAY BE INTERESTED IN

[Visible-blind and solar-blind detection induced by defects in AlGaIn high electron mobility transistors](#)

Journal of Applied Physics **123**, 114502 (2018); <https://doi.org/10.1063/1.4997605>

[Carbon nanotube-based black coatings](#)

Applied Physics Reviews **5**, 011103 (2018); <https://doi.org/10.1063/1.5009190>

[“Negative capacitance” in resistor-ferroelectric and ferroelectric-dielectric networks: Apparent or intrinsic?](#)

Journal of Applied Physics **123**, 105102 (2018); <https://doi.org/10.1063/1.5016152>

### Ultra High Performance SDD Detectors



See all our XRF Solutions

## **In situ observation of carbon nanotube layer growth on microbolometers with substrates at ambient temperature**

Vojtěch Svatoš,<sup>1</sup> Imrich Gablech,<sup>1</sup> B. Robert Ilic,<sup>2</sup> Jan Pekárek,<sup>1</sup> and Pavel Neužil<sup>1,3</sup>

<sup>1</sup>Brno University of Technology, Technická 3058/10, 616 00 Brno, Czech Republic

<sup>2</sup>Center for Nanoscale Science and Technology, National Institute of Standards and Technology, Gaithersburg, Maryland 20899, USA

<sup>3</sup>Northwestern Polytechnical University, 127 West Youyi Road, Xi'an, Shaanxi, People's Republic of China

(Received 20 November 2017; accepted 1 March 2018; published online 20 March 2018)

Carbon nanotubes (CNTs) have near unity infrared (IR) absorption efficiency, making them extremely attractive for IR imaging devices. Since CNT growth occurs at elevated temperatures, the integration of CNTs with IR imaging devices is challenging and has not yet been achieved. Here, we show a strategy for implementing CNTs as IR absorbers using differential heating of thermally isolated microbolometer membranes in a C<sub>2</sub>H<sub>2</sub> environment. During the process, CNTs were catalytically grown on the surface of a locally heated membrane, while the substrate was maintained at an ambient temperature. CNT growth was monitored *in situ* in real time using optical microscopy. During growth, we measured the intensity of light emission and the reflected light from the heated microbolometer. Our measurements of bolometer performance show that the CNT layer on the surface of the microbolometer membrane increases the IR response by a factor of (2.3 ± 0.1) (mean ± one standard deviation of the least-squares fit parameters). This work opens the door to integrating near unity IR absorption, CNT-based, IR absorbers with hybrid complementary metal-oxide-semiconductor focal plane array architectures. *Published by AIP Publishing.*

<https://doi.org/10.1063/1.5016465>

### **INTRODUCTION**

Infrared (IR) imaging in the wavelength range from 8 μm to 14 μm, also known as thermal imaging, has found widespread applications spanning disparate fields of engineering and life and physical sciences. Room-temperature and cooled thermal imagers have been used in preventive maintenance, night vision, medical imaging, security, and space applications.<sup>1</sup> Heat sensing, uncooled microbolometers<sup>2</sup> in the form of focal plane arrays (FPAs) represent a class of integrated, two-dimensional ensemble thermal detector arrays with multiplexed readout. In contrast to cryogenically cooled devices, uncooled IR microbolometers have numerous advantages including higher reliability, reduced power consumption and smaller physical dimensions. Modern microbolometer devices, operating at room temperature, are based on thermally isolated membrane architectures with integrated temperature sensors. The incident radiation, absorbed as heat, increases the temperature of the microbolometer membrane. The temperature change ( $\Delta T_{\text{IR}}$ ), proportional to the power of incident radiation ( $P_{\text{IR}}$ ), is given by

$$\Delta T_{\text{IR}} = \frac{P_{\text{IR}}}{G}, \quad (1)$$

where  $G$  is the thermal conductance of the microbolometer.

The FPA imagers are mass produced using Si-based complementary metal-oxide-semiconductor (CMOS) architectures. The imager consists of an array of pixels, with each pixel connected to a read-out integrated circuit. The microbolometer pixels are created using microelectromechanical system (MEMS) technology. The microbolometer membranes are typically made from various CMOS-compatible

materials such as silicon dioxide (SiO<sub>2</sub>), silicon nitride, amorphous Si and SiGe. Mid-IR absorption ( $\eta$ ), in the range of interest from 8 μm to 14 μm of these materials, depends on the film thickness and composition. For instance,  $\eta$  for SiO<sub>2</sub> with a thickness of ≈0.6 μm ranges from ≈35% (Ref. 3) to ≈48%.<sup>4</sup> The key challenge is then to maximize  $\eta$ , while using a CMOS compatible process. Several developed strategies to increase  $\eta$  suffer from a significant increase in processing costs and complexity.

The first reported IR absorbing carbon nanotube (CNT) layer was implemented on the surface of a pyroelectric detector<sup>5</sup> sparking an interest in CNTs as an electromagnetic radiation absorber.<sup>6,7</sup> Controlled placement of vertically aligned CNT layers requires growth in a chemical vapor deposition (CVD) reactor at elevated temperatures above 550 °C,<sup>8</sup> using lithographically patterned catalytic materials.<sup>9</sup> The highest temperature that CMOS devices can withstand is typically below 475 °C. This value represents the eutectic temperature of the commonly used Al-Si contacts in CMOS chips. Modern CMOS devices with titanium silicide, tantalum nitride, nickel silicide<sup>10</sup> and other barrier materials between aluminum and silicon can be heated to higher temperatures. Nevertheless, exposing the CMOS chips to a temperature of 550 °C required for CNT growth is undesirable, thereby making the CNT growth on the surface of CMOS chips a major integration challenge. Shulaker *et al.*<sup>11</sup> showed a complex, thermal release tape process for transferring CNTs from one substrate to another. This method is not suitable for mechanically suspended devices such as MEMS-based microbolometer FPAs.

Here, we demonstrate a spatially localized Joule heating technique, warming up only the bolometer membrane, for

Fe-based catalytic CNT growth on the surface of the bolometer membrane, while the rest of the substrate remains at room temperature. This method enables the integration of a highly efficient, IR-absorbing CNT layer into existing monolithic CMOS FPA imagers.

## RESULTS AND DISCUSSION

### Microbolometer design and fabrication

Using the Nanolithography Toolbox,<sup>12</sup> we designed  $40\ \mu\text{m} \times 40\ \mu\text{m}$  microbolometer membranes<sup>4</sup> using a fabrication flow outlined in Fig. 1. Microbolometers, with an embedded Ti resistive temperature detector (RTD) and a Fe layer for catalytic CNT growth, were fabricated using conventional Si bulk-micromachining techniques. Prior to membrane release, we measured the RTD resistance and the temperature coefficient of resistance ( $\alpha$ ) using a probe station with a heated wafer chuck. The corresponding measured ambient temperature resistance ( $R_0$ ) and  $\alpha$  values were  $(7.726 \pm 0.250)\ \text{k}\Omega$  and  $(0.53 \pm 0.01)\ \text{m}\ \text{K}^{-1}$ , both representing the measured mean  $\pm$  standard deviation, respectively. The experimental procedure and uncertainties are described

in the [supplementary material](#) section 1. Membranes were then released by removing the underlying Si using  $\text{XeF}_2$  vapors. Subsequently, CNT growth was carried out on individual chips.

### Microbolometer characterization

Following membrane release, microbolometer chips were mounted onto a leadless chip carrier with 68 pads and electrically connected with gold wires using wire-bonding. Packaged bolometer devices were then placed into a vacuum chamber with a Ge window. Using a method described by Gu *et al.*,<sup>13</sup> at a pressure of  $\approx 7.7 \times 10^{-4}\ \text{Pa}$  and an applied voltage amplitude ( $V_b$ ) of  $\approx 0.6\ \text{V}$  with known values of  $R_0$  and  $\alpha$ , we determined the thermal capacitance ( $H$ ),  $G$  and the thermal time constant ( $\tau = H/G$ ). Our measurements over three sets of bolometer devices show  $H = (3.113 \pm 0.009)\ \text{nJ}\cdot\text{K}^{-1}$ ,  $G = (160.9 \pm 2.7)\ \text{nW}\cdot\text{K}^{-1}$  and  $\tau = (19.35 \pm 0.34)\ \text{ms}$  (mean  $\pm$  standard deviation). The experimental procedure and uncertainties are described in the [supplementary material](#) section 2. At a constant pressure of  $\leq 5\ \text{Pa}$  and ambient temperature of  $\approx 25\ ^\circ\text{C}$ , the convective heat transfer and

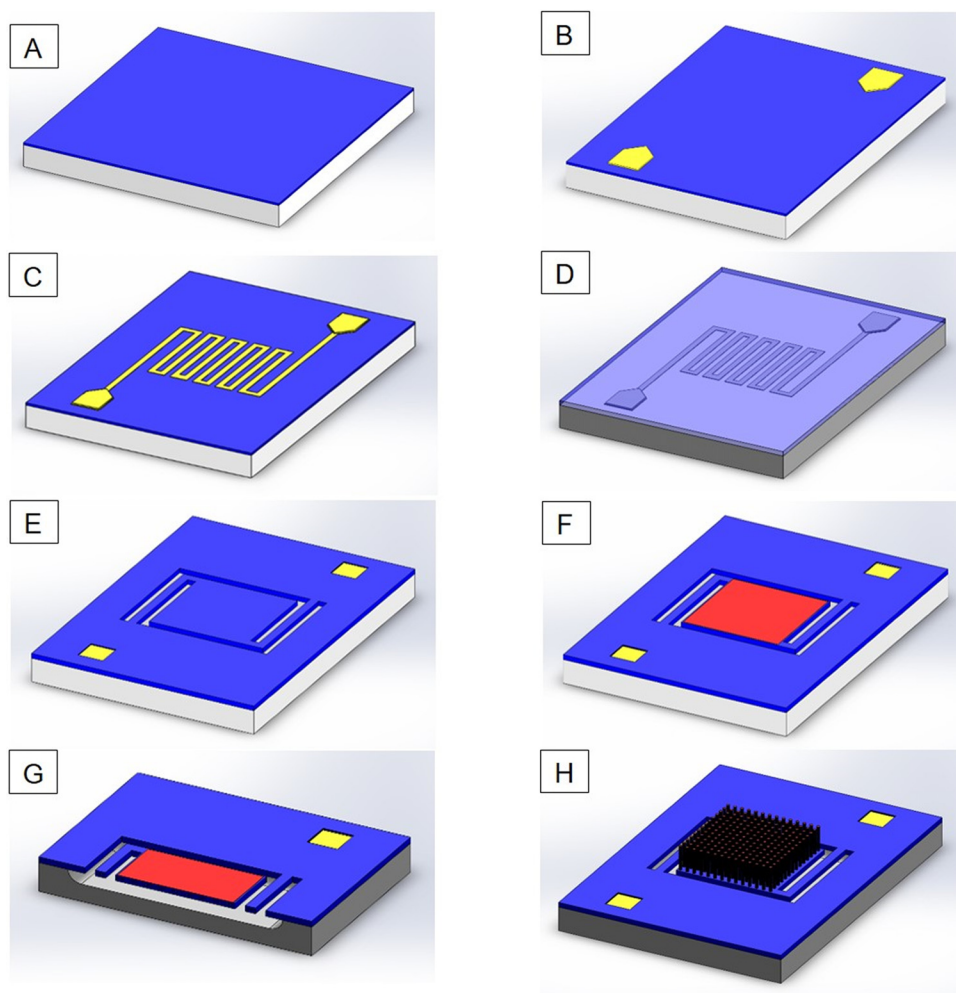


FIG. 1. Fabrication process flow of the MEMS based microbolometer. (a) Deposition of  $\approx 0.25\ \mu\text{m}$  plasma enhanced CVD (PECVD)  $\text{SiO}_2$  on the Si substrate. (b) Lithographic definition of  $\approx 0.9\ \mu\text{m}$  thick Al bond pads. (c)  $\approx 30\ \text{nm}$  sputter deposited Ti temperature sensor definition using optical lithography and reactive ion etching. (d) Deposition of  $\approx 0.25\ \mu\text{m}$  PECVD  $\text{SiO}_2$  for the protection of metal layers. (e)  $\text{SiO}_2$  patterning to create access to bonding pads and etch holes for the microbolometer membrane release. (f) Deposition of the catalytic Fe layer using a photoresist lift-off process. (g) Cross-section of a microbolometer chip following microbolometer membrane release using  $\text{XeF}_2$  vapors. (h) Catalytic CNT growth on the surface of the membrane.

radiation loss are negligible and consequently,  $G$  is solely determined by the thermal conduction of the microbolometer legs ( $P_C$ ).<sup>14</sup> Once the microbolometer membrane warms up by the dissipated Joule heat ( $P_J$ ), the radiation heat loss ( $P_R$ ), based on the Stefan-Boltzmann law, cannot be neglected. The amplitude of  $P_J$ , distributed between  $P_R$  and  $P_C$ , is given by

$$P_J = P_R + P_C = A \cdot \varepsilon \cdot \sigma \cdot T^4 + G \cdot \Delta T, \quad (2)$$

where  $A=2 \cdot a^2$  is the top and bottom areas of the square microbolometer membrane of length  $a$ ,  $\varepsilon$  is the emissivity of the microbolometer membrane,  $\sigma$  is the Stefan-Boltzmann constant,  $T$  is the thermodynamic temperature, and  $\Delta T$  is the temperature difference between the microbolometer membrane and the substrate chip. We measured the bolometer response to a square wave pulse<sup>13</sup> over a range of  $V_b$  values [Fig. S4(a) in [supplementary material](#) section 3]. In the vicinity of  $V_b=0$ , where self-heating effects are neglected, our calculations show  $G=(180.4 \pm 1.2) \text{ nW} \cdot \text{K}^{-1}$ ,  $H=(3.602 \pm 0.024) \text{ nJ} \cdot \text{K}^{-1}$  and  $\tau=(19.96 \pm 0.02) \text{ ms}$  (all are mean  $\pm$  fitting error). Here and below, the fitting error corresponds to one standard deviation of the least-squares fit parameters. The values are in good agreement with the ones determined at  $V_b \approx 0.6 \text{ V}$ . Collectively, these data show that self-heating plays a minor role in the bolometer performance.

### Monitoring of CNT growth

The packaged bolometer devices were then placed into a vacuum chamber equipped with a glass window, tubes for gas and vacuum connections, and an electrical feedthrough, as schematically shown in Fig. 2(a). The chamber was then placed under an optical microscope equipped with  $\approx 9 \text{ mm}$  working distance,  $50\times$  objective with a numerical aperture (NA) of 0.55. The  $\approx 7 \text{ mm}$  distance between the bolometer membrane and the glass window allowed for high-resolution, *in situ* observation of the subsequent CNT growth

processes. Thermal conditioning of the catalytic layer was accomplished by heating the microbolometer using  $P_J \approx 200 \mu\text{W}$  in the  $5\% \text{ H}_2 + 95\% \text{ N}_2$  forming gas (FG) environment for  $\approx 15 \text{ min}$ . To determine the Joule heat threshold required for growth, we increased  $P_J$  until the onset of CNT growth. Further increase in  $P_J$  revealed an upper limit of  $750 \mu\text{W}$  above which the bolometer membrane was physically damaged from the excessive power dissipation. To circumvent the membrane damage,  $P_J$  was set to  $650 \mu\text{W}$ . Using a closed-loop feedback configuration,  $P_J$  was maintained by the controlling voltage  $V_{\text{BOL}}$ , while measuring the current  $I_{\text{BOL}}$  through the microbolometer resistor. During CNT growth, we maintained a chamber pressure of  $\approx 5 \text{ Pa}$  by adjusting the partial pressures of individual gases at  $\approx 1.5 \text{ Pa}$  and  $\approx 3.5 \text{ Pa}$  for FG and  $\text{C}_2\text{H}_2$ , respectively. Under the above conditions, the CNT thickness was controlled by growth time. Following CNT growth, surface passivation was not carried out. Figures 2(b) and 2(c) show optical micrographs of the microbolometer membrane before and after growth, at  $\approx 65\%$  of the field of view, respectively. A typical microbolometer membrane with grown CNTs is shown in Figs. 3(a) and 3(b). A video [Fig. 2(d)] (Multimedia view) shows real time CNT growth on the surface of the bolometer membrane.

We used finite element modelling (FEM) to show the temperature distribution within the thermally isolated membrane and the surrounding substrate. For the computation, we considered a silicon volume of  $160 \mu\text{m} \times 180 \mu\text{m} \times 75 \mu\text{m}$  with a suspended bolometer membrane and materials of dimensions resembling the fabricated devices. We used 20-node thermal solid elements for the Si substrate and 10-node tetrahedral thermal solid elements for Ti and  $\text{SiO}_2$  layers. The initial boundary condition for the Si substrate was set to  $25^\circ\text{C}$ . Directly following this, we applied a voltage of  $0.8 \text{ V}$  between the ends of the two Ti metal traces. The FEM results [Figs. 3(c) and 3(d)] show heat concentration within the

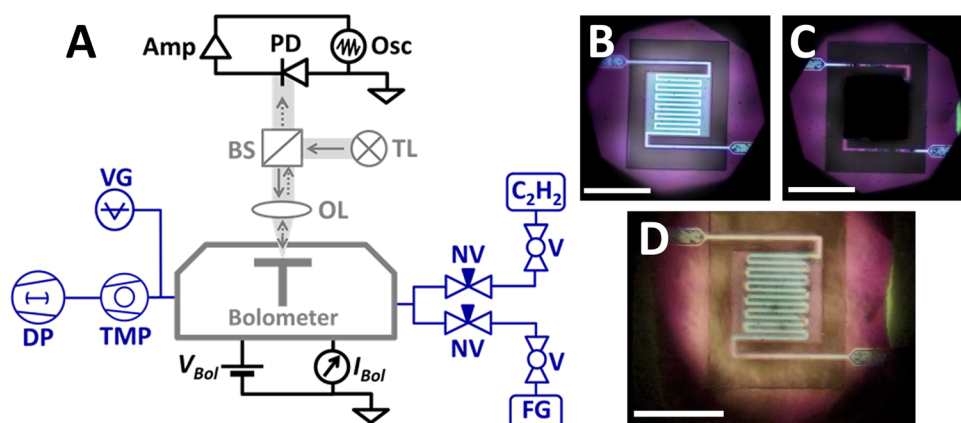


FIG. 2. (a) Schematic illustration of the experimental setup. The microbolometer was placed into a vacuum chamber with an inlet for gas delivery and a pumping port. Gas flow was controlled by needle valves (NV). Chamber evacuation was accomplished using a combination of a turbo molecular pump (TMP) with a backing dry vacuum pump (DP). Using an optical microscope with a  $50\times$  objective lens (OL), the optical window flange allowed for real-time monitoring of the CNT growth process. Reflectance measurements during CNT growth were accomplished using a tungsten lamp (TL) in conjunction with a beam splitter (BS) to illuminate the microbolometer membrane. Emission and reflection during CNT growth were measured using a silicon photodiode (PD). The  $I_p$  was converted to a voltage using a current preamplifier (Amp) that was monitored using an oscilloscope (Osc). The  $P_J$  amplitude dissipated in the microbolometer membrane was set using a closed-loop feedback system by controlling the amplitude of  $V_{\text{BOL}}$  while measuring  $I_{\text{BOL}}$  and keeping the  $P_J$  at a predetermined value. Optical micrographs of a microbolometer (b) before and (c) after the CNT growth. The scale bars in (b), (c) and (d) represent a length of  $\approx 40 \mu\text{m}$ . (d) A video showing the real-time CNT growth at the bolometer membrane captured with a microscope equipped with a  $50\times$  objective lens. Multimedia view: <https://doi.org/10.1063/1.5016465.1>

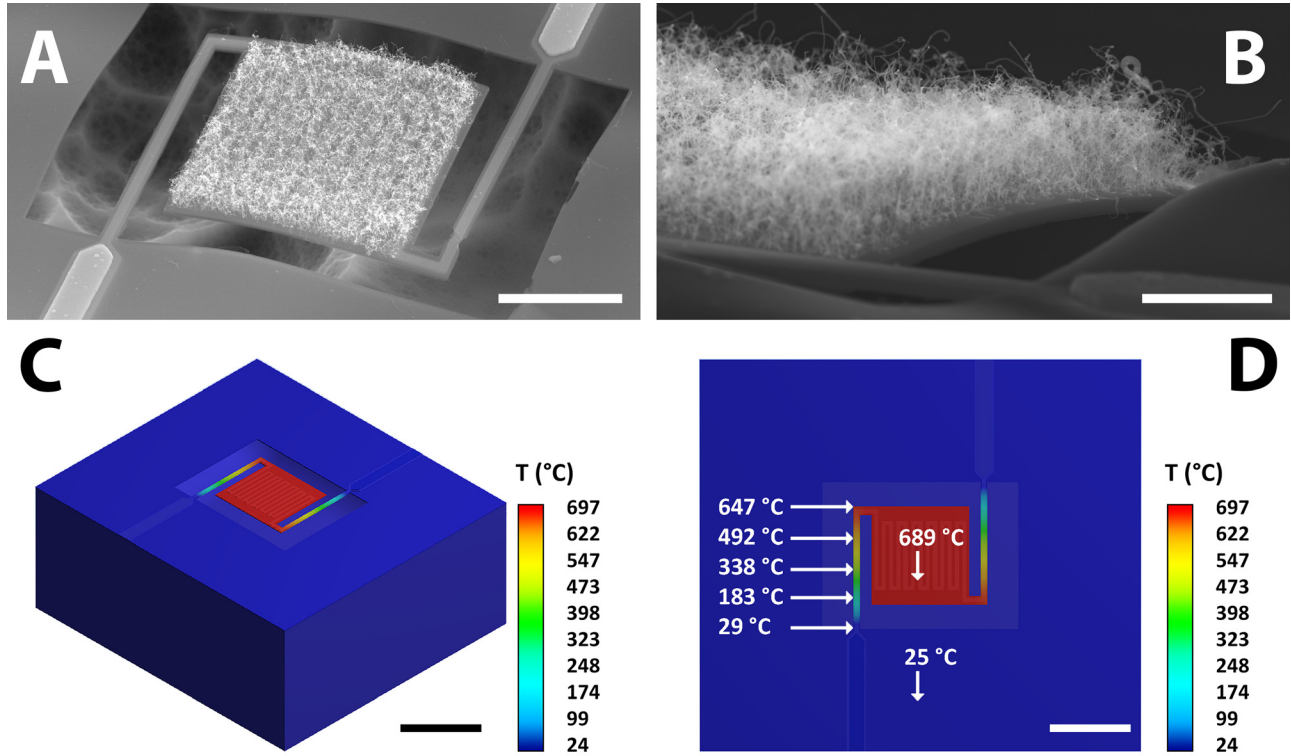


FIG. 3. Scanning electron micrographs of a fabricated microbolometer showing (a) a thermally isolated, undercut microbolometer membrane following CNT layer growth. (b) Zoomed-in view of the CNTs near the membrane edge. The scale bars in (a) and (b) represent the lengths of  $\approx 20 \mu\text{m}$  and  $\approx 5 \mu\text{m}$ , respectively. FEM analysis with (c) perspective and (d) top-down views of the temperature distribution within the structure. The heat is localized within the suspended, membrane region with the surrounding Si substrate at  $25^\circ\text{C}$ . The scale bars in (c) and (d) represent lengths of  $\approx 40 \mu\text{m}$ . The annotations in (D) represent temperatures at various locations, denoted by the corresponding arrows, along the structure.

suspended membrane with the substrate at approximately room temperature.

The measured photocurrent ( $I_p$ ) from the silicon photodiode during the CNT growth was related to the emitted radiation from the heated membrane [Fig. 4(a), [supplementary material](#) section 5]. During the measurements, the microscope light source was turned off.  $I_p$  was converted into a voltage ( $V_p$ ) using a current preamplifier with an active low-pass filter. The amplitude of  $V_p$  was monitored using an oscilloscope.  $I_p$  as a function of time ( $t$ ) during the growth phase, initiating at  $t \approx 112$  s, can be approximated by a first order exponential decay in combination with a linear decay

$$I_p = I_0 + I_1 \cdot e^{-\frac{t-t_0}{\tau_e}} + I_2 \cdot t, \quad (3)$$

where  $I_0$  is the steady state photocurrent offset,  $I_1$  is the maximum photocurrent,  $t_0$  is the time at the onset of amplitude decay [ $\approx 112$  s in Fig. 4(a)],  $\tau_e$  is the emission time constant, and  $I_2$  is the coefficient of linear  $I_p$  decay. Our measurements show values of  $\tau_e = (34.91 \pm 1.26)$  s and  $I_2 = (-15.94 \pm 2.02)$   $\text{fA} \cdot \text{s}^{-1}$ , both values are mean  $\pm$  one standard deviation measured from 3 devices [Fig. 4(a)]. The uncertainties are calculated from the functional fitting error using Eq. (3). Details of the measurement results are in the [supplementary material](#) section 4. The value of  $\tau_e$  can serve as a guide to minimize the CNT growth time with a saturated absorbance value.

Since the amplitude of  $I_p$  is proportional to  $P_J$ , the exponential decay of the  $I_p$  as a function of  $t$  can be derived from

Eq. (2), while accounting for the geometric change of the radiation emitting area during CNT growth. The  $G$  value of a microbolometer is determined by the cross-sectional areas, length and thermal conductivity of the two microbolometer legs. Since the CNT layer was grown from the lithographically defined catalyst spanning the square shaped microbolometer membrane with an area of  $A$  [see Figs. 1(g) and 1(h)], the value of  $G$  remains constant during CNT growth.

During the growth, since  $P_J$  was held constant at  $\approx 650 \mu\text{W}$ , the terms  $A$  and  $G$  in Eq. (2) can be also considered as constant. Consequently, the CNT layer on the surface of the membrane increased  $\varepsilon$  and decreased  $T$ . With increasing  $\varepsilon$ , the membrane emits radiation in all directions thereby lowering the temperature. Consequently, the power emitted per unit area of the microbolometer membrane decreases ([supplementary material](#) section 5). Measured resistance during the CNT growth allowed a qualitative determination of the microbolometer temperature change  $\Delta T$

$$R_b = \frac{V_{\text{BOL}}}{I_{\text{BOL}}}; \quad R_b = R_0(1 + \alpha \cdot \Delta T); \quad \text{and} \quad (4)$$

$$\Delta T = \frac{1}{\alpha} \left( \frac{V_{\text{BOL}}^2}{P_J \cdot R_0} - 1 \right),$$

where  $R_0$  and  $\alpha$  are the corresponding ambient resistance at  $T \approx 298$  K and the temperature coefficient of resistance of the temperature sensor, respectively. The  $\Delta T$  amplitude dropped once  $P_J$  reached an amplitude of  $\approx 650 \mu\text{W}$  at the onset of CNT growth.

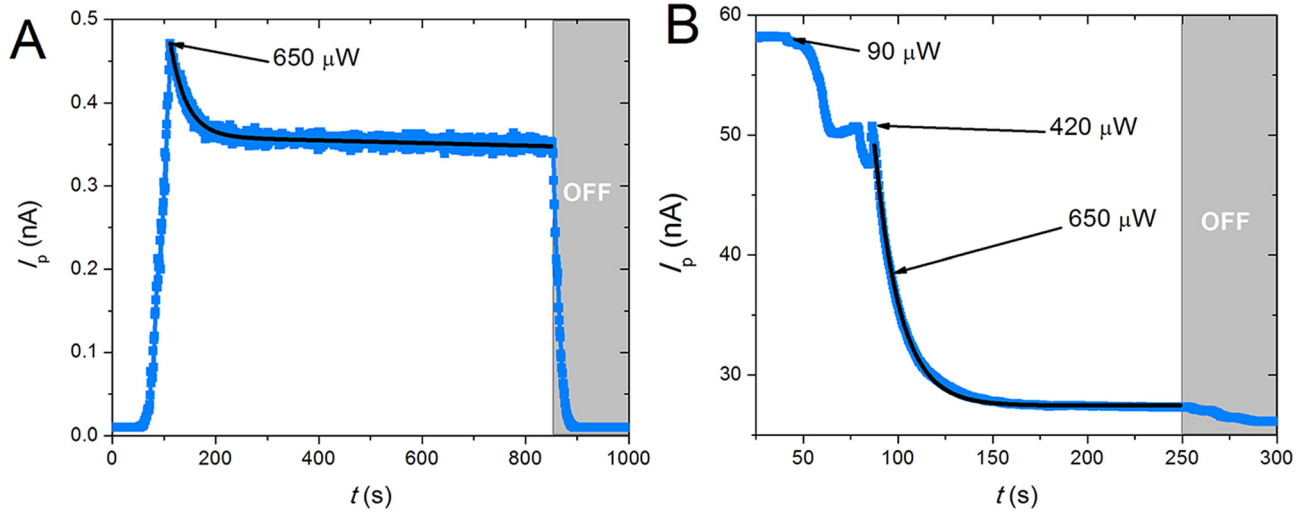


FIG. 4. (a) Typical optical emission from the microbolometer membrane as a function of  $t$  during CNT growth.  $P_J$  was gradually increased at a rate of  $\approx 8 \mu\text{W}\cdot\text{s}^{-1}$  up to  $650 \mu\text{W}$ . At  $t \approx 53$  s, we observed light emission from the membrane. CNT growth, initiating at  $t \approx 112$  s with  $P_J \approx 650 \mu\text{W}$ , increased the microbolometer emissivity and thereby lowered the microbolometer membrane temperature. At  $t \approx 850$  s, heating was switched off ( $P_J = 0$ ) and the CNT growth ceased. Directly following this, the light emission quickly decayed to zero. We determined the value of  $\tau_e$  using Eq. (3) as  $(32.03 \pm 0.82)$  s (mean  $\pm$  fitting error). The solid line represents a first-order exponential decay functional fit. (b) Under similar conditions, we measured the optical reflection from the microbolometer. At  $t \approx 40$  s, an increase from a steady state of  $P_J \approx 90 \mu\text{W}$  caused the membrane reflectivity to drop. The CNT growth initiated at  $t \approx 86.5$  s with  $P_J \approx 420 \mu\text{W}$ . The newly grown CNT layer lowered the membrane reflection with a time constant  $\tau_r = (13.44 \pm 0.07)$  s (mean  $\pm$  fitting error). The maximum  $P_J \approx 650 \mu\text{W}$  occurred at  $t \approx 96$  s. At  $t \approx 250$  s, the heating was switched off, following which the reflection amplitude changed marginally. The solid line represents a first-order exponential decay functional fit.

Above, we assumed a negligible emission contribution from the membrane sidewalls and considered the source of emission solely from  $A$ . However, during CNT growth, the total surface area as a function of the CNT layer thickness ( $t_c$ ) increases by a factor of  $4 \cdot a \cdot t_c$  (supplementary material section 6), while the sidewall emission increases with  $t_c$ . This increase is not negligible and consequently, results in a decrease of  $I_p$  at a rate of  $(-15.70 \pm 1.38)$   $\text{fA}\cdot\text{s}^{-1}$  (mean  $\pm$  fitting error) [Fig. 4(a)].

Using a  $\approx 100$  W tungsten lamp, we illuminated the bolometer membrane and measured the reflectance during CNT growth [Fig. 4(b) and supplementary material section 7]. The dynamics of the reflection-based experiment differed from the emissivity measurement. Once the CNT growth is initiated at  $P_J \approx 420 \mu\text{W}$ , the amplitude of light reflected from the membrane decreased following an exponential decay of the first order with time constant  $\tau_r = (13.44 \pm 0.07)$  s (mean  $\pm$  one standard deviation from 3 devices). The faster  $\tau_r$ , in comparison with  $\tau_e$ , shows that the related reflection from the membrane in the visible spectrum of electromagnetic radiation is sensitive to small changes in surface properties, whereas a much thicker layer of CNTs is required to cause significant changes to  $\tau_e$ .<sup>6</sup>

Inserting the parameters obtained from the above microbolometer characterization into Eq. (2) allowed us to calculate the amplitude of  $P_J$  as a function temperature, without the CNT layer and for various CNT thickness values of up to  $30 \mu\text{m}$  [Fig. 5(a)]. In our calculations, we used  $\varepsilon_{\text{SiO}_2} = 0.48$  and  $\varepsilon_{\text{CNT}} = 1$  for the emissivity of membranes without<sup>4</sup> and with<sup>11,15</sup> CNTs, respectively. Furthermore, the area of the CNT membrane was  $A = 2 \cdot a^2 + 4 \cdot a \cdot t_c$  (see supplementary material section 6). The results in Fig. 5(a) show that the  $P_J$  amplitude required to heat up the bolometer membrane

without and with the CNT layer to the same value of  $T$  increases with increasing thickness of the CNT layer.

We then calculated the power of emitted radiation  $P_{\text{ER}} = b \cdot \varepsilon \cdot \sigma \cdot T^4$  from a  $1 \mu\text{m}^2$  area ( $b$ ) of the bolometer membrane without CNTs and for various CNT layer thicknesses. Figure 5(b) shows a significant emission dependence with respect to the CNT layer thickness.

Experimental data in Fig. 6 show that membranes with CNTs are cooler and emit  $\approx 0.23$  of the power emitted by membranes without CNTs. Our results further show that the CNT layers increased the value of thermal capacitance  $H$  by a factor  $\approx 5$ , to  $(14.83 \pm 0.53)$   $\text{nJ}\cdot\text{K}^{-1}$  (mean  $\pm$  standard deviation, 3 measurements).

### CNT layer performance

We placed the bolometer, connected in a balanced Wheatstone bridge configuration, into a vacuum chamber and evaluated the  $P_{\text{IR}}$  response. The amplitude of  $P_{\text{IR}}$  was controlled by the distance ( $D$ ) between the black body at  $T \approx 673.15$  K and the bolometer from  $D \approx (59.5, 74.5, 89.5, 104.5, \text{ and } 119.5)$  mm. The  $P_{\text{IR}}$  was estimated using the equation<sup>4</sup>

$$P_{\text{IR}} = a^2 \cdot \varepsilon_{\text{bb}} \cdot \tau_{\text{F}} \cdot M \left[ \frac{\left(\frac{d}{2}\right)^2}{D^2 + \left(\frac{d}{2}\right)^2} \right], \quad (5)$$

where  $\varepsilon_{\text{bb}}$  is the emission of the black body with an amplitude of  $\approx 0.95$  (manufacturer's datasheet value),  $\tau_{\text{F}}$  is the average experimentally determined transmittance of the Ge window with a value of  $\tau_{\text{F}} \approx 0.76$ ,  $M$  is the integrated radiant exitance of the black body (supplementary material section 8)

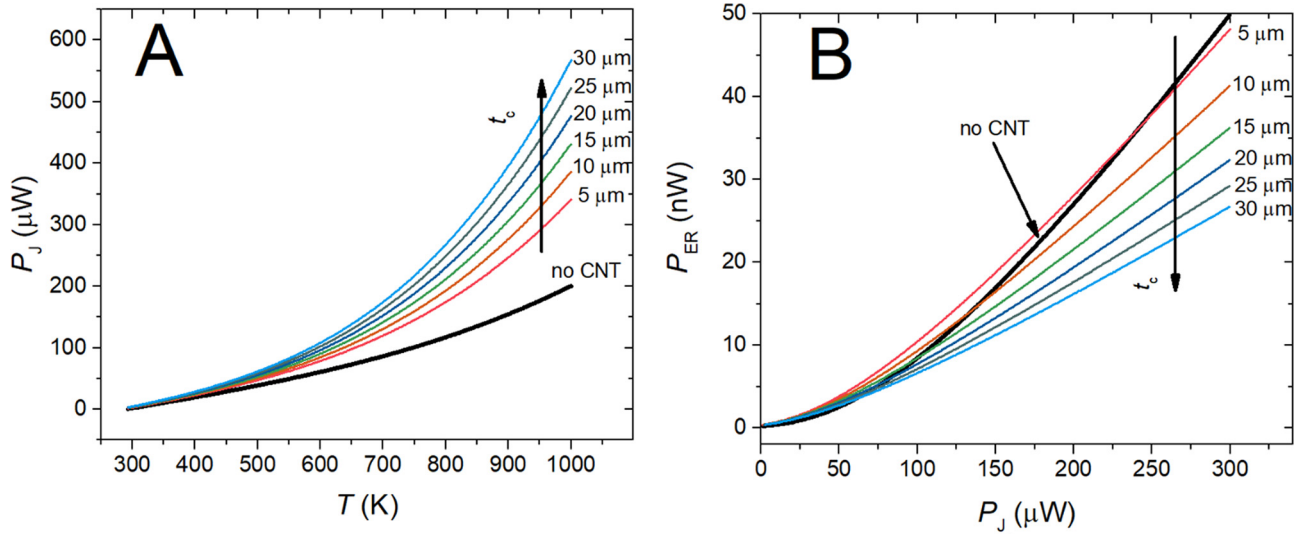


FIG. 5. (a) Calculated values of dissipated Joule heat  $P_J$  as a function of  $T$  for microbolometers without CNTs (thick black line) and for various CNT thickness values. The CNT membranes require a larger  $P_J$  to remain at a distinct  $T$ . (b) Calculated values of  $P_{ER}$  as a function of  $P_J$  for microbolometers without CNTs (thick black line) and for various  $t_c$  values.

according to Planck's radiation law with an amplitude of  $\approx 2588 \text{ W}\cdot\text{m}^{-2}$  and  $d \approx 10.5 \text{ mm}$  is the diameter of the black body radiation source. The value of  $\tau_F$  was determined by a ratio of an output signal of a commercial microbolometer based IR camera with and without the Ge window. The microbolometer responsivity to IR radiation ( $\mathfrak{R}_{IR}$ ) is defined as

$$\mathfrak{R}_{IR} = \frac{\Delta V_{out}}{P_{IR}}. \quad (6)$$

Our results show that by adding the CNT absorbing layer, the  $\mathfrak{R}_{IR}$  increased by a factor of  $(2.3 \pm 0.1)$  (mean  $\pm$  fitting error) (Fig. 7).

## CONCLUSIONS

Our work presented here for the first time demonstrates CNT growth on the surface of suspended microbolometer membranes while keeping the device substrate at room temperature. By taking advantage of the thermally isolated nature of the released microbolometer membrane, the developed CMOS fabrication compatible method allows for the integration of IR absorbing CNTs with a variety of active device architectures including FPAs. Our results show  $\approx 2.3$ -fold IR responsivity increase with grown CNT absorbers and reached a  $\mathfrak{R}_{IR}$  of  $(16.35 \pm 0.48) \text{ kV}\cdot\text{W}^{-1}$ . Furthermore, the IR absorption near unity is determined solely by the CNT

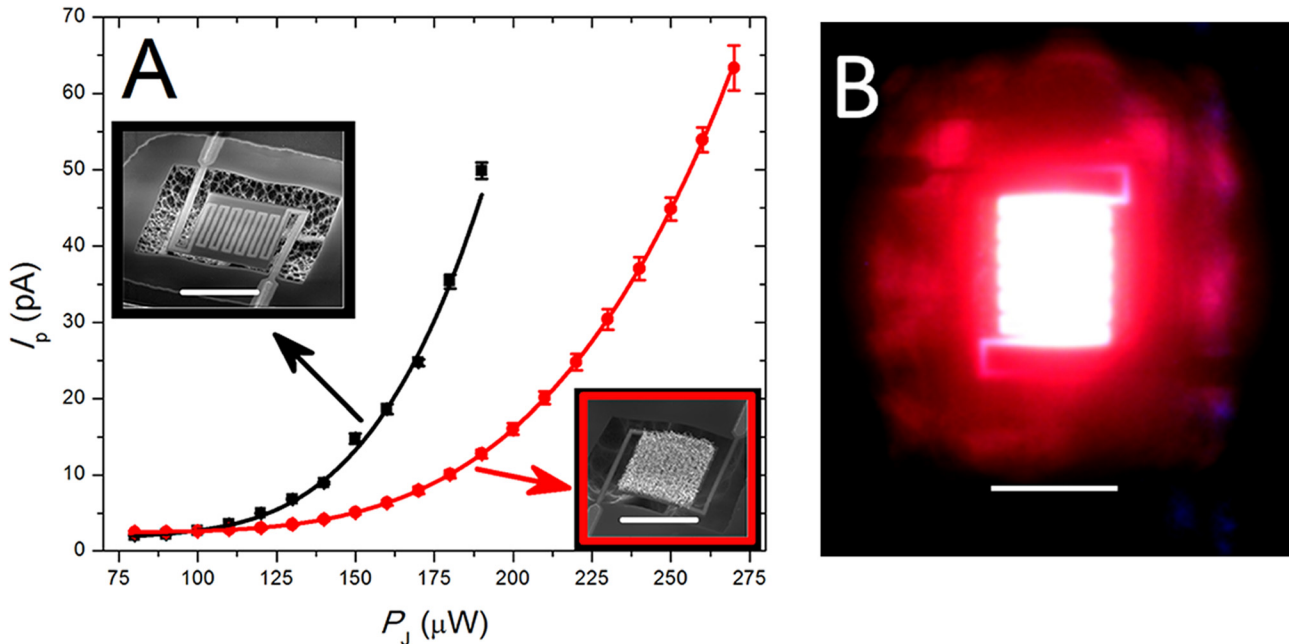


FIG. 6. (a) Measured light emission amplitude from bare (black squares) and CNT covered (red circles) microbolometer membrane as a function of dissipated  $P_J$ . The two insets are scanning electron micrographs of microbolometers with and without the CNT layer. Scale bars represent  $40 \mu\text{m}$ . Solid lines represent a 4th order polynomial curve fitting with the cubic coefficient set to zero. The radiation power amplitude of the microbolometer with the CNT is  $\approx 0.23$  of the one without. Filled in markers are average values and vertical bars represent one standard deviation resulting from repeated measurements across a device. (b) Optical micrograph showing light emission from the membrane at  $P_J \approx 650 \mu\text{W}$ . The scale bar represents  $40 \mu\text{m}$ .

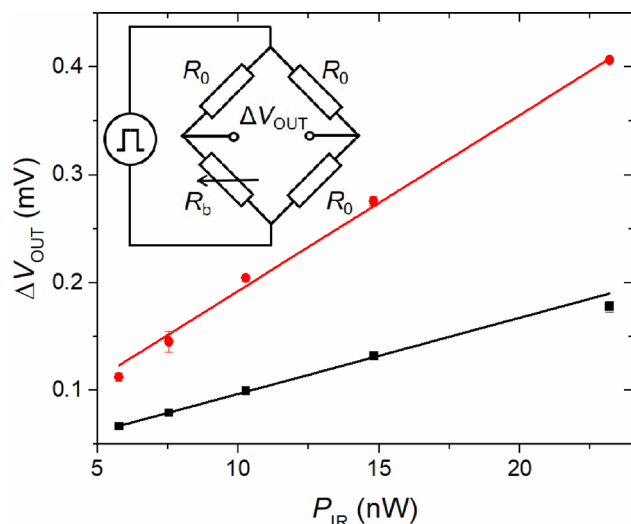


FIG. 7. Wheatstone bridge output voltage change  $\Delta V_{OUT}$  as a function of incident  $P_{IR}$  for microbolometers with (red circles) and without (black squares) a CNT layer. The amplitude of  $P_{IR}$  was calculated from the black body bolometer distance as per Eq. (5) and supplementary material section 8. The bridge was biased with a square wave pulse of amplitude  $\approx 0.6$  V and duration  $\approx 200$  ms. The  $\Delta V_{OUT}$  amplitude was captured at  $t \approx 200$  ms. Using linear regression, the microbolometer  $\mathfrak{R}_{IR}$  with and without CNTs is  $(16.35 \pm 0.48)$   $\text{kV} \cdot \text{W}^{-1}$  and  $(7.08 \pm 0.24)$   $\text{kV} \cdot \text{W}^{-1}$ , both (mean  $\pm$  standard deviation, across 3 measurements), respectively. Filled-in markers are average values and vertical bars represent one standard deviation resulting from repeated measurements across three devices. Overall, with CNTs,  $\mathfrak{R}_{IR}$  increases by a factor of  $(2.3 \pm 0.1)$  (mean  $\pm$  fitting error).

layer, regardless of the membrane material and thickness, the cavity and the underlying IR reflector. The promising growth technique of highly absorbing CNT layers using spatially localized heating on the surface of suspended membranes opens opportunities for complex integration of these absorbing layers for efficient IR imaging and FPA emission applications.

## SUPPLEMENTARY MATERIAL

See supplementary material for microbolometer resistance and temperature coefficient of resistance measurement, evaluation of microbolometer thermal parameters, microbolometer response to varying  $V_b$ , details of emission measurement during CNT growth, resistance measurement during CNT growth, emission measurement from the microbolometer with CNTs, reflection measurement from bolometer

membrane during CNT growth, and calculation of blackbody radiant exitance.

## ACKNOWLEDGMENTS

V. Svatoš, I. Gablech, J. Pekárek, and P. Neuzil acknowledge the financial support by the Ministry of the Interior of the Czech Republic under VI20152019043 project. We also acknowledge the support of CEITEC Nano Research Infrastructure (ID LM2015041, MEYS CR, 2016–2019) and the SIX Center of Brno University of Technology, where measurements were conducted. The authors would also like to acknowledge great help from Mr. Jaroslav Klempa for performing the FEM of temperature distribution in the bolometer and the staff of the Center for Nanoscale Science and Technology facility at the National Institute of Standards and Technology, Gaithersburg, USA, where these devices were fabricated.

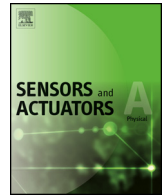
- <sup>1</sup>A. Rogalski, *Infrared Phys. Technol.* **54**, 136 (2011).
- <sup>2</sup>K. C. Liddiard, *Infrared Phys.* **24**, 57 (1984).
- <sup>3</sup>P. Neuzil, Y. Liu, H. H. Feng, and W. J. Zeng, *IEEE Electron Device Lett.* **26**, 320 (2005).
- <sup>4</sup>T. Mei, P. Neuzil, G. Karunasiri, and W. Zeng, *Appl. Phys. Lett.* **80**, 2183 (2002).
- <sup>5</sup>J. H. Lehman, C. Engtrakul, T. Gennett, and A. C. Dillon, *Appl. Opt.* **44**, 483 (2005).
- <sup>6</sup>Z.-P. Yang, L. Ci, J. A. Bur, S.-Y. Lin, and P. M. Ajayan, *Nano Lett.* **8**, 446 (2008).
- <sup>7</sup>J. Lehman, A. Sanders, L. Hanssen, B. Wilthan, J. Zeng, and C. Jensen, *Nano Lett.* **10**, 3261 (2010).
- <sup>8</sup>M. Meyyappan, D. Lance, C. Alan, and H. David, *Plasma Sources Sci. Technol.* **12**, 205 (2003).
- <sup>9</sup>S. M. Huang, L. M. Dai, and A. W. H. Mau, *Adv. Mater.* **14**, 1140 (2002).
- <sup>10</sup>S.-L. Zhang and M. Östling, *Crit. Rev. Solid State Mater. Sci.* **28**, 1 (2003).
- <sup>11</sup>M. M. Shulaker, G. Hills, N. Patil, H. Wei, H.-Y. Chen, H. S. P. Wong, and S. Mitra, *Nature* **501**, 526 (2013).
- <sup>12</sup>K. C. Balram, D. A. Westly, M. Davanco, K. Grutter, Q. Li, T. Michels, C. H. Ray, L. Yu, R. Kasica, C. B. Wallin, I. Gilbert, B. A. Bryce, G. Simelgor, J. Topolancik, N. Lobontiu, Y. Liu, P. Neuzil, V. Svatoš, K. A. Dill, N. A. Bertrand, M. Metzler, G. Lopez, D. A. Czaplowski, L. Ocola, K. Srinivasan, S. Stavis, V. Aksyuk, J. A. Liddle, S. Krylov, and B. R. Ilic, *J. Res. Natl. Inst. Stand.* **121**, 464 (2016).
- <sup>13</sup>X. Gu, G. Karunasiri, G. Chen, U. Sridhar, and B. Xu, *Appl. Phys. Lett.* **72**, 1881 (1998).
- <sup>14</sup>X. He, G. Karunasiri, T. Mei, W. J. Zeng, P. Neuzil, and U. Sridhar, *IEEE Electron Device Lett.* **21**, 233 (2000).
- <sup>15</sup>K. Mizuno, J. Ishii, H. Kishida, Y. Hayamizu, S. Yasuda, D. N. Futaba, M. Yumura, and K. Hata, *Proc. Natl. Acad. Sci. U.S.A.* **106**, 6044 (2009).

## Příloha 5

PEKÁREK, J. et al. Self-compensating method for bolometer-based IR focal plane arrays. *Sensors and Actuators, A: Physical*, 2017, vol. 265, pp. 40-46. ISSN 0924-4247.

### ABSTRAKT

V článku je představen samočinně kompenzující systém pro redukci šumu z pevných obrazců (FPNR) v ohniskových polích (FPA) pro infračervené snímání pomocí mikrobolometrů. Je založen na sigma delta modulátoru prvního řádu, který slouží jako nesaturující integrátor signálů. Bylo dokázáno, že navrhovaná metoda potlačuje jak účinek bolometrického odporu vůči nerovnoměrnosti napříč FPA, tak vlastní ohřev struktur. Navrhovaný systém nevyžaduje žádnou vnější nebo vnitřní zpětnou vazbu pro FPNR. Tento přístup lze použít i pro jiné aplikace, kde je vyžadována kompenzace signálu.



## Self-compensating method for bolometer-based IR focal plane arrays



Jan Pekárek<sup>b</sup>, Roman Prokop<sup>b</sup>, Vojtěch Svatoš<sup>b</sup>, Imrich Gablech<sup>b</sup>, Jaromír Hubálek<sup>b</sup>, Pavel Neužil<sup>a,b,\*</sup>

<sup>a</sup> Northwestern Polytechnical University, 127 West Youyi Road, 710072, Xi'an, Shaanxi, PR China

<sup>b</sup> Centre of SIX, Dept. of Microelectronics, FEEC, Brno University of Technology, Technická, 3058/10, CZ-616 00Brno, Czech Republic

### ARTICLE INFO

#### Article history:

Received 26 April 2017

Received in revised form 5 August 2017

Accepted 10 August 2017

Available online 16 August 2017

#### Keywords:

Bolometers

Self-heating

Infrared imaging

Readout integrated circuit

Sigma-delta modulation

### ABSTRACT

We present a self-compensating system for fixed pattern noise reduction (FPNR) of focal plane arrays (FPAs) of infrared bolometer detectors. It is based on a first-order  $\Delta\Sigma$  modulator serving as a non-saturating signal integrator. The demonstrated method suppresses both the effect of bolometer resistance due to non-uniformity across the FPA as well as the self-heating effect. The proposed system does not require any external or internal feedback loop for FPNR. This approach can be also used for other applications where a signal compensation is required.

© 2017 Elsevier B.V. All rights reserved.

### 1. Introduction

Infrared (IR) radiation in the wavelength range from 8  $\mu\text{m}$  to 14  $\mu\text{m}$  is used in many applications such as astronomy, thermal scanning to search for people or animals, and recently very popular the preventive maintenance of electrical appliances and monitoring the thermal isolation of buildings. The emission of IR radiation can be detected by numerous methods. One of the early IR detectors was the Golay cell [1], where the incident IR radiation heated a medium inside its cavity, thus increasing its pressure. A flexible membrane expanded with the pressure and its expansion was monitored. It was an extremely sensitive IR detector, but unsuitable for integration into an array necessary for IR imaging. Later on, there was developed a photon detecting device based on large band gap semiconductors, such as HgCdTe [2]. This device is an excellent imager, but it requires cooling by the liquid nitrogen. Bolometers comprise a thermally isolated membrane integrated together with a temperature-sensitive device, most often a resistive temperature detector (RTD). The membrane warms up due to the incident radiation and the corresponding temperature change is then monitored. The first bolometer was developed in 1878 by astronomer

S. P. Langley [3]. With the advent of integrated circuit technology and microelectromechanical systems (MEMS), focal plane arrays (FPAs) based on microbolometers were developed. The temperature sensing devices are typically RTDs composed of material with a high temperature coefficient of resistance (TCR). The resistors are typically made of metal, such as titanium [4], nickel [5], and platinum [6] or semiconductors, such as silicon, germanium [7], and vanadium oxide [8,9].

The MEMS based bolometers are used as the uncooled sensors for IR detection either for astronomy or night imaging. In the past three decades of development, uncooled infrared FPA imagers based on the surface micromachined bolometers have been successfully developed and found to have many applications in areas such as surveillance, night vision, firefighter's aids, and military [10,11].

The size of a contemporary imager with 17  $\mu\text{m}$  pixel-pitch forming the FPA is  $1024 \times 768$  pixels [12,13], with a total number of  $\approx 786$  thousands of pixels. Considering typical PAL or NTSC frame rates of  $25 \text{ s}^{-1}$  and  $30 \text{ s}^{-1}$ , respectively, there are only  $\approx 0.04 \mu\text{s}$  available to process data from a single pixel using the serial data processing scheme. Parallel processing of the signal in each column increases the time available for each pixel to  $\approx 32 \mu\text{s}$ .

There are two fundamental problems of bolometer-based FPAs. First, the bolometer resistance  $R$  is measured by passing electrical current  $I$  through the bolometer. Its membrane warms up by dissipated Joule  $P_j$  heat as Eq. (1):

$$P_j = V \cdot I = \frac{V^2}{R}, \quad (1)$$

\* Corresponding author at: Northwestern Polytechnical University, 127 West Youyi Road, 710072, Xi'an, Shaanxi, PR China.

E-mail addresses: [pekarek@feec.vutbr.cz](mailto:pekarek@feec.vutbr.cz) (J. Pekárek), [prokop@feec.vutbr.cz](mailto:prokop@feec.vutbr.cz) (R. Prokop), [vojtech.svatos@ceitec.vutbr.cz](mailto:vojtech.svatos@ceitec.vutbr.cz) (V. Svatoš), [imrich.gablech@ceitec.vutbr.cz](mailto:imrich.gablech@ceitec.vutbr.cz) (I. Gablech), [hubalek@feec.vutbr.cz](mailto:hubalek@feec.vutbr.cz) (J. Hubálek), [pavel.neuzil@ceitec.vutbr.cz](mailto:pavel.neuzil@ceitec.vutbr.cz), [pavel.neuzil@nwpu.edu.cn](mailto:pavel.neuzil@nwpu.edu.cn) (P. Neužil).

where  $V$  is the voltage across the bolometer resistor. The bolometer's temperature can raise  $\approx 100$  K per  $\approx 100$   $\mu$ s of integration time, which is several orders of magnitude higher than the temperature change due to IR radiation. This self-heating effect on the bolometer readout can be suppressed by common mode rejection using either a thermally shorted bolometer [14], a bolometer with inhibited sensitivity for IR radiation, a bolometer shielded from incident IR radiation, or by injecting a current ramp into the bolometer [15] or skimming technique [16]. The second fundamental problem of bolometer-based FPAs is their nominal value in the range of a few k $\Omega$  and the incident IR radiation can cause its change by less than  $\approx 1$   $\Omega$ . The FPA fabrication process results in variation of both pixel nominal values and their TCR, which produces fixed pattern noise (FPN). There are several known methods of bolometer signal readout to suppress FPN [17–21].

The readout integrated circuit (ROIC) as shown earlier [14] cannot integrate for unlimited time and it also needs a digital-to-analog converter (DAC) with off-chip memory for correction of pixel non-uniformity, i.e., fixed pattern noise reduction (FPNR). A modern  $\Delta\Sigma$  principle was used in bolometer-based FPAs. Researchers massively used parallel  $\Delta\Sigma$  analog-to-digital converters (ADC) together with multiplexing principle to process the bolometer-FPA data [22]. Another principle of data processing with  $\Delta\Sigma$  modulator was shown with a heat balanced bolometer operating in a closed-loop mode [23].

The bolometer-based FPA is illuminated by a source of IR radiation with known intensity producing an image FPN. The digital processing unit (or analog circuit) introduces correction coefficients to get identical signals from all pixels [24].

In this contribution, we propose a signal processing system using a non-saturating integrator. This integrator was achieved using the first-order  $\Delta\Sigma$  modulator combined with a sample and hold circuit (S/H). It does not require a DAC and/or any extra off-chip circuits to perform FPNR. It can be combined with a self-heating correction technique to improve the performance of the proposed system.

## 2. Theory—principle of non-saturating integrator ( $\Delta\Sigma$ ) for FPNR

The signals from the bolometers forming the FPA are processed by ROIC to eventually form an image of IR radiation. Integrating the bolometer output signal improves the signal-to-noise (SNR) ratio, a key performance parameter of circuit processing such minute electrical signals. As mentioned above, the fundamental problem with bolometer measurement is its small  $\Delta R$  due to incident IR radiation and a few orders of magnitude smaller than the nominal value of  $R$ . In addition, the actual  $R$  value fluctuates due to uncertainty in the FPA fabrication process.

First-order  $\Delta\Sigma$  modulation consists of a current integrator followed by a clocked comparator. The current source  $I_{REF}$  is activated from time to time based on clocked comparator status to keep the integrator out of saturation (Fig. 1A).

The integrator output voltage  $V_{BAL}$  at time  $t$  can be described as Eq. (2):

$$V_{BAL} = \frac{1}{C_{INT}} \left( \int_0^t I_{in} dt - I_{REF} \cdot T \cdot N - \int_0^{t_1} I_{REF} dt \right), \quad (2)$$

where  $C_{INT}$  is the capacitance value of an integrating capacitor,  $I_{in}$  is an integrator input current,  $T$  is clock period,  $N$  the number (positive integer) of clock periods the  $I_{REF}$  switch was closed, and  $t_1$  is the time when the last period started and the switch for  $I_{REF}$  was activated. If not, the last integral in Eq. (2) has value of 0 V.

This system produces a pattern of two logical levels at the clocked comparator output and a residual value of  $V_{BAL}$  and the

integrator output at the end of the conversion. The magnitude of unknown current  $I_{in}$  can be then calculated from  $N$  value and  $I_{REF}$ . It is typical cooperation of a  $\Delta\Sigma$ -based AD conversion while the residual value of  $V_{BAL}$  at the end of the conversion is dumped.

We propose an employment of this scheme for extraction value of IR radiation from bolometer-based FPAs. The absolute value of  $N$  will represent a nominal bolometer resistance and its variation (FPN). The power of incident IR radiation will contribute to an amplitude of  $V_{BAL}$  signal.

The system first scans the entire FPA with the shutter closed and stores all the outputs values of  $V_{BAL1}$  and  $N$  value from the entire FPA, in an internal or external memory. Next, the FPA is scanned again with the shutter open and the new outputs of  $V_{BAL2}$  are recorded. The image of IR radiation is then formed by subtracting  $\Delta V_{BAL} = V_{BAL2} - V_{BAL1}$  (Fig. 1B) from each pixel of the FPA as well as comparing the  $N$  value with and without the applied IR radiation.

In the ideal situation,  $N$  values Eq. (2) for both  $V_{BAL}$  signals with and without IR radiation are identical (labeled as 1 in Fig. 1B). There are special conditions with different values of  $N$  (labeled as 2 in Fig. 1B), with and without IR, such as  $V_{BAL1}$  without activated switch  $S$  and  $V_{BAL2}$  with activated switch  $S$  and vice versa, and then the equivalent value of the  $\Delta V_{BAL}$  has to be calculated.

The signal from DFF during SH activation shows the comparator status and will determine further digital signal processing (DSP) of  $\Delta V_{BAL}$  signals. This DSP module for image construction can also perform a task to calibrate the chip and calculate the integrator's output as a function of time.

## 3. Application-specific integrated circuit (ASIC) design

The proposed ASIC ROIC circuit based on a  $\Delta\Sigma$  non-saturating integrator was designed to evaluate bolometer sensors with nominal resistance and changes of  $>4$  k $\Omega$  and  $\leq 20$   $\Omega$ , respectively. Its simplified transistor-level schematic in 0.7  $\mu$ m complementary metal oxide semiconductor (CMOS) 5 V technology is shown as Fig. 2.

The NMOS cascode mirror ( $M_{M3}$ ,  $M_{M4}$ ) was designed with 3% asymmetry adding to FPN. This allows to compensate the measured and reference bolometer mismatch using unipolar system of clocked  $I_{REF}$  regardless of which bolometer nominal resistance is greater. Further compensation can be conducted by the  $V_{COMP}$  signal as described in detail at the end of this chapter.

The NMOS cascode mirror was designed with large transistors with proportion of the channel width/length of 150/2 and 155/2  $\mu$ m, respectively, to minimize their noise level. Long channel length of 2  $\mu$ m having small transconductance also results in improve accuracy and low level of white and  $1/f$  noise. The system is based on an integrator leading to further suppressing the noise from the signal. Only the equivalent input noise of the integrator as well as voltage reference noise affect the integrator's output and can further be processed via S/H by the ADC.

The  $V_{BAL}$  is affected by the triggering of the clocked comparator. We selected the S/H activation in the middle of the clock signal pulse to suppress this effect.

We selected a clock signal frequency of  $\approx 1$  MHz. With an assumption that the bolometer has similar properties as determined previously [25] and the power supply voltage  $V_{DDA} \approx 5$  V, this circuit should have a dynamic range of bolometer temperature excursion of up to  $\approx 256$  mK with a resolution of 8 bits.

The proposed system consists of two bolometers: the first is sensitive and the second one is insensitive to the incident IR radiation with resistance  $R_{IR}$  and  $R_{REF}$ , respectively. We used a cascode current mirror composed of transistors  $M_{M1}$ ,  $M_{M3}$  and  $M_{M2}$ ,  $M_{M4}$ , the first connected to the sensing  $R_{REF}$ , the second to  $R_{IR}$  bolometer. The electrical currents flowing through both branches of the mirror are

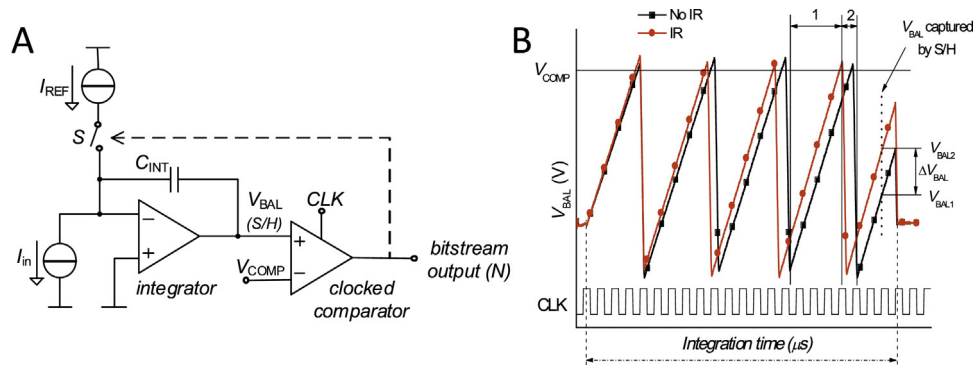


**Fig. 1.** (A) Principle of non-saturating integration based on  $\Delta\Sigma$  modulator of first-order. Once the output signal amplitude at the integrator output  $V_{BAL}$  crosses  $V_{COMP}$  level, the clocked comparator activates  $I_{REF}$  and this additional electrical current in the opposite direction decreases the amplitude of  $V_{BAL}$ , keeping the integrator out of saturation. (B) (black) Signal  $V_{BAL}$  with no incident power of IR radiation. (red) The bolometer resistance increases as its membrane heats up due to incident IR radiation and increasing  $\Delta I$  of input current  $I_{in}$ , causing  $V_{BAL}$  to increase. (For interpretation of the references to colour in this figure legend, the reader is referred to the web version of this article.)

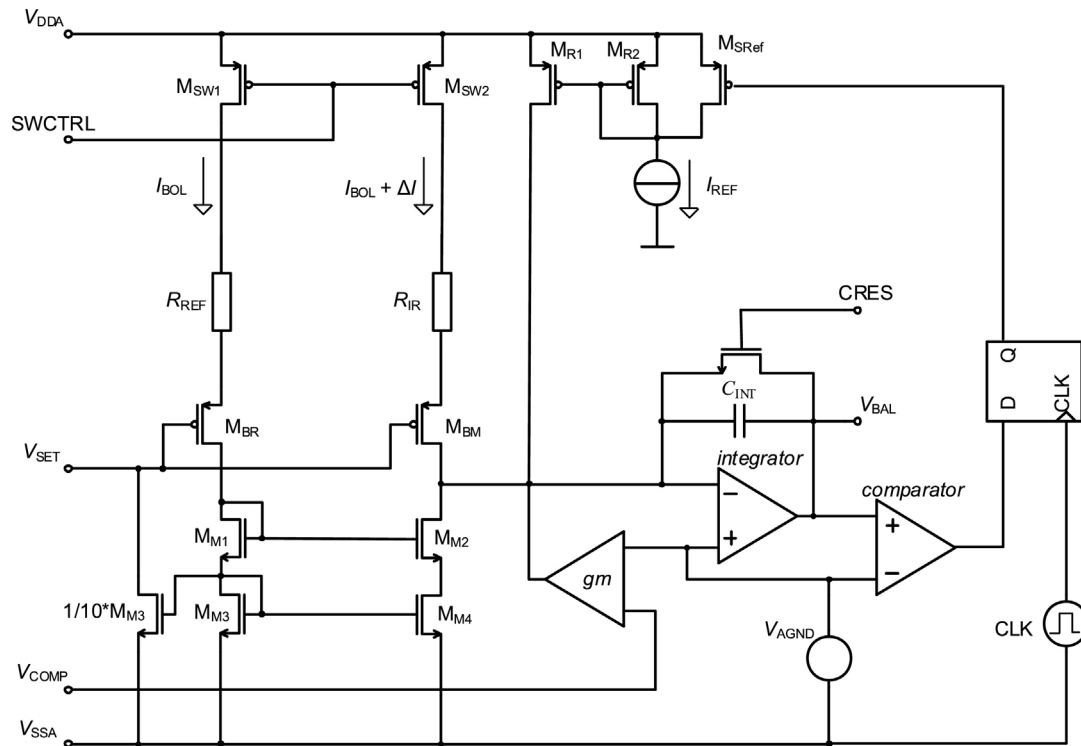


**Fig. 2.** Simplified electrical schematic of non-saturating integrator for FPNR for IR bolometer detectors in FPAs. The  $V_{COMP}$  voltage input is used to inject additional current into the integrator, thus emulating the nominal bolometer resistance mismatch.

ideally identical. Nevertheless, the electrical currents in bolometers differ by  $\Delta I$  due to their differences in resistance  $\Delta R$  caused by incident IR radiation and manufacturing process fluctuations (FPN). This  $\Delta I$  is then integrated using an operational amplifier with capacitor  $C_{INT}$  in its feedback loop, resulting in voltage change  $\Delta V_{BAL}$  at the integrator output. The self-heating effect occurs in both bolometers simultaneously and rejected as common mode [15].

### 3.1. Simple operation

The current mirror is equipped with a power-down function made with the two P-channel switches,  $M_{SW1}$  and  $M_{SW2}$ , both controlled by the digital signal SWCTRL. The digital control signal CRES allows to discharge  $C_{INT}$  by activating another MOS switch. In normal operation, when the  $\Delta R$  is relatively small,  $V_{COMP}$  is set to  $\approx 0$  V and  $V_{SET}$ , buffered by  $M_{BM}$  and  $M_{BR}$ , controls the required voltage

drop across the bolometers. The signal SWCTRL is changed from logical “1” to logical “0” at  $t \approx 0$  s and both bolometers are then powered. Signal CRES releases the switch with a delay of  $\approx 3 \mu\text{s}$  and the integrator starts to integrate  $\Delta I$  from the bolometers at the  $C_{INT}$  and increasing the integrator output voltage  $V_{BAL}$ . This delay of  $\approx 3 \mu\text{s}$  was chosen to eliminate the effect of current mirror propagation delay avoiding to integrate a spurious transient.

The  $\Delta I$  is then processed by the  $\Delta\Sigma$  modulator for a chosen integration period, which is usually determined by the time available for signal processing from a single line of the FPA and also to avoid excessive bolometer self-heating. Typically, this can be as long as  $100 \mu\text{s}$  or even a bit longer, depending on bolometer nominal resistance and, thus, self-heating as well as FPA frame rate. Here, we proposed an integration period in the range of  $\approx (80\text{--}90) \mu\text{s}$ . The integrator output voltage  $V_{BAL}$  was monitored by an oscilloscope for system optimization during the development. Once the integration is completed, the signal SWCTRL is changed into logical “1”

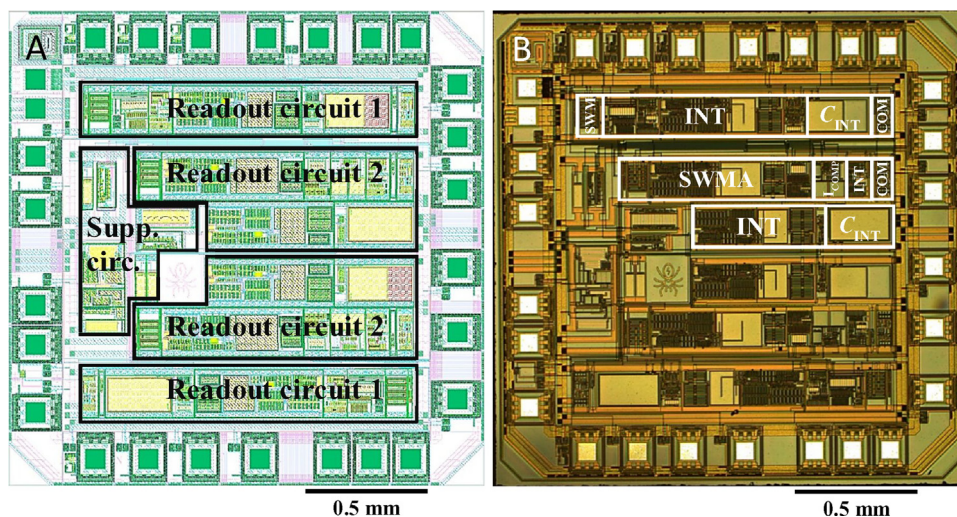


**Fig. 3.** (A) Layout of an ROIC chip in 0.7  $\mu\text{m}$  CMOS 5 V technology with highlighted two versions of readout circuits. (B) Optical image of a fabricated ROIC chip in 0.7  $\mu\text{m}$  CMOS 5 V technology with located main elements of  $\Delta\Sigma$  modulators (COM – clocked comparator, INT – integrator OPAMP,  $C_{\text{INT}}$  – integrating capacitor, SWM – switches and main mirror, SWMA – switches, main mirror including voltage follower,  $I_{\text{COMP}}$  – fixed pattern compensating current circuit).

resulting in bolometers losing power and cooling down; then, CRES activates the switch, discharges  $C_{\text{INT}}$ , and the ASIC is ready for a new readout period once the bolometer cools down completely, which is determined by its thermal properties especially the thermal time constant  $\tau$ .

### 3.2. Additional compensation

The mismatch between the reference and the sensing bolometer can be so large that the  $\Delta\Sigma$  feedback loop system is not capable of FPNR at the maximum power supply voltage of the ASIC. For this reason, we chose another option to compensate excessive  $\Delta I$  by injecting constant current from an additional current source formed by a  $gm$  stage, controlled by  $V_{\text{COMP}}$  voltage as Eq. (3):

$$I_{\text{COMP}} = gm \cdot (V_{\text{COMP}} - V_{\text{AGND}}), \quad (3)$$

where  $gm$  is  $\approx 40 \mu\text{A V}^{-1}$  and  $I_{\text{COMP}}$  is limited to the range of  $\approx -30$  to  $30 \mu\text{A}$ . If not needed, this compensating current can be inhibited by an external digital signal.  $I_{\text{COMP}}$  can be also used to emulate a bolometer resistance mismatch (FPN). This compensating feature is expected to be implemented only for the development phase of this system.

## 4. ASIC simulation

The preliminary results using the simulation program with integrated circuit emphasis (SPICE) at transistor level were presented in detail in a published paper [26]. The ASIC circuit was simulated using transistor models supplied with 0.7  $\mu\text{m}$  CMOS 5 V process design kit in Cadence Design Environment. The bolometer was represented as a sub-circuit emulating temperature dependent resistor with a nominal value of  $\approx 10 \text{ k}\Omega$ , TCR of  $3 \cdot 10^{-3} \text{ K}^{-1}$ , and  $\tau$  of  $\approx 7 \text{ ms}$  [27]. This sub-circuit was equipped with the feature to emulate the self-heating effect and to respond to an external power of IR radiation. We considered an incident IR radiation with power of 1.61 nW which increased the bolometer temperature  $\Delta T$  by only  $\approx 10 \text{ mK}$  to demonstrate the sensitivity of the proposed method. This  $\Delta T$  causes a bolometer resistance change of only  $\approx 0.3 \Omega$ . The simulation results suggested that this  $\Delta\Sigma$ -based method represents a viable technique to suppress both resistors' non-uniformity as well as self-heating effect for FPA ROIC for IR imaging as we will be showing later in IR measurement section.

## 5. ASIC verification

Once the transistor-level simulation program with integrated circuit emphasis (SPICE) simulation of the system was completed, we designed the layout of the ROIC (Fig. 3A) in 0.7  $\mu\text{m}$  double metal CMOS technology following the conventional rules of layout, such as East–West North–South transistor topography to suppress the influence of thermal gradient and also considering the matching and the noise effects. The chip was fabricated in 0.7  $\mu\text{m}$  CMOS 5 V technology with a size of  $\approx (2 \times 2) \text{ mm}$  (Fig. 3B) containing two versions of  $\Delta\Sigma$  modulators.

It was then packaged into a dual-in-line 40 (DIL40) socket. The test printed circuit board (PCB) was designed and fabricated for the basic verification of this ROIC chip. The signals needed to control and set up the ROIC chip (i.e., SWCTRL, CRES, CLK, and  $V_{\text{AGND}}$ ,  $V_{\text{SET}}$ ,  $V_{\text{COMP}}$  voltages) were generated externally at the PCB.

The bolometer behavior was emulated by a fixed resistor with values of  $\approx 10 \text{ k}\Omega$  in series with a precise variable resistor  $R_V$  with values between  $0 \Omega$  and  $\approx 20 \Omega$ . Let's assume that the bolometer nominal resistor value is  $\approx 10 \text{ k}\Omega$  and its TCR is  $3 \cdot 10^{-3} \text{ K}^{-1}$ , then the temperature change of  $\approx 10 \text{ mK}$  will cause the bolometer resistance change of  $\approx 0.3 \Omega$ . The system has a sensitivity of  $(-65.6 \pm 1.6) \text{ mV } \Omega^{-1}$  (mean  $\pm$  standard deviation). The preliminary results of  $\Delta\Sigma$  system tested with external nominal resistors were published earlier [28].  $\Delta V_{\text{BAL}}$  of 1 mV corresponds to  $\approx 15 \text{ m}\Omega$  resistance change corresponding to the bolometer membrane temperature change of the  $\approx 0.5 \text{ mK}$ .

## 6. Bolometer fabrication

The bolometer chip layout was generated using a recently developed method [29]. First we coated a silicon substrate with a  $\text{SiO}_2$  layer with thickness of  $\approx 250 \text{ nm}$ . We subsequently deposited a  $\approx 300 \text{ nm}$  thick Au layer with  $\approx 20 \text{ nm}$  thin Cr adhesion layer. This metal sandwich was lithographically patterned followed by an ion milling process forming the electrical paths and bonding pads. A Ti layer with a thickness of  $\approx 30 \text{ nm}$  was deposited and patterned by reactive ion etching to serve as RTDs at membranes of bolometers. We again deposited a layer of  $\text{SiO}_2$  with thickness of  $\approx 250 \text{ nm}$  to cover all metals. We subsequently deposited a layer of Al with thickness of  $\approx 50 \text{ nm}$  on areas with reference bolometers to serve as reflectors of IR radiation to suppress their response to IR radiation. We used an additional lithography step to open etching holes in

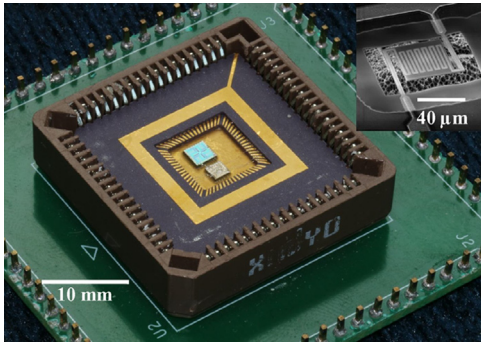


**Fig. 4.** Photograph of ASIC and bolometer chips mounted in an LCC 68 package and placed into a testing socket. (inset) SEM image of fabricated bolometer.

SiO<sub>2</sub> as well as to open access to bonding pads. Wafers were diced into individual chips by a diamond blade dicing saw.

We then measured the nominal  $R_B$  at a probe station and, in combination with a temperature controlled hotplate, also its amplitude of TCR. We determined that the ambient resistance of the bolometers was  $(7.735 \pm 0.254)$  k $\Omega$  and its TCR value was  $(0.53 \pm 0.01) 10^{-3}$  K<sup>-1</sup>, both values were identified with (mean  $\pm$  standard deviation). The last fabrication step was removal of silicon underneath the membrane to release them with XeF<sub>2</sub> vapors (see SEM image in inset of Fig. 4). The chips were electrically connected by the wire bonding method into lead less chip carrier 68 (LCC68) and placed into a vacuum chamber where the bolometer thermal properties were determined. The bolometer was connected into a balanced Wheatstone bridge and we evaluated the values of bolometer thermal capacitance  $H$  and thermal conductance  $G$ , and extracted  $\tau$  according the equation  $\tau = H/G$  by the method described earlier [25]. The thermal capacitance  $H$  was  $(3.113 \pm 0.009)$  nJ K<sup>-1</sup>, thermal conductance  $G$  was  $(160.9 \pm 2.7)$  nW K<sup>-1</sup>, and extracted  $\tau$  was  $(19.35 \pm 0.34)$  ms. All values were identified with (mean  $\pm$  standard deviation). Finally, the bolometer responsivity  $\mathfrak{R}_{IR}$  was determined to be  $(7.08 \pm 0.24)$   $\mu$ V nW<sup>-1</sup> (mean  $\pm$  standard deviation) by the method as before [30].

## 7. ASIC testing with bolometers

Both the chips, ASIC as well as bolometers, were placed into the same leadless chip carrier LCC 68 and connected either to a socket or to each other by wire bonding method (Fig. 4).

The LCC 68 with the devices was then placed into a vacuum chamber equipped with transparent window for IR radiation made of germanium. The chamber was then pumped into pressure of  $<4 \cdot 10^{-4}$  Pa using a turbomolecular pump backed by a scroll pump. The LCC 68 socket was connected with external electronics outside of the chamber via vacuum feed-through. We exposed the bolometer to different powers of IR radiation using a calibrated blackbody source and measured the output signal of the ASIC. The power of IR radiation was set by changing distance between the bolometer and the blackbody (see testing setup in Fig. 5) and calculated by the method described earlier [30].

We then monitored  $V_{BAL}$  voltage as a function of compensating current  $I_{COMP}$  showing performance of  $\Delta\Sigma$  serving as non-saturating integrator (Fig. 6). The clocked comparator did not allow the integrator to overflow regardless of the charging rate of  $C_{INT}$ . Once the comparator input exceeded the decision level, a compensation  $I_{in}$  was activated and the  $C_{INT}$  was discharged.

We used this  $I_{COMP}$  to emulate variation of nominal resistance of a bolometer, typically FPN. Subsequently, we used six different distances between the blackbody source and the bolometer corresponding to the following amplitude of incident IR radiation at the bolometer membrane: 0, 7.54, 10.28, 14.80, 23.18, 41.28, and

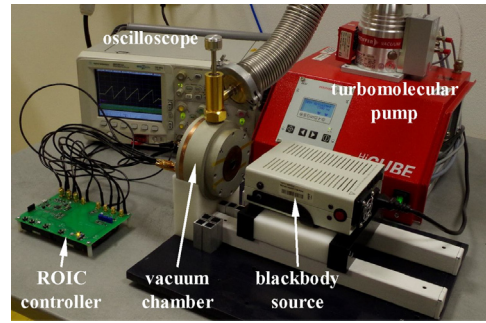


**Fig. 5.** Photograph of a testing setup for bolometer and ROIC chip measurement. It consists of a blackbody source and a vacuum chamber evacuated by a vacuum system employing a turbomolecular pump backed by a scroll pump.

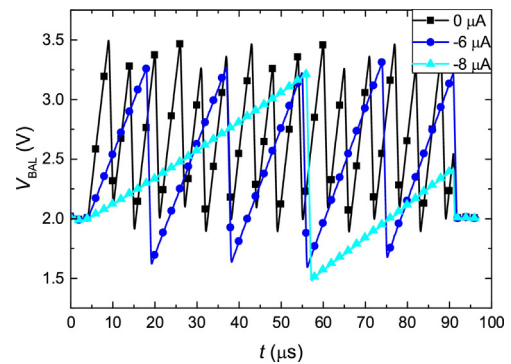


**Fig. 6.** Time dependency of output voltage for different values of  $I_{COMP}$  here emulating differences in nominal resistance of the sensing and reference bolometers.

**Table 1**  
The ROIC sensitivity with  $I_{COMP}$  as a parameter.

$I_{COMP}$ ( $\mu$ A)	ROIC sensitivity (mean value $\pm$ standard deviation) (mV nW <sup>-1</sup> )
0	$7.14 \pm 0.32$
2	$7.58 \pm 0.39$
4	$6.00 \pm 0.45$
6	$7.54 \pm 0.51$
8	$7.47 \pm 0.39$
Average sensitivity	$7.43 \pm 0.20$

92.45 nW (Fig. 7A). We plotted the  $V_{BAL}$  voltage as function of dissipated power with  $I_{COMP}$  as a parameter (Fig. 7B).

The results of the ROIC sensitivity for  $I_{COMP}$  as a parameter are shown in Table 1. The system average sensitivity was determined to be  $(7.43 \pm 0.20)$  mV nW<sup>-1</sup> (mean  $\pm$  standard deviation) independent of  $I_{COMP}$  amplitude demonstrating the method excellent suppression of FPN. Data with applied  $I_{COMP}$  of 4  $\mu$ A were not considered for average calculation as there was a measurement error.

The integrator improves the bolometer readout from its original responsivity  $\mathfrak{R}_{IR}$  of  $(7.08 \pm 0.24)$   $\mu$ V nW<sup>-1</sup> to ROIC readout sensitivity of  $(7.43 \pm 0.20)$  mV nW<sup>-1</sup>, both (mean  $\pm$  standard deviation), which is  $\approx 1000 \times$  improvement due to the integration, regardless of  $I_{COMP}$  amplitude. The  $I_{COMP}$  is used here to emulate variations in amplitude of nominal bolometer resistance, also known as FPN. We then demonstrated that the non-saturating integrator can be used as the basis of an ROIC system for FPNs.

We can derive the limit of system sensitivity of  $V_{BAL}$  at  $\approx 200$   $\mu$ V based on the standard deviation. This corresponds to a power level of IR radiation of  $\approx 200$  pW. The sensitivity can be further improved using a bolometer with a Ti layer and with its TCR closer to bulk properties of  $0.38 \cdot 10^{-3}$  K<sup>-1</sup>. Ti layer used in this work had TCR

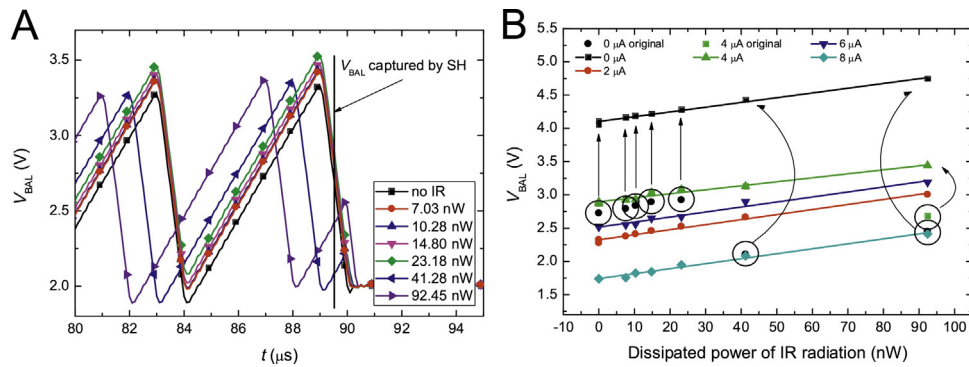


**Fig. 7.** (A) Time dependency of  $V_{BAL}$  voltage for different values of dissipated power of IR radiation close to the end of the integration period from  $\approx 80 \mu\text{s}$  to  $\approx 95 \mu\text{s}$ . The compensating feature was blocked by an external digital signal. (B)  $V_{BAL}$  captured at an integration time of  $\approx 89.5 \mu\text{s}$  as a function of dissipated power of IR radiation with  $I_{COMP}$  as a parameter. The values labeled by arrows were recalculated as per discussion in Section II. The  $\Delta\Sigma$  response values to IR radiation (slopes) were  $(7.14 \pm 0.32) \text{ mV nW}^{-1}$ ,  $(7.58 \pm 0.39) \text{ mV nW}^{-1}$ ,  $(6.00 \pm 0.45) \text{ mV nW}^{-1}$ ,  $(7.54 \pm 0.51) \text{ mV nW}^{-1}$ , and  $(7.47 \pm 0.39) \text{ mV nW}^{-1}$  all with (mean  $\pm$  standard deviation) for  $I_{COMP}$  of 0, 2, 4, 6, and  $8 \mu\text{A}$ , respectively. The average slope (sensitivity) was then  $(7.43 \pm 0.20) \text{ mV nW}^{-1}$  (mean  $\pm$  standard deviation) as it is independent of  $I_{COMP}$  amplitude. Data with applied  $I_{COMP}$  of  $4 \mu\text{A}$  were not considered for average calculation as there was a measurement error.

with a value of  $\approx 0.05 \cdot 10^{-3} \text{ K}^{-1}$ , which is more than  $\approx 7 \times$  lower than a bulk value and  $\approx 6 \times$  lower than the one we used during previously performed experiments [25]. The higher voltage biasing the bolometers can further increase the sensitivity. The output signal is linearly proportional to the voltage at bolometers. Even the self-heating effect is proportional to the cube of voltage at the bolometers. Nevertheless, here the self-heating effect is rejected as common mode so that should not influence the  $V_{BAL}$  signal.

Current  $\Delta\Sigma$  chip requires an area of  $\approx (2 \times 2) \text{ mm}$  including all bond pads and areas around. The chip layout also contained two types of  $\Delta\Sigma$  modulators with different mode of the offset compensation. For all measurements, we used the  $\Delta\Sigma$  modulator which occupies area of  $\approx 0.4 \text{ mm}^2$ . This circuit is too large to make it practical for the FPA as each column requires its own  $\Delta\Sigma$  modulator. Nevertheless, the current IC design was not optimized and it was meant to operate at one chip connected to the bolometer via wire-bonding. This setup caused additional parasitic capacitances and resistances which the IC chip had to compensate. Furthermore, the integrating capacitor occupied 15% of total chip area. Once this  $\Delta\Sigma$  modulator is used in an actual FPA chip, the  $C_{INT}$  would be smaller as well as other blocks shrinking the total circuit area by more than 50%. Finally, it will be necessary to use technology with smaller critical dimensions making the circuit area significantly smaller.

## 8. Conclusion

The fabricated ROIC was tested with variable resistors to emulate the change of the bolometer resistance due to the IR incident radiation and, thus, demonstrated viability of the proposed solution. The mean values of output voltage were recorded at time close to the end of the integration period. The measured sensitivity is  $\approx 65.6 \text{ mV } \Omega^{-1}$ ; thus, we concluded that the ROIC is conceptually appropriate for the readout of the relatively small changes of temperature (resistivity) in the IR applications.

The  $\Delta\Sigma$  system was demonstrated to determine the IR signal from a bolometer using a reference bolometer for the common mode rejection. The measurements of a bolometer chip with ROIC were performed for the different dissipated power by the blackbody calibrator using the variable distances between the bolometer detector and the blackbody source.

The system average sensitivity was determined to be  $(7.43 \pm 0.20) \text{ mV nW}^{-1}$  (mean  $\pm$  standard deviation) independent of  $I_{COMP}$  amplitude demonstrating the method excellent suppression of FPN.

In actual serial–parallel configurations of an ROIC for FPA there would be only a single reference bolometer for an entire row of sensing bolometers. The majority of future  $\Delta\Sigma$  circuits would be part of a column amplifier. The proposed system based on the first-order  $\Delta\Sigma$  modulator is well suited as a core of the ROIC for bolometer-based FPAs.

## Acknowledgements

This work was supported by the Grant Agency of the Czech Republic under GA13-19947S project, by the Ministry of the Interior of the Czech Republic under VI20152019043 project and by Czech Ministry of Education in frame of National Sustainability Program under grant LO1401. The measurement was conducted at SIX Center of Brno University of Technology. Authors are grateful to Cadence Academic Network for providing the license for Cadence software.

## References

- [1] M.J. Golay, Theoretical consideration in heat and infra-red detection, with particular reference to the pneumatic detector, *Rev. Sci. Instrum.* 18 (1947) 347–356.
- [2] P. Norton, HgCdTe infrared detectors, *Elec. Soc. S 98* (1999) 49–70.
- [3] S.P. Langley, The Bolometer, *Nature* 5 (1881) 14–16.
- [4] R.S. Saxena, R.K. Bhan, P.S. Rana, A.K. Vishwakarma, A. Aggarwal, K. Khurana, et al., Study of performance degradation in Titanium microbolometer IR detectors due to elevated heating, *Infrared Phys. Technol.* 54 (2011) 343–352.
- [5] C.F. Middleton, G.D. Boreman, Technique for thermal isolation of antenna-coupled infrared microbolometers, *J. Vac. Sci. Technol. B* 24 (2006) 2356–2359.
- [6] O.Y. Mang, Measurement of effective absorptance on microbolometers, *IEEE Trans. Instrum. Meas.* 55 (2006) 1012–1016.
- [7] E. Iborra, M. Clement, L.V. Herrero, J. Sangrador, IR uncooled bolometers based on amorphous GexSi1-xOy on silicon micromachined structures, *J. Microelectromech. Syst.* 11 (2002) 322–329.
- [8] B. Wang, J.J. Lai, E.J. Zhao, H.M. Hu, Q. Liu, S.H. Chen, Vanadium oxide microbolometer with gold black absorbing layer, *Opt. Eng.* 51 (2012).
- [9] N. Chi-Anh, H.J. Shin, K.T. Kim, Y.H. Han, S. Moon, Characterization of uncooled bolometer with vanadium tungsten oxide infrared active layer, *Sens. Actuat A Phys.* 123–24 (2005) 87–91.
- [10] T. Breen, N. Butler, M. Kohin, A. Marshall Charles, R. Murphy, T. Parker, et al., Summary of applications of uncooled microbolometer sensors, *IEEE Aerosp. Appl. Conf. Proc.* 3 (1999) 361–374.
- [11] A. Rogalski, Recent progress in infrared detector technologies, *Infrared Phys. Technol.* 54 (2011) 136–154.
- [12] U. Mizrahi, N. Argaman, S. Elkind, A. Giladi, Y. Hirsh, M. Labilov, et al., Large format 17 (m high-end VOx mu-Bolometer infrared detector, *Proc. SPIE* 8704 (2013).
- [13] M. Steffanson, I.W. Rangelow, Microthermomechanical infrared sensors, *Opto-Electron. Rev.* 22 (2014) 1–15.

- [14] M.V.S. Ramakrishna, G. Karunasiri, P. Neuzil, U. Sridhar, W.J. Zeng, Highly sensitive infrared temperature sensor using self-heating compensated microbolometers, *Sens. Actuat A Phys.* 79 (2000) 122–127.
- [15] P. Neuzil, T. Mei, A method of suppressing self-heating signal of bolometers, *IEEE Sens. J.* 4 (2004) 207–210.
- [16] P. Robert, J.L. Tissot, D. Pochic, V. Gravot, F. Bonnaire, H. Clerambault, et al., Uncooled 17  $\mu\text{m}$  1/4 VGA IRFPA development for compact and low power systems Electro-Optical and Infrared Systems, 8541, Technology and Applications IX, 2012.
- [17] A. Tanaka, Y. Tanaka, T. Endoh, K. Okuyama, K. Kawano, A non-uniformity correction scheme using multiple analog buses for an uncooled infrared sensor, in: 2003 Symposium on Vlsi Circuits, Digest of Technical Papers, 2003, pp. 161–164.
- [18] X.Q. Chen, Theoretical analysis and experimental application of CDS CMOS integrated circuit for uncooled infrared focal plane arrays, *Optik* 122 (2011) 792–795.
- [19] F. Niklaus, C. Vieider, H. Jakobsen, MEMS-based Uncooled Infrared Bolometer Arrays: a Review, 2007, pp. 8360D–D-15.
- [20] L.C. Que, L.H. Wei, J. Lv, Y.D. Jiang, A digital output readout circuit with substrate temperature and bias heating compensation for uncooled micro-bolometer infrared focal plane arrays, *Infrared Phys. Technol.* 71 (2015) 252–262.
- [21] D. Svard, C. Jansson, A. Alvandpour, A readout IC for an uncooled microbolometer infrared FPA with on-chip self-heating compensation in 0.35  $\mu\text{m}$  CMOS, *Analog. Integr. Circ. S* 77 (2013) 29–44.
- [22] D. Weiler, F. Hochschulz, D. Wurfel, R. Lerch, T. Geruschke, S. Wall, et al., Uncooled digital IRFPA-family with 17 (m pixel-pitch based on amorphous silicon with massively parallel Sigma-Delta-ADC readout, in: B.F. Andresen, G.F. Fulop, C.M. Hanson, P.R. Norton (Eds.), *Infrared Technology and Applications XI*, Spie-Int Soc Optical Engineering, Bellingham, 2014.
- [23] M. Denoual, D. Brouard, A. Veith, O. De Sagazan, M. Pouliquen, P. Attia, et al., A heat balanced sigma-delta uncooled bolometer, *Meas. Sci. Technol.* 25 (2014).
- [24] W.J. Parrish, J.T. Woolaway, Methods and circuitry for correcting temperature-induced errors in microbolometer focal plane array Google Patents (1998).
- [25] P. Neuzil, T. Mei, Evaluation of thermal parameters of bolometer devices, *Appl. Phys. Lett.* 80 (2002) 1838–1840.
- [26] R. Prokop, P. Neuzil, L. Fucik, Self-corrected compensating measurement of bolometer signal using sigma-delta modulation, *Telecommunications and Signal Processing (TSP)*, 38th International Conference on 2015 (2015) 717–720.
- [27] S.R. Kiran, G. Karunasiri, Electro-thermal modelling of infrared microemitters using PSPICE, *Sens. Actuat A Phys.* 72 (1999) 110–114.
- [28] P. Neuzil, J. Pekarek, V. Svatos, R. Prokop, I. Gablech, M. Pavlik, et al., A self-compensating system for fixed pattern noise reduction of focal plane arrays of infrared bolometer detectors, *Procedia Eng.* 168 (2016) 1007–1011.
- [29] K.C. Balam, D.A. Westly, M. Davanco, K.E. Grutter, Q. Li, T. Michels, et al., The nanolithography toolbox, *J. Res. Natl. Inst. Stan.* 121 (2016) 464–475.
- [30] T. Mei, P. Neuzil, G. Karunasiri, W. Zeng, Approach to measure thermal efficiency of bolometer sensors, *Appl. Phys. Lett.* 80 (2002) 2183–2185.

## Biographies

**Jan Pekárek** was born in Ostrava, Czech Republic, in 1984. He received the M.S. and Ph.D. degrees in electrical engineering from the Brno University of Technology in 2008 and 2014, respectively. He is currently a Junior researcher at Centre of SIX at Brno University of Technology and at Central European Institute of Technology. His current research interest includes development and fabrication of devices based on micro- or nanostructured surfaces. He is an author and co-author of 32 publications and his h-index is 5.

**Pavel Neuzil** obtained his PhD in Electrical Engineering from Czech Technical University, Czech Republic. He worked at University of Illinois, Stanford University (both USA), A\*STAR institutes in Singapore, KIST-Europe, Germany, Brno University of Technology, Czech Republic and Northwestern Polytechnical University, P.R. China. His research interests are advanced MEMS and nanotechnology for applications such as magneto optical recording and thermal imaging as well as medical devices for molecular diagnostics such as portable real-time PCR. He is a co-author of 70 journal publications and co-inventor of 10 patents.

## Příloha 6

SVATOŠ, V. et al. Precise determination of thermal parameters of a microbolometer. *Infrared Physics and Technology*, 2018, vol. 93, pp. 286-290. ISSN 1350-4495.

### ABSTRAKT

Vyhodnocení tepelných vlastností mikrobolometrů, jako jsou tepelná kapacita, tepelná vodivost, časová konstanta a odezva na infračervené záření, je nesmírně důležité, neboť tyto vlastnosti přímo ovlivňují výkon mikrobolometru. Zde uvádíme techniku jejich měření pomocí minimalizace vlastního ohřevu, což vede k jejich přesnému stanovení pomocí měření založeném na Wheatstoneově můstku, který obsahoval mikrobolometr. Výstupy můstku byly od sebe odděleny diferenčním napěťovým předzesilovačem, jehož výstup byl zpracován lock-in zesilovačem. Výstup z lock-in zesilovače jako funkce amplitudy střídavého signálu poskytuje amplitudu tepelné vodivosti mikrobolometru. Teplotní odezva mikrobolometru na pulzní signál poskytla hodnotu časové konstanty a tím i její tepelnou kapacitu. Na závěr jsme extrahovali odezvu mikrobolometru na infračervené záření použitím kalibrovaného zdroje infračerveného záření. Metoda byla experimentálně ověřena pomocí vyrobeného mikrobolometru, který vykazoval vynikající shodu s analytickým řešením.



## Regular article

## Precise determination of thermal parameters of a microbolometer

Vojtěch Svatoš<sup>a,b</sup>, Imrich Gablech<sup>a,b</sup>, Jan Pekárek<sup>a,b</sup>, Jaroslav Klempa<sup>a,b</sup>, Pavel Neuzil<sup>a,b,c,\*</sup><sup>a</sup> Central European Institute of Technology, Brno University of Technology, Purkyňova 123, 61200 Brno, Czech Republic<sup>b</sup> Brno University of Technology, Faculty of Electrical Engineering and Communication, SIX Centre, Department of Microelectronics, Technická 3058/10, 61600 Brno, Czech Republic<sup>c</sup> Northwestern Polytechnical University, 127 West Youyi Road, Xi'an, Shaanxi, PR China

## ARTICLE INFO

## Keywords:

Microbolometer  
MEMS  
Thermal parameters  
Lock-in amplifier  
IR response

## ABSTRACT

Determination of microbolometer thermal properties such as thermal capacitance, conductance, time constant, and IR responsivity is of the utmost importance as they directly influence microbolometer performance. Here we show a technique to measure them by using a minimized self-heating effect, thus leading to their precise determination via measurements based on an AC-biased Wheatstone bridge containing a microbolometer. The bridge outputs were subtracted from each other by a differential voltage preamplifier with its output processed by a lock-in amplifier. The lock-in amplifier output as a function of the amplitude of AC bias provided an amplitude of microbolometer thermal conductivity. A microbolometer temperature response to pulse irradiation of its membrane provided the value of its thermal time constant and, thus, its thermal capacitance. Finally, we also extracted microbolometer responsivity using a blackbody IR source. The method was experimentally verified using a micromachined bolometer, which showed excellent agreement with the analytical solution.

## 1. Introduction

Midrange infrared (IR) with a wavelength range from ( $\approx 8$  to  $\approx 14$ )  $\mu\text{m}$  has a wide range of applications such as security and commercial uses. Among security applications, IR surveillance can help firefighters look for people in dense smoke or to identify fire hot spots to extinguish. IR devices can also help police identify cars recently arrived in a parking area. Typical commercial applications are as an aid for driving in poor visibility, looking for hot spots in an electrical power distribution system, finding heat leakages from buildings to conserve energy, precise tumor identification during surgery, and many others. The development of midrange IR detectors dates back to 1947 with the invention of a pneumatic IR detector, called the “Golay cell [1]”. In 1984 [2], and following an improvement in 1986 [3], a new concept of a microbolometer as part of a microelectromechanical system (MEMS) device was introduced. This allowed the integration of an array of microbolometers with read-out integrated circuits into a focal plane array, i.e., a true IR imager. The microbolometer, operating in a vacuum, consists of an IR-absorbing thermally isolated membrane integrated with an embedded temperature sensor. Most commonly, the resistive temperature detector (RTD) is made of metal such as Ti [2], phase transition materials such as  $\text{VO}_x$  [4], or semiconductors such as amorphous Si [5]. Their resistance amplitude  $R$  changes with temperature change  $\Delta T$  as per the equation

$$R = R_0(1 + \alpha \cdot \Delta T) \quad (1)$$

where  $R_0$  is sensor resistance at ambient temperature  $T_0$  and  $\alpha$  is its temperature coefficient of resistance. Microbolometer membrane  $\Delta T$  expressed as change of sensor resistance change ( $\Delta R$ ) is:

$$\Delta R = R - R_0 = R_0 \cdot \alpha \cdot \Delta T \quad (2)$$

The  $\Delta T$  value is linearly proportional to the amplitude of absorbed IR radiation ( $P_{\text{IR}}$ ) and inverse to the value of the microbolometer thermal conductance ( $G$ ) [6], making the  $G$  amplitude the parameter of utmost importance

$$\Delta T = \frac{P_{\text{IR}}}{G} \quad (3)$$

Other important parameters are thermal capacitance ( $H$ ) and the thermal time constant ( $\tau$ ), which determine the rate of the microbolometer response as

$$\tau = \frac{H}{G} \quad (4)$$

Thus, all three parameters  $G$ ,  $H$ , and  $\tau$  have to be determined to optimize the microbolometer performance.

A well-established technique to determine specific heat and thermal conductivity of thin film materials and structures based on  $3\omega$  method were proposed earlier [7,8]. The structures were thermally modulated

\* Corresponding author at: Northwestern Polytechnical University, 127 West Youyi Road, Xi'an, Shaanxi, PR China.

E-mail address: [pavel.neuzil@nwpu.edu.cn](mailto:pavel.neuzil@nwpu.edu.cn) (P. Neuzil).

making this method especially suitable for thin film materials, less for slow MEMS devices such as IR microbolometers. A single measurement-based method to determine parameters  $G$ ,  $H$ , and  $\tau$  was proposed and demonstrated by biasing an unbalanced Wheatstone bridge, including a microbolometer with an RTD sensor made of Ti, by a single voltage pulse with a bias amplitude ( $V_B$ ) with time period  $\ll \tau$  at a pressure of  $\approx 7.7 \times 10^{-4}$  Pa [9]. The microbolometer behavior is governed by a differential heat balance equation

$$H \frac{d\Delta T}{dt} + G \cdot \Delta T = P_J - P_R = \frac{V_B^2}{4R_0} - P_R, \quad (5)$$

where  $P_J = \frac{V_B^2}{4R_0}$  is dissipated joule heat in the microbolometer resistor with an actual value of  $R_0$ . At a constant pressure of  $\leq 5$  Pa, heat convection due to energy transfer by the movement of gas molecules surrounding the membrane and radiation losses  $P_R$  at ambient temperature of 25 °C are also negligible [10]. The Eq. (5) with neglected amplitude of  $P_R$  can be solved as

$$\Delta T = \frac{V_B^2}{4G \cdot R_0} \left[ 1 - \exp\left(-\frac{t}{\tau}\right) \right], \quad (6)$$

where  $t$  is time. The researchers expressed the Wheatstone bridge output in simplified form as function of time [9]

$$\Delta V = \frac{\alpha \cdot V_B^3}{16G \cdot R_0} \left[ 1 - \exp\left(-\frac{t}{\tau}\right) \right] \quad (7)$$

With knowledge of  $V_B$ ,  $R_0$  and  $\alpha$  of  $\approx 1$  V,  $\approx 3.9$  k $\Omega$ , and  $\approx 0.0025$  K $^{-1}$ , respectively, researchers extracted the value of  $G$  from Eq. (7) at steady-state and the value of  $H$  from the pulse response slope for  $t = 0$  s. The thermal time constant was calculated using Eq. (4). The proposed method was simple; however, during the measurement the  $P_J$  amplitude was  $\approx 64.1$   $\mu$ W causing the microbolometer membrane with calculated  $G$  value of  $\approx 7.8 \times 10^{-7}$  W K $^{-1}$  warming by the excessive value of  $\Delta T \approx 82.2$  K affecting the  $R_0$  value, which was considered to be constant. The modulated amplitude of  $R_0$  value due to  $\Delta T$  resulted in a measurement error as Eq. (7) assumes  $R_0$  to be constant. Lowering the  $V_B$  amplitude does lower the error due to smaller variation of  $R$  amplitude, but the measurement precision suffered due to the low output voltage of the system and signal-to-noise ratio (SNR) because the system response is linearly proportional to the amplitude of  $V_B$ .

In addition, at ambient temperature, the radiation determined by the Stefan–Boltzmann law can no longer be neglected. The amplitude of  $P_J$  is then split between power loss due to thermal conduction ( $P_C$ ) and amplitude of  $P_R$ :

$$P_J = P_C + P_R = G \cdot \Delta T + A \cdot \varepsilon \cdot \sigma \cdot T^4 \quad (8)$$

where  $A = 2a^2$  is the total area of a microbolometer membrane with square shape and side length of  $a$  with neglecting its sidewalls area,  $\varepsilon$  is the emissivity of the microbolometer membrane material,  $\sigma$  is the Stefan–Boltzmann constant with value of  $\sigma \approx 5.6704 \times 10^{-8}$  W m $^{-2}$  K $^{-4}$ , and  $T$  is the thermodynamic temperature. This situation becomes even worse once the microbolometer membrane is heated up by  $\Delta T \approx 82.2$  K as the  $P_R$  amplitude increases by a factor of  $\approx 2.7$ .

A method to determine all thermal parameters, such as  $G$ ,  $H$ , and  $\tau$ , based on a short voltage pulse with duration of  $\approx 60$   $\mu$ s was proposed [11]. This technique allowed employment of  $V_B$  with amplitude up to  $\approx 5$  V, resulting in an improved SNR. Due to short pulse duration, the self-heating effect was negligible as it resulted in minimal influence by variation of  $R$ . Modern microbolometers use two [12,13] or three-level membrane configurations or carbon nanotubes as IR-sensitive materials [14] and their responses to the  $P_J$  are more complicated. Therefore the short pulse technique [11] cannot be utilized and the long pulse method [9] does not provide results with sufficient precision.

Here we show a technique of precise determination of  $G$ ,  $H$ , and  $\tau$  of an AC-powered Wheatstone bridge containing a microbolometer device with the bridge output signal processed by lock-in amplification

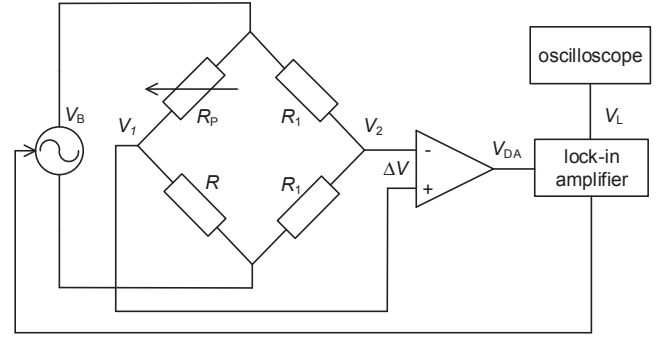


**Fig. 1.** Schematic of the system used for microbolometer testing. The microbolometer was connected into a Wheatstone bridge powered by an AC signal supplied by a lock-in amplifier. The balancing resistor  $R_p$  represents two potentiometers with maximum resistance value of 20 k $\Omega$  and 100  $\Omega$ , respectively, each with 20 turns for fine-tuning of the bridge balance. The  $R_1$  represents two resistors with the fixed value of 20 k $\Omega$  and  $R$  stands for microbolometer resistance. The voltage difference of the bridge outputs was amplified by a differential voltage preamplifier with gain  $B$  set to 1000, its output voltage processed by a lock-in amplifier, and its output recorded by an oscilloscope.

technique. The colossal SNR of a lock-in amplifier allowed us to perform the microbolometer testing using a  $V_B$  value as low as  $\approx 10$  mV root mean square (RMS). This low amplitude of  $V_B$  resulted in  $P_J$  of  $\approx 26$  nW, leading to marginal microbolometer membrane temperature increase of  $\approx 59$  mK and allowing precise determination of the value of  $G$  with  $P_R$  having a minimized effect on the measurement. The value of  $\tau$  was then extracted by observing the transient response of the microbolometer output to modulated external power supply and calculated  $H$  using Eq. (4) as  $H = \tau G$ .

## 2. Results and discussion

### 2.1. Theory and analytical solution

Let us consider the microbolometer connected to a Wheatstone bridge powered by an AC voltage with an amplitude of  $V_B$  RMS with its outputs processed by a differential amplifier with a gain factor of  $B$  and its output signal processed by a lock-in amplifier with gain of  $S$  (Fig. 1). The lock-in amplifier output voltage ( $V_L$ ) can be expressed as function of  $\Delta T$  and  $V_B$  (see Supplementary S1 for derivation of the equation) as

$$V_L = 10 \frac{\left[ \frac{R_0(1 + \alpha \Delta T)}{R_0(1 + \alpha \Delta T) + R_0} - \frac{1}{2} \right] V_B \cdot B}{S} \quad (9)$$

defining transfer function of entire system. For small values of  $\Delta T$  the value of  $\alpha \Delta T \ll 1$  the Eq. (9) can be simplified as

$$V_L = 10 \frac{\alpha \Delta T}{4 \cdot S} V_B \cdot B \quad (10)$$

The bridge was power by an AC voltage frequency  $\gg$  than the one corresponding to the  $\tau$  of the microbolometer. As the microbolometer membrane cannot be modulated by the AC, the total  $P_J$  can be considered as  $P_J = \frac{V_B^2}{4R_0}$  warming up the membrane by  $\Delta T = \frac{P_J - P_R}{G}$ . Assuming the microbolometer membrane had the size of  $(25 \times 25)$   $\mu$ m $^2$  and  $\varepsilon$  of 0.48 (as per Ref. [15]), the amplitude of  $P_R$  at  $T_0$  would be  $\approx 251$  nW. This  $P_R$  would cause the microbolometer membrane with  $G$  value of 180.4 nW K $^{-1}$  (in Ref. [16]) to increase its membrane temperature only by  $\approx 1.39$  K. Nevertheless, as the  $\Delta T$  during the microbolometer measurement is minimal, the  $P_R$  does not significantly change; thus, Eq. (8) can be simplified to  $G = P_C / \Delta T$  as the  $P_R$  only causes an offset of the  $\Delta V$ . We can then express  $V_L$  as function of  $G$  (Supplementary S1) as

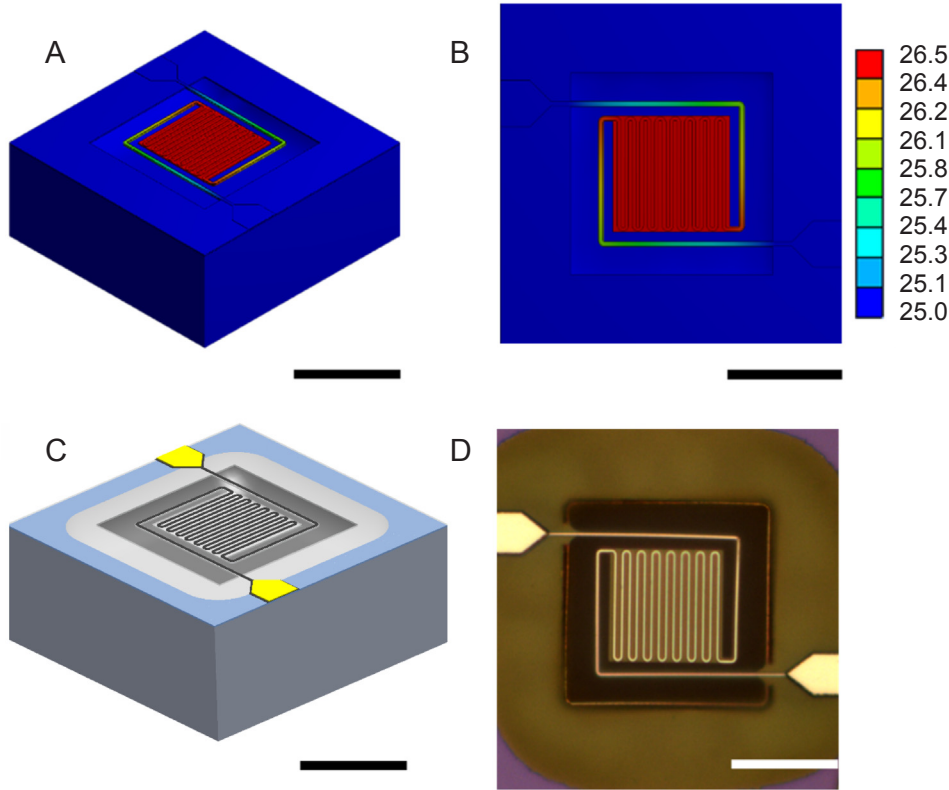


**Fig. 2.** Finite element modeling of the microbolometer membrane temperature using an AC-powered microbolometer with 100 mV RMS with (A) isometric and (B) top view. The temperature values are depicted in units of °C. First, we created the 3D model according to the actual device to be fabricated. The metal trace made of titanium with thickness of 80 nm and width of 0.8 μm was sandwiched between two layers of SiO<sub>2</sub> with same thickness of 0.25 μm. The microbolometer legs had width of 1.2 μm and length of 62 μm, and the membrane had size of (25 × 25) μm<sup>2</sup>. The silicon substrate had size of (160 × 180) μm<sup>2</sup> and thickness of 75 μm (for simulation purpose only). The membrane was undercut by 25 μm both vertically and laterally. We set the temperature at the chip bottom to a fixed value of 25 °C. The electro-thermal simulation was performed for  $V_B = 100$  mV RMS, showing the temperature distribution and the minimal temperature increase of ≈ 1.5 °C. (C) 3D model of microbolometer structure and (D) optical micrographs of an actual fabricated microbolometer. The bar represent length of 25 μm.

$$V_L = 10 \frac{\alpha \cdot V_B^3 \cdot B}{16 \cdot S \cdot G \cdot R_0} \quad (11)$$

## 2.2. Microbolometer design and fabrication

With an assumption of a microbolometer membrane with size of (25 × 25) μm<sup>2</sup>, its legs made of SiO<sub>2</sub> and with width, thickness, and length of 1.2 μm, 0.424 μm, and 62 μm, respectively, we calculated the predicted microbolometer parameters  $G$ ,  $H$ , and  $\tau$  using the analytical model described in Supplementary S2 as  $G = 57.8$  nW K<sup>-1</sup>,  $H = 0.55$  nJ K<sup>-1</sup>, and  $\tau = 9.6$  ms. We also performed an electro-thermal simulation for the model using the identical dimension for  $V_B$  of 100 mV RMS. The resulted temperature distribution of the final element modeling is shown in Fig. 2A and B and the temperature increase is estimated to be ≈ 1.5 °C.

The actual device layout was generated by a script-based Nanolithography Toolbox [16]. The chip with microbolometers was fabricated using Ti RTDs [17,18] embedded in a SiO<sub>2</sub> layer using the conventional Si bulk-micromachining techniques shown earlier [14]. Once the fabrication was almost completed and with the membrane still firmly attached to the substrate, we measured the  $R_0$  and  $\alpha$  values using a probe station with a temperature-controlled wafer holder (Supplementary Section 1 in Ref. [14]). The corresponding measured values of  $R_0$  and  $\alpha$  were ≈ 9.58 kΩ and ≈ 0.0023 K<sup>-1</sup>, respectively. The wafer was then diced into individual chips by a diamond blade dicing saw and individual chips were exposed to vapors of XeF<sub>2</sub> until the membranes were completely released as schematically shown by three dimensional drawing (Fig. 2C) and fabricated device in the microphotograph in Fig. 2D. The chips were mounted onto a leadless chip carrier with 68 pads and electrically connected with Al wires using an ultrasonic wire-bonding. The packaged microbolometer devices were subsequently placed into a vacuum chamber with either glass or a Ge window and evacuated to pressure of  $4.3 \times 10^{-2}$  Pa, well below the limiting pressure of 5 Pa, thus eliminating the thermal convection as well as thermal conduction of the surrounding environment [10].

## 2.3. Measurement and discussion

The microbolometer with parameters described in previous paragraph was then connected into a Wheatstone bridge as per Fig. 1 and balanced by two adjustable resistors, one with maximum resistance of ≈ 20 kΩ for a rough balance of the bridge and a second one with maximum resistance of ≈ 100 Ω for bridge fine-tuning: both were types with 20 turns. The bridge was powered by a sine wave generator with an adjustable amplitude of  $V_B$  RMS provided by a lock-in amplifier. Both bridge outputs were connected to two inputs of a differential voltage preamplifier with gain set to 1000. We also activated an internal band pass filter set to 10 dB/decade with low and high cut-off frequencies set to 300 Hz and 3 kHz, respectively, to further improve the SNR. The  $\Delta V$  signal was processed by a lock-in amplifier with  $S$  value set to 0.1 V. We numerically determined the Eq. (9) as function of  $V_B$  and  $\Delta T$  (Supplementary S3):

$$V_L = 57.44 \cdot \Delta T \cdot V_B \quad (12)$$

We measured an amplitude of the  $V_L$  as a function of the  $V_B$  in a set range from 10 mV RMS to 100 mV RMS with a set step of 10 mV RMS. This experiment was repeated three times and we plotted the  $V_L$  as a function of  $V_B$  (Fig. 3) and performed the curve-fitting using a polynomial function of third order with first and second coefficients set to zero based on Eq. (11) as

$$V_L = A_3 \cdot V_B^3 + A_0, \quad (13)$$

with  $A_3 = 10 \frac{B \cdot \alpha}{16 \cdot S \cdot G \cdot R_0}$  and  $A_0$  is the bridge offset due to its imbalance, which is always presented. The  $A_3$  fitting coefficient had value of  $(3633.1 \pm 4.7) \text{ V}^{-2}$ , resulting in a  $G$  value of  $(41.23 \pm 0.05) \text{ nW K}^{-1}$ , both (mean ± fitting error).

A vacuum chamber equipped with a glass window was placed under an optical microscope with an objective lens magnification of 50× and numerical aperture of 0.55. We then monitored the Wheatstone bridge response once the microbolometer was exposed to the blue light with principal wavelength of 470 nm from the microscope. Even though the

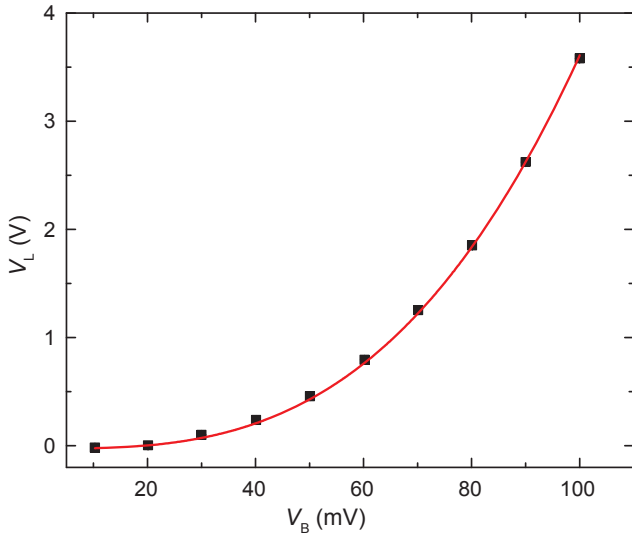


**Fig. 3.** Microbolometer response at the lock-in amplifier output as a function of  $V_B$  RMS, measured three times (black squares). We performed a function curve fit (red line) using polynomial function of third order  $V_L = A_0 + A_1 \cdot V_B + A_2 \cdot V_B^2 + A_3 \cdot V_B^3$  setting values of linear and parabolic coefficient  $A_1$  and  $A_2$  to zero. The fitting value of  $A_3 = (3633.0 \pm 4.7) \text{ V}^{-2}$  (mean  $\pm$  fitting error) resulted in a  $G$  value of  $(41.23 \pm 0.05) \text{ nW K}^{-1}$ . The nearly perfect fitting  $R^2$  value of 0.99999 suggests that the fitting model is correct.

microbolometer membrane absorption at the light emitting diode (LED) wavelength is rather limited, the heating the microbolometer by a LED with  $V_B$  set to 0.1 V caused the change of  $V_L$  ( $\Delta V_L$ ) of  $(783.31 \pm 0.65) \text{ mV}$  (mean  $\pm$  standard deviation). We applied Eq. (12) and we found corresponding  $\Delta T$  value as  $(136.47 \pm 0.11) \text{ mK}$  (mean  $\pm$  standard deviation). As we already determined value of  $G$  to be  $(41.23 \pm 0.05) \text{ nW K}^{-1}$  (mean  $\pm$  fitting error), we can now calculate dissipated power in the membrane due incident light from a blue LED as  $\approx 5.63 \text{ nW}$ .

We performed the experiment of detecting the amplitude of  $\Delta V_L$  with blue light off and on with different value of  $V_B$  value from 20 mV RMS to 100 mV RMS with a step of 20 mV (Fig. 4). We did the curve-fitting using an exponential function of first-order to the  $\Delta V_L$  signal

$$\Delta V_L = V_{L2} + (V_{L1} - V_{L2}) \cdot e^{-\frac{t-t_0}{\tau}} \quad (14)$$

where  $V_{L1}$  and  $V_{L2}$  are the lock-in amplifier output voltages without and with irradiation by an LED, respectively and  $t_0$  is time when the light was switched on. The value of  $\tau$  was determined as  $\tau = (15.46 \pm 0.56) \text{ ms}$  (mean  $\pm$  standard deviation from 30 measurements) and, with modified Eq. (4) ( $H = \tau \cdot G$ ), we also calculated the value of  $H = (0.637 \pm 0.34) \text{ nJ K}^{-1}$ , (mean  $\pm$  standard deviation) and as predicted due to small amplitude of  $\Delta T$  the value of  $V_B$  had no influence on the  $\tau$  amplitude.

We also used this measurement to determine the system power resolution. The  $V_L$  amplitude with  $V_B = 100 \text{ mV}$  RMS had a value of  $(783.31 \pm 0.65) \text{ mV}$  (mean  $\pm$  standard deviation) and the sensitivity can be defined as  $3 \times$  standard deviation value, which is  $1.95 \text{ mV}$ . With the system transfer function of  $\approx 57.44 \text{ V V}^{-1} \text{ K}^{-1}$  (Supplementary Section 3) and  $G$  value of  $(41.23 \pm 0.05) \text{ nW K}^{-1}$ , both (mean  $\pm$  fitting error), the  $1.95 \text{ mV}$  of  $3 \times$  standard deviation corresponded to the  $\Delta T$  value of  $\approx 340 \mu\text{K}$  resulting in system power resolution ( $\Delta P$ ) of  $\approx 14 \text{ pW}$ . This  $\Delta P$  value could be further lowered by increase of the lock-in amplifier sensitivity, which would require thermal shield of the its vacuum chamber to suppress its temperature fluctuation.

Finally, we replaced the glass window of the vacuum chamber with a window made of Ge and exposed the microbolometer to IR radiation from a blackbody with an aperture  $d$  of  $\approx 10.5 \text{ mm}$  and temperature set

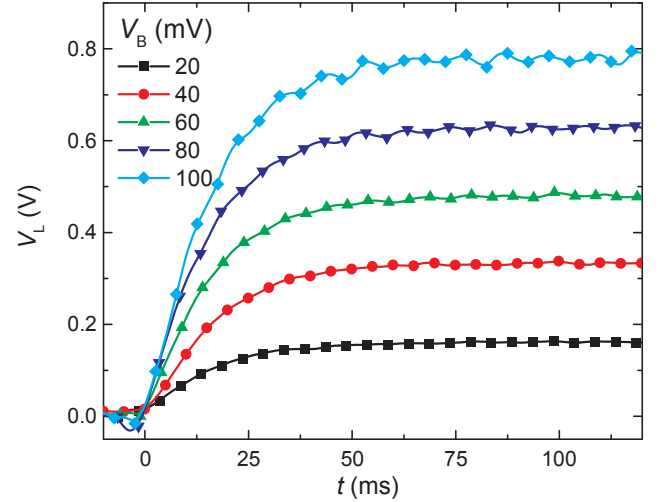


**Fig. 4.** Microbolometer response at the lock-in amplifier output  $V_L$  as a function of time with microbolometer on/off illuminated by a LED dissipated power in the microbolometer of  $\approx 5.63 \text{ nW}$ . We set the  $V_B$  amplitude as (20, 40, 60, 80, and 100) mV RMS marked by black squares, red circles, green up triangles, dark-blue down triangles, and light-blue rotated squares, respectively. We performed function curve-fitting using Eq. (12) and extracted value of  $\tau = (15.46 \pm 0.56) \text{ ms}$  (mean  $\pm$  standard deviation from 30 measurements), exhibiting no influence of  $V_B$  on the  $\tau$  value in the entire range of used  $V_B$  values. (For interpretation of the references to colour in this figure legend, the reader is referred to the web version of this article.)

to  $200^\circ\text{C}$ ,  $300^\circ\text{C}$ , and  $400^\circ\text{C}$ , respectively. The Wheatstone bridge was biased with  $V_B$  set to 50 mV RMS warming up the microbolometer membrane only by  $\approx 160 \text{ mK}$ . We monitored the  $\Delta V_L$  amplitude while the microbolometer was irradiated by a blackbody with different set temperatures and distances ( $D$ ). The distance was modulated by the number ( $n$ ) of spacers with identical thickness  $w$  of  $\approx 15.2 \text{ mm}$  placed between the chamber and the blackbody from  $n = 1$  to  $n = 8$ , which varied the distance change from  $D = D_0$  to  $D = D_0 + n w$ .  $D_0$  is minimal distance between the blackbody and the microbolometer membrane and estimated to be  $\approx 30 \text{ mm}$  (Fig. 5A). We calculated the amplitude of incident IR power radiation absorbed by the microbolometer membrane as was done previously [14]:

$$P_{\text{IR}} = \alpha^2 \cdot \varepsilon_{\text{bb}} \cdot \tau_{\text{F}} \cdot M \left[ \frac{\left(\frac{d}{2}\right)^2}{D^2 + \left(\frac{d}{2}\right)^2} \right] \quad (15)$$

where  $\varepsilon_{\text{bb}}$  is the emission of blackbody radiation ( $\approx 0.95$  as per manufacturer's datasheet),  $\tau_{\text{F}}$  is the average experimentally determined transmittance of the Ge window ( $\tau_{\text{F}} \approx 0.95$ ), and  $M$  is the integrated radiant excitation of the blackbody according to Planck's radiation law ( $\approx 2588 \text{ W m}^{-2}$ ) [15]. We plotted the microbolometer system response as a function of the number of spacers of the function of  $P_{\text{IR}}$  (Fig. 5B) and the linear curve-fitting slope

$$\mathfrak{R}_{\text{IR}} = \frac{\Delta V_L}{P_{\text{IR}}} \quad (16)$$

which provided us with system responsivity  $\mathfrak{R}_{\text{IR}}$  of  $(5.55 \pm 0.38) \text{ MV W}^{-1}$ ,  $(7.42 \pm 0.21) \text{ MV W}^{-1}$ , and  $(7.94 \pm 0.11) \text{ MV W}^{-1}$  for blackbody temperatures of  $200^\circ\text{C}$ ,  $300^\circ\text{C}$ , and  $400^\circ\text{C}$ , respectively, all (mean  $\pm$  fitting error).

### 3. Conclusion

We demonstrated a method to extract thermal parameters such as  $G$ ,  $H$ , and  $\tau$  as well as  $\mathfrak{R}_{\text{IR}}$  from the microbolometer using the lock-in amplification technique. The proposed method is applicable with a

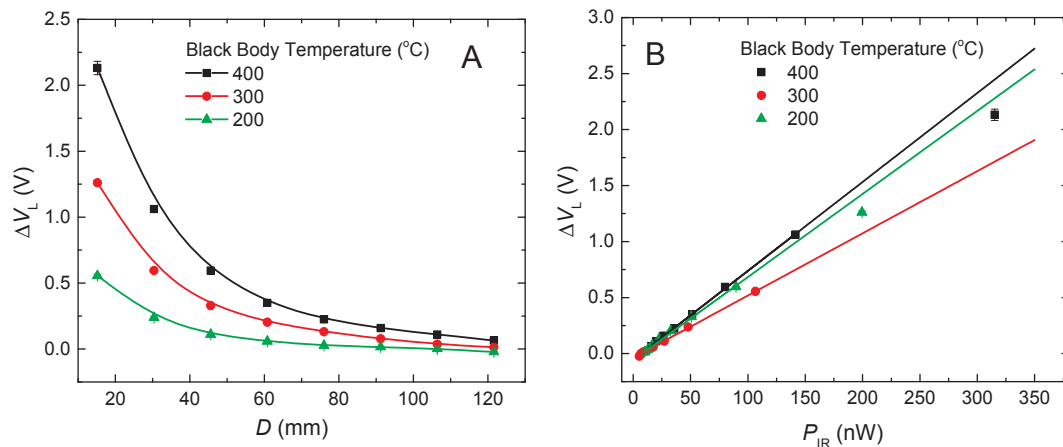


Fig. 5. Microbolometer response to the IR radiation (A) as a function of the distance with black body temperature as parameter. (B) Microbolometer response at the lock-in amplifier output as a function of incident IR radiation power.

biasing microbolometer with small voltage that causes negligible warming of its membranes during the measurement. This suppresses the self-heating effect and loses due to radiation change during the measurement and, thus, provides a precise value of the  $G$  parameter. With intentionally increased power dissipated in the microbolometer membrane by a step function, the transient analysis of the system output provided the  $\tau$  value as well as  $H$ . Finally, the microbolometer response to irradiation with IR from a black body source provided the IR responsivity in a range from  $(5.55 \pm 0.38) \text{ MV W}^{-1}$ ,  $(7.42 \pm 0.21) \text{ MV W}^{-1}$  to  $(7.94 \pm 0.11) \text{ MV W}^{-1}$ . This measurement demonstrated that the proposed method is suitable for applications where extreme sensitivity is required. We also determined the system having an excellent power resolution of  $\approx 14 \text{ pW}$ . This could be increased further by lock-in amplifier setting, making this one of the most sensitive calorimeters.

#### Acknowledgment

Authors would like to acknowledge financial support of GACR Project Number 17-20716S, support of Czech Ministry of Education under grant LO1401, technical support of Nano+, Centrum SIX, as well as help from staff at the Center for Nanoscale Science and Technology of NIST, Gaithersburg, MD, USA. Finally, the authors are also grateful to Pavel Podešva for his help with graphical design.

#### Conflict of interest

Authors declare no conflict of interested related to the submitted manuscript.

#### Appendix A. Supplementary material

Supplementary data associated with this article can be found, in the online version, at <https://doi.org/10.1016/j.infrared.2018.07.037>.

#### References

- [1] M.J.E. Golay, A pneumatic infra-red detector, *Rev. Sci. Ins.* 18 (1947) 357–362.
- [2] K.C. Liddiard, Thin-film resistance bolometer IR detectors, *Infrared Phys.* 24 (1984) 57–64.

- [3] K.C. Liddiard, Thin-film resistance bolometer IR detectors .2, *Infrared Phys.* 26 (1986) 43–49.
- [4] B. Cole, R. Horning, B. Johnson, K. Nguyen, P.W. Kruse, M.C. Foote, High performance infrared detector arrays using thin film microstructures, in: *Proceedings of 1994 IEEE International Symposium on Applications of Ferroelectrics*, 1994, pp. 653–656.
- [5] A.J. Syllaios, T.R. Schimert, R.W. Gooch, W.L. McCardel, B.A. Ritchey, J.H. Tregilgas, Amorphous silicon microbolometer technology, *MRS Proc.* 609 (2011) A14–14.
- [6] P.W. Kruse, Chapter 2 principles of uncooled infrared focal plane arrays, in: P.W. Kruse, D.D. Skatrud (Eds.), *Semiconductors and Semimetals*, Elsevier, 1997, pp. 17–42.
- [7] L. Lu, W. Yi, D.L. Zhang, 3 Omega method for specific heat and thermal conductivity measurements, *Rev. Sci. Ins.* 72 (2001) 2996–3003.
- [8] T. Yamane, N. Nagai, S. Katayama, M. Todoki, Measurement of thermal conductivity of silicon dioxide thin films using a 3 omega method, *J. Appl. Phys.* 91 (2002) 9772–9776.
- [9] X. Gu, G. Karunasiri, G. Chen, U. Sridhar, B. Xu, Determination of thermal parameters of microbolometers using a single electrical measurement, *Appl. Phys. Lett.* 72 (1998) 1881–1883.
- [10] X. He, G. Karunasiri, T. Mei, W.J. Zeng, P. Neuzil, U. Sridhar, Performance of microbolometer focal plane arrays under varying pressure, *IEEE Electron Device Lett.* 21 (2000) 233–235.
- [11] P. Neuzil, T. Mei, Evaluation of thermal parameters of bolometer devices, *Appl. Phys. Lett.* 80 (2002) 1838–1840.
- [12] D.F. Murphy, A. Kennedy, M. Ray, R. Wyles, J. Wyles, J.F. Asbrock, C. Hewitt, D.V. Lue, T. Sessler, J.S. Anderson, D. Bradley, R. Chin, H. Gonzales, C.L. Pere, T. Kostrzewa, Resolution and sensitivity improvements for VOx microbolometer FPAs, in: *AeroSense 2003*, SPIE, 2003, pp. 12.
- [13] L. Hyung-Kew, Y. Jun-Bo, Y. Euisik, J. Sang-Baek, Y. Yoon-Joong, L. Wook, K. Sang-Gook, A high fill-factor infrared bolometer using micromachined multilevel electrothermal structures, *IEEE Trans. Electron Devices* 46 (1999) 1489–1491.
- [14] V. Svatoš, I. Gablech, B.R. Ilic, J. Pekárek, P. Neuzil, In situ observation of carbon nanotube layer growth on microbolometers with substrates at ambient temperature, *J. Appl. Phys.* 123 (2018) 114503.
- [15] T. Mei, P. Neuzil, G. Karunasiri, W. Zeng, Approach to measure thermal efficiency of bolometer sensors, *Appl. Phys. Lett.* 80 (2002) 2183–2185.
- [16] K.C. Balram, D.A. Westly, M. Davanco, K. Grutter, Q. Li, T. Michels, C.H. Ray, L. Yu, R. Kasica, C.B. Wallin, I. Gilbert, B.A. Bryce, G. Simelgor, J. Topolancik, N. Lobontiu, Y. Liu, P. Neuzil, V. Svatos, K.A. Dill, N.A. Bertrand, M. Metzler, G. Lopez, D.A. Czaplewski, L. Ocola, K. Srinivasan, S. Stavits, V. Aksyuk, J.A. Liddle, S. Krylov, B.R. Ilic, The nanolithography toolbox, *J. Res. Natl. Inst. Stand.* 121 (2016) 464–475.
- [17] I. Gablech, V. Svatoš, O. Caha, M. Hrabovský, J. Prašek, J. Hubálek, T. Šikola, Preparation of (001) preferentially oriented titanium thin films by ion-beam sputtering deposition on thermal silicon dioxide, *J. Mater. Sci.* 51 (2016) 3329–3336.
- [18] I. Gablech, O. Caha, V. Svatoš, J. Pekárek, P. Neuzil, T. Šikola, Stress-free deposition of [001] preferentially oriented titanium thin film by Kaufman ion-beam source, *Thin Solid Films* 638 (2017) 57–62.

## Příloha 7

BOUŠA, M. et al. Stress and charge transfer in uniaxially strained CVD graphene. *Physica Status Solidi B-Basic Solid State Physics*, 2016, vol. 253, no. 12, pp. 2355-2361. ISSN 0370-1972.

### ABSTRAKT

Mechanické vlastnosti grafenu připraveného metodou chemické depozice z plynné fáze (CVD) nejsou snadno srovnatelné s vlastnostmi téměř dokonalého grafenu připraveného mechanickým štěpením. V této práci prověříme mechanickou odolnost CVD grafenu (jednoduše naneseného nebo zabudovaného v polymerní matrici), přenášeného dvěma různými technikami, při zatížení v jedné ose se simultánním monitorováním Ramanovou mikroskopií. Množství přenosu dopovaného náboje a deformace je vyhodnocena za použití vektorové analýzy modifikované pro zatížení v jedné ose. Distribuce pnutí ve vzorcích se výrazně liší v důsledku procesu růstu a přenosu, který způsobuje vrásky a vady v CVD grafenu. U jednoduše podepřených vzorků je efektivita přenosu napětí obecně velmi nízká a změny v Ramanových spektrech jsou dominantní díky změnám v přenosu náboje, které vznikají při přeměně domén při zatížení. Naproti tomu vzorky pokryté dodatečnou vrstvou polymeru vykazují lepší účinnost přenosu napětí a změny úrovně dopovaného náboje jsou zanedbatelné. U plně integrovaných vzorků jsou změny v efektivitě přenosu napětí způsobeny velikostí grafenových domén definovaných prasklinami, záhyby a/nebo vráskami.

# Stress and charge transfer in uniaxially strained CVD graphene

Milan Bousa<sup>\*1,2</sup>, George Anagnostopoulos<sup>3</sup>, Elena del Corro<sup>1</sup>, Karolina Drogowska<sup>1</sup>, Jan Pekarek<sup>4</sup>, Ladislav Kavan<sup>1,2</sup>, Martin Kalbac<sup>1</sup>, John Parthenios<sup>3</sup>, Konstantinos Papagelis<sup>3</sup>, Costas Galiotis<sup>3,5</sup>, and Otakar Frank<sup>1</sup>

<sup>1</sup> J. Heyrovsky Institute of Physical Chemistry of the AS CR v.v.i., Dolejskova 2155/3, CZ 182 23 Prague 8, Czech Republic

<sup>2</sup> Faculty of Science, Department of Inorganic Chemistry, Charles University in Prague, Albertov 6, CZ 128 43 Prague 2, Czech Republic

<sup>3</sup> Institute of Chemical Engineering Sciences, Foundation for Research and Technology – Hellas (FORTH/ICE-HT), P.O. Box 1414, 265 04 Patras, Greece

<sup>4</sup> Faculty of Electrical Engineering and Communication, Centre of Sensors, Information and Communication Systems, Brno University of Technology, Technicka 3058/10, CZ 616 00 Brno, Czech Republic

<sup>5</sup> Department of Chemical Engineering, University of Patras, 26504 Patras, Greece

Received 15 April 2016, revised 20 June 2016, accepted 27 June 2016

Published online 20 July 2016

**Keywords** chemical vapour deposition, graphene, Raman spectroscopy, uniaxial tension

\* Corresponding author: e-mail milan.bousa@jh-inst.cas.cz, Phone: +420 266 053 955, Fax: +420 286 582 307

Mechanical properties of graphene prepared by chemical vapour deposition (CVD) are not easily comparable to the properties of nearly perfect graphene prepared by mechanical cleavage. In this work, we attempt to investigate the mechanical performance of CVD graphene (simply supported or embedded in polymer matrix), transferred by two different techniques, under uniaxial loading with simultaneous *in situ* monitoring by Raman microspectroscopy. The level of charge transfer doping and strain is assessed using the vector analysis modified for uniaxial strain. The strain distribution across the samples varies significantly, owing to the growth and transfer process, which induces wrinkles and faults in the CVD

graphene. In simply supported specimens, the stress transfer efficiency is generally very low and the changes in Raman spectra are dominated by variations in the charge transfer originating from the realignment of the domains on the substrate upon the application of strain. In contrast, samples covered with an additional polymer layer exhibit an improved stress transfer efficiency, and the alterations of charge doping levels are negligible. In fully embedded specimens, the variations in stress transfer efficiencies are caused by the size of the effective graphene domains defined by cracks, folds and/or wrinkles.

© 2016 WILEY-VCH Verlag GmbH & Co. KGaA, Weinheim

**1 Introduction** The presence of strain [1] and substrate-induced charge transfer doping [2] in graphene requires reliable methods for their monitoring and correct evaluation. Both strain and doping are known to alter the electronic structure of graphene, intentionally [3] as well as accidentally [4]. Hence, the ability to correctly assess and discriminate strain and doping in graphene and graphene-based devices is of utmost importance.

Raman spectroscopy has been established as a work horse for a swift and non-destructive analysis of graphene-related materials, providing not only basic characterisation in terms of the layer number or disorder in the samples, but also a more detailed information about the levels of doping or strain [5, 6]. Nevertheless, when these two

effects intermix, such an analysis can become very difficult. A method using the correlation of the G and 2D peak frequencies (Pos(G) and Pos(2D), respectively) has been introduced [7] and successfully tested recently [8–11] to separate biaxial strain from charge doping in various graphene samples. This approach, based on a vector analysis of the data points in the Pos(G)–Pos(2D) space, is relatively simple to conduct in certain well-defined cases, but the interpretation of the results has to be performed carefully when the experimental conditions deviate from the above mentioned biaxial strain–uniform doping situation. In that case, to monitor the changes in the system, other parameters of the G and 2D peaks have to be analysed, such as their widths (further defined as full width at half-maxima,

FWHM), or their intensity ratio [8]. Alternatively, another Raman feature, such as the 2D' peak can be included to provide more accuracy in the analysis [12].

The G peak corresponds to a first order Raman scattering process with a phonon of almost zero momentum. It is associated with the in-plane, doubly degenerate phonon from the transverse optical (TO) and longitudinal optical (LO) branches with  $E_{2g}$  symmetry at the Brillouin zone (BZ) centre ( $\Gamma$  point) [13]. Both frequency and width of the G mode are strongly influenced by the presence of doping [14, 15] and the application of stress [1, 16]. The increase of Pos(G) in both electron- and hole-doped graphene is caused by a non-adiabatic removal of the Kohn anomaly at  $\Gamma$  point [17], and the simultaneous decrease of FWHM(G) is caused by the Pauli blocking of phonon decay into electron-hole pairs. In general, strain causes G peak downshift under tension and upshift under compression with a rate of  $\sim 62 \text{ cm}^{-1}/\%$  for biaxial tension [18]. Under uniaxial strain the G peak splits into two components,  $G^-$  and  $G^+$ , with the shift rates of  $\sim -31$  and  $-10 \text{ cm}^{-1}/\%$ , respectively, for graphene on polymer substrates [19, 20], or of  $\sim -37$  and  $-19 \text{ cm}^{-1}/\%$ , respectively, for suspended graphene [21].

The 2D mode originates from a second-order triple resonant process between non-equivalent K points in graphene BZ, involving two zone-boundary, TO-derived phonons with opposite momenta [22, 23]. As shown recently, the 2D peak in suspended graphene is not fully symmetrical [24], which is even more pronounced in strained samples [25–28]. In a simplified one-dimensional picture of the 2D mode origin there are two dominant directions of the contributing phonon wavevectors – along  $K-\Gamma$  (so called inner) or  $K-M$  (outer) symmetry lines. Recent studies show a greater contribution of the inner processes [22, 25, 26, 29]. Nevertheless, a full two-dimensional description of the electronic peaks, phonon dispersion and matrix elements [22] has shown that the notation of inner or outer phonons is of a weaker relevance [28]. The 2D mode is dispersive, and its frequency changes with the excitation energy ( $E_L$ ) with the slope  $\partial \text{Pos}(2D)/\partial E_L \sim 100 \text{ cm}^{-1} \text{ eV}^{-1}$  [6]. The 2D peak is also sensitive to doping and mechanical stress but these effects manifest themselves differently from those of the G peak [1]. Strain causes the 2D peak shift in the same direction as the G peak, with the shift rates for biaxial strain larger by a factor of  $\sim 2.2\text{--}2.5$  [18, 30, 31]. Broadening and splitting of the 2D peak under uniaxial strain is very different to that of the G peak [25], but no such effects are observed for biaxial deformation [31]. Hole doping causes increase of Pos(2D) with a  $\partial \text{Pos}(2D)/\partial \text{Pos}(G) \sim 0.5\text{--}0.7$  [7, 14, 32], whereas electron doping causes only a negligible Pos(2D) change for  $n \leq 2 \times 10^{13} \text{ cm}^{-2}$  followed by a non-linear Pos(2D) decrease for higher n-doping levels [14, 32]. FWHM(2D) increases upon both p- and n-doping mainly due to electron–electron interactions, and also electron–phonon coupling strength [22, 33].

The effect of the grain size on the stress transfer was reported for mechanically exfoliated graphene, showing that a critical dimension of approximately  $4 \mu\text{m}$  (parallel with the

strain axis), is needed to achieve a full transfer of the applied strain from the substrate to the interior of the flake [34–36]. The strain-induced behaviour of CVD graphene is much less explored [37, 38], and the influence of absolute grain sizes is taken over by the wrinkles, which effectively rule the stress transfer, or rather the lack thereof, in this case [37]. The shift rate of 2D peak with strain was less than 25% of the shift rate corresponding to a full stress transfer ( $\sim 60 \text{ cm}^{-1}/\%$ ), in spite of the flake being covered by an additional polymer layer [37]. The analysis of the G peak was not possible due to intense overlapping peaks originating from the poly(ethylene terephthalate) (PET) substrate.

In the present work, we have focused on the separation of the effects of strain and doping in the Raman spectra of uniaxially strained CVD graphene prepared by two different transfer methods: (i) with separated grains introduced intentionally using an elastomer sacrificial layer (polyisobutylene, PIB) and (ii) the standard poly(methyl-methacrylate) (PMMA) technique. Apart from confirming the influence of grain sizes, both absolute and ‘wrinkle-limited’, we have shown the applicability of the strain-doping separation method also for uniaxially strained graphene samples.

**2 Methods** Graphene was grown on copper foils by low-pressure CVD as detailed in Ref. [39]. Alternatively, single layer graphene produced by CVD method and grown on copper foil supplied by AIXTRON Ltd. was used in the experiments.

The samples were transferred either by the dry transfer method using PIB as support polymer [40] or the standard PMMA method [41]. Scanning Electron Microscopy (SEM) images of the samples transferred by the two methods are shown in Fig. 1. The images were acquired using a HR-SEM Hitachi S4800 and a LEO SUPRA 35 VP scanning electron microscopes. In the case of PIB-assisted transfer, the SEM images were obtained in samples transferred to Si substrate due to a lower conductivity of the monolayer caused by the fragmentation during transfer.

As the target substrate for tensile experiments, clean and flexible PMMA beams of 3 mm thickness were used. They were previously spin coated with different polymers, SU8 photoresist (SU8 2000.5, MicroChem) or PMMA (3% in anisole, MicroChem). After the graphene transfer, some of the samples were covered by parylene C (120 nm thickness) or PMMA, in order to improve the strain transfer efficiency from the flexible substrate to the graphene flake. Further in text, the uncovered samples are denoted as simply supported and the covered ones as fully supported. Tensile strain in the graphene was imposed through a cantilever beam [19] or a four-point bending device [36]. In both cases, the strain response was monitored *in situ* using a micro-Raman setup with a  $100\times$  objective (N.A. = 0.9) (InVia Reflex, Renishaw or LabRAM HR, Horiba), and 514.5 nm (2.41 eV) or 632.8 nm (1.96 eV) excitation laser. The laser power was kept below 1.5 mW to avoid laser-induced heating. Typical spectra of single layer CVD graphene, as transferred onto SU8 and strained, are plotted in Fig. 2.

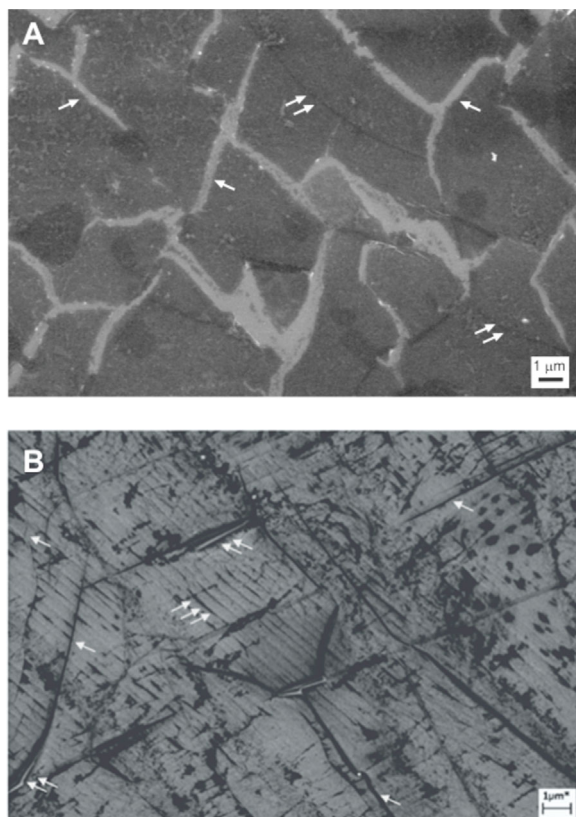


**Figure 1** SEM images of the CVD graphene samples transferred by PIB (A; on Si) and PMMA (B; on SU8). The scale bar is 1  $\mu\text{m}$ .

**3 Results** Figures 2 and 3 show the evolution of the monolayer graphene flake covered by parylene under uniaxial strain. In the Raman spectra (Fig. 2), downshifts of both the G and 2D peaks of graphene are visible in the spectrum strained to  $\varepsilon_m = 0.5\%$ . The Raman peaks of the polymers do not shift with strain. The measurement was done using incident laser polarisation parallel to the strain

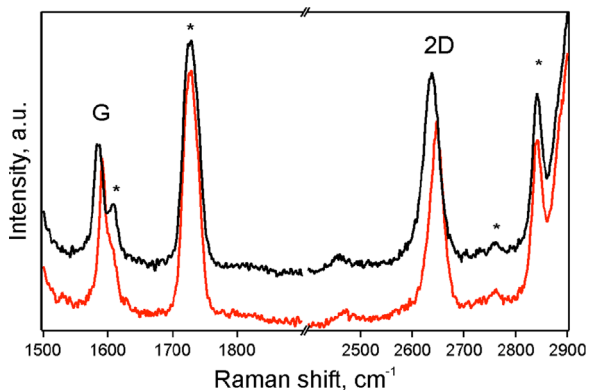


**Figure 2** Raman spectra of CVD graphene embedded between two polymer layers (SU8 at the bottom, parylene C on top) at 0 (red line) and 0.5% (black line) of nominal strain. Raman peaks of the polymer are marked by asterisks. Laser excitation energy was 1.96 eV.

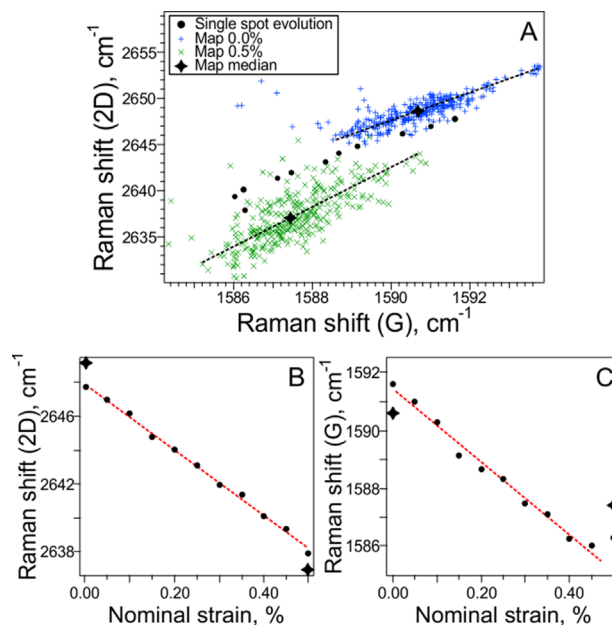


**Figure 3** Evolution of G and 2D peaks in the PIB-transferred, fully supported sample: (A) data points from large area mapping (0% – blue, 0.5% – green) with stars as their medians and full lines as least-squares line fits, black points follow the evolution on a single spot with 0.05% step, which is then detailed individually in (B) and (C) for the evolution of 2D and G peaks with strain. Laser excitation energy was 1.96 eV.

axis; no selection of the scattered light polarisation (via an ‘analyzer’) was employed. The graphene Raman peaks thus correspond to a sum of signals from all scattered polarisation directions and the shift rates can be taken from single Lorentzian shapes fitted to the Raman peaks. The evolution of the Raman shifts of the G and 2D peaks with strain is plotted in Fig. 3c and b, with their shift rates being 12.7 and 19.4  $\text{cm}^{-1}/\%$ , respectively. In the case of the 2D peak (Fig. 3b), the data points lie on a line, whereas the G peak data points are markedly more scattered and its position at 0.5% strain is even increased compared to the previous step (note, the shift rate is, therefore, calculated only between 0 and 0.45% of strain). The erratic behaviour of the G peak compared to the smooth evolution of the 2D peak is a first indication of another influence on the Raman spectra apart from the strain. A second indication comes from the shift rates. Compared to the theoretical peak shifts ( $\sim 65 \text{ cm}^{-1}/\%$  for the 2D peak and  $\sim 21.5 \text{ cm}^{-1}/\%$  for the G peak), we can see a serious discrepancy in the ratios between the measured and theoretical values: a factor of  $\sim 0.33$  and 0.59 for the 2D and G peaks, respectively. Note that the theoretical G band shift is the average of the shift rates for  $G^+$  and  $G^-$  [1].

Both above mentioned observations – the discrepancy between the measured and theoretical values of the G and 2D peaks and the scatter of the G peak Raman shifts – can be explained by doping. The variations in the G peak position can be rationalised by the presence of spatial fluctuations of

carrier concentrations, sometimes termed as charge puddles [42], and by their fluctuation caused by the strain-induced changes in the graphene–substrate interactions. The different ratios of the G and 2D peak shifts with respect to the theoretical values can reflect a continuous change in the doping level, which influences more the G peak shift. Hence, the strain shift rates should be checked and adjusted (if needed) using the vector separation method to account for the different shifts caused by strain and doping (Fig. 3a). Apart from the point at  $\varepsilon_m = 0.5\%$  strain, the evolution of the G and 2D Raman shifts at the single-spot (Fig. 3a) can be fitted by a line with the slope of  $\sim 1.5$ . This value indicates a substantial influence from changes in doping. We apply the vector analysis using the slope for strain (i.e. iso-doping) line of three obtained from the average peak shifts for uniaxial strain in fully supported graphene [1] and the slope for hole doping of 0.7 [7] and subsequently quantify the data using the above mentioned shift rates for strain and a simplified formula for doping estimation  $\Delta\text{Pos}(G) = -0.986n^2 + 9.847n$  ( $10^{13} \text{ cm}^{-2}$ ) [8], where  $n$  is the carrier concentration. We obtain  $\Delta n \sim -0.37 \times 10^{13} \text{ cm}^{-2}$ . The corresponding adjusted G peak strain shift rate is  $4.3 \text{ cm}^{-1}/\%$ , amounting to  $\sim 0.2$  of the theoretical shift rates.

As can be seen, even a small change in the doping level can lead to considerable changes in the quantified strain. The decrease in carrier concentration (dedoping) observed during the single-spot measurement is, however, counterintuitive. In general, such lower carrier concentration should be accompanied also by a loss of adhesion to the substrate, which in turn would be reflected in smaller Raman shifts of both G and 2D peak per strain step. Nevertheless, the Raman shifts – especially of the 2D peak – show a linear evolution in the whole experiment (Fig. 3b and c). It can be hypothesised that the laser spot was located in a graphene grain (charge puddle) with a higher p-doping level than the rest of sample and by flattening out the graphene’s surface during the tensile test, the charge has been distributed along the neighbouring grains. Indeed, the data points acquired in maps taken at 0% and 0.5% of nominal strain (Fig. 3b) clearly evidence that the behaviour in the one spot randomly selected to follow the stretching experiment shows an anomalous evolution compared to the bulk of the data. The medians of the distributions lie on a line with a slope of  $\sim 3.6$ , indicating that even a minor overall increase in the net doping took place. The increased doping level is expected due to an increasing contact between graphene and the substrate. The vector analysis performed on the medians yields the strain G peak shift rate of  $\sim 8.9 \text{ cm}^{-1}/\%$  and  $\Delta n$  of  $\sim 0.10 \times 10^{13} \text{ cm}^{-2}$ , giving the ratio to the theoretical strain shift rate of 0.44. The ratio is higher than the one previously measured for CVD graphene on a different system with a PET as the bottom and PMMA as the top substrate [37]. If the 2D peak shift would be compared without adjusting for the doping effects, the ratio to the theoretical shift rate would give 0.38 in our case. We can also see that the distributions of the map points in Fig. 3a changed their orientation: from 1.5 at 0% to 2.2 at 0.5% indicating again that upon tension

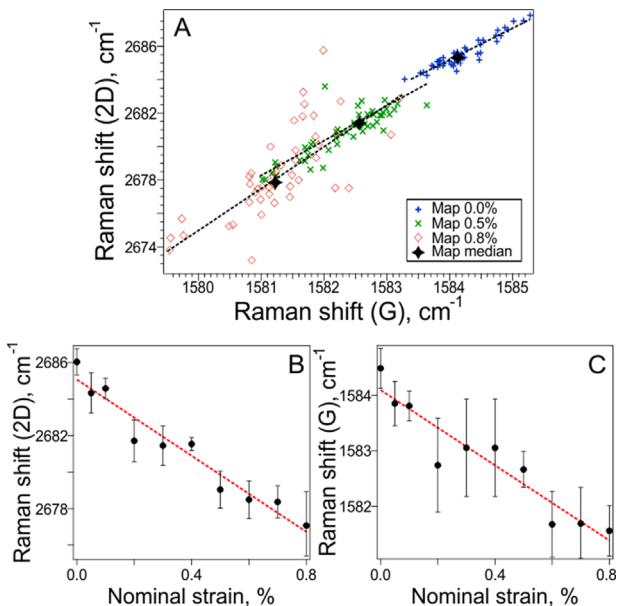


**Figure 4** Evolution of G and 2D peaks in the PMMA-transferred, fully supported sample: (A) data points from large area mapping (0% – blue, 0.5% – green, 0.8% – red) with stars as their medians and full lines as least-squares line fits; (B) and (C) show the evolution of 2D and G peaks with strain. Laser excitation energy was 2.41 eV.

the doping levels are equalised, whereas the differences between the points are dominated by strain.

The case of the fully supported CVD monolayer transferred by PMMA is depicted in Fig. 4. The distribution of the mapping points changes its orientation from 1.9 to almost 2.6 at 0.8% of nominal strain (Fig. 4a), indicating the increased domination of strain. The average shift rates of the 2D and G peaks (Fig. 4b and c) are  $10.4$  and  $3.4 \text{ cm}^{-1}/\%$ , respectively, and their ratio  $\sim 3.1$  showing a minor increase in net doping level. After an adjustment of those doping effects, the G peak shift rate increases to  $3.6 \text{ cm}^{-1}/\%$  and the overall ratio to the theoretical shift rate is 0.17.

The reasons for difference in the shift rates between the PIB- and PMMA-transferred samples can be attributed to the effective grain sizes. The polymer-assisted transfer induces all kinds of disorder and inhomogeneities to the sample, mostly due to a larger area of the graphene film compared to the copper surface, and large surface tension when dissolving the polymer. The most common features thus formed are tears or cracks, individual folds or periodic wrinkles. In Fig. 1, we can see a marked difference between the two samples. While the PIB-transferred one shows predominantly cracks and folds, the PMMA transfer retains a much better continuity of the film, but induces many wrinkles. When we measure the mean sizes of individual graphene domains separated by either of those discontinuities, we get  $\sim 2 \mu\text{m}$  for PIB transfer and less than  $\sim 0.5 \mu\text{m}$  for PMMA transfer. The larger effective domain size of the PIB-transferred samples is then reflected in the higher strain transfer efficiency.

**Table 1** Raman peak widths for PIB- and PMMA-transferred, fully supported samples.

	strain <sup>a</sup> (%)	FWHM(G) <sup>b</sup> (cm <sup>-1</sup> )	FWHM(2D) <sup>b</sup> (cm <sup>-1</sup> )
PIB	0.00	8.9 ± 0.8	31.2 ± 0.9
	0.22	11.6 ± 1.2	33.8 ± 1.5
PMMA	0.00	15.7 ± 0.9	30.2 ± 0.7
	0.14	18.6 ± 0.8	33.8 ± 2.4

<sup>a</sup>The real strain, calculated by multiplying the stress transfer efficiency and the maximum achieved nominal strain  $\varepsilon_m$  [12].

<sup>b</sup>Average values ± standard deviation obtained from Raman maps.

Let us now discuss the differences between the two above mentioned cases from the viewpoint of Raman peak widths. The mean values of FWHMs of the G and 2D peaks at zero and maximum achieved strain for both the PIB- and PMMA-transferred samples are given in Table 1.

In general, three major effects are responsible for changes in the Raman peak widths in monolayer graphene. Both G and 2D peaks broaden and eventually split into two (G peak) or more (2D peak) components with increasing uniaxial strain due to symmetry lowering [1]. The G peak broadening (splitting) follows a monotonic trend (in the case when scattered light with all polarisation directions is registered), whereas the evolution of the 2D peak width with uniaxial strain is more complicated, non-linear and also dependent on the laser excitation energy [25]. Charge doping induces narrowing of the G peak (already at small doping levels) and broadening of the 2D peak (more pronounced for higher doping levels); neither of the effects being linear [15]. And finally, broadening of both peaks can be caused by disorder, stemming either from structural defects [43] and/or from random fluctuations of strain and doping within the laser spot [44]. As can be seen, the peak widths represent an intricate superposition of several factors, especially if uniaxial strain is present, therefore, the interpretation of FWHM values has a limited usage. However, several simple assumptions can be made comparing the numbers in Table 1 and the peak shifts from Figs. 3 and 4 and the discussion thereof. At zero strain level, the small FWHM(G) of the PIB-transferred sample shows a high doping level. The FWHM(G) of the PMMA-transferred sample is significantly higher, and thus smaller doping can be expected. In the same time, the FWHM(2D) of the two samples is larger than 30 cm<sup>-1</sup> and alike within the error margin. This indicates that apart from differences in doping [15], also varying amount of disorder [44] can be traced between the two samples. As the D band intensity is very small in both cases, the main source of disorder comes from strain/doping fluctuation in the laser spot. In the PIB sample at zero strain, the main source of 2D peak broadening comes from doping, while in the PMMA sample, the broadening originates in nanoscale strain/doping fluctuations. The latter conclusion is also in line with the much higher density of discontinuities like folds or wrinkles in the PMMA sample, as discussed above.

Upon uniaxial loading, both peaks broaden in both sample types. However, we shall consider only the evolution of the G peak width due to the complicated nature of 2D peak broadening. The theoretical rate of G peak splitting with uniaxial strain is  $\sim 21$  cm<sup>-1</sup>/%, a value almost identical to the average shift rate of the two components ( $\sim 20.5$  cm<sup>-1</sup>/%). Hence, at smaller strains, where the two components are strongly overlapping and not discernible, one can expect the rate of G peak broadening as a function of G peak shift,  $\Delta\text{FWHM(G)}/\Delta\text{Pos(G)}$ , of  $\sim -1$ . While the G peak evolution of the PMMA-transferred sample follows exactly this trend,  $\Delta\text{FWHM(G)}/\Delta\text{Pos(G)}$  in the PIB sample reaches only  $-0.83$ . The difference can be caused either by decreasing disorder in the PIB sample, or more likely – in accordance with the results obtained from the vector analysis – by a small increase of the doping level in the PIB sample, which would slightly counterbalance the strain-induced broadening. As a final note, the different doping level in the initial state of the samples seems to be reflected also in the stress-transfer efficiency – a better contact between the sample and the substrate(s) would lead to a higher doping level as well as to a better stress transfer.

As another example of the usefulness of the vector analysis, a simply supported PIB-transferred CVD graphene was tested. In this case, the evolution of the G and 2D peaks in one spot shows a completely different scenario, where the frequency of the 2D peak decreases, while the G peak frequency increases (Fig. 5b and c). Such a behaviour can be explained only by a commanding

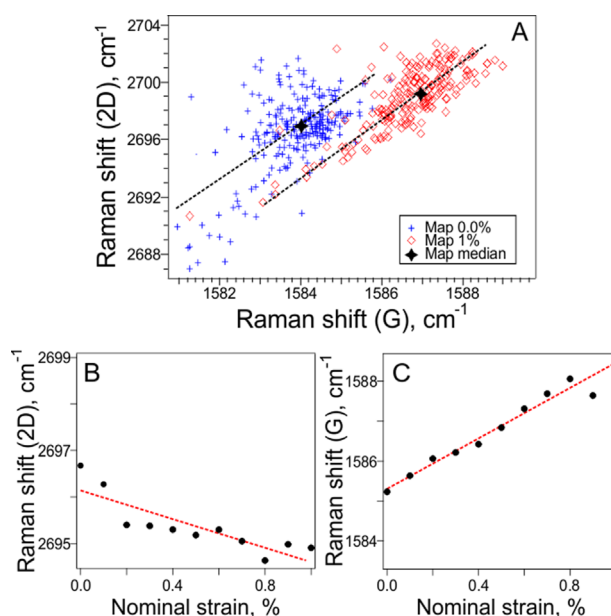


**Figure 5** Evolution of G and 2D peaks in the PIB-transferred, simply supported sample: (A) data points from large area mapping (0% – blue, 1.0% – red) with stars as their medians and full lines as least-squares line fits; (B) and (C) show the evolution of 2D and G peaks with strain on a single spot. Laser excitation energy was 1.96 eV.

change in the doping level ( $\Delta n \sim 0.27 \times 10^{13} \text{ cm}^{-2}$ ) with a minor contribution of a tensile strain (ratio to the theoretical shift rates of  $\sim 0.01$ ). On top of that, the large spread of the values from the linear fit evidences substantial heterogeneities into the laser spot. The statistical evaluation in a larger area documents a slightly different overall evolution, which is dominated even more strongly by an increased doping level, where the medians of the two groups of data points are connected by a line with a slope of 0.7. Hence, during the experiment, most of the area of the sample experiences only a better alignment along the substrate, thereby increasing the doping level, and only in a few points the graphene is pinned to the substrate causing a minor interfacial stress transfer.

**4 Conclusions** We have shown the usability of vector analysis, performed on data points acquired by analysing the Raman G and 2D peak positions in graphene, to separate effects of strain and charge transfer doping in uniaxially strained CVD graphene samples. In all examined cases, uniaxial strain causes alignment of the graphene monolayer on the substrate resulting in an increase of doping level, however, only specimens covered by an additional polymer layer exhibit a certain amount of interfacial stress transfer. Its level is defined by the size of the effective graphene domains, which are separated by any kind of cracks, folds or wrinkles. The stress transfer efficiency is found to be  $\sim 44\%$  for PIB-transferred graphene with domain sizes of  $\sim 2 \mu\text{m}$  and  $\sim 17\%$  for PMMA-transferred sample with domain sizes of  $\sim 0.5 \mu\text{m}$ . A qualitative study of the G and 2D peak widths supports the conclusions from the vector analysis. It is also worth noting that single spot analysis can lead to misleading interpretation, as the samples display large strain variations and/or doping inhomogeneities. Therefore, a larger area Raman mapping has to be conducted and evaluated to provide quantifiable information about the real strain and doping levels induced by the arrangement and flattening of the domains upon loading.

**Acknowledgements** This project has received funding from the European Union's Horizon 2020 research and innovation programme under grant agreement no. 696656–GrapheneCore1. O.F., M.B and E.d.C. acknowledge the support of Czech Science Foundation project no. 14-15357S and M.K. acknowledges the support from ERC-CZ project no. LL1301. J.Pe. acknowledges the support by the project of National Sustainability Program under grant LO1401 of SIX Research Centre. Also, G.A., J.Pa., K.P. and C.G. acknowledge the financial support of, 'Tailor Graphene' ERC Advanced Grant (no. 321124) and the programme 'Graphene physics in the time domain and applications to 3D optical memories', Aristeia II (no. 4470).

## References

- [1] C. Galiotis, O. Frank, E. N. Koukaras, and D. Sfyris, *Annu. Rev. Chem. Biomol. Eng.* **6**, 121 (2015).
- [2] Y. Shi, X. Dong, P. Chen, J. Wang, and L.-J. Li, *Phys. Rev. B* **79**, 115402 (2009).
- [3] M. A. Bissett, M. Tsuji, and H. Ago, *Phys. Chem. Chem. Phys.* **16**, 11124 (2014).
- [4] N. J. G. Couto, D. Costanzo, S. Engels, D.-K. Ki, K. Watanabe, T. Taniguchi, C. Stampfer, F. Guinea, and A. F. Morpurgo, *Phys. Rev. X* **4**, 041019 (2014).
- [5] A. C. Ferrari and D. M. Basko, *Nature Nanotechnol.* **8**, 235 (2013).
- [6] L. M. Malard, M. A. Pimenta, G. Dresselhaus, and M. S. Dresselhaus, *Phys. Rep.* **473**, 51 (2009).
- [7] J. E. Lee, G. Ahn, J. Shim, Y. S. Lee, and S. Ryu, *Nature Commun.* **3**, 1024 (2012).
- [8] O. Frank, J. Vejpravova, V. Holy, L. Kavan, and M. Kalbac, *Carbon* **68**, 440 (2014).
- [9] F. Fromm, P. Wehrfritz, M. Hundhausen, and T. Seyller, *New J. Phys.* **15**, 113006 (2013).
- [10] T. G. A. Verhagen, K. Drogowska, M. Kalbac, and J. Vejpravova, *Phys. Rev. B* **92**, 125437 (2015).
- [11] J. Vejpravova, B. Pacakova, J. Endres, A. Mantlikova, T. Verhagen, V. Vales, O. Frank, and M. Kalbac, *Sci. Rep.* **5**, 15061 (2015).
- [12] E. del Corro, L. Kavan, M. Kalbac, and O. Frank, *J. Phys. Chem. C* **119**, 25651 (2015).
- [13] F. Tuinstra and J. L. Koenig, *J. Chem. Phys.* **53**, 1126 (1970).
- [14] A. Das, S. Pisana, B. Chakraborty, S. Piscanec, S. K. Saha, U. V. Waghmare, K. S. Novoselov, H. R. Krishnamurthy, A. K. Geim, A. C. Ferrari, and A. K. Sood, *Nature Nanotechnol.* **3**, 210 (2008).
- [15] O. Frank, M. S. Dresselhaus, and M. Kalbac, *Acc. Chem. Res.* **48**, 111 (2015).
- [16] R. J. Young, I. A. Kinloch, L. Gong, and K. S. Novoselov, *Compos. Sci. Technol.* **72**, 1459 (2012).
- [17] M. Lazzeri and F. Mauri, *Phys. Rev. Lett.* **97**, 266407 (2006).
- [18] C. Androulidakis, E. N. Koukaras, J. Parthenios, G. Kalosakas, K. Papagelis, and C. Galiotis, *Sci. Rep.* **5**, 18219 (2015).
- [19] O. Frank, G. Tsoukleri, J. Parthenios, K. Papagelis, I. Riaz, R. Jalil, K. S. Novoselov, and C. Galiotis, *ACS Nano* **4**, 3131 (2010).
- [20] T. M. G. Mohiuddin, A. Lombardo, R. R. Nair, A. Bonetti, G. Savini, R. Jalil, N. Bonini, D. M. Basko, C. Galiotis, N. Marzari, K. S. Novoselov, A. K. Geim, and A. C. Ferrari, *Phys. Rev. B* **79**, 205433 (2009).
- [21] I. Polyzos, M. Bianchi, L. Rizzi, E. N. Koukaras, J. Parthenios, K. Papagelis, R. Sordan, and C. Galiotis, *Nanoscale* **7**, 13033 (2015).
- [22] P. Venezuela, M. Lazzeri, and F. Mauri, *Phys. Rev. B* **84**, 035433 (2011).
- [23] J. Maultzsch, S. Reich, and C. Thomsen, *Phys. Rev. B* **70**, 155403 (2004).
- [24] S. Berciaud, X. Li, H. Htoon, L. E. Brus, S. K. Doorn, and T. F. Heinz, *Nano Lett.* **13**, 3517 (2013).
- [25] O. Frank, M. Mohr, J. Maultzsch, C. Thomsen, I. Riaz, R. Jalil, K. S. Novoselov, G. Tsoukleri, J. Parthenios, K. Papagelis, L. Kavan, and C. Galiotis, *ACS Nano* **5**, 2231 (2011).
- [26] M. Huang, H. Yan, T. F. Heinz, and J. Hone, *Nano Lett.* **10**, 4074 (2010).
- [27] D. Yoon, Y.-W. Son, and H. Cheong, *Phys. Rev. Lett.* **106**, 155502 (2011).

- [28] R. Narula, N. Bonini, N. Marzari, and S. Reich, *Phys. Rev. B* **85**, 115451 (2012).
- [29] V. N. Popov and P. Lambin, *Carbon* **54**, 86 (2013).
- [30] K. Filintoglou, N. Papadopoulos, J. Arvanitidis, D. Christofilos, O. Frank, M. Kalbac, J. Parthenios, G. Kalosakas, C. Galiotis, and K. Papagelis, *Phys. Rev. B* **88**, 045418 (2013).
- [31] J. Zabel, R. R. Nair, A. Ott, T. Georgiou, A. K. Geim, K. S. Novoselov, and C. Casiraghi, *Nano Lett.* **12**, 617 (2012).
- [32] M. Kalbac, A. Reina-Cecco, H. Farhat, J. Kong, L. Kavan, and M. S. Dresselhaus, *ACS Nano* **4**, 6055 (2010).
- [33] D. M. Basko, S. Piscanec, and A. C. Ferrari, *Phys. Rev. B* **80**, 165413 (2009).
- [34] C. Androulidakis, E. N. Koukaras, O. Frank, G. Tsoukleri, D. Sfyris, J. Parthenios, N. Pugno, K. Papagelis, K. S. Novoselov, and C. Galiotis, *Sci. Rep.* **4**, 5271 (2014).
- [35] L. Gong, I. A. Kinloch, R. J. Young, I. Riaz, R. Jalil, and K. S. Novoselov, *Adv. Mater.* **22**, 2694 (2010).
- [36] G. Anagnostopoulos, C. Androulidakis, E. N. Koukaras, G. Tsoukleri, I. Polyzos, J. Parthenios, K. Papagelis, and C. Galiotis, *ACS Appl. Mater. Interfaces* **7**, 4216 (2015).
- [37] Z. Li, I. A. Kinloch, R. J. Young, K. S. Novoselov, G. Anagnostopoulos, J. Parthenios, C. Galiotis, K. Papagelis, C.-Y. Lu, and L. Britnell, *ACS Nano* **9**, 3917 (2015).
- [38] S. Jegal, Y. Hao, D. Yoon, R. S. Ruoff, H. Yun, S. W. Lee, and H. Cheong, *Chem. Phys. Lett.* **568–569**, 146 (2013).
- [39] J. Ek-Weis, S. Costa, O. Frank, and M. Kalbac, *J. Phys. Chem. Lett.* **5**, 549 (2014).
- [40] J. Song, F.-Y. Kam, R.-Q. Png, W.-L. Seah, J.-M. Zhuo, G.-K. Lim, P. K. H. Ho, and L.-L. Chua, *Nature Nanotechnol.* **8**, 356 (2013).
- [41] A. P. A. Raju, A. Lewis, B. Derby, R. J. Young, I. A. Kinloch, R. Zan, and K. S. Novoselov, *Adv. Funct. Mater.* **24**, 2865 (2014).
- [42] R. Jalilian, L. A. Jauregui, G. Lopez, J. Tian, C. Roecker, M. M. Yazdanpanah, R. W. Cohn, I. Jovanovic, and Y. P. Chen, *Nanotechnology* **22**, 295705 (2011).
- [43] R. Beams, L. Gustavo Cancado, and L. Novotny, *J. Phys.: Condens. Matter* **27**, 083002 (2015).
- [44] C. Neumann, S. Reichardt, P. Venezuela, M. Drogeler, L. Banszerus, M. Schmitz, K. Watanabe, T. Taniguchi, F. Mauri, B. Beschoten, S. V. Rotkin, and C. Stampfer, *Nature Commun.* **6**, 8429 (2015).

## Příloha 8

GABLECH, I. et al. Monoelemental 2D materials-based field effect transistors for sensing and biosensing: Phosphorene, antimonene, arsenene, silicene, and germanene go beyond graphene. *Trac-Trends in Analytical Chemistry*, 2018, vol. 105, pp. 251-262. ISSN 0165-9936.

### ABSTRAKT

Grafen je ohromně zajímavý díky svým vynikajícím elektronickým vlastnostem a stejně tak tím, že má nulový zakázaný pás polovodiče. Nicméně, aby bylo možné vhodně použít grafen v elektronice, senzorech elektronického přenosu a biosenzorech, je třeba mít otevřený zakázaný pás. Dokázat toto je velice náročné z hlediska reprodukovatelnosti a měřitelnosti. Existují však další 2D monoelementární materiály, které vykazují vhodnou šířku zakázaného pásu a které mohou být použity pro senzory založené na tranzistorech řízených elektrickým polem (FET) a biosenzory. V tomto článku jsou uvedeny trendy ve vývoji snímačů na struktuře FET využívající 2D fosforen, arzenen, antimonen, silicen a germanen.



# Monoelemental 2D materials-based field effect transistors for sensing and biosensing: Phosphorene, antimonene, arsenene, silicene, and germanene go beyond graphene

Imrich Gablech<sup>a, b</sup>, Jan Pekárek<sup>a, b</sup>, Jaroslav Klempa<sup>a, b</sup>, Vojtěch Svatoš<sup>a, b</sup>,  
Ali Sajedi-Moghaddam<sup>a</sup>, Pavel Neuzil<sup>c, \*\*</sup>, Martin Pumera<sup>a, d, \*</sup>

<sup>a</sup> Central European Institute of Technology, Brno University of Technology, Purkyňova 123, CZ-61200 Brno, Czech Republic

<sup>b</sup> Brno University of Technology, Faculty of Electrical Engineering and Communication, Department of Microelectronics, Technická 3058/10, CZ-61600 Brno, Czech Republic

<sup>c</sup> Northwestern Polytechnical University, 127 West Youyi Road, Xi'an, Shaanxi, PR China

<sup>d</sup> Division of Chemistry & Biological Chemistry, School of Physical Mathematical Science, Nanyang Technological University, Singapore 637371, Singapore

## ARTICLE INFO

### Article history:

Available online 25 May 2018

### Keywords:

Antimonene  
Arsenene  
Phosphorene  
Silicene  
Germanene  
Graphene  
FET  
Sensing

## ABSTRACT

Graphene has been of immense interest for its interesting electronic properties, such as being a zero-band gap semiconductor. However, to be able to usefully employ graphene for electronics and electronic-transduction system sensors and biosensors, one needs to open this band gap. This proves to be challenging on a reproducible, scalable way. There are other 2D monoelemental materials that exhibit useful band gap and which can be used for field effect transistor- (FET-) based sensing and biosensing. Here we discuss trends in the development of FET-based sensors utilizing 2D phosphorene, arsenene, antimonene, silicene, and germanene.

© 2018 Published by Elsevier B.V.

## 1. Introduction

In the past two years, there has been great interest in 2D monoelemental materials beyond graphene, such as Group IVA silicene and germanene and Group VA phosphorene, arsenene, and antimonene (Fig. 1). While graphene, which is a single sheet of graphite (see IUPAC definition from 1995 [1]), has received enormous interest over the past 14 years, its utilization for some applications, such as field effect transistors (FETs), is limited as it does not show any band gap. Such a band gap needs to be engineered by modification of the graphene. Other layered systems and their 2D layered counterparts, such as transition metal dichalcogenides (typical example is MoS<sub>2</sub>) and transition metal oxides, have been investigated in recent years as they show a

sizable band gap. One can find a large variety of layered materials comprising two, three, or more elements. Here, we wish to focus on materials that are layered but monoelemental. The number of monoelemental layered materials is limited and includes layered forms of phosphorus (called “black phosphorus” and known from 1916 [2] and rediscovered in 2017 [3]), arsenic, antimony, and bismuth [4]. Unlike graphene, these materials are semiconductors (that is, materials with an energy band gap) when exfoliated to a single layer and are, therefore, immensely useful for the construction of FETs.

Group VA materials include phosphorus, arsenic, antimony, and bismuth. These materials have either (A) rhombohedral structure or (B) orthorhombic structure (see Fig. 2). Note that two layers of atoms are chemically bonded in an “armchair” or “boat” configuration to create one sheet (thus, the sheet is not atomically thin as in the case of graphene, but naturally two-atoms-thick and with no double bond between the sheets). Note that layers of black phosphorus are held together by rather weak van der Waals forces while layers of As, Sb, and Bi are held by stronger chemical bonds.

Layered and 2D materials based in Group IVA, germanene [6], and silicene [7] are 2D analogs of graphene; however, the atoms are

\* Corresponding author. Division of Chemistry & Biological Chemistry, School of Physical Mathematical Science, Nanyang Technological University, Singapore 637371, Singapore.

\*\* Corresponding author.

E-mail addresses: [pavel.neuzil@npwu.cn](mailto:pavel.neuzil@npwu.cn) (P. Neuzil), [pumera.research@gmail.com](mailto:pumera.research@gmail.com) (M. Pumera).

1 H hydrogen																	2 He helium													
3 Li lithium	4 Be beryllium																	5 B boron	6 C carbon	7 N nitrogen	8 O oxygen	9 F fluorine	10 Ne neon							
11 Na sodium	12 Mg magnesium																	13 Al aluminum	14 Si silicon	15 P phosphorus	16 S sulfur	17 Cl chlorine	18 Ar argon							
19 K potassium	20 Ca calcium	21 Sc scandium	22 Ti titanium	23 V vanadium	24 Cr chromium	25 Mn manganese	26 Fe iron	27 Co cobalt	28 Ni nickel	29 Cu copper	30 Zn zinc	31 Ga gallium	32 Ge germanium	33 As arsenic	34 Se selenium	35 Br bromine	36 Kr krypton													
37 Rb rubidium	38 Sr strontium	39 Y yttrium	40 Zr zirconium	41 Nb niobium	42 Mo molybdenum	43 Tc technetium	44 Ru ruthenium	45 Rh rhodium	46 Pd palladium	47 Ag silver	48 Cd cadmium	49 In indium	50 Sn tin	51 Sb antimony	52 Te tellurium	53 I iodine	54 Xe xenon													
55 Cs cesium	56 Ba barium	57 La lanthanum	72 Hf hafnium	73 Ta tantalum	74 W tungsten	75 Re rhenium	76 Os osmium	77 Ir iridium	78 Pt platinum	79 Au gold	80 Hg mercury	81 Tl thallium	82 Pb lead	83 Bi bismuth	84 Po polonium	85 At astatine	86 Rn radon													
87 Fr francium	88 Ra radium	89 Ac actinium	104 Rf rutherfordium	105 Db dubnium	106 Sg seaborgium	107 Bh bohrium	108 Hs hassium	109 Mt meitnerium	110 Ds darmstadtium	111 Rg roentgenium	112 Cn copernicium	113 Uut ununtrium	114 Fl flerovium	115 Uup ununpentium	116 Lv livermorium	117 Uus ununseptium	118 Uuo ununoctium													
* 58 Ce cerium																		59 Pr praseodymium	60 Nd neodymium	61 Pm promethium	62 Sm samarium	63 Eu europium	64 Gd gadolinium	65 Tb terbium	66 Dy dysprosium	67 Ho holmium	68 Er erbium	69 Tm thulium	70 Yb ytterbium	71 Lu lutetium
** 90 Th thorium																		91 Pa protactinium	92 U uranium	93 Np neptunium	94 Pu plutonium	95 Am americium	96 Cm curium	97 Bk berkelium	98 Cf californium	99 Es einsteinium	100 Fm fermium	101 Md mendelevium	102 No nobelium	103 Lr lawrencium

Fig. 1. Periodic table with elements of interest marked in blue.

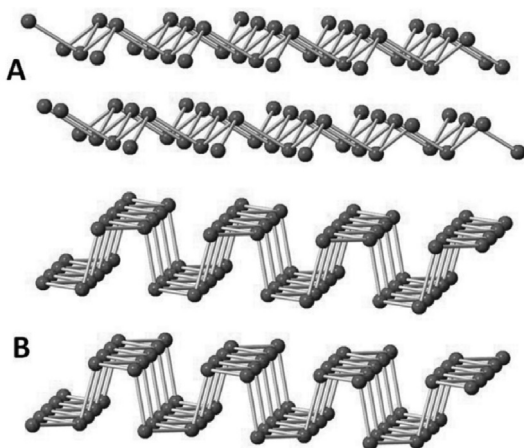


Fig. 2. Structures of rhombohedral layered (black) phosphorus, arsenic, antimony, and bismuth (A) and orthorhombic layered arsenic and (black) phosphorus (B). Reprinted from Ref. [4].

not aligned in a perfect plane such as in graphene [5]. The structures of germanene and silicene are shown in Fig. 3.

The FET principle was proposed as early as 1926 [8] and practically demonstrated more than 30 years ago [9]. This paved the way to create the modern metal oxide semiconductor FET (MOS-FET) in complementary configuration (CMOS) based on silicon technology, which has become the default technology used nowadays in practically all electronic devices. The basic FET is a four-terminal structure (Fig. 4A) consisting of a gate, source, drain, and a substrate. The device can operate in three different modes [10]: subthreshold, linear [Equation (1)] and saturated [Equation (2)], depending on the voltages connected to the terminals (here we assume that the source and the substrate are connected):

$$I_D = \frac{\mu_n \cdot C_d \cdot W}{2 \cdot L} \cdot \left[ \left( V_{GS} - V_T - \frac{V_{DS}}{2} \right) \cdot V_{DS} \right] \text{ for } V_{GS} \geq V_T \text{ and } V_{DS} \ll V_{GS} - V_T \quad (1)$$

or

$$I_D = \frac{\mu_n \cdot C_d \cdot W}{2M \cdot L} \cdot (V_{GS} - V_T)^2 \text{ for } V_{GS} \geq V_T \text{ and } V_{DS} \geq V_{GS} - V_T, \quad (2)$$

where  $I_D$  is drain current,  $V_{GS}$  is gate-source voltage,  $V_T$  is threshold voltage,  $\mu_n$  is electron mobility in the substrate and with a value of  $1400 \text{ cm}^2 \cdot \text{V}^{-1} \cdot \text{s}^{-1}$  for silicon at  $25^\circ\text{C}$ ,  $C_d$  is dielectric capacitance per unit area of the gate material,  $W$  and  $L$  are width and length of the transistor, respectively,  $V_{DS}$  is the drain-source voltage, and  $M$  is a function of substrate doping concentration and gate dielectric properties (Fig. 4A). Normally, the device operates in any of two active regions: either linear or saturated. The  $I_D$  amplitude can be affected electrically by  $V_{GS}$  or  $V_{DS}$  as well as by modulation of  $V_T$ ,  $\mu_n$ , and  $C_d$ . The last three items are constant in CMOS devices as they are encapsulated by light opaque materials. On the other hand, the FET sensors operate differently as the gate is in contact with an analyte. Then, the values of either  $V_T$ ,  $\mu_n$ , or  $C_d$  are modulated by the analyte and affect the  $I_D$  amplitude, which is measured and provides information regarding the analyte.

The gate dielectric material is electrically insulated; thus, ideally, the steady-state direct electrical current (DC) flowing through the gate dielectric can be considered to have a value of  $I_G = 0 \text{ A}$ . That makes the FET a transducer affecting the  $I_D$  by an induced electric field without loading the gate voltage source. It can be considered also as a high-to-low impedance converter. Soon after the MOSFET introduction, researchers started to investigate if the FET principle can be also used for sensing applications and several FET clones were proposed and tested.

A family of chemical and biochemical sensors based on  $V_T$  modulation starting with pH-detecting ion-sensitive FETs (ISFETs) [11] (Fig. 4B) is currently used also to detect other ions, such as  $\text{Na}^+$ ,  $\text{K}^+$ ,  $\text{Ca}^{2+}$ ,  $\text{Cl}^-$ , and the ISFET clone, called “enzyme FET” (ENFET) for glucose, urea, and cholesterol. Originally,  $\text{H}_2$  gas-sensing FETs were introduced with the gate made from an ultrathin Pd layer that allows  $\text{H}_2$  to diffuse at an elevated temperature of  $150^\circ\text{C}$  through the Pd layer to the Pd–insulator interface to affect the device threshold voltage [12]. The device operation was extended to sensing other gases such as CO,  $\text{H}_2\text{S}$ , and  $\text{NH}_3$ .

The utility of 2D materials for FET-based devices was investigated more than decade ago for graphene [13,14] by studying the electric field effect in this 2D material. It was found that its  $\mu_n$  has an

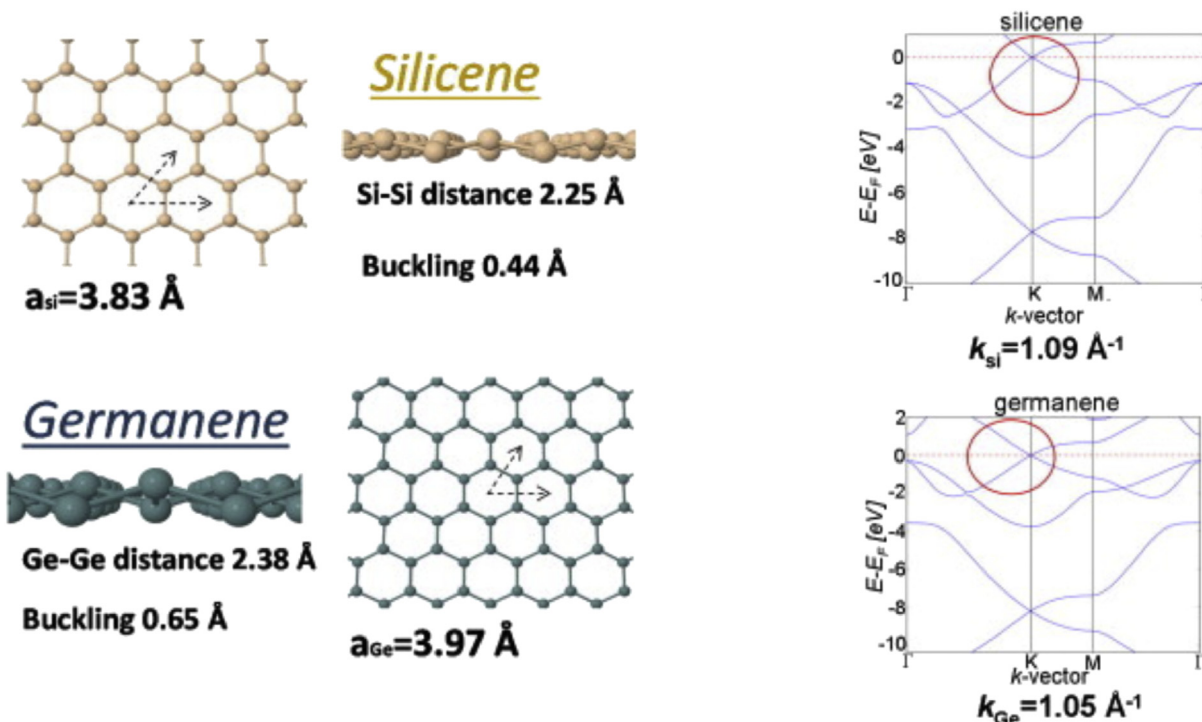


Fig. 3. Structures of silicene and germanene. Reprinted with permission from Ref. [5].

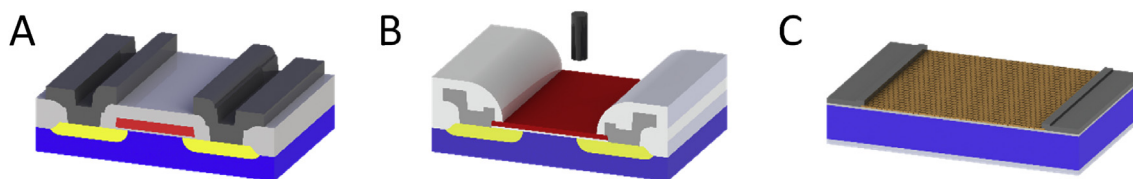


Fig. 4. (A) A MOSFET (ISFET) and (C) graphene FET. Blue and yellow colors represent silicon substrate with both types of doping, n and p, respectively or vice versa, light gray color represents  $\text{SiO}_2$ , (A) red polycrystalline silicon layer for the MOSFET gate or (B) ISFET gate materials such as  $\text{Si}_3\text{N}_4$ , and (C) brown graphene.

exceptionally high value of  $15,000 \text{ cm}^2 \cdot \text{V}^{-1} \cdot \text{s}^{-1}$ , which is more than  $10\times$  higher than the one of Si. As per Eqs. (1) and (2),  $10\times$  higher amplitude of  $\mu_n$  causes 10 times greater  $I_D$  with the same change of  $V_T$  and  $C_D$ . Since then, graphene has been extensively studied, including graphene-based FETs for various sensing applications [15] as the  $I_D$  value can be affected by modulating the  $\mu_n$  either mechanically by stretching the 2D material or by chemically modifying its properties. The first can be used for mechanical sensing and the second for chemical or biochemical sensing.

There are two types of graphene-based FETs: those with a top-gate as well as the back-gate and those with a back gate only [16]. The first one is easier to control as modulating the electric field in the 2D material is simple; however, its fabrication is more complicated. In addition, the FET with 2D material sandwiched between two dielectrics is not very suitable for any chemical or biochemical sensing application as there is no direct access to the 2D material unless the top dielectric layer is extremely thin. The device with the back gate only has an advantage of 2D material direct exposure by the environment making its response fast but also more difficult to control [16]. To construct FET-based sensing devices, the presence of an energy band gap is important as the material properties are strongly dependent on it. The conductivity of the material is determined by the electrons with enough energy to be excited across the energy band gap. This feature can be modulated by the presence of an analyte at the FET surface as this

will affect the energy band gap and, thus, its conductivity. Higher mobility also allows more sensitive measurement as per Eqs. (1) and (2).

We overview key theoretical studies and applications of 2D materials as the main parts of FET-based sensors for sensing of gases, small molecules, and biomolecules (see Table 1).

## 2. 2D materials for FET sensors and biosensors

### 2.1. Phosphorene

Kou et al. [21] performed first-principle calculations to study the interaction of phosphorene with physisorbed small molecules such

**Table 1**  
Summarized properties of antimonene, arsenene, phosphorene, silicene, and germanene.

Material	Energy band gap (eV)	Carrier mobility ( $\text{cm}^2 \cdot \text{V}^{-1} \cdot \text{s}^{-1}$ )
Antimonene	1–1.5	10–100 or 500–1200 [17]
Arsenene	2.5	10–100 or 500–1200 [17]
Phosphorene	1.5	260 [18]
Silicene	0.002–0.5	100 (measured) $2.57 \times 10^5$ (calculated) [19]
Germanene	<0.05	$6 \times 10^5$ (calculated) [20]

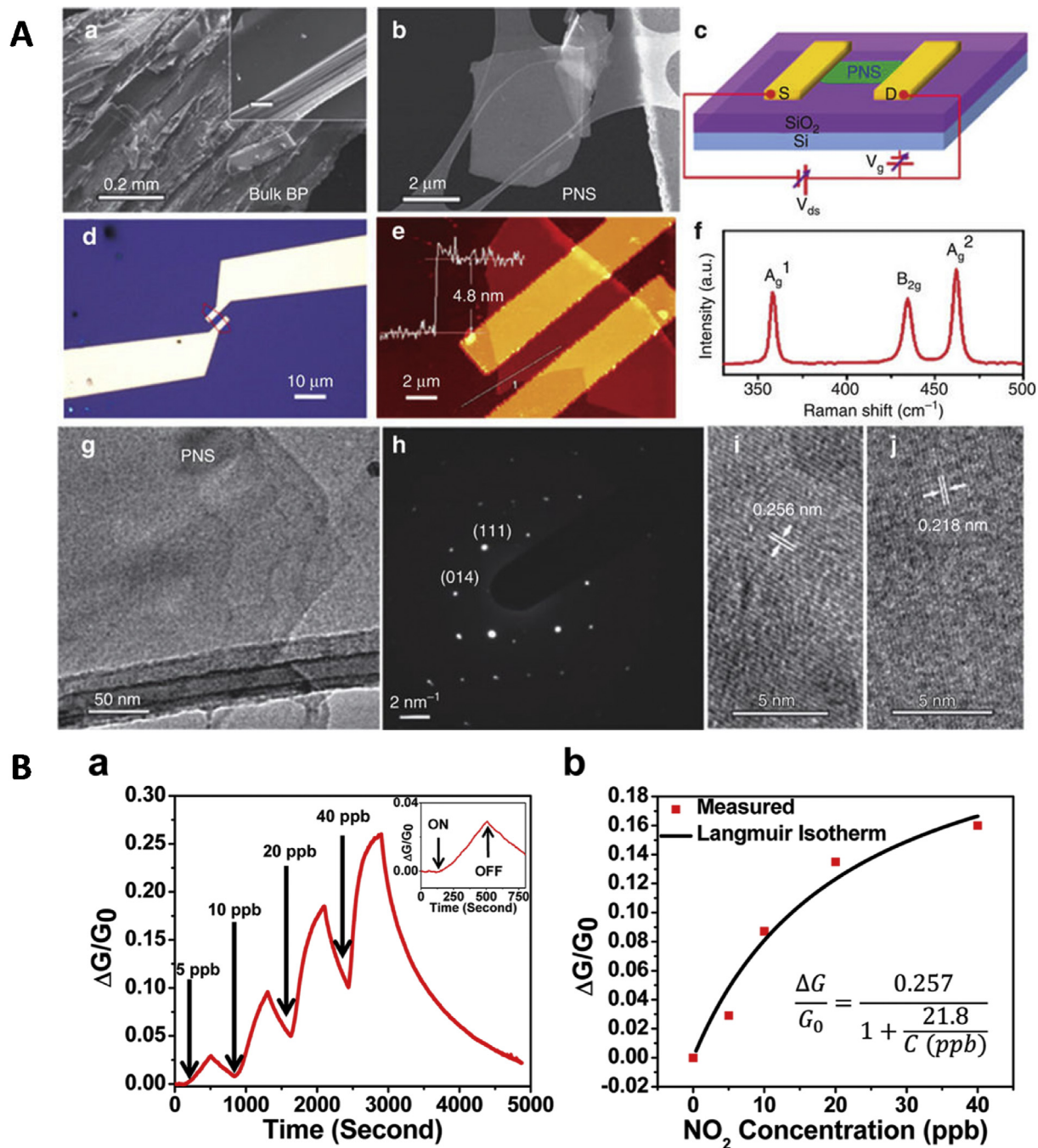


**Fig. 5.** Black phosphorus (BP) FET for gas sensing (A): (a) scanning electron microscopy (SEM) image of bulk BP. The inset is a magnified image showing the layered structure; scale bar, 10  $\mu\text{m}$ ; (b) SEM image of exfoliated PNS; (c) schematic of an FET device based on the PNS and the circuit for electrical and sensing measurements; (d, e) optical microscopy and AFM images of the PNS sensor device showing that the PNS electrically bridges the gold electrodes. The profile in (e) indicates the PNS has a thickness of 4.8 nm; (f) Raman spectrum of PNS; and (g, h, i, j) TEM image, selected area electron diffraction (SAED) pattern, and high-resolution TEM (HRTEM) images of PNS. The two HRTEM images (i, j) demonstrate two representative lattice spacings of PNS. (B)  $\text{NO}_2$  gas sensing performance of multilayer BP FET: (a) relative conductance change ( $\Delta G/G_0$ ) vs. time in seconds for a multilayer BP sensor showing sensitivity to  $\text{NO}_2$  concentrations (5–40 ppb). Inset shows a zoomed-in image of a 5 ppb  $\text{NO}_2$  exposure response with identification of points in time where the  $\text{NO}_2$  gas is switched on and off and (b)  $\Delta G/G_0$  plotted vs.  $\text{NO}_2$  concentration applied to the BP FET showing an agreement between the measured values (red squares) and the fitted Langmuir isotherm. The equation in the bottom right is the fitted Langmuir isotherm.

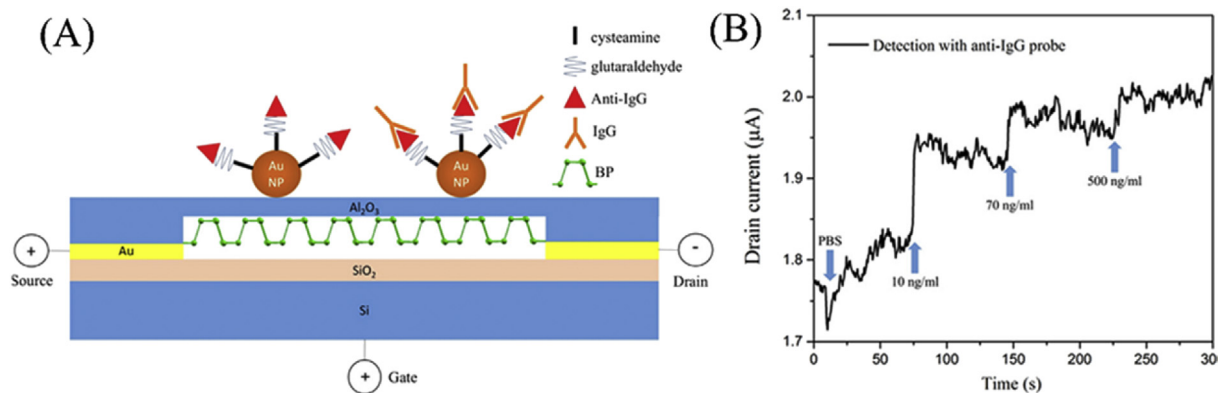


Fig. 6. (A) Cross sectional schematic illustration of the BP-based FET biosensor. (B) Dynamic response of the biosensor to different concentrations of IgG. Reproduced from Ref. [26].

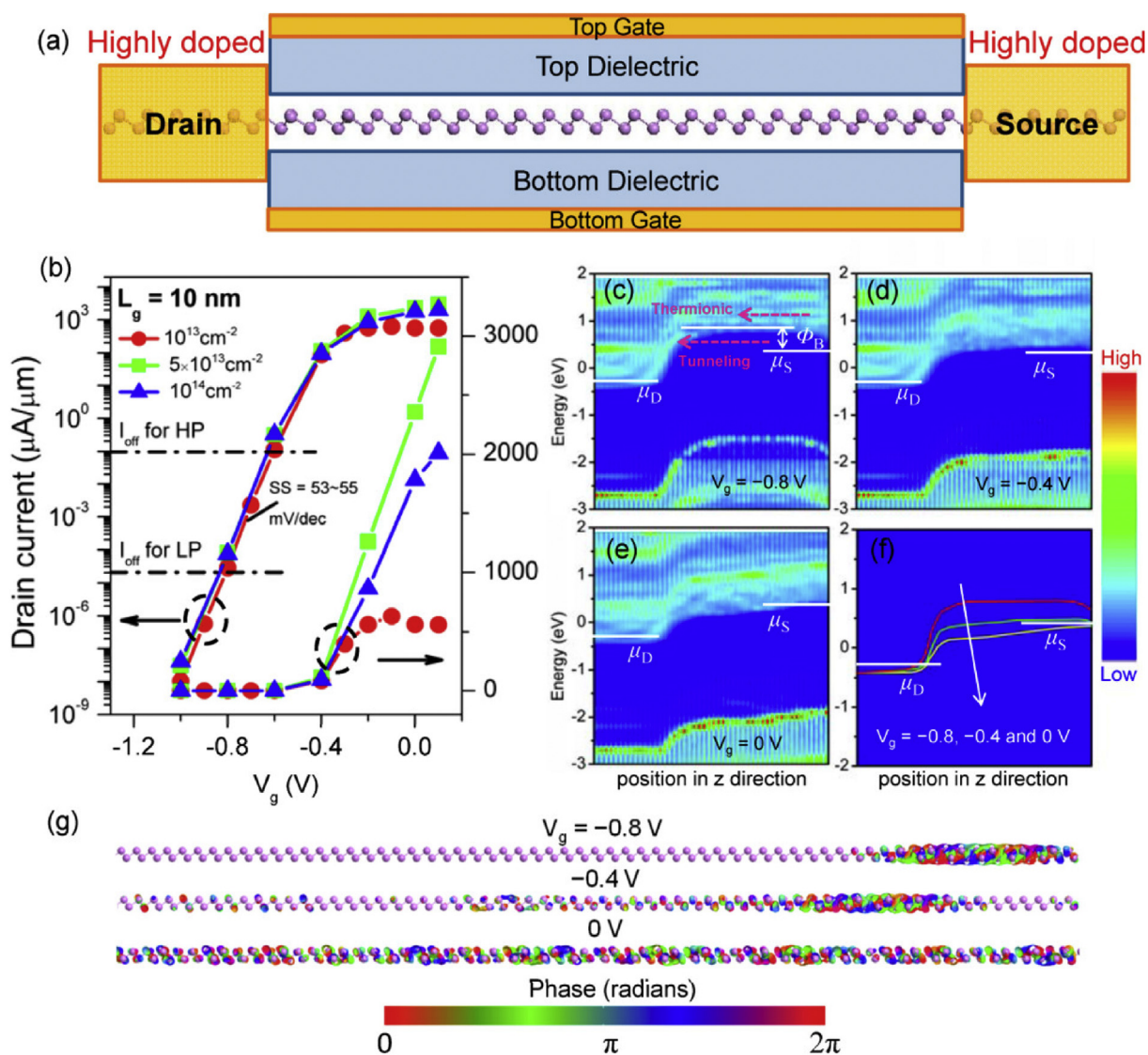
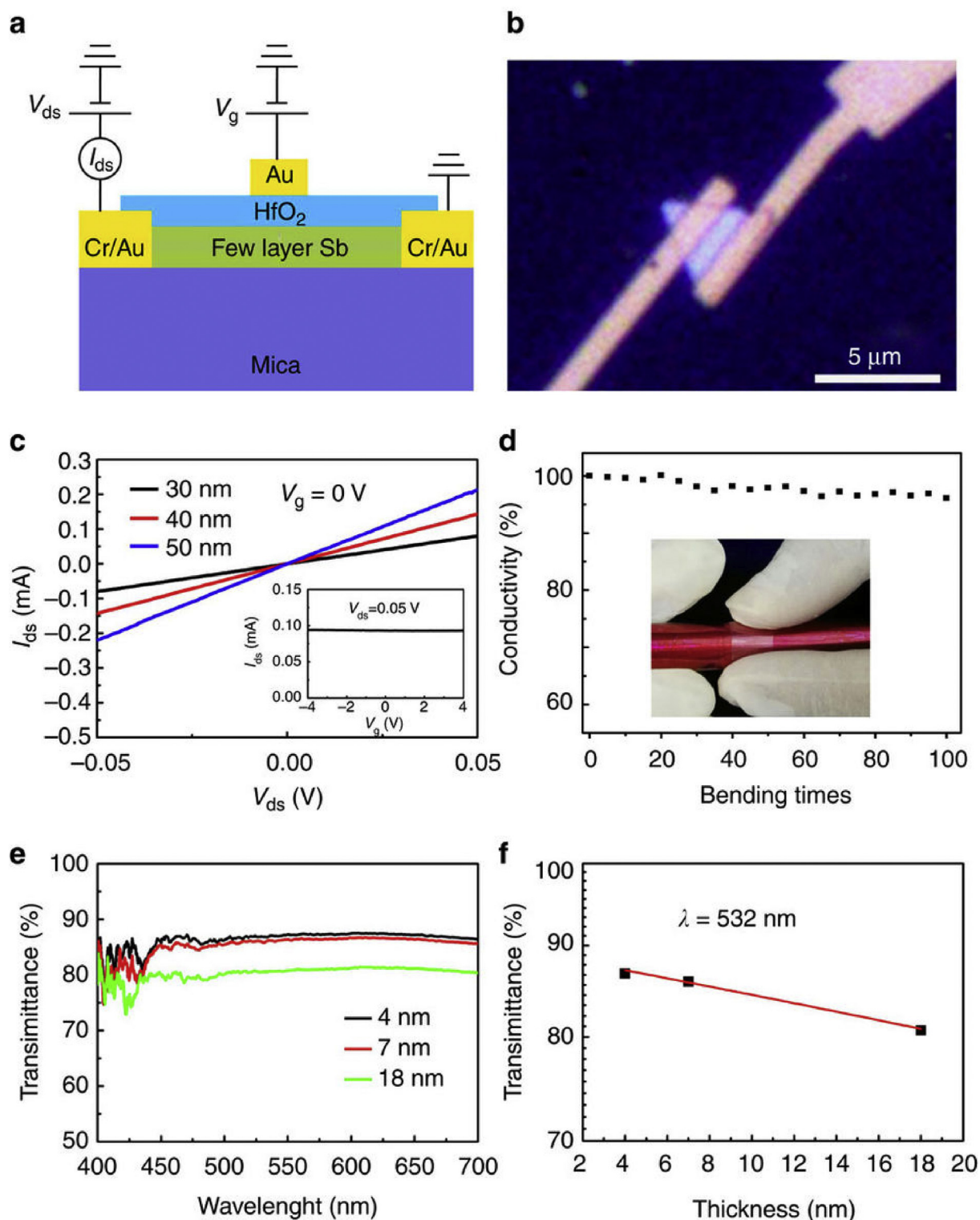


Fig. 7. ML arsenene DG MOSFET with  $L_g = 10$  nm: (a) schematic of an arsenene DG MOSFET without UL structures; (b) transfer characteristics for different source and drain electron doping concentrations ( $N_e$ ) on log (left-hand axis) and linear scales (right-hand axis). Position-resolved LDOS in the channel region at  $V_g =$  (c)  $-0.8$ , (d)  $-0.4$ , and (e)  $0$  V for  $N_e = 5 \times 10^{13} \text{ cm}^{-2}$ . The responding conduction band profiles along the channel are given in (f). The white solid line represents the Fermi level at the source or drain. Illustrated in (c) as an example, red dashed arrows represent the thermionic and tunneling electron transports, and  $\Phi_B$  is the effective barrier height; and (g) transmission eigenstates at  $E = V_{ds}/2$  and  $k = (1/3, 0)$  for  $V_g = -0.8, -0.4, \text{ and } 0$  V, respectively. The isovalue is 0.2 au. Reproduced from Ref. [27].



**Fig. 8.** Flexible transparent conductivity of antimonene polygons: (a) schematic illustration of top-gated antimonene thin film transistors; (b) optical image of a typical device fabricated on a triangular antimonene sheet; (c)  $I_{ds}$ – $V_{ds}$  characteristics of three tested devices acquired at  $V_g = 0$  V. Inset:  $I_{ds}$ – $V_g$  curve of the 30-nm thick antimonene device acquired at 0.05 V bias voltage; (d) electrical conductivity of the tested device after bending. Inset: Photograph of bended antimonene devices on mica substrate; (e) transmittance spectra of three typical antimonene polygons of 4, 7, and 18 nm thicknesses, respectively; and (f) transmittance of antimonene polygons versus sample thickness. Reproduced from Ref. [29].

as CO, H<sub>2</sub>, NH<sub>3</sub>, NO<sub>x</sub>, O<sub>2</sub>, and H<sub>2</sub>O. They investigated energetics, charge transfer, and magnetic moment on the basis of dispersion-corrected density functional theory (DFT). The authors concluded that CO, H<sub>2</sub>, NH<sub>3</sub>, and H<sub>2</sub>O molecules behave as weak donors, whereas O<sub>2</sub> and NO<sub>2</sub> behave as strong acceptors. NO<sub>2</sub> molecules also have the strongest interaction with the material [22].

The experimental study reported by Cui et al. [23] proved the theoretical calculations. The phosphorene nanosheets (PNS) devices can still detect contents of NO<sub>2</sub> molecules below than 100 parts per billion (ppb) due to significant change of the hole concentration in the PNS while its carrier mobility is negligible (Fig. 5A). The sensitivity of black phosphorus FET to NO<sub>2</sub> was further improved to the ppb levels for NO<sub>2</sub> (Fig. 5B) [24]. Black phosphorus is sensitive to water in general; this has been utilized for water vapor sensing by FET based on electrochemically exfoliated FET [25].

The ultrathin BP layers are subject of oxidation, thereby hindering its performance [3]. Recently, a solution to this problem was demonstrated by Chen and co-workers who reported a mechanically exfoliated BP biosensor passivated by a very thin film of Al<sub>2</sub>O<sub>3</sub> in order to detect human immunoglobulin G (IgG) through anti-human IgG-conjugated gold nanoparticles [26]. The IgG detection was accomplished by measuring changes in source-drain current upon the antibody–antigen binding interactions (Fig. 6A). The BP biosensor demonstrated a limit of detection (LOD) of 10 ng·mL<sup>-1</sup> and fast response time on the order of seconds (Fig. 6B).

## 2.2. Arsenene

Wang et al. [27] performed the first investigation of the many-body effect, carrier mobility and, performance of monolayer arsenene (Fig. 7). The carrier mobility in arsenene 10 nm FET was estimated to be 21 cm<sup>2</sup>·V<sup>-1</sup>·s<sup>-1</sup> for electrons and 66 cm<sup>2</sup>·V<sup>-1</sup>·s<sup>-1</sup> for holes, respectively.

Liu et al. [28] performed the first-principle calculation to determine the adsorption of CO, CO<sub>2</sub>, N<sub>2</sub>, NH<sub>3</sub>, NO, and NO<sub>2</sub> molecules on pristine arsenene. The interaction between these gas molecules and the arsenene monolayer is intermediate between the physisorbed and chemisorbed states. The authors predicted a significant modification of density of states near the Fermi level caused by the adsorption of NO and NO<sub>2</sub> molecules, and this adsorption also leads to a magnetic moment of 1 μB. The theoretical basis shows the great potential of an arsenene monolayer for gas detection using electrical and magnetic methods.

## 2.3. Antimonene

Ji et al. [29] synthesized high-quality, few-layer antimonene polygons on mica substrate through van der Waals epitaxy (Fig. 8). Their electrical characterizations demonstrate that the synthesized antimonene polygons have good electrical conductivity on the order of 10<sup>4</sup> S·m<sup>-1</sup>. HRTEM microscopy and Raman spectroscopy also revealed that the obtained antimonene polygons are consistent

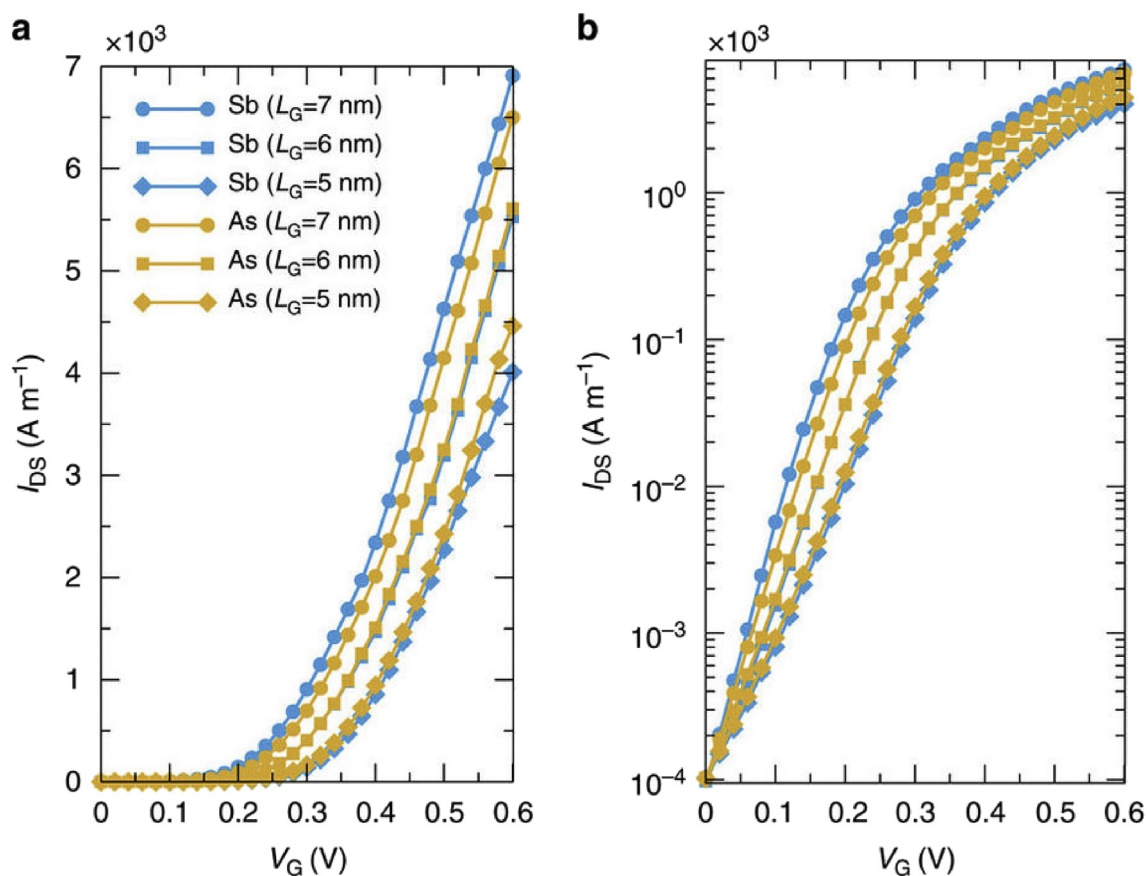


**Fig. 9.** Transfer characteristics of As- and Sb-based MOSFETs:  $I_{DS}$ – $V_G$  curve in (a) linear and (b) semi-logarithmic scales for Sb (light-blue lines) and As (yellow lines) transistors with  $L_G = 7$  nm,  $V_{DS} = 0.6$  V, and  $t_{ox} = 0.5$  nm (circles),  $L_G = 6$  nm,  $V_{DS} = 0.57$  V, and  $t_{ox} = 0.45$  nm (squares) and  $L_G = 5$  nm,  $V_{DS} = 0.54$  V, and  $t_{ox} = 0.42$  nm (diamonds). Reproduced from Ref. [30].

with the atomic structure of the most stable allotrope of monolayer antimonene. Optical microscopy, AFM, Raman spectroscopy, and XPS also proved the good stability of antimonene polygons when exposed in air. Pizzi et al. [30] provided a comprehensive analysis of 2D FET transistors based on arsenene and antimonene (Fig. 9). They showed that these materials are promising for high-performance devices for digital applications. Due to the channel lengths below 10 nm and the atomic thickness of the exploited 2D materials, short channel effects are suppressed and tunneling starts to play a major role.

The pristine antimonene was evaluated as a high-performance gas sensor based on its gas-adsorption behaviors [31]. It was reported that the polluted gas adsorbates ( $\text{NH}_3$ ,  $\text{SO}_2$ ,  $\text{NO}$ , and  $\text{NO}_2$ ) showed a stronger affinity toward antimonene with considerable absorption energies and elevated charge transfers while the atmospheric gas molecules ( $\text{N}_2$ ,  $\text{CO}_2$ ,  $\text{O}_2$ , and  $\text{H}_2\text{O}$ ) bind weakly. The monolayered antimonene seems a promising sensing material for pollutant gas detection due to the susceptibility of its electronic properties induced by the absorbed molecules. The antimonene was predicted as the most suitable candidate for acetone sensors due to sensitivity and high selectivity [32].

#### 2.4. Silicene

The silicene band gap can be opened without degrading its carrier mobility, which is ideal for the fabrication of high-performance FET devices. Tao et al. [33] performed measurements of silicene FET at room temperature. His results (Fig. 10) on silicene prepared by encapsulated delamination with native electrodes show carrier mobility of  $\sim 100 \text{ cm}^2 \cdot \text{V}^{-1} \cdot \text{s}^{-1}$ .

Prasongkit et al. [34] estimated silicene sensitivity and selectivity on detection of  $\text{NO}$ ,  $\text{NO}_2$ ,  $\text{NH}_3$ , and  $\text{CO}$  gases using DFT and the no-equilibrium Green's function method. They revealed strong sensitivity of pristine silicene for  $\text{NO}$  and  $\text{NO}_2$  but unusable for  $\text{CO}$  and  $\text{NH}_3$  detection. Doping of silicene with B or N atoms resulted to enhanced binding energy (Fig. 11A) and charge transfer (Fig. 11B), which positively affected the sensitivity. Silicene-based devices are predicted to be very selective and sensitive gas sensors.

#### 2.5. Germanene

Madhushankar et al. [35] synthesized and experimentally studied the electronic properties of germanene FET (Fig. 12A).

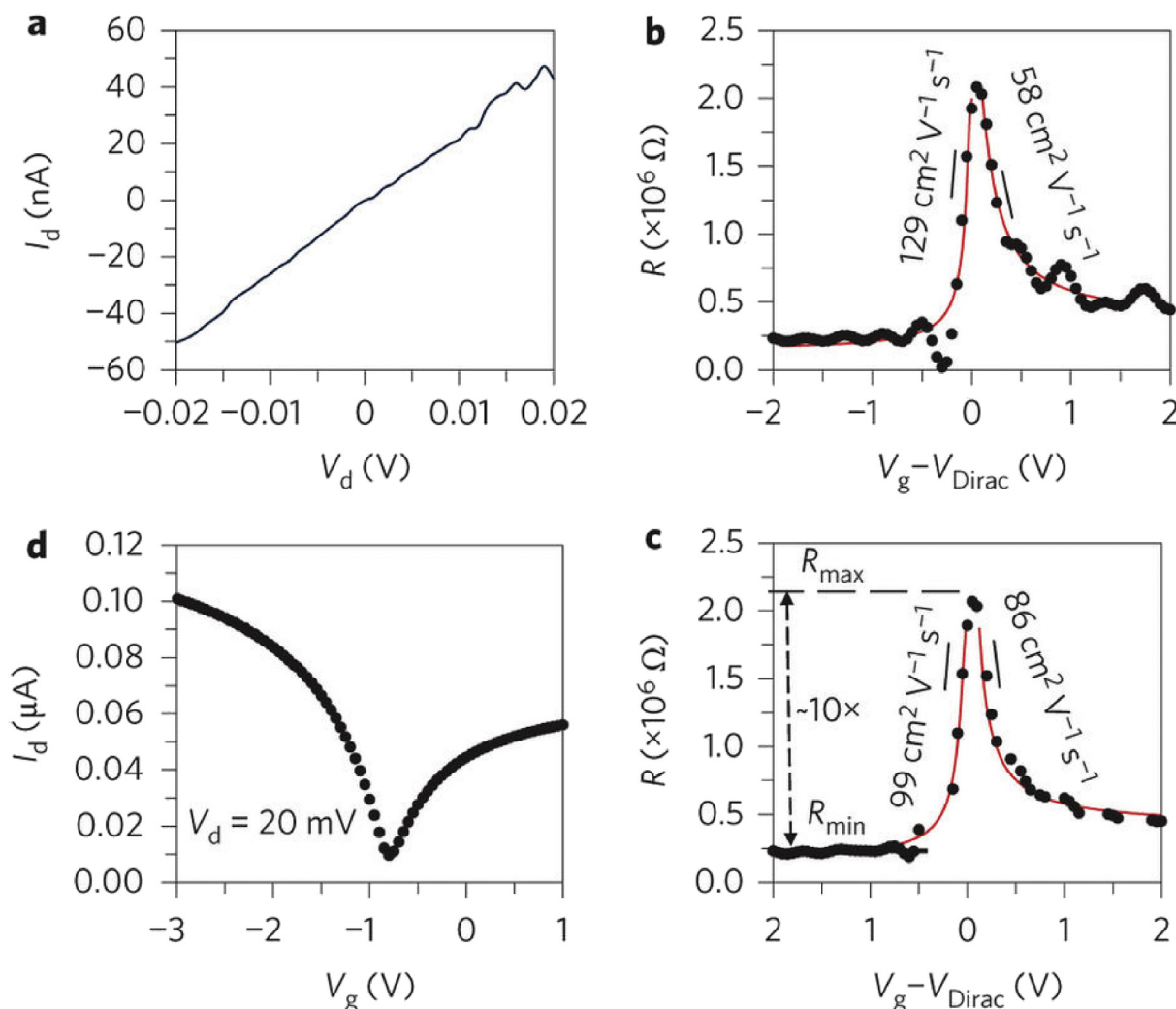


**Fig. 10.** (a) Low-field linear  $I_d$  vs.  $V_d$  response at  $V_g = 0$ . (b, c)  $R$  vs.  $(V_g - V_{\text{Dirac}})$  of silicene devices 1 and 2, respectively. Measured transfer characteristics (dots) are in good agreement with a widely used ambipolar diffusive transport model (line), which yields extracted low-field hole and electron carrier mobilities of  $129$  and  $99 \text{ cm}^2 \cdot \text{V}^{-1} \cdot \text{s}^{-1}$  and  $58$  and  $86 \text{ cm}^2 \cdot \text{V}^{-1} \cdot \text{s}^{-1}$  in devices 1 and 2, respectively, with similar residual carrier concentration of  $\sim 3\text{--}7 \times 10^9 \text{ cm}^{-2}$ , more than an order of magnitude lower than in graphene transistors. (d)  $I_d$  vs.  $V_g$  curve of silicene device 2 displays ambipolar electron–hole symmetry expected from silicene. In B–D, both devices are from the same mixed-phase silicene sample with channel length of  $1.8 \mu\text{m}$  and width of  $230 \text{ nm}$ , and fixed  $V_d = 20 \text{ mV}$  for the measurements. Reproduced from Ref. [33].

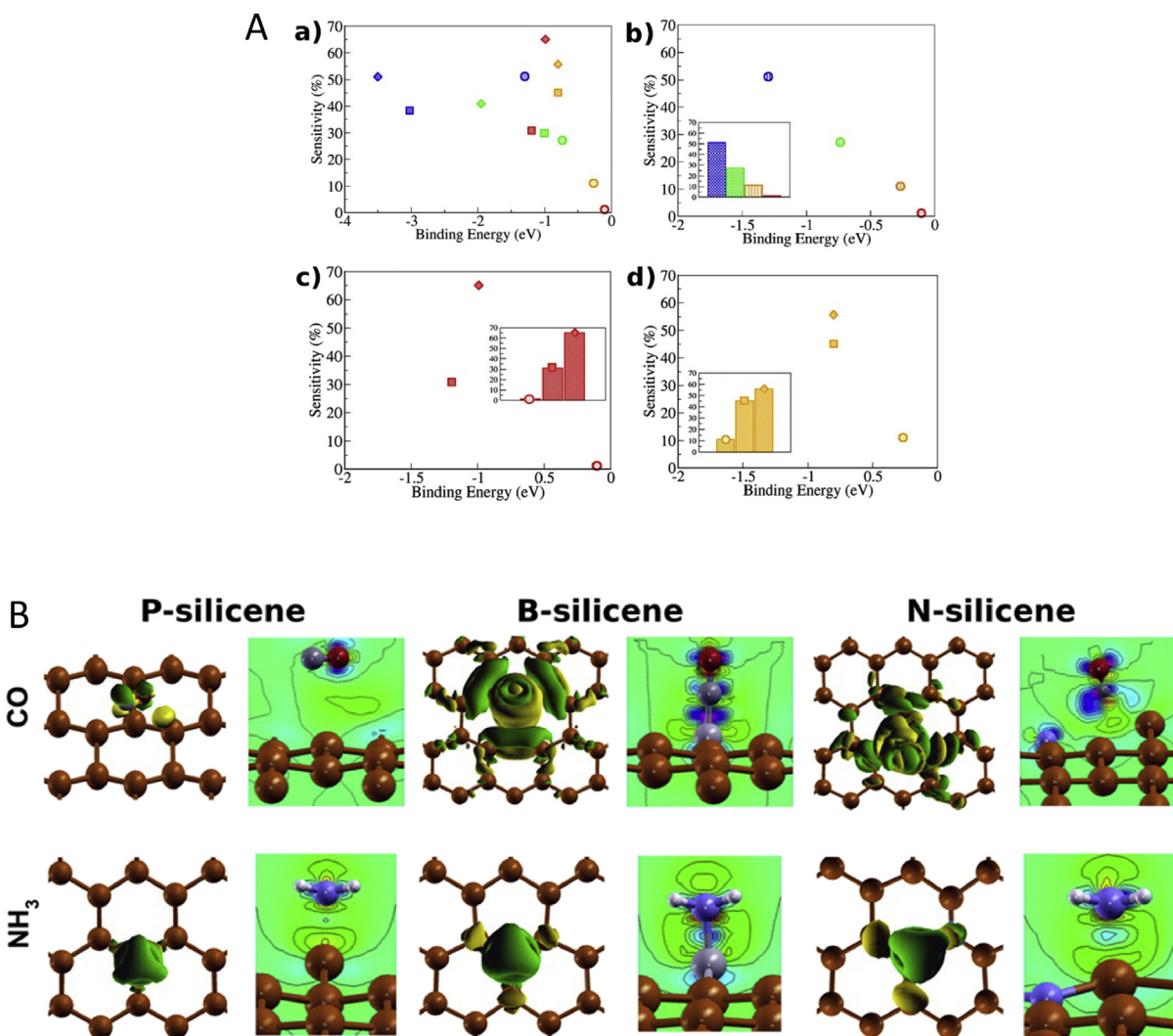


**Fig. 11.** Silicene sensitivity estimation for gas sensing (A): (a) sensitivity versus binding energy for NO (green), NO<sub>2</sub> (blue), NH<sub>3</sub> (orange), and CO (red) gas molecules on P-silicene (circle), B-silicene (square) and N-silicene (diamond) devices, respectively; (b) the four gas species on P-silicene (the inset shows the sensitivity comparison for P-silicene); (c) CO on three devices; and (d) NH<sub>3</sub> on three devices. The insets of parts (c) and (d) are the sensitivity comparison for one gas on the three different devices. (B) Charge density difference for CO (upper) and NH<sub>3</sub> (lower panel) on P-, B-, and N-silicene devices for each type of nanosensor. Isosurfaces are plotted for isovalues of  $0.0004$  ( $0.002$ )  $\times \text{bohr}^{-3}$  for CO (NH<sub>3</sub>) alongside contour plots. For the isosurface plots, the green color represents negative charge density difference while yellow corresponds to a positive change in charge density. Reproduced from Ref. [34].

Authors performed initial electrical characterization at room temperature in the linear regime (Fig. 12B). Their germanene devices demonstrated transport in both electron- and hole-doped regimes with on/off current ratio of up to  $10^5$  ( $10^4$ ) and carrier mobilities of  $150 \text{ cm}^2 \cdot \text{V}^{-1} \cdot \text{s}^{-1}$  ( $70 \text{ cm}^2 \cdot \text{V}^{-1} \cdot \text{s}^{-1}$ ) at room temperature.

Gupta et al. [36] used a first-principles DFT calculation to show the possibility of the germanene monolayer for toxic gas detection. Theoretical prediction showed that molecules of NH<sub>3</sub>, NO<sub>2</sub>, and SO<sub>2</sub> are physisorbed on germanene. Based on these results (Fig. 13A), the NO<sub>2</sub> has the strongest interaction with the hexagonal armchair germanene monolayer (273.72 meV). The NO<sub>2</sub> molecule has also much higher values of the charge transfer (Fig. 13B) than other investigated gases, which results in the highest stability and sensitivity for this molecule. Reported results indicate the germanene monolayer has a huge potential as a miniaturized sensor for detecting NO<sub>2</sub> gas.

### 3. Conclusions

The many potential applications of ultrathin 2D materials in sensing and biosensing FETS have taken the chemistry and physics fields by storm. There has been intensive research on the utilization of graphene for FET sensors, and more recently by 2D transition metal dichalcogenides (TMD, for an example MoS<sub>2</sub>, WS<sub>2</sub>, MoSe<sub>2</sub> and others) for FET based sensors. While the band-gap of TMD depends not only on their composition but also on phase purity, which is in many cases challenging to control, this is not a main issue for mono-elemental materials, such 2D phosphorene, arsenene, antimonene and group IVA materials, such as silicene and germanene. Therefore it is not surprising that the utilization of 2D Group VA materials, such as phosphorene, arsenene, antimonene, and Group IVA materials, such as silicene and germanene, for FET sensors, is in rapid development. We have shown here only selected examples

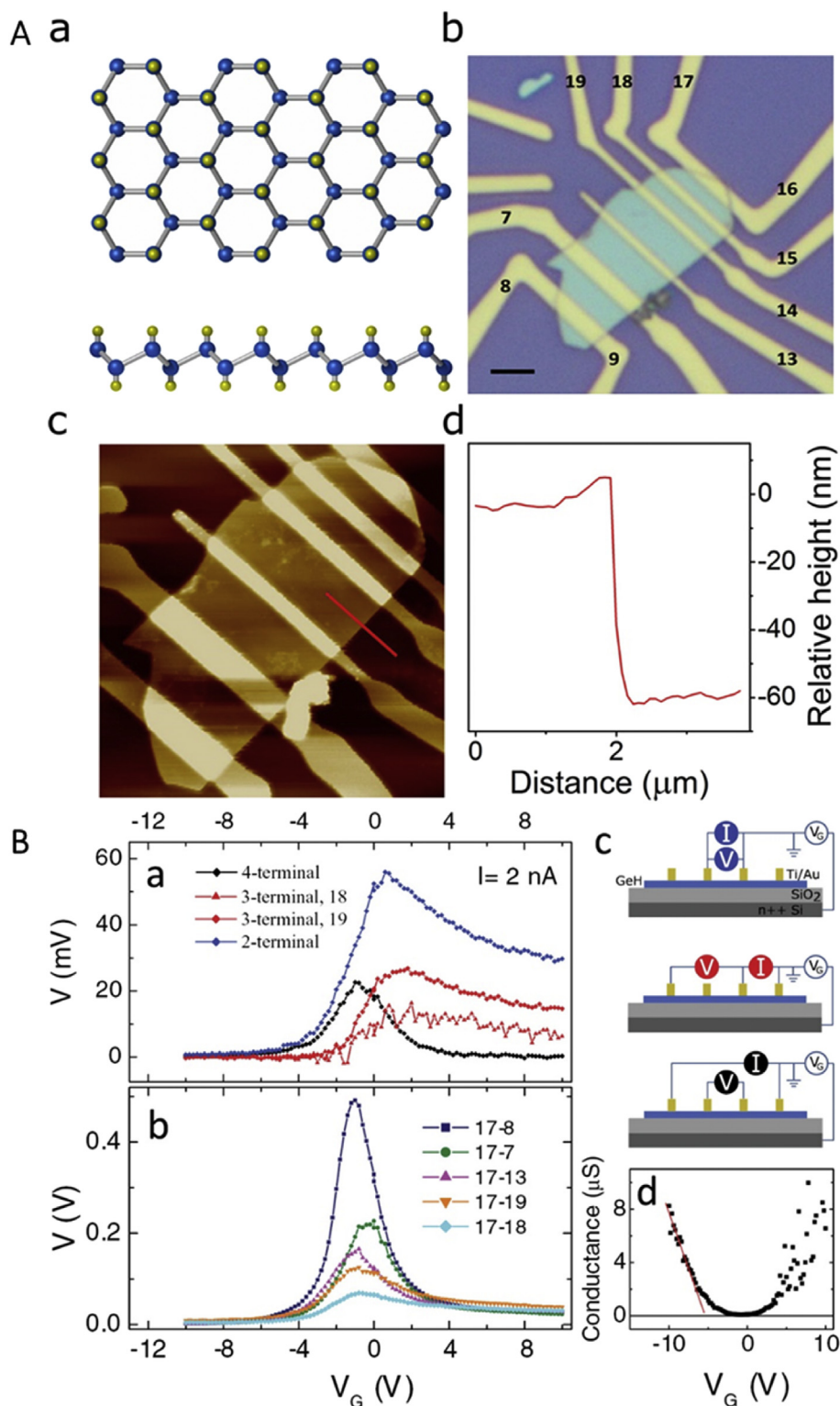


**Fig. 12.** Germanene as FET (A): (a) schematic representation of a germanene monolayer (top and side views) with Ge atoms (blue) at the corners of hexagons and H atoms (yellow) bonded to Ge; (b) optical image of the germanene flake-based device on top of a Si/SiO<sub>2</sub> substrate with Ti/Au electrodes (scale bar is 3 μm); (c) AFM image of the germanene transistor; and (d) height profile is plotted along the red line as shown in panel (c) giving the flake thickness to be 60 nm. (B) (a) Measured signal  $V$  plotted for 2-terminal (blue), 3-terminal (red), and 4-terminal (black) configurations as a function of the gate voltage. The applied constant current between source and drain was 2 nA, and the measurements were performed at room temperature; (b) 2-terminal measurements as a function of  $V_G$  performed using different distances between the contacts while keeping the same source contact. The resistance values at the curve maxima scale approximately with the channel length (for the sample geometry, see Fig. 12A(b)).  $I = 2$  nA; (c) 2-, 3-, and 4-terminal measurement configurations allow the contact and channel-related resistances to be extracted separately; and (d) room temperature conductance calculated from the 4-terminal measurement shown in panel (a). The red line represents a linear fit resulting in a mobility of  $\sim 30$  cm<sup>2</sup>·V<sup>-1</sup>·s<sup>-1</sup>. Reproduced from Ref. [35].

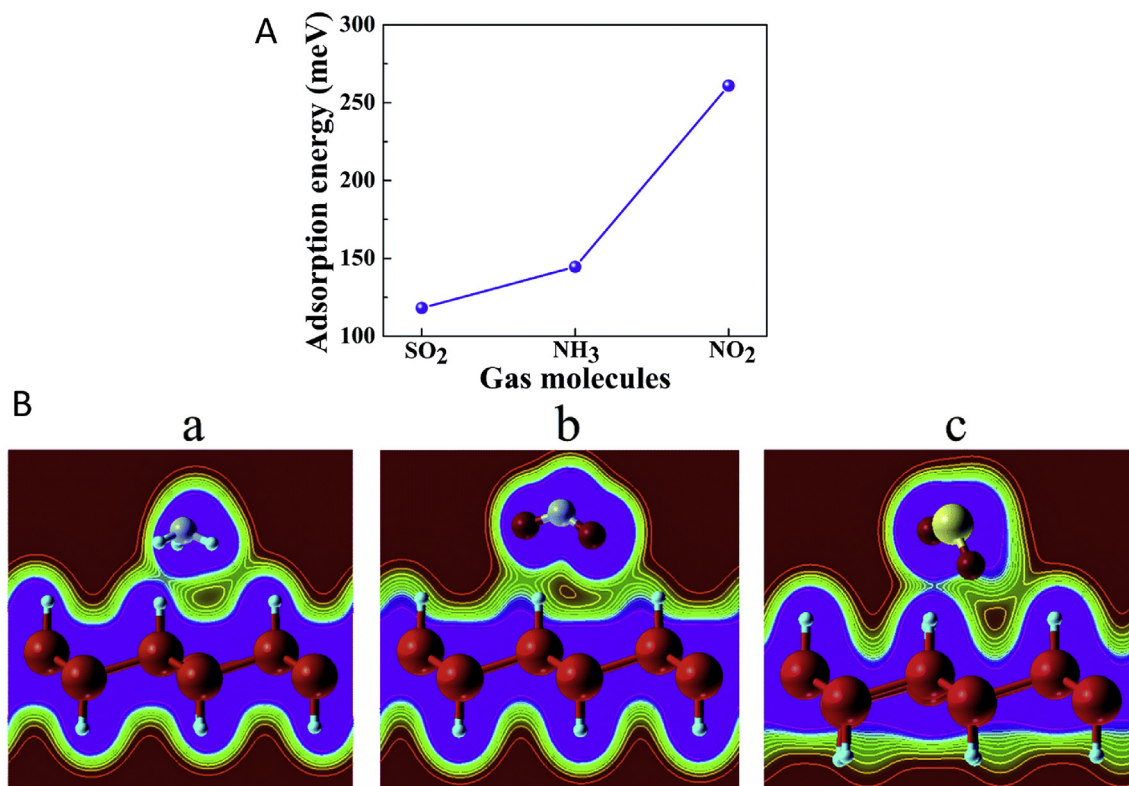


**Fig. 13.** (A) Adsorption energies (meV) of NH<sub>3</sub>, SO<sub>2</sub>, and NO<sub>2</sub> gas molecules on the hexagonal armchair (3 × 3 × 1) germanene monolayer of lowest energy (E-type) configuration. (B) Charge density difference plots for (a) NH<sub>3</sub> (b) NO<sub>2</sub>, and (c) SO<sub>2</sub> gas molecules interacting with the top surface of the hexagonal armchair 3 × 3 × 1 germanene monolayers of E-type configurations.

describing trends in this area with applications in the field of analytical chemistry.

#### Acknowledgement

We acknowledge the support of Grant Agency of the Czech Republic under the contract GJ18-06498Y and support of the Ministry of Education, Youth and Sports of the Czech Republic under the project OP VVV CEITEC Nano+ (CZ.02.1.01/0.0/0.0/16\_013/0001728). Authors I. Gablech and J. Pekárek also acknowledge the foundation support FEKT/STI-J-17-4136. M.P. thanks A\*Star grant (No. SERC A1783c0005), Singapore.

#### References

- [1] E. Fitzer, K.H. Kochling, H.P. Boehm, H. Marsh, Recommended terminology for the description of carbon as a solid – (IUPAC recommendations 1995), *Pure Appl. Chem.* 67 (1995) 473–506.
- [2] P.W. Bridgman, Further note on black phosphorus, *J. Am. Chem. Soc.* 38 (1916) 609–612.
- [3] R. Gusmao, Z. Sofer, M. Pumera, Black phosphorus rediscovered: from bulk material to monolayers, *Angew. Chem. Int. Ed.* 56 (2017) 8052–8072.
- [4] M. Pumera, Z. Sofer, 2D mono-elemental arsenene, antimonene, and bismuthene: beyond black phosphorus, *Adv. Mater.* 29 (2017).
- [5] A. Dimoulas, Silicene and germanene: silicon and germanium in the “flatland”, *Microelectron. Eng.* 131 (2015) 68–78.
- [6] E. Golias, E. Xenogiannopoulou, D. Tsoutsou, P. Tsipas, S.A. Giamini, A. Dimoulas, Surface electronic bands of submonolayer Ge on Ag(111), *Phys. Rev. B* 88 (2013).
- [7] P. Vogt, P. De Padova, C. Quaresima, J. Avila, E. Frantzeskakis, M.C. Asensio, A. Resta, B. Ealet, G. Le Lay, Silicene: compelling experimental evidence for graphenelike two-dimensional silicon, *Phys. Rev. Lett.* 108 (2012).
- [8] L.J. Edgar, in: U. Grant (Editor), *Device for Controlling Electric Current*, Lilienfeld Julius Edgar USA, 1928.
- [9] D. Kahng, in: U.P. Office (Editor), *Electric field controlled semiconductor device*, Bell Telephone Laboratories, Inc., N.Y. USA, US, 1963.
- [10] S.M. Sze, K.K. Ng, *MOSFETs, Physics of Semiconductor Devices*, John Wiley & Sons, Inc., 2006, pp. 293–373.
- [11] P. Bergveld, Development of an ion-sensitive solid-state device for neurophysiological measurements, *IEEE Trans. Biomed. Eng.* 17 (1970) 70–71.
- [12] K.I. Lundstrom, M.S. Shivaraman, C.M. Svensson, Hydrogen-sensitive Pd-Gate Mos-transistor, *J. Appl. Phys.* 46 (1975) 3876–3881.
- [13] A.K. Geim, K.S. Novoselov, The rise of graphene, *Nat. Mater.* 6 (2007) 183–191.
- [14] K.S. Novoselov, A.K. Geim, S.V. Morozov, D. Jiang, Y. Zhang, S.V. Dubonos, I.V. Grigorieva, A.A. Firsov, Electric field effect in atomically thin carbon films, *Science* 306 (2004) 666–669.
- [15] B.B. Zhan, C. Li, J. Yang, G. Jenkins, W. Huang, X.C. Dong, Graphene field-effect transistor and its application for electronic sensing, *Small* 10 (2014) 4042–4065.
- [16] F. Schwierz, Graphene transistors, *Nat. Nanotechnol.* 5 (2010) 487–496.
- [17] Y. Wang, Y. Ding, Electronic structure and carrier mobilities of arsenene and antimonene nanoribbons: a first-principle study, *Nanoscale Res. Lett.* 10 (2015) 1–10.
- [18] H. Liu, A.T. Neal, Z. Zhu, Z. Luo, X.F. Xu, D. Tomanek, P.D. Ye, Phosphorene: an unexplored 2D semiconductor with a high hole mobility, *ACS Nano* 8 (2014) 4033–4041.
- [19] J. Zhao, H. Liu, Z. Yu, R. Quhe, S. Zhou, Y. Wang, C.C. Liu, H. Zhong, N. Han, J. Lu, Y. Yao, K. Wu, Rise of silicene: a competitive 2D material, *Prog. Mater. Sci.* 83 (2016) 24–151.
- [20] X.-S. Ye, Z.-G. Shao, H. Zhao, L. Yang, C.-L. Wang, Intrinsic carrier mobility of germanene is larger than graphene's: first-principle calculations, *RSC Adv.* 4 (2014) 21216–21220.
- [21] L.Z. Kou, T. Frauenheim, C.F. Chen, Phosphorene as a superior gas sensor: selective adsorption and distinct I-V response, *J. Phys. Chem. Lett.* 5 (2014) 2675–2681.
- [22] Y.Q. Cai, Q.Q. Ke, G. Zhang, Y.W. Zhang, Energetics, charge transfer, and magnetism of small molecules physisorbed on phosphorene, *J. Phys. Chem. C* 119 (2015) 3102–3110.
- [23] S.M. Cui, H.H. Pu, S.A. Wells, Z.H. Wen, S. Mao, J.B. Chang, M.C. Hersam, J.H. Chen, Ultrahigh sensitivity and layer-dependent sensing performance of phosphorene-based gas sensors, *Nat. Commun.* 6 (2015).
- [24] A.N. Abbas, B. Liu, L. Chen, Y. Ma, S. Cong, N. Aroonyadet, M. Koepf, T. Nilges, C. Zhou, Black phosphorus gas sensors, *ACS Nano* 9 (2015) 5618–5624.
- [25] M.B. Erande, M.S. Pawar, D.J. Late, Humidity sensing and photodetection behavior of electrochemically exfoliated atomically thin-layered black phosphorus nanosheets, *ACS Appl. Mater. Interfaces* 8 (2016) 11548–11556.
- [26] Y.T. Chen, R. Ren, H.H. Pu, J.B. Chang, S. Mao, J.H. Chen, Field-effect transistor biosensors with two-dimensional black phosphorus nanosheets, *Biosens. Bioelectron.* 89 (2017) 505–510.

- [27] Y.Y. Wang, P. Huang, M. Ye, R. Quhe, Y.Y. Pan, H. Zhang, H.X. Zhong, J.J. Shi, J. Lu, Many-body effect, carrier mobility, and device performance of hexagonal arsenene and antimonene, *Chem. Mater.* 29 (2017) 2191–2201.
- [28] C. Liu, C.S. Liu, X.H. Yan, Arsenene as a promising candidate for NO and NO<sub>2</sub> sensor: a first-principles study, *Phys. Lett.* 381 (2017) 1092–1096.
- [29] J.P. Ji, X.F. Song, J.Z. Liu, Z. Yan, C.X. Huo, S.L. Zhang, M. Su, L. Liao, W.H. Wang, Z.H. Ni, Y.F. Hao, H.B. Zeng, Two-dimensional antimonene single crystals grown by van der Waals epitaxy, *Nat. Commun.* 7 (2016).
- [30] G. Pizzi, M. Gibertini, E. Dib, N. Marzari, G. Iannaccone, G. Fiori, Performance of arsenene and antimonene double-gate MOSFETs from first principles, *Nat. Commun.* 7 (2016).
- [31] R.S. Meng, M. Cai, J.K. Jiang, Q.H. Liang, X. Sun, Q. Yang, C.J. Tan, X.P. Chen, First principles investigation of small molecules adsorption on antimonene, *IEEE Electron. Device Lett.* 38 (2017) 134–137.
- [32] D.W. Wang, A.J. Yang, J.F. Chu, P.L. Lv, L. Yang, X.H. Wang, M.Z. Rong, Antimonene: A Promising Candidate for Acetone Sensors with High Selectivity and Sensitivity, *IEEE SENSORS*, 2017, pp. 1–3.
- [33] L. Tao, E. Cinquanta, D. Chiappe, C. Grazianetti, M. Fanciulli, M. Dubey, A. Molle, D. Akinwande, Silicene field-effect transistors operating at room temperature, *Nat. Nanotechnol.* 10 (2015) 227–231.
- [34] J. Prasongkit, R.G. Amorim, S. Chakraborty, R. Ahuja, R.H. Scheicher, V. Amornkitbamrung, Highly sensitive and selective gas detection based on silicene, *J. Phys. Chem. C* 119 (2015) 16934–16940.
- [35] B.N. Madhushankar, A. Kaverzin, T. Giouis, G. Potsi, D. Gournis, P. Rudolf, G.R. Blake, C.H. van der Wal, B.J. van Wees, Electronic properties of germanene field-effect transistors, *2D Mater.* 4 (2017).
- [36] S.K. Gupta, D. Singh, K. Rajput, Y. Sonvane, Germanene: a new electronic gas sensing material, *RSC Adv.* 6 (2016) 102264–102271.